Solar Thermochemical Cycles for Hydrogen Production (STCH)

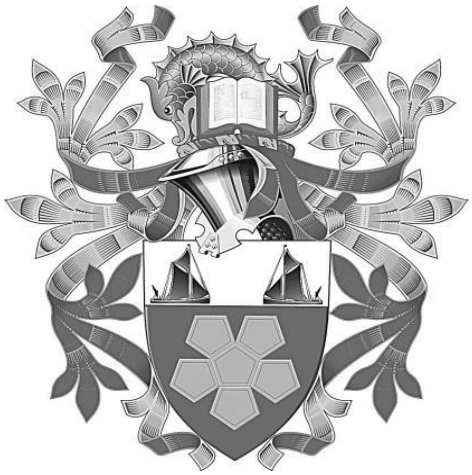

Elaheh Hojaji Najafabadi

This thesis submitted in partial fulfilment of requirement at
London South Bank University for the degree of
Doctor of Philosophy

In

Chemical, Process and Energy Engineering

This research programme was funded by

School of Engineering, London South Bank University

April 2020

Declaration

I declare that the thesis has been composed by myself with fabulous support of my supervisor. The thesis is submitted for examination in consideration of the award of a higher degree of Doctor of Philosophy in Chemical, Process and Energy Engineering. I would like to emphasise that it is my personal effort and that the work has not be submitted for any other degree or professional qualification. Furthermore, I took reasonable care to ensure that the work is original and to the best of my knowledge, does not breach copyright law and has not been taken from other sources except where such work has been cited and acknowledged within the text. The copyright of this thesis rests with the author and no quotation from it or information derived from it may be published without the prior written consent of the author.

Elaheh Hojaji Najafabadi
April, 2020

Acknowledgement

I would like to express my thanks to my supervisors especially, Dr. Anna-Karin Axelsson, for all her endless support, guidance, patience and foresight throughout my PhD. I felt very lucky and honoured to be a part of her group as I really admired her work and science ethics. She was always there to give ideas and always was very encouraging when I struggled with my PhD.

I would also like to extend my gratitude especially to Mr. Charles Coster for providing technical advice on furnace performance, Mr. Mehdi Zahiri for light instalment on the photoreactor, Mr. Richard White for measuring LEDs light intensity, Mr. William Cheung for his help with Ion Chromatography and GC analysis and Dr. Hassan Zabihi for helping me in the setting up of the photoreactor.

Furthermore, I would like to thank Professor Matjaz Valant ,University of Nova Gorica in Slovenia for his help in analysing my synthesised particles with XRD and TG-DSC.

I warmly thank Dr. Jeremy Ball, Dr. Issa Chaer and Dr. Lowry Gordon for their valuable advice and friendly help with photo spectra measurements. Their extensive discussions around my work have been very helpful for the progress of this study.

I also would like to thank London South Bank University for providing me with the golden opportunity to do this PhD project. Their financial support assisted me tremendously in finishing this project under four years' time.

My final and greatest thanks are for my family and especially my husband for his support, love and dedication. Without his encouragement, help and understanding it would have been impossible for me to finish this work.

Dedication

I would like to dedicate

To my whole family especially, my husband Dr Navid Izady, my parents Dr. Ahmad Hojaji and Mehri Mortazavi, my siblings Amin Hojaji and Elham Hojaji. To the director of studies Dr Anna-Karin Axelsson for trusting me from the start and keeping me smiling and motivated until the end. Lastly, this dedication would not be complete if I do not mention God Almighty. I am grateful to him for providing me a great chance of reaching my milestone.

Abstract

In the last decade, there have been major developments in the generation of green fuel sources to replace fossil fuels with the aim of reducing greenhouse gas emissions. Hydrogen is one of these sources that can be used either in the power generating fuel cells or as a direct combustion fuel. To produce large hydrogen on a large scale successfully, the whole process plant ought to utilise clean energy and avoid fossil derived sources as much as possible.

This study focuses on a large scale solar driven hydrogen production in form of a closed sulphur-ammonia thermochemical water-splitting cycle. The cycle utilises both the thermal and quantum components of free and widely available solar irradiation to drive the oxygen and hydrogen generation respectively. The only fluid input to the cycle is water, and only output is hydrogen and oxygen gases. However, in the most common type of sulphur-ammonia cycle, the hydrogen producing step is undertaken by a high energy demanding electrolyser at high operating temperature. In this research, the electrolyser step is replaced by a solar driven photocatalytic reactor step, as a mean to make the cycle more economical and greener. To begin with, an energy efficient and economically viable photoreactor based on LED lightning, which could mimic the quantum part of solar irradiation, was designed and benchmarked. Light intensity and flux analysis of the LED lightning indicated that cool LEDs would be the most suitable option for a reactor using visible light driven cadmium sulphide (CdS) photocatalyst particles. To further increase the photostability of the CdS catalyst and improve its photonic yield, a suitable cocatalyst was searched for. Among the cocatalysts under investigation, cobalt phosphides (Co_xP) was found to be most promising for an increased hydrogen evolution at a reduced cost, if compared with more common noble metals such as Pt and Pd. Different synthesis method and synthesis parameters showed different Co_xP composition could be tuned and optimised, resulting in different hydrogen evolution

yields. The CoP synthesised through an organometallic method loaded on CdS by sonication, showed exceptionally high hydrogen yield compared to the other tested Co_xP/CdS, and even more than the most referred Pt/CdS, when an aqueous lactic acid solution was used in the reactor. All investigations involved optimising different working parameters such as; cocatalyst loading on CdS, reactor particle loading, solution concentration variation and irradiation flux. For a solar driven sulphur ammonia thermochemical cycle, the working fluid would be ammonium sulphite rather than lactic acid and therefore, the same various CdS photocatalytic composites and various working parameters were tested again but using ammonium sulphite solution instead. Once again, the organometallic synthesised CoP/CdS composite performed excellent with a comparable hydrogen yield than the more understood and elaborated Pt/CdS.

For the photocatalytic reactions of both lactic acid (aq.) and ammonium sulphite (aq.) a mathematical predictive model of the hydrogen production was developed. The model was based on a pseudo-steady state approach of the Langmuir-Hinshelwood adsorption isotherm, which further incorporated the total radiative flux effect into the model. The Langmuir-Hinshelwood part reflected the mechanism of the surface adsorption/desorption and the surface reaction rates whereas the irradiation part of the model was based on an approximate solution of radiation field theory (RTE) and the derivation of geometrical positions of the particles in a cross-section of the reactor which was further expanded to incorporate the total visible radiative flux density received by the particles in the whole photoreactor volume. One of the main advantages of the model was the successful incorporation of both the measured photocatalyst's optical scattering and absorption coefficients in the relevant LED output range of 410-500 nm, increasing the accuracy of the model. The obtained model parameters were then successfully validated for a range of photocatalytic hydrogen generation experiments conducted at various reaction conditions. These results show that the developed model can be used to predict photocatalytic hydrogen production satisfactory regardless of the radiation type, reactor size or catalyst particle, with minor computational effort or use of any commercial software. The obtained model information is suggested to work as a supporting aid for any

photocatalytic reactor scale-up, which can easily be altered to either reduction product (hydrogen) or oxidation product if the most dominating initial reactions are known. A feasibility study of a complete thermochemical cycle was also done, where implementing several groups of parallel hydrogen photoreactors was suggested as the best option for large scale hydrogen production with the main purpose of replacing the energy demanding electrolyser in the thermochemical cycle. The parallel photoreactor configuration can be easily implemented and be operationally efficient in any thermochemical cycle configuration. Finally, it was shown that an increased hydrogen efficiency (due to an increased photonic energy conversion) and an improved hydrogen economy of the cycle (due to use of cheaper catalyst & reactor materials and a reduced power consumption) can be achieved.

Table of Contents

List of Figures

List of Tables

Summary of Notations

b [dimensionless]	parameter
β [rad]	FWHM of the XRD peak
C_{cat} [g cm^{-3}]	catalyst concentration
C [m/s]	speed of light λ
d [m]	interplanar spacing within the crystal
Eg [eV]	energy of the optical band gap
G^{α} [s^{-1} m^{-3} nm^{-1}]	total radiative flux
$G_{\lambda}[L_1, \theta_1]$ [W m^{-2} nm^{-1}]	total radiative flux at segment of $[L_1, \theta_1]$
hv [eV]	the photon energy
h[cm]	reaction height
h' [J/s]	Planck's constant
$I_{\Omega,\lambda}$ ([W m^{-2} nm^{-1}]	light intensity is a function of direction (Ω) and wavelength (λ)
$I_{bb,\lambda}$ [W m^{-2} nm^{-1}]	black body light intensity
I_0 [W m^{-2} nm^{-1}]	incident radiative flux density at the reactor wall
$I_{\lambda}[L_i, \theta_i]$ [W m^{-2} nm^{-1}]	radiative flux density at segment of $[L_1, \theta_1]$
k [cm^{-1}]	light absorption coefficient
k_1 [μmol^{-1} s^{-1}]	adsorption equilibrium constant
k_{-1} [Litre^{-1} s^{-1}]	desorption equilibrium constant
k' [m^2 Litre^{-1} J^{-1}]	proportionality constant
L [cm]	light path length
$[LA]$ (M)	lactic acid concentration
r_{H_2} [μmol/s]	rate of hydrogen production

R_∞ [dimensionless]	diffuse reflectance of the catalyst
r_1[cm]	distance between a particle inside the reactor and light of 1
r_0 [cm]	distance between light 1 and the surface of the reactor
r_1^L[cm]	distance from light 1 and circumference point farer from the light
s [cm^{-1}]	scattering coefficient
s^* [cm^2 g^{-1}]	scattering coefficient per unit catalyst concentration
S [cm^2]	area of cross-section of the reactor
t[min]	reaction time
v [cm^3]	reactor volume
θ [rad]	cylindrical angular coordinate
θ' [rad]	angle between the incoming and scattered X-ray beam
α [dimensionless]	light absorbing parameter
α' [dimensionless]	absorption coefficient
ε [dimensionless]	emissivity constant
Ω [sr]	solid angle
λ[nm]	radiation wavelength

Chapter 1: Introduction

In this chapter the main outline for this thesis is presented. First, solar-driven hydrogen technologies are briefly compared to identify the research gap for this thesis purpose, which is a visible light driven photocatalytic hydrogen production step replacing the energy demanding electrolyser in a sulphur ammonia thermochemical cycle. Then the current challenges of the hydrogen produced by the solar driven photocatalysis are presented, which by solving would offer a high solar hydrogen efficiency of the thermochemical cycle. Extra attention is also given to produce and use correct catalytic particles in the reactor that are stable, inexpensive and efficient.

Moreover, suitable descriptive mathematical models for the photocatalytic reactors are explained. Building on these models, a predictive hydrogen model is developed and solved numerically. By solving the model an accurate predication of the rate of the hydrogen generation over time can be achieved regardless of the reactor size or type of irradiation source.

Finally, the aims and objectives of this research are presented, followed by the structure of the thesis.

1-1 Background

In recent years, the use of fossil fuels has gained significant attention due to their extensive utilisation and acceleration of their depletion[1]. However, these fuels often contribute to the harmful production of greenhouse gases, responsible for the global warming. To replace the fossil fuels, sustainable energy alternatives such as solar energy have been proposed [2]. Solar energy is a free and clean energy carrier which can be converted to produce hydrogen fuel. There are various ways to utilise solar energy for hydrogen production such as photochemical methods, photoelectrochemical and thermochemical methods [2]. Photochemical methods

(photocatalytic surface reactions) are currently of limited use due to the small portion of solar spectrum that can be absorbed in a commercially available semiconductor to drive the reaction and the current visible light absorbing components are of low efficiency and very expensive [3]. Photoelectrochemical set ups, using separated photoanodic or cathodic reactions in a cell, for a solar driven water splitting are more promising. The benefit here is that O_2 (g) and H_2 (g) products are spatially separated and therefore there would be no recombination to form water again. Thermochemical routes that can combine solar energy input and chemical reactions to produce O_2 (g) and H_2 (g) in a closed fluid cycle also suffer from some drawbacks that hinder their practical applications for solar hydrogen production, such as; (i) limitation to only use of part of the solar spectrum to drive any reaction (often the thermal part is considered), (ii) requirement of very high operation temperature that cannot be achieved from solar energy and (iii) high energy demanding of the electrolysers currently used in thermochemical cycles [4]. From all thermochemical routes studied to date, only one cycle has advantages that outweighs its disadvantages which is the Westinghouse cycle; a two-step water splitting process for the hydrogen and oxygen production with sulphuric acid as the working fluid. To improve performance of this cycle and improve the cycle efficiency, ammonium sulphite as a less corrosive cycling fluid has been proposed [5]. This cycle which is known as sulphur-ammonia thermochemical cycle, could potentially address all drawbacks encountered by the thermochemical cycles as both thermal and quantum components of the solar spectrum can be utilised to drive both the oxygen and hydrogen generation respectively. For an optimum overall cycle efficiency, the oxygen production step of the cycle would theoretically need to utilise 80.9% of the solar thermal energy (at wavelengths approximately >520 nm) and the hydrogen production step of the cycle the remaining 19.1% of the solar irradiance (wavelengths < 520 nm), as previously suggested by the researchers [6,7]. In a process simulation study (Aspen Plus) of the cycle, utilisation of the solar thermal portion (O_2 segment) was estimated 73.33% [8], where no solar photonic energy was utilised for the hydrogen producing step and only instead a high energy demanding electrolyser that resulted in the overall cycle efficiency of only 13-20% was used [9].This poor result suggested improvements in both the oxygen and hydrogen producing steps of the

cycle to increase the cycle efficiency. For the hydrogen producing step, the electrolyser could be replaced by a solar driven photoreactor, to improve the efficiency up to 30% but most importantly, an improved hydrogen economy would be achieved. An initial investigation on the replacement of the electrolyser with a photocatalytic reactor found an energy conversion efficiency of 12% when bare CdS photocatalyst was used and 22 % if CdS was coloaded with 0.5 w.t % Pt/Pd/Ru [7]. These initial found photonic conversion efficiencies would need to be improved if the total portion of the solar photonic energy irradiance is aimed to be utilised for the hydrogen production segment of the cycle. In addition, the proposed photocatalytic particles would introduce high cost due to the use of expensive noble metal used. These initial studies were also undertaken on an expensive reactor construction, using a high energy demanding (1000 W) solar simulator to irradiate the photoreactor. All factors together would make an upscaling hard to achieve.

In a solar driven photocatalytic step for the cycle, the hydrogen would be produced on the surface of a semiconductor upon absorption of incoming photon. One of the commonly used semiconductors is TiO_2 which is non-toxic, cost effective and chemically stable in the photocatalytic reactions. However, TiO_2 with the bandgap of 3.1 eV only allows absorption of a small portion of the solar spectrum (majority in the UV region). In addition, the formed charge carriers that diffuse to the surface would have electron potentials, not suitable for a visible light driven water splitting [10]. Other suggested photocatalyst alternatives are g-C_3 N_4 [11], WO_3 [12], $BiVO_4$ and Fe_2O_3 that have narrower bad gaps of 2.7 eV, 2.6 eV, 2.2 eV and 2.1 eV respectively and thus are more favourable for visible light driven photocatalysis. However, their utilisation for hydrogen evolution reaction is again limited due to not having suitable electron potentials of the conduction and valance bands [12]. Metal sulphide systems are instead more promising semiconductors for visible light driven hydrogen production. One of the most efficient semiconductors of this type for hydrogen evolution that ever been reported to date is cadmium sulphide (CdS) with the band gap of 2.4 eV, that owns merits such as cost-effectiveness, chemical stability and thermostability. CdS is driven by the visible light and has the right bad gap and suitable electron band potentials for driving the requested reduction and oxidation

reactions needed for the water splitting and can therefore be successfully used for the thermochemical cycle's purpose. However, prolonged irradiation of CdS leads to photocorrosion of itself, producing elemental sulphur (S^0) and therefore poor photocatalytic activity as a result. Strategies such as addition of a suitable cocatalyst on the CdS surface for entrapping electrons and/or using a sacrificial reagent in solution to be oxidised by the holes are promising to overcome the disadvantages of both the internal electron-hole recombination and the photocorrosion[13,14]. The most common cocatalyst to use with CdS is noble metal of platinum (Pt), which has shown an excellent electrocatalytic activity for the photocatalytic hydrogen production[15]. However, its high price has created a room for identifying non-noble metal alternatives with an improved efficiency. These alternatives are (i) Pd-Cr_2O_3 or Pt-PdS[7,16], (ii) $Ni(OH)_2$ [17,18] and $Co(OH)_2$ [19,20], (iii) graphene [13,16], (iv) Fe_2O_3 when loaded on (CdS +ZnS)[21], (v) $BiVO_4$[22], (vi) transition metal compounds of MoS_2 [23] or NiS [24] and MS(M=Co, Cu)/CdxZn1-xS [25], and (vii) transition metal phosphides of Ni_2P [26], FeP [27] or MoP [28] or CoP [104, 105]. The hydrogen produced from the transition metal phosphide of CoP/CdS system represents the highest value found for a CdS-based photocatalysts until today, with an excellent stability and high photocatalytic activity even after 100 h of irradiation[29]. They are also inexpensive and stable options [30]. In this thesis, cobalt phosphides were chosen to be investigated further and be used with CdS (despite their less green natures) in a visible light driven photocatalytic reactor, aimed for an ammonium sulphite thermochemical cycle.

The cobalt phosphides synthesis, which can be done by various routes, is reported to be challenging [33], where the solid phase and solution phase synthesis routes have been most-dominantly reported [30,34–37]. It is clear that the different synthesis conditions applied will result in different size and crystal morphology of the nanoparticles, and ultimately affecting the photocatalytic activities. As a comprehensive information on the cobalt phosphide (CoP and Co_2P) synthesis methods is lacking in the literature, it was put forward in this thesis, that a comparative study to evaluate the success of each synthesis method is needed. Such comparisons are essential for understanding functionality of the composite photocatalysts in the aimed photocatalytic reactions. There is also a lack of

comparative published data on the hydrogen evolution of the CdS composites using CoP and Co_2P cocatalyst in the presence of sacrificial reagents (hole donors). Obtaining a good physical contact between the main photocatalyst (CdS) and the cocatalyst surface and maintaining it over the whole photocatalytic reaction is another challenge which need more elaboration.

In the recent decade, several investigations have been conducted on describing the reaction mechanisms of the photocatalytic hydrogen production [13,14,26,38–45]. Some research efforts have also focused more towards the development of descriptive photocatalytic reaction kinetics, but mainly aimed for the photo-oxidation purposes using UV-light driven TiO_2 semiconductors [46,47]. So far, there have been only a few conducted reaction kinetics studies using visible light-driven CdS with a suitable cocatalysts [48–50], where none have been aimed for hydrogen reactor scale-up purposes. The accurate prediction for a scale-up of a photocatalytic hydrogen reactor requires a reliable and comprehensive model that incorporates both the surface reaction kinetics alongside the irradiation (photonic) mechanism. For the surface reaction kinetics, consideration of all dominating surface adsorption mechanism is needed, and for the irradiation part both the geometry of the particle filled reactor with regards to the lights, and the total radiative flux received by the particles are needed. Furthermore, a thorough validation of the developed model with empirical data, as to confirm the accuracy of the model, is essential. Over the years, David F. Ollis has developed several important publications describing in-depth the kinetics of photocatalysed chemical mechanisms [51–53], and in particular how the Langmuir-Hinshelwood parameters, *k* and *K*, vary with light intensity in what is described as a *pseudo-steady state* approach, which is considered more appropriate method to apply here than a standard equilibrated adsorption Langmuir-Hinshelwood model. In addition, several researchers have previously developed various irradiation models for different photoreactor configurations. In 2000 Cassano et al. [54] reported the importance of the light scattering effect to be included in a mathematical model describing a UV light reactor. In 2003 Brandi et al. [55] developed for the first time an important 1D model, describing more physically the quantum yield of a photocatalytic reactor relative to the incoming wavelength

spectra in a TiO_2 + UV light slurry reactor set up. Li Puma et al. also developed in 2003, a simple two-flux [56] model in a similar manner and later in 2004 the same authors presented a six-flux absorption-scattering model [57] representing the radiation field dependency to various reactor geometries. In 2018 Alvarado-Rolón et al. [58] used a comprehensive four-flux absorption-scattering model and compared its accuracy with the six-flux and two-flux absorption-scattering models in a TiO_2 + cylindrical UV light photocatalytic reactor system. As a conclusion and the shared view among these published studies, is the importance of incorporating light distribution inside a photocatalytic reactor for a complete photocatalytic reaction rate evaluation.

The actual photon-particle interaction inside the photoreactor can be described mathematically by the basis of the radiative transfer equations (RTE), which allow quantification of the radiation distribution on photocatalyst particles at a certain wavelength [59]. The RTE contains integro-differential equations that can be solved through various methods, such as Monte Carlo method [60], discrete ordinates (DO) radiation methods [61] or Finite Volume Methods (FVM) [47]. However, these approaches are usually computationally expensive and prone to discretization error. In 2012, Palmisano et. al. [62] successfully reduced these complications by simplifying the RTE integro-differential equations, which resulted in a substantial reduction of computational time. The accuracy of the proposed radiation model was then successfully validated, by the same group in 2015, against a UV irradiated photoreactor for the photocatalytic oxidation of 4-nitrophenol using TiO_2 [47].

1-2 Research aim and objectives

The aim of this research is to investigate a photocatalytic hydrogen producing step for a solar-driven sulphur ammonia thermochemical cycle. Despite several published work on the development of hybrid sulphur-ammonia thermochemical cycle[7,63,64], this type of cycle still have obstacles to solve until it can be considered as a safe and low energy input technology with reduced process temperature. Introduction of a photocatalytic hydrogen step to replace the traditional electrolytic step of the cycle, is an attractive solution to achieve higher hydrogen efficiency and therefore a higher hydrogen economy of the cycle. In this research, the quantum

energy absorption in the cycle will be investigated using an energy efficient and economically viable photoreactor with appropriate photocatalyst materials.

Therefore, research objectives are as follows:

- Synthesising visible light driven photocatalyst composites such as Pt/CdS, CoP/CdS and Co_2P/CdS.
- Designing an economical viable hydrogen generating photoreactor based on cool-LED lightning system (representing the visible light in the solar spectrum).
- Evaluating the photocatalytic hydrogen performance of the synthesised composite systems at different operational parameters of irradiation time, temperature effect, loading effect, photolyte concentration.
- Developing a descriptive mathematical model for a hydrogen photoreactor using CdS composite photocatalyst at different operational parameters of irradiation time, temperature effect, loading effect, photolyte concentration.
- Adaption of the developed models for upscaling purpose, where ammonium sulphite (aq.) is the cycle working fluid.
- Conducting a feasibility study of replacing photocatalytic reactors instead of electrolyser in a fully working solar driven ammonium sulphite thermochemical cycle.

1-3 Structure of this thesis

Chapter 1: Introduction

Chapter 1 gives a brief background information on the solar driven hydrogen technologies, the different photocatalysts materials for the hydrogen generation, the different photocatalytic reaction mechanisms, available irradiation mathematical models developed for different photoreactor. Finally, the aims and objectives of this PhD thesis are stated.

Chapter 2: Literature review

In this Chapter, solar energy for the hydrogen production is reviewed, focusing towards the solar thermochemical cycles for the hydrogen generation. This will be followed by the definition of photocatalysis and photocatalytic mechanism for hydrogen production with enhancement towards visible light driven photocatalysis for hydrogen generation. The choice of using CdS based photocatalyst with an explanation of the necessary co-catalyst requirement will be justified. For the photocatalyst, description of different synthesis methods of the nanoparticles will be reviewed. Finally, different available design options of photoreactors will be briefly explained.

Chapter 3: Methodology

Chapter 3 describes all particle synthesis procedures and the principles of the analytical material characterization techniques used in this research. The design details of an energy-efficient LED photoreactor as an economical alternative to more the expensive Xenon lamps or solar simulator systems, is also presented here with the LED light arrangement for a homogeneous illumination throughout the photoreactor alongside the light intensity and flux analysis of the LEDs. For the photocatalytic hydrogen generation, the hydrogen collection arrangement, photonic energy conversion efficiency and the relevant hydrogen performance tests are described.

Chapter 4: Photocatalyst characterisation

In this Chapter, the material characterisation of the synthesised photocatalyst composites are presented, starting from the CdS synthesis, then followed by the cocatalyst Pt synthesis and its loading on the CdS. This is followed by the cobalt phosphate synthesis, Co_xP, through solid-phase reaction and solution-phase reactions and their loadings on the CdS semiconductor.

Chapter 5: Photocatalytic hydrogen generation

This Chapter presents a comprehensive investigation of the photocatalytic hydrogen evolution. Initially, lactic acid (aq.) as a working fluid is investigated, followed by a

study of the variable operational parameters on the H_2 generation using catalyst composition, Pt/CdS, which will be used as the model catalyst for comparison of published data. Then, the H_2 performance of all synthesised composite photocatalysts are compared (all Co_xP and Pt cocatalyst with photocatalyst CdS); one selection by standard grinding assisted loading method and one part with various improved loading methods. This will be followed by a stability analysis of the most promising Co_xP/CdS photocatalyst.

Chapter 6: Hydrogen photoreactor modelling

In this Chapter a descriptive mathematical hydrogen model to predict the hydrogen production rate is developed. The model is based on surface reaction kinetics in conjunction with the radiation field dependency within the LED driven reactor vessel. The model accuracy is further improved by taking into account the optical parameters over catalyst's entire absorption wavelength as well as the chemical reaction parameters. The model is then validated by comparing it with empirical data. The least-square best fitting approach, using an optimization method in MATLAB is employed for the estimation of the model's kinetic parameters.

Chapter 7: Photocatalytic hydrogen production in the sulphur ammonia thermochemical cycle

In this Chapter, the replacement of traditional electrolyser unit with a solar driven hydrogen generation unit for the hydrogen production in a sulphur–ammonia thermochemical cycle is investigated. The chapter will draw conclusion from previous result chapters (Chapter 4, 5 and 6) and bring forward a plausible suggestion for this replacement. First the photocatalytic conversion of ammonium sulphite is described, followed by the effect of various operational parameters on the H_2 generation when using the best performing photocatalyst composite (CoP/CdS) aimed for the thermochemical cycle. All results with the novel CoP/CdS catalyst are compared with the more documented Pt/CdS. Next, an adapted hydrogen prediction model (based on Chapter 6) is presented, using ammonium sulphite (aq.) as the photolyte, CoP/CdS as the photocatalyst and an upscaled reactor size with a corresponding visible light

arrangement for that size. Finally, a feasibility study of upscaling visible light driven reactors towards a large scale solar driven thermochemical cycle is outlined.

Chapter 8: Conclusions and future work

This Chapter summarises the conclusions of all previous chapters and suggests future research work in this topic.

Chapter 2: Literature review

2-1 Introduction

In this Chapter, solar energy for the hydrogen production including thermochemical cycles is reviewed. As this thesis will focus towards solar driven photocatalysis for hydrogen generation, the working principle, current state and various synthesis processes of relevant photocatalysis will be explained and reviewed. Finally, different available design options of photoreactors and how they can be incorporated into a thermochemical cycle will be explained.

2-2 Solar energy for hydrogen production

Hydrogen is an ideal fuel for the future because it is clean, energy efficient, abundant, and has high energy capacity. From the current hydrogen generation technologies, only a few are considered environmentally friendly. The most free and clean energy source is solar energy which can be explored to be used as the driving energy form in a large-scale hydrogen production plant.

Currently there are three major pathways for hydrogen production using solar energy; (i) photochemical route, (ii) photoelectrochemical route, and (iii) thermochemical route. In the photochemical (photocatalytic water splitting) route, solar light is absorbed by a semiconductor material (photocatalyst), which generates reactive electric potentials (formed electrons and holes) and sets off simultaneous reduction and oxidation reactions on the particle surface. If the medium is water and the electron potentials are favourable, possibility hydrogen(g) and oxygen(g) are produced[65]. To utilise a wide range of the solar spectrum, a semiconductor with narrow band gap energy is recommended [66]. However, too narrow band gap semiconductors, will generate electrons (excited to the conduction band) and holes (electron vacancy in the valence band) that possess potentials that are not suitable to drive a water splitting mechanism [65]. Commonly used photocatalytic materials such as TiO_2 with the bandgap of 3.1 eV only absorb a small portion of solar spectrum (majority in the UV region), and the formed electrons and holes that diffuses to the

surface have electron potentials to drive many redox reactions instead, in particular forming the reactive OH-radicals which rapidly breaks down many water pollutants. Since no single photocatalyst material is available to meet all the requirement needed for the high solar light absorption and simultaneously provide the proper electron potentials to drive the water splitting mechanism, other means of driving the reactions is sought for.

In the photoelectrochemical route (PEC), water is split into hydrogen and oxygen in a membrane separated device by using an electric field and two separate electrodes. The configuration of photoelectrochemical cells varies, but they often consist of one photoanode and one metal electrode, where an applied bias is utilised to drive electron movement between the electrodes, see Fig 2.1. This bias can be powered by a photovoltaic cell making it fully solar driven. There is also the option of making a tandem PEC , where both the anode and cathode are solar driven, as seen in Fig 2.2. In both PEC cases, a suitable photocatalysts with the corresponding electron potentials are needed. However, the difference is that in the normal PEC when the photons are absorbed by the semiconductor, it creates electron-hole pairs which are split by the electric field in the space-charge region between the semiconductor and the electrolyte.

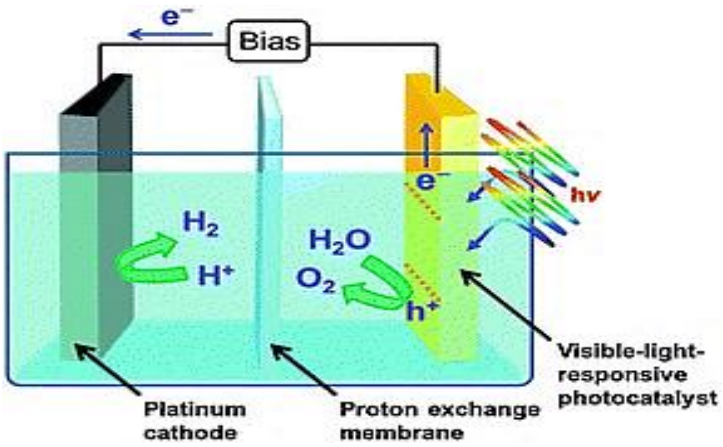

Figure 2. 1 Working principle of a PEC with one photoanode and one metal cathode with option of photovoltaic powering [67]**.**

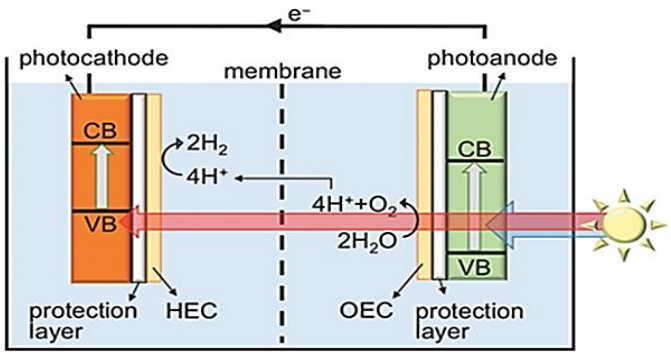

Figure 2.2 Working principle of a solar driven tandem PEC with both photoanode and photocathode [68]**.**

Then, the electron movement from the photoexcited anode travels to the cathode and will reduce the water to hydrogen (in case of correct potential from the applied bias) and oxygen will be formed at the photoanode (the potential determined from the hole potential of the photocatalyst coating), see Fig 2.1. On the other hand, in the tandem PEC, the photoelectrode aimed for the H_2 generation needs a suitable conduction band potential over -0.5 eV to drive the reaction, whereas the oxygen generating photoelectrode need to have a suitable valance band potential of 1.23 eV for the formed holes to drive the reaction. Both PEC configurations can be developed to be 100% solar driven if correct photon-absorbing materials are used for the photoelectrodes, hence the main challenge is to design the photoelectrode configuration and circuit and assure that the catalyst materials are highly efficient and chemically stable or not prone to the photocorrosion.

Many thermochemical water splitting cycles (TCWSCs) have been developed over the years to achieve relatively what is called; high solar-to-hydrogen energy conversion [69]. However, only a few of them have been proved to be economically and technically feasible [69] for real commercialisation and even fewer are possible to be even partly solar driven. Thermochemical cycles combine heat sources with chemical reactions to split water into its hydrogen and oxygen components in a fluid-based cycle. In this research, a hybrid solar thermochemical route for hydrogen and oxygen generation is explored which will be based on the adaption of current thermochemical cycles and incorporation of photocatalysis, which all will be explained in the following section.

2-3 Solar thermochemical cycles for hydrogen generation

The simplest solar driven water splitting is the direct decomposition of water to produce hydrogen. This involves thermolysis of the water molecules at temperature above 2500 K, which can only be achieved by high flux solar irradiation [70]. However, there are two disadvantages associated with the solar thermolysis: (i) the high operational temperature and (ii) very hard separation of the explosive hydrogen-oxygen mixture. Solar driven thermochemical cycles on the other hand can significantly address these problems as the temperatures required are comparatively lower than that of solar thermolysis plus that oxygen and hydrogen are produced in the different stages of the cycle and will be well-separated. A few variations of solar thermochemical cycles aimed for the solar hydrogen production part of the cycle have been identified, with operating temperatures between 850–2200 K [71]. However, not all cycles are practical for commercialisation due to the high energy consumption, challenging thermodynamic operation and safety and environmental considerations [72]. Based on these criteria, there are only two major cycle classifications that are considered for the solar thermochemical cycles in this research: (i) metal-oxide cycles and (ii) multi-step thermochemical cycles.

2-3-1 Solar metal-oxide thermochemical cycles

Metal-oxide cycles use of metal oxide as the redox material [73]. The first step of these cycles can be described as a solar thermal endothermic oxidation step where the metal oxide (M_xO_y) produces O_2 gas as;

$$M_xO_y \rightarrow xM + y/2\ O_2 \quad (2\text{-}1)$$

This is followed by a non-solar exothermic hydrolysis step where the metal (M) reacts with water to form an oxide and the H_2 gas as;

$$xM + yH_2O \rightarrow M_xO_y + y\ H_2 \quad (2\text{-}2)$$

In this type of the cycles, hydrogen and oxygen gases are generated in two separated steps which eliminates the need for the high temperature gas separation. Examples of several metal oxide cycles are presented in Table 2.1, where it can be seen that a

lower temperature is needed in the cycles using MnO/Mn_3O_4, Hg/HgO and Cd/CdO. However, the amount of hydrogen produced in these cycles is insignificant and the heavy metals such as Cd and Hg making these cycles environmentally undesirable. The most favourable candidate for a two-step metal oxide cycle is probably the Zn/ZnO cycle. Although, several chemical aspects of this cycle have been previously investigated, Xiao et al. [74] stated that the high temperature requirement of its reduction step generates serious difficulty in finding durable reactor materials for the operation and that zinc deposition on the reactor walls causes an additional separation stage and an increase in the total cost.

Table 2. 1 Metal oxide cycles.

	Cycles	Max Temp.	Reference
Hg/HgO	$\mathrm{HgO} \rightarrow \mathrm{Hg} + {}^{1}/_{2}\,\mathrm{O_2}$ $\mathrm{Hg} + \mathrm{H_2O} \rightarrow \mathrm{HgO} + \mathrm{H_2}$	600 ℃	[73]
Cd/CdO	$\mathrm{CdO} \rightarrow \mathrm{Cd} + {}^{1}/_{2}\,\mathrm{O_2}$ $\mathrm{Cd} + \mathrm{H_2O} \rightarrow \mathrm{CdO} + \mathrm{H_2}$	1400℃	[73,75]
MnO/Mn_3O4	$2\mathrm{Mn_3O_4} \rightarrow 6\mathrm{MnO} + \mathrm{O_2}$ $3\mathrm{MnO} + \mathrm{H_2O} \rightarrow \mathrm{Mn_3O_4} + \mathrm{H_2}$	1537℃	[76,77]
Zn/ZnO	$\mathrm{ZnO} \rightarrow \mathrm{Zn} + {}^{1}/_{2}\,\mathrm{O_2}$ $\mathrm{Zn} + \mathrm{H_2O} \rightarrow \mathrm{ZnO} + \mathrm{H_2}$	2000℃	[74,78]

2-3-2 Multi-step thermochemical cycles

The multi-step thermochemical cycles can operate at lower temperatures than the two-step metal oxide cycles with the help of an additional reaction step, where the complete formation of hydrogen and oxygen occurs [79]. Examples of the most common multi-step thermochemical cycles are presented in the following section.

2-3-2-1 Hybrid copper-chloride cycle

The first cycle of multi-step thermochemical cycles is the hybrid copper-chloride (Cu-Cl) which uses both thermochemical and electrochemical reactions, see Fig 2.3. The process is described by the hydrolysis of $CuCl_2$ to form copper oxychloride (Cu_2OCl_2) and hydrochloride acid (HCl) as;

$$2\,CuCl_2(s) + H_2O(g) \rightarrow\ Cu_2OCl_2\ (s) + 2HCl\ (g) \qquad (2\text{-}3)$$

Next, the Cu_2OCl_2 proceeds to the high temperature thermochemical step, where it is decomposed forming CuCl (s) and O_2 gas as;

$$Cu_2OCl_2\ (s) \rightarrow 2CuCl(s) + 1/2O_2(g) \qquad (2\text{-}4)$$

The CuCl and HCl then proceed to the electrochemical step, where they are electrolysed to release H_2 gas and $CuCl_2$ as;

$$2CuCl\ (s) + 2HCl(g) \rightarrow 2CuCl_2 + H_2(g) \qquad (2\text{-}5)$$

In a comparative study conducted by Ratlamvala et al. [80] in 2012, it was mentioned that this cycle was more efficient and practical than the conventional thermolysis because of its maximum operating temperature of only 500°C and the use of active, cheap and abundant materials. However, the cycle has drawbacks of using highly corrosive chemicals such as hydrochloric acid, plus if making it partly solar driven, the energy would be only used in the hydrolysis and decomposition steps and the electrolyser would still need a high energy input (electricity).

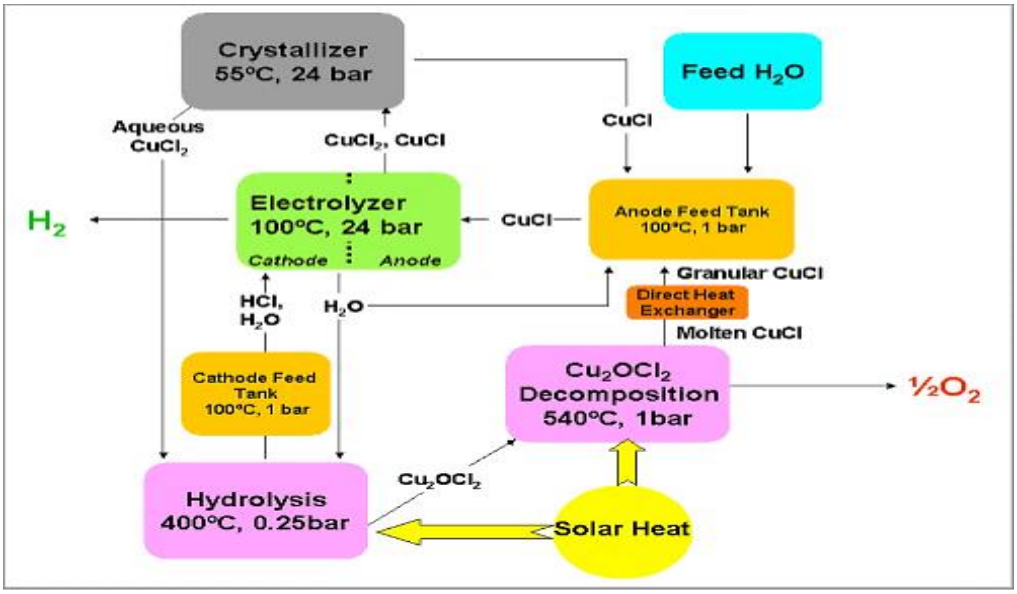

Figure 2. 3 Conceptual flow diagram of Cu-Cl thermochemical cycle [81–83].

2-3-2-2 Sulphur-iodine cycle

The sulphur-iodine(S-I) cycle is another multi-step thermochemical cycle consisting of three thermochemical reaction steps, as shown in Fig 2.4. In the first step, sulphuric acid is decomposed under high temperature (~870 °C) to produce water, sulphur dioxide and oxygen [75], as:

$$H_2SO_4 \rightarrow H_2O + SO_2 + 1/2O_2(g) \quad (2\text{-}6)$$

In the following step (Eq. 2-7), known as Bunsen reaction, the aqueous SO_2 reacts with iodine to produce sulphuric and hydriodic acids, where the produced H_2SO_4 is cycled back to the previous step, oxygen gas is collected, and the HI undergoes further decomposition step.

$$SO_2 + 2H_2O + I_2 \rightarrow H_2SO_4 + 2HI \quad (2\text{-}7)$$

In the third step, the hydriodic acid (aqueous solution of HI) undergoes decomposition at 573–623 K to produce iodine and hydrogen gas as:

$$2HI \rightarrow I_2 + H_2 \quad (2\text{-}8)$$

Then formed Iodine is sent back to the previous Bunsen reaction while the hydrogen product is collected.

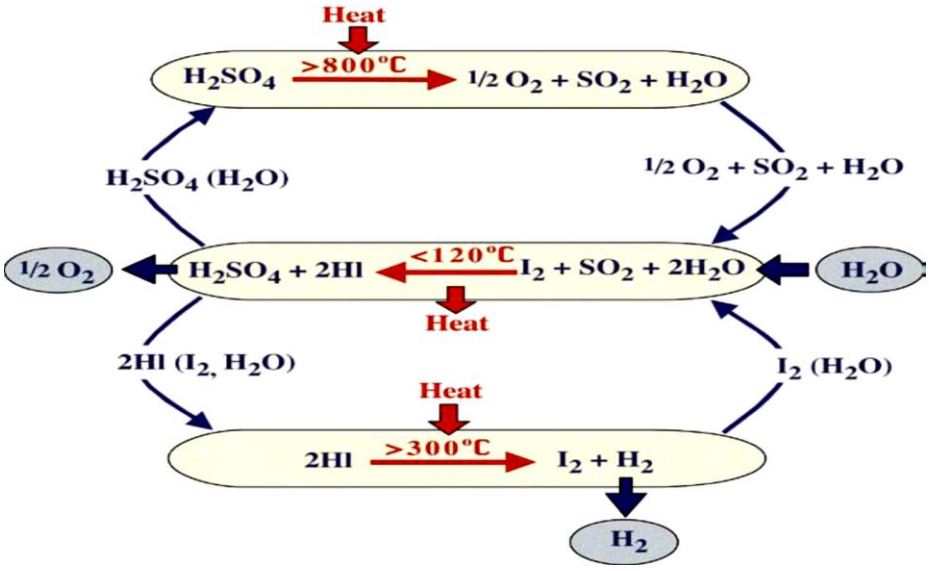

Figure 2. 4 Conceptual flow diagram of a multistep sulphur iodine cycle[84].

Despite moderate temperatures needed for the thermochemical reactions here, this cycle also suffer from the several disadvantages, as reported by O'Keefe et al. [85] in 1980 such as, handling of corrosive chemicals and high energy requirement of the separation steps.

2-3-2-3 Sulphur-bromine cycle

The sulphur-bromine thermochemical cycle also consists of a thermochemical and an electrochemical reaction steps, as shown in Fig 2.5. In the first thermochemical step, sulphuric acid is decomposed under high temperature (~870°C) to produce water, sulphur dioxide and oxygen [75].

$$H_2SO_4 \rightarrow H_2O + SO_2 + 1/2O_2(g) \quad (2\text{-}9)$$

In the following step, the aqueous SO_2 reacts with bromine to produce sulphuric and hydrobromic acids, where the produced H_2SO_4 is cycled back to the previous step (2-9) and the HBr proceeds to the electrochemical step.

$$SO_2 + 2H_2O + Br_2 \rightarrow H_2SO_4 + 2HBr \quad (2\text{-}10)$$

In the electrochemical step, hydrobromic acid is electrolysed at 77°C to produce bromine and hydrogen gas as:

$$2HBr \rightarrow Br_2 + H_2 \quad (2\text{-}11)$$

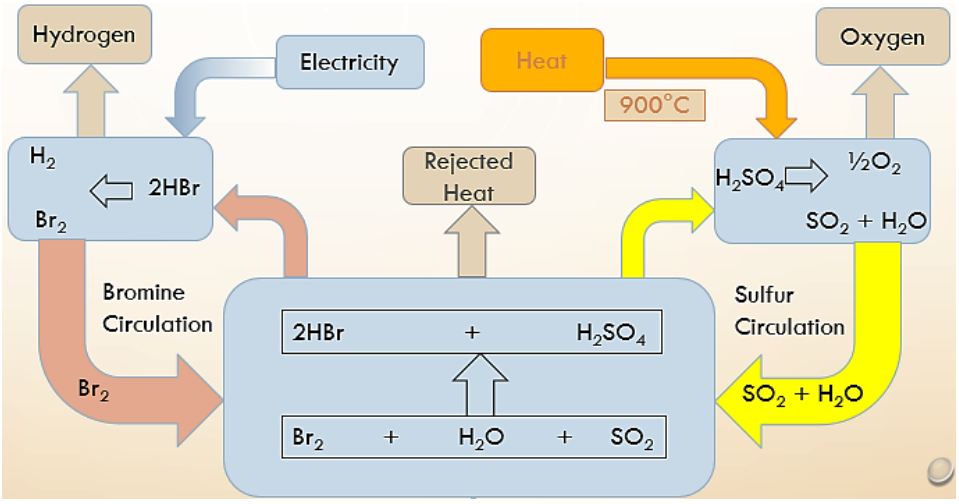

Figure 2. 5 Conceptual flow diagram a sulphur bromine thermochemical cycle [75].

The main challenges in this type of thermochemical cycle are handling of corrosive chemicals and a hard separation of sulphuric acid from HBr[86]. To make this cycle partly solar driven, it could be by using photovoltaics for the hydrogen production part as the thermal part still needs relatively high temperatures.

2-3-2-4 Hybrid sulphur cycle (Westinghouse Cycle)

The Westinghouse Cycle (WC) is a two-step cycle as shown in Fig 1.6, that also uses one thermochemical and one electrochemical reactions steps for oxygen and hydrogen production respectively [87]. The cycle has the advantages of using cheap and abundant materials and has far better potentials to utilise solar energies through easier separations steps at relatively lower powered working conditions. In the first thermochemical step, sulphuric acid is decomposed under high temperature (~850°C) to form sulphur dioxide, water and O_2 gas as;

$$H_2SO_4 \rightarrow H_2O + SO_2 + 1/2O_2(g) \quad (2\text{-}12)$$

The aqueous solution of SO_2 is further cycled to the electrolytic process as:

$$SO_2 + 2H_2O \rightarrow H_2SO_4 + H_2 \quad (2\text{-}13)$$

The produced H_2SO_4 is cycled back to the previous step and hydrogen gas is collected.

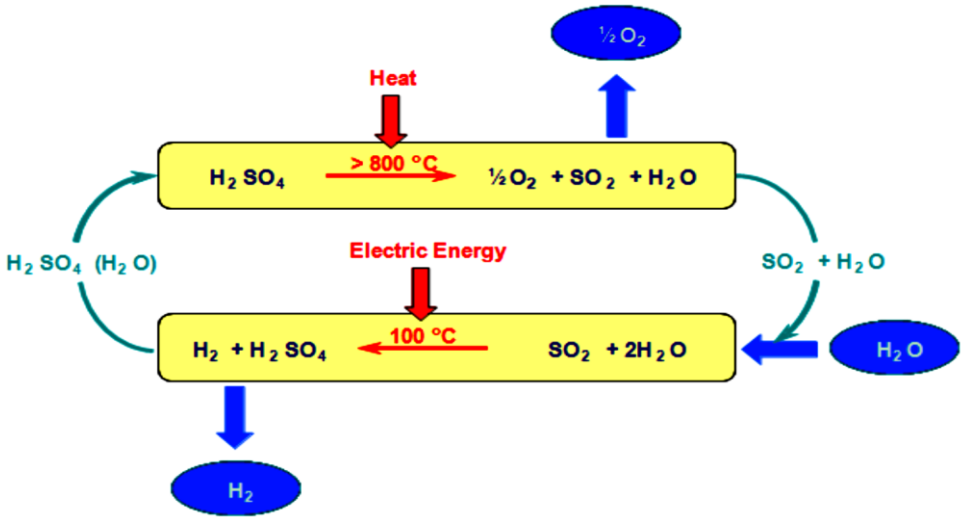

Figure 2. 6 Conceptual flow diagram of hybrid sulphur thermochemical cycle (Westinghouse Cycle)[87].

However, Brecher et al. [5] in 1977 stated that this cycle's success was hindered by the low solubility of SO_2 in water, the use of corrosive chemicals, the high acidity of SO_2 in the electrolytic redox process, and the challenging electrolytic cell design due to high level of sulphur deposition. Many efforts were made to improve performance of this cycle such as usage of a depolarised electrolyser to reduce the sulphuric deposition[88]. However, the cycle efficiency needed improvement for gaining a higher overall solar-to-hydrogen conversion. Ali T-Raissi et al. [87] suggested an alternative hybrid cycle, by incorporating ammonia into the Westinghouse Cycle, called sulphur-ammonia thermochemical cycle. It was suggested that this cycle could potentially address many of the drawbacks encountered to all solar thermochemical cycles studied to date, if both thermal and quantum components of the solar energy could be incorporated to drive the cycle. If only the thermal component of solar irradiation is utilised, it would limit the overall solar-to-hydrogen conversion efficiency of the cycle. If both solar components are utilised to drive O_2 and H_2 production, it could certainly increase the cycle efficiency.

2-3-2-5 Sulphur-ammonia thermochemical cycle

The sulphur-ammonia thermochemical cycle, as shown in Fig 2.7, is a four-step hybrid thermochemical cycle. This type of cycle which is a modified version of the Westinghouse cycle, consists of two well-separated oxygen and hydrogen producing half cycles. For the hydrogen producing half cycle, ammonia gas and sulphur dioxide gas are absorbed in water at a chemical absorber as:

$$2\mathrm{NH_3(g)} + \mathrm{SO_2(g)} + \mathrm{H_2O(l)} \rightarrow (\mathrm{NH_4})_2\,\mathrm{SO_3(aq)} \qquad \mathrm{T} = 25^{\circ}\mathrm{C} \qquad (2\text{-}14)$$

The formed $(NH_4)_2SO_3$ (aq) then undergoes an electrolytic redox reaction in an electrolyser at reasonably low pressure to yield hydrogen gas and $(NH_4)_2SO_4$(aq) as:

$$(\mathrm{NH_4})_2\,\mathrm{SO_3(aq)} + \mathrm{H_2O(l)} \rightarrow (\mathrm{NH_4})_2\,\mathrm{SO_4(aq)} + \mathrm{H_2(g)} \qquad \mathrm{T} = 77^{\circ}\mathrm{C} \qquad (2\text{-}15)$$

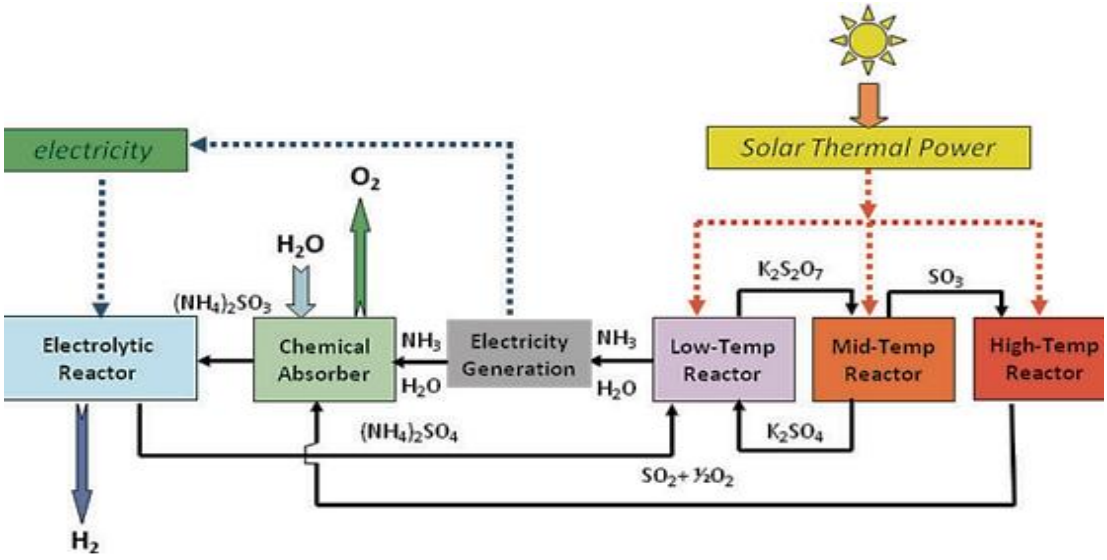

Figure 2. 7 The working principle of solar driven sulphur-ammonia thermochemical cycle[89].

For the oxygen producing half cycle, the formed ammonium sulphate $(NH_4)_2SO_4(aq)$ is transferred to a low-temperature reactor at 400°C, where it reacts with potassium sulphate (K_2SO_4) as:

$$(NH_4)_2\,SO_4(aq) + K_2SO_4(l) \rightarrow 2NH_3(g) + H_2S_2O_7(l) + H_2O(l) \qquad T = 400^{\circ}C \tag{2-16}$$

The produced gases of NH_3 (g) and H_2O(g) at high pressure are further utilised for the electricity generation (via turbines) and therefore able to drive the electrolytic reactor by cycling back into the chemical absorber. The produced pyrosulphate ($H_2S_2O_7$) is fed to the medium temperature reactor, where it is decomposed to SO_3 and K_2SO_4 as:

$$H_2S_2O_7(l) \rightarrow SO_3(g) + K_2SO_4(l) \qquad T = 790^{\circ}C \tag{2-17}$$

The produced K_2SO_4 (l) is then sent back to low-temperature reactor while SO_3 (g) is further decomposed at high temperature reactor over a suitable catalyst to separate oxygen (O_2) from SO_2 (g) as:

$$2SO_3(g) \rightarrow 2SO_2(g) + O_2(g) \qquad T = 1000^{\circ}C \tag{2-18}$$

The principle of this cycle has been proposed by Ali T-Raissi group in Forida State [87,90], and is still under investigation to improve the cycle efficiency as much as possible. This can be achieved by a high solar-to-hydrogen conversion efficiency through a full utilisation of the solar spectra energy and mainly by substituting the electrolytic reactor with a photoreactor. A photocatalytic hydrogen step has a potential for a higher hydrogen generation rate with minimal power consumption, leading to the higher hydrogen efficiency and improved hydrogen economy of the cycle. This research will therefore explore the option of developing an economical photocatalytic reactor to generate hydrogen gas which can be integrated into a solar driven sulphur-ammonia thermochemical cycle.

2-4 Photocatalysis

Photocatalysis is normally referred to a process in which light is used to activate a substance (the photocatalyst) which then produce energy carriers (electron and holes) which as a result of their potential at the catalyst surface can accelerate reaction (a photoreaction in the presence of a catalyst). The photocatalytic activity (PCA) depends on the ability of the catalyst to create electron–hole pairs, [91]. Heterogeneous photocatalytic reactions such as solid-gas or solid-liquid has gained lots of attention for environmental purposes, energy generation and organic syntheses [36, 37, 38].

2-4-1 Photocatalyst

A photocatalyst is defined as a material that does not undergo any chemical change but could accelerate the reaction by gaining energy from the light photons. These characteristics coupled with the favourable electronic structure of the photocatalyst make it quite distinctive compared to a non-photocatalyst material. The activity of photocatalyst is also believed to be proportional to the amount of possible light absorption. Other factors that could influence the photocatalyst activity are surface properties, particle size and synthesis route [92].

2-4-2 Photocatalytic mechanism

The solar radiation consists of electromagnetic waves in different regions; (i) visible at the wavelength of 400-700 nm, (ii) ultraviolent (UV) at the wavelength less than

400 nm, and (iii) infrared (IR) at the wavelength greater than 700 nm. The energy of the photons at each wavelength (λ) is usually described as;

$$E = h' c/\lambda \quad (2\text{-}19)$$

,where h' is Planck's constant $(6.266 \times 10^{-34}(J/sec))$, c is the speed of light $(3 \times 10^{8}\,(m/sec))$ and λ is the wavelength (nm).

For any photocatalyst there exists a bad gap (E_{bg}) in energy between the valance band (VB) (with lower energy) and the conduction band (CB) (with higher energy), as shown in Fig 2.8.

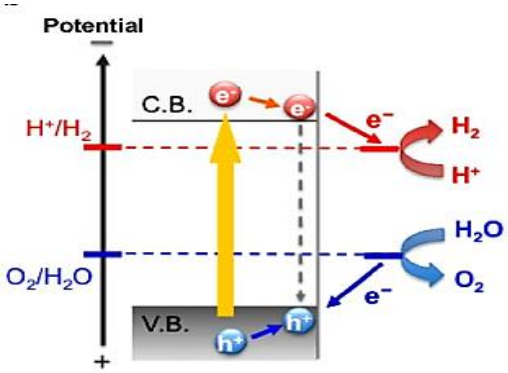

Figure 2. 8 Schematic showing the conduction band (C.B) and valence band (V.B) potentials forming the bandgap potential in a photocatalyst aimed for water splitting (38).

Upon absorption of a photon with energy equal to or higher than the band gap energy, light-induced electron-hole pairs are generated (collectively known as charge carries)[92]. The photo-generated electrons and holes then migrate to the surface of the photocatalyst and take part in driving oxidation-reduction reactions. For a photocatalyst to be effective for solar driven water splitting purposes, the band position of the bottom of the conduction band should be more negative than the reduction potential of water to produce H_2 and that of the top of the valence band must be more positive than the oxidation potential of water to produce O_2, creating sufficient narrow band gap i.e <3 eV for a visible light absorption, where the value of 2.4 eV is a good compromise [43]. There are only few photocatalysts that have been successful to be used under the visible light, which will be further explained in section 2-4-3.

One of the main problems encountered by most of the photocatalysts is their large overpotentials, leading to some difficulties in transferring charge carriers between

the photocatalysts and the water molecules. To overcome this problem, a co-catalyst can be loaded on the surface of the semiconducting photocatalyst [25,93]. When a co-catalyst is loaded onto the surface, the photo-generated electrons that migrate to the surface of the host photocatalyst can be entrapped by the co-catalyst depending on the work function of the cocatalyst. If choosing a cocatalyst with a lower Fermi-level (E_f) compared to that of the host photocatalyst, the electron can be successfully transferred, see Fig 2.9. Therefore, the photogenerated electrons at the cocatalyst will be involved in the reduction reaction and the holes in the host photocatalyst will be involved in the oxidation reaction.

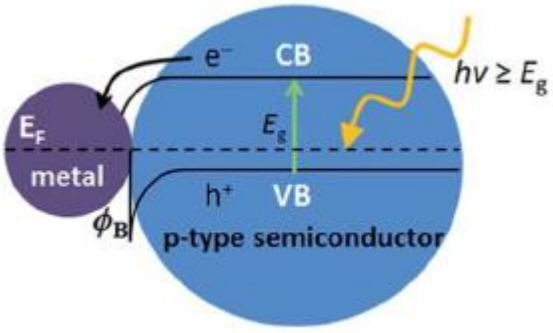

Figure 2. 9 Schematic showing the charge transfer between a photo excited semiconductor and a metal co-catalyst [93].

Examples of commonly used co-catalysts are Pt, Ru, Rh, Pd and metal oxides of NiO and RuO_2[94]. Another important problem encountered by the photocatalysts is the electron-hole pair's recombination i.e. the formed electron and hole are recombined before they successfully diffuse to the particle surface, to their respectively trapped sites. This recombination is often found in the bulk of the particle rather than on the surface and it is very rapid, which is rate-limiting for a successful hydrogen production. If the purity of the semiconductor is low, "trap sites" are formed. This is also found in particles with low crystallinity, where crystal defects form trap-sites too. With this knowledge, it is important to synthesise the photocatalysts with as high crystallinity as possible to reduce the charge recombination [95]. The use of sacrificial reagents (hole scavengers) in the solution can also help reduce the charge recombination [96], because sacrificial reagents act as electron donors to the valence band of the semiconducting photocatalyst as being oxidised by the holes, therefore drive away the holes from the surface of the photocatalyst. If sacrificial reagents are

used in conjunction with the co-catalyst, further separation of photo-generated electrons and holes would be expected as photo-generated holes and electrons will be simultaneously involved in the oxidation and redaction reactions and therefore electro-stability of the photocatalyst system can be better maintained. The particle size and the surface area of the photocatalyst are equally important for reducing the electron-holes recombination. Small particles will allow more diffused holes and electron to the surface, leading to an improved photocatalytic activity. Smaller size means that the particles surface area increases too, and it would allow higher surface trapped electron and holes, leading to a reduced rate of bulk electron-holes recombination and therefore higher photoreaction rate [97].

2-4-3 Visible light photocatalysts for H_2 production

The development of a highly efficient photocatalyst with good visible light responses for producing hydrogen has recently gained attention [98,99]. One of the most commonly used photocatalyst has been metal-oxide titania (TiO_2) due to being non-toxic, cost effective and chemically stable in the photocatalytic reactions. However, with a band gap of 3.2 eV only the ultraviolent region of the solar spectrum can be absorbed, inhibiting its practical application in the green energy sector [10]. To improve the photocatalytic properties of TiO_2 into the visible light region, Zhong et al. [10] proposed an elemental doping approach that could reduce the absorption threshold of TiO_2, extend its spectral response from ultraviolent to visible region, avoid electron–hole recombination, and further facilitate the charge transfer. For instance, doping of non-metals of B, C, N, S has shown an efficient extension of TiO_2 photo response from UV to visible light region (48, 50 and 51). Apart from titania based photocatalytic systems, metal sulphide systems have also been suggested (50). Metal sulphide systems with a narrower band gap, i.e. corresponding to the wavelengths less than 700 nm, have demonstrated to be promising photocatalysts under visible light for the hydrogen production [42]. Figure 2.10 shows the electron band gaps for the most commonly used semiconductors at neutral pH and ambient conditions [44,93].These band levels normally shift with a change in the pH, impurities, absorbed compounds, which will be discussed further in the Result

Chapter where lactic acid and ammonium sulphate solutions will be compared. One of the better known metal sulphide systems is cadmium sulphide (CdS) with the conduction band potential of around -0.7 eV, which is sufficient to reduce water and a valence band potential of 1.7 eV which is well-suited to allow the oxidation of water at pH=7 (band gap of 2.4 eV)[15,43]. The potentials can be seen clearer in Figure 2.10.

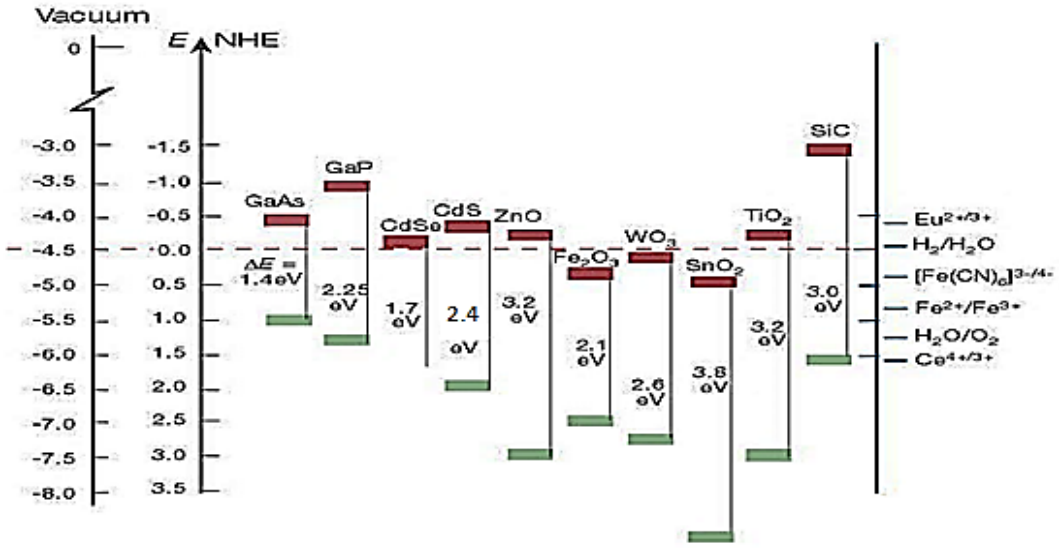

Figure 2.10 Bandgaps of commonly used photocatalysts with the conduction band potential (red) and valence band potential (green) measured against normal hydrogen electrode (NHE) [44,93].

However, many researchers such as D. Meissner et al. [45] stated that prolonged irradiation of CdS suspensions would lead to the photocorrosion of CdS to the elemental sulphur (in the absence of oxygen) or sulphate (in the presence of oxygen), and therefore a very low photocatalytic yield [65, 63 , 66]. The photocorrosion is usually caused by the accumulation of photo-generated holes on the CdS surface. The main strategy to overcome the photocorrosion is the use of a sacrificial reagent together with a cocatalyst. Some published examples of CdS coloaded photocatalysts composites include; Pt/CdS or Pd/CdS[20], $Ni(OH)_2$/CdS [18], graphene/CdS [105], $Co(OH)_2$/CdS [106], MoS_2/CdS [23], NiS/CdS[24], MS(M=Ni, Co, Cu)/$Cd_xZn_{1-x}S$ [25] and metal phosphides/CdS [107].

Modifying CdS surface with the noble metals such as platinum (Pt), palladium(Pd), rhodium (Ph), or nickel (Ni) is the most common approach to minimise the

photocorrosion [18,33,108–111]. However, Wang et al. [25] argued that although platinum and palladium were the most efficient co-catalysts for a photocatalytic hydrogen evolution, they suffered from high cost, which considerably limited their practical large-scale application. Minimising the mass of loading of noble metals by combining them as a functional composite type of cocatalyst such as Pd-Cr_2O_3 or Pt-PdS on CdS did not resolve the problem, despite their promising hydrogen yield [7,16]. Ran et al. [17,18] modified CdS nano-rods with $Ni(OH)_2$ and tested them in a triethanolamine aqueous solution under visible light, which resulted in a promising H_2 production rate of 5085 µmol h^{-1} g^{-1} . Graphene (G) with its unique two-dimensional honeycomb structure and large specific surface area and excellent conductivity has attracted much attention as an electron transfer media. The flat carbon configuration in the graphene structure can be served as a scaffold to anchor metal and/or semiconductor nano-particles and therefore assists in the efficiency of the catalytic processes. Lv et al. [13,16] showed how graphene attached to CdS surfaces could efficiently transfer the photoexcited electrons, and therefore reduce the electron-hole recombination. Another enhancement structure was in the form of $Co(OH)_2$/CdS nano-wires (NWs) which effectively accelerated the charge separation, leading to an improved hydrogen production rate of 14430 µmol h^{-1} g^{-1} [19,20]. A more recent approach to reduce electron-hole recombination and therefore increase photocatalytic activity under the visible light irradiation is the use of transition metal compounds [31]. In a study carried out by Zong et al. [23], it was shown that CdS loaded with only 0.2 wt.% of MoS_2 in lactic acid solution could improve the photocatalytic hydrogen generation up to 36 times, compared to the same particles loaded with 0.2 wt.% Pt instead. NiS was also reported [24] as a robust transition metal co-catalyst that if loaded on CdS, it would lead to a hydrogen evolution of 7267 µmol h^{-1} g^{-1}. Another transition metal strategy was incorporation of ZnS into the structure of CdS to form $CdxZn_{1-x}S$ solid solutions, where the potentials of conduction and valence bands were modified by adjusting the Cd/Zn stoichiometry ratio, and then loading of small amount of transition-metal sulphides of NiS, CoS or CuS was made onto the surface of the $CdxZn_{1-x}S$ [25]. Recently, transition metal phosphides such as Ni_2P, CoP, FeP and MoP loaded on CdS have attracted an interest in hydrogen production due to their metallic nature, high stability and low cost and earth-

abundant nature. Yue et al. [28] showed an impressive photocatalytic H_2 production rate of 163200 µmol h^{-1} g^{-1} under visible light illumination (λ > 420 nm) for the MoP loaded on CdS system. Cheng et al. [27] reported how a loading of FeP nano-particles onto CdS nano-crystals (FeP/CdS) delivered a H_2 production rate of 202000 µmol h^{-1} g^{-1} in a lactic acid solution and Cao et al. [26] reported a hydrogen evolution rate of 143 600 µmol h^{-1} g^{-1} when nickel phosphide was loaded on CdS (NiP/CdS), again in a lactic acid solution. An impressive H_2 evolution rate of 251 500 µmol h^{-1} g^{-1} (quantum efficiency of 25.1%) was presented by Cao et al. [104, 105] in 2015 for loading of cobalt phosphide on CdS (CoP/CdS), once again when lactic acid solution was used as a hole donor. The hydrogen produced from the latter system represents the highest values found for a CdS-based photocatalysts until the date of this literature review, with an excellent stability and high photocatalytic activity even after 100 h of irradiation[29].

Comparing all visible light-driven photocatalysts based on their hydrogen evolution capabilities shows that the earth-abundant transition metal phosphides, especially cobalt phosphide on CdS surface, not only have high hydrogen generation rates but also high photocatalytic stability. As far as known, this type of photocatalyst has never been reported to be employed in a solar driven sulphur-ammonia thermochemical cycle where a solar driven photocatalytic reactor configuration can replace the electrolyser step. Based on this literature review, it was therefor decided to take the photocatalytic composite of Co_xP/CdS into further investigation for this thesis.

2-5 Photocatalytic particle synthesis

Numerous methods have been developed so far to synthesise cadmium sulphide nanoparticles, including chemical precipitation methods [19], ion exchange strategies [112], solvothermal methods [14], hydrothermal methods [113] and microwave assisted processes[114]. The synthesis method chosen will directly affects the size and the crystal structure of the particles and ultimately their photocatalytic

activities [113]. From all suggested methods, the hydrothermal routes produced the most efficient CdS particles for the photocatalytic hydrogen evolution [115].

For the cocatalyst chosen for this research, cobalt phosphide (Co_xP) , less successful synthesis publications are available, where the found methods mostly include; solution phase reaction methods[38], or solid phase reaction methods [38]. Cao et al. [29], reported a solid phase reaction method for the CoP preparation, while Wentuan et al.[116] reported a solution phase synthesis of Co_xP, but both with a very little detail of the method success or explanation of how and why it would work for a photocatalytic purpose. In this research, it was decided to investigate the two above mentioned methods and compare the photocatalytic hydrogen generation of the Co_xP/CdS system which could be used in the solar-driven thermochemical cycle.

2-6 Photocatalytic reactors

There have been previous reviews describing different photoreactor configurations in the area of photocatalytic water treatment application[2], however, only a few described the reactor design for the water splitting purposes and only one was found describing a photoreactor design that can be used in a thermochemical cycles[7]. There are some important parameters that need to be considered for any type of particle photocatalytic reactor design; (i) irradiation of a large catalyst surface area, (ii) uniform light distribution throughout the reactor, (iii) adequate light intensity for the electron-hole generations, (iv) continues mixing of solution to allow even irradiation of all catalyst particles and (v) constant temperature during the irradiation[117]. Based on these parameters, the design features of the particle photoreactors are classified in terms of (i) physical geometry (position of irradiation source relative to the catalyst particles), (ii) type of radiation, and (iii) reaction tank material. The following section will briefly explain these design features.

2-6-1 Physical geometry of photoreactor

The physical geometry is of the great importance in the reactor design, as it determines the photon collection efficiency of the overall photochemical system.

Xing et al. [93] reviewed different photoreactor designs with various shapes and different light positions and explained this diversity as a result of different reaction systems. Therefore, an optimised geometrical configuration is needed to increase the chance of efficient photon collection by the catalyst particles.

2-6-2 Type of radiation

A wide range of visible light sources are available where each one can be categorised according to their specific spectrum of wavelengths. For a visible light photocatalytic hydrogen generation purpose, a successful coupling between the visible light spectrum and the absorption properties of semiconductor can effectively promote water splitting. Examples of commercial available visible light sources include tungsten lamp, mercury lamp, solar simulator and very recently LED [93]. Figure 2.11 shows the relative amount of energy versus wavelength for several different light sources in the visible region. The red curve represents the relative energy of tungsten lamps over the entire visible spectrum as opposed to light distribution of white-LED lamp (green), mercury lamp (blue) and natural sun light (yellow).

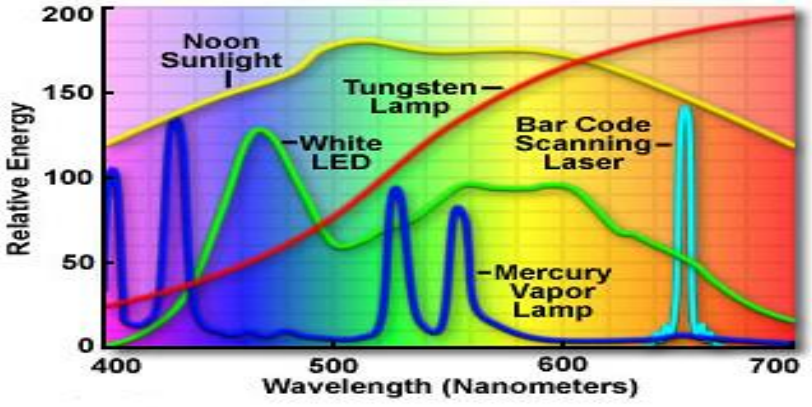

Figure 2. 11 Different spectra from different visible light emitting sources [118].

The main drawbacks of mercury and tungsten lamps are their fragility such as danger of explosion for high pressures, high working temperatures, inner gas leakage, and short life span. Tungsten light provides mainly radiation towards infrared where no semiconductor can be excited. On the contrary, white LEDs in the different ranges of colour temperature index (cool-white or warm-white) have shown benefits of incredibly long life span, lower power consumption, improved physical strength and

smaller sizes in comparison with other commercial available light sources[118]. With majority of radiation energy around 450-600nm, LEDs can be used to mimic the sun emission spectrum in the visible region pretty well.

It has been reported that the maximum absorption of photons by the CdS particles in the visible region is at the wavelength of nearly 520 nm [3]. This implies that only white-LEDs could promote electron-holes generation in a CdS photocatalyst. In Fig 2.12, the difference of cool and warm white-LED can be seen ,where the cool white-LEDs have far more radiation intensity and power below 520 nm, making it more suitable for a CdS photocatalyst.

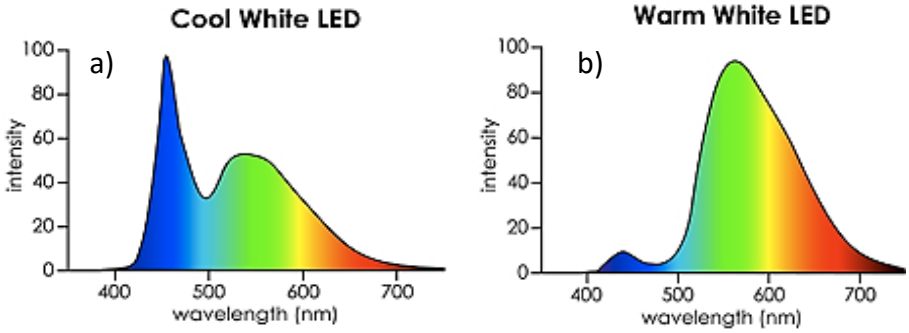

Figure 2. 12 Radiation spectra for (a) cool white-LED and (b) warm white-LED lamps [119].

2-6-3 Reaction tank material

The material of the tank or vessel for the photoreactor is also an important design feature as it determines the possible light transmission into the particle reactor. The vessel material could be stainless steel, Pyrex® or quartz. Quartz is an ideal material choice for the optical transmittance, but its high cost hinders its application for large scale [93]. Stainless steel would effectively block light from a surrounding environment, which is the case if using solar light. If using other light sources, a dedicate illumination area or optical window would be incorporated and should be relatively precisely designed. A stainless-steel tank , despite being stable and corrosive resistant would add high cost for a scaled-up application. Pyrex® has low refractive index and relatively lower cost, in addition to being safe, making it a popular photoreactor material of choice [7].

2-7 Conclusion

In this chapter, solar-driven hydrogen techniques together with the solar thermochemical cycles for the hydrogen generation were reviewed. It was found that the sulphur ammonia thermochemical cycle was the most promising cycle due to the possible incorporation of both thermal and quantum components of the solar energy to drive the cycle. It was concluded that the first strategic step to improve the cycle would be replacing the energy demanding electrolyser with a photocatalytic step, for the hydrogen production in the cycle. This replacement strategy could possibly reduce both time and temperature for the hydrogen production while driving it by solar energy only. To investigate what photocatalytic system could be utilised for a solar thermochemical cycle, a review of possible visible light driven photocatalysts was conducted, were it was identified that the CdS semiconductor had the suitable band potentials for the hydrogen evolution or water splitting. The challenge of overcoming CdS' photocorrosion at prolonged irradiation could be reduced by using a co-catalyst and/or using a sacrificial reagent. In the search for a cocatalyst that would work (being inexpensive) and be compatible with CdS (also for electron transfer purpose), the transition metal phosphide of Co_xP showed to satisfy the required criteria of the most active cocatalyst. It was found in the literature review that the use of a suitable sacrificial reagent alongside the co-loading on CdS strategy would further improve the H_2 evolution reaction.

Different photoreactor configurations to be used in this research were also reviewed, where it was concluded that for any reaction system an optimised geometrical configuration with the corresponding type of light and type of vessel material was required. To increase the photon absorption efficiency in a slurry reactor configuration, a Pyrex ® vessel with irradiation from surrounding around the reactor would be the best option. To increase the irradiation opportunity of the particle slurry, agitation would also be needed. Among the possible artificial lights, it was concluded that cool white-LEDs had an irradiation spectra that would excite a CdS system. The cool white-LED can also be treated as a cost-effective visible radiation source, rather than more expensive solar simulators and therefore easily be utilised in a scale-up if to be used in a large-scale photochemical cycle.

Therefor in this research, a photoreactor will be designed with a cool white LED irradiation source to mimic the solar visible irradiation satisfactory, while being able to photoexcite a Co_xP/CdS catalyst slurry. The information obtained in this research will then be incorporated into the hydrogen step of the sulphur-ammonia thermochemical cycle, where ammonium sulphite (aq.) will be used as the cycle working fluid.

Chapter 3: Methodology

3-1 Introduction

This chapter describes the different experimental procedures undertaken in this research including material synthesis, instrumental analysis and reactor design (such as hydrogen measurement and collection, photonic energy conversion efficiency and the light analysis).

3-2 Material synthesis

3-2-1 CdS synthesis

The synthesis of cadmium sulphide (CdS) nanoparticles was undertaken by a hydrothermal method. All chemicals used were of analytical grade or higher. First the precursor solutions of 0.14 M sodium sulphide nonahydrate, $Na_2S{\cdot}9H_2O$ (>98%, Sigma Aldrich), and 0.14 M cadmium acetate dehydrate, $Cd(CH_3CO_2)_2.2H_2O$ (>98%, Sigma Aldrich), were prepared in 200 mL and 250 mL deionised water respectively. Then, the Na_2S solution was added slowly to the $Cd(CH_3CO_2)_2$ solution under vigorous stirring (with 100 rpm agitation speed), forming yellow precipitates. The mixture was stirred for 24 h and kept for an additional 24 h at room temperature to assure formation of a stable product. The precipitate was an amorphous CdS phase, as reported by the following equation [29]:

$$Cd(CH_3CO_2)_2 + Na_2S \rightarrow CdS\ (\text{amorphous}) + 2\ CH_3COONa(aq.) \quad (3\text{-}1)$$

Impurities in the solution were removed by filtering through 8 μm filter paper. The yellow filtrate was then dispersed into 160 mL deionised water. To form crystalline CdS, a hydrothermal method was used, where the mixture reacted hydrothermally at 473 K for 72 h using a 250 mL Teflon-lined stainless-steel autoclave (Lab Glassware and Equipment). After cooled to room temperature, the product was filtered (8 μm

filter paper) and washed with 3:7 water/ethanol mixture at least three times and dried in a vacuum oven at ambient temperature. Note that for the synthesis of CdS, experiments were conducted in an inflatable glove box (Sigma Aldrich) and under the ambient lab conditions to understand effect of oxygen on the synthesis, see Fig 3.1. To make inflatable glove box air-free, a vacuum pump was attached to the glove box to remove the air, followed by refiling it with inert argon gas and purging several times.

Figure 3. 1 Experimental set-up for the CdS synthesis in an inflatable glove box.

3-2-2 Pt synthesis

The synthesis of the cocatalyst platinum was undertaken by the reduction of chloroplatinic acid H_2PtCl_6. $6H_2O$ (37.5% Pt basis, Sigma Aldrich) to elemental platinum (Pt^o) using sodium citrate dihydrate $C_6H_5Na_3O_7$. $2H_2O$ (>99%, Sigma Aldrich). First, 5% w/w aqueous solution of H_2PtCl_6. $6H_2O$ was prepared in 4 ml deionised water, followed by its dilution into 340 ml deionised water. This solution was treated as the titrate. The titrate solution was then transferred into a 500 ml three-necked round-bottom flask and heated to 80°C. The flask, as shown in Fig 3.2, was equipped with a reflux condenser, bubbler, thermocouple and a heating mantle and was continuously deaerated by the purging of the argon gas. For the titrant, a solution of 1% w/w sodium citrate dihydrate was prepared in a 60 mL deionised water. Then, the titrant solution was added to the titrate solution dropwise at 80°C, using a syringe. The course of reduction was monitored by taking 1 ml sample

solution every five minutes, where the samples were analysed for their optical absorbance. The end of the reduction reaction was marked as disappearance of the absorption band of $PtCl_6$ and formation of Pt^o metal as:

$$9H_2PtCl_6 + 2Na_3C_6H_5O_7 + 10H_2O \rightarrow \quad 9Pt^o + 12CO_2 + 6NaCL + 48H^+ + 48Cl^- \tag{3-2}$$

The UV-Vis absorption spectra was recorded between 200 and 500 nm with the scan rate of 150 nm/min. The UV-Vis spectroscopy samples were prepared by diluting 1 part reaction mixture with 7 parts of MilliQ water. The blank solution containing water and sodium citrate was also subject to the same treatment as for the reaction mixture samples for the UV-vis analysis.

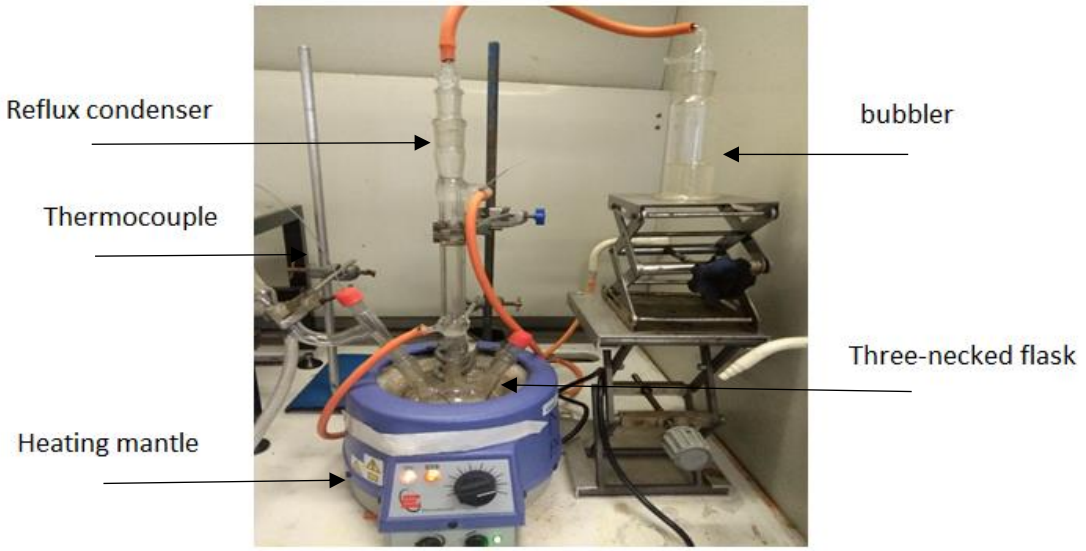

Figure 3. 2 Experimental set-up for the Pt synthesis under argon gas atmosphere.

3-2-2-1 Loading of Pt on CdS

Platinum was loaded on the synthesised CdS by two means; once by adding the CdS before the reduction reaction of $PtCl_6$ ion to the elemental Pt^o and once where the CdS was added at the end of the reduction reaction (the point which was determined by the UV-Vis analysis). At both cases, certain amount of the synthesised CdS was introduced into the reduction reactions to make 2, 5, 7 and 10 wt. % Pt/CdS. Then,

the solutions were allowed to be stirred for an extra 4 hours before they were cooled down from 80°C to room temperature. The resulting products were then filtered through 8 μm filter paper and dried in a vacuum oven at the ambient temperature overnight.

3-2-3 Co_xP synthesis

Two routes are normally considered for the synthesis of cobalt phosphide (Co_xP); one is solid phase synthesis (through thermal phosphidation reaction), and the other one is solution phase synthesis (through organometallic reaction or hydrothermal reaction) . In this research, all these three synthesis routes will be conducted, and their results will be compared.

3-2-3-1 Solid phase synthesis (thermal phosphidation reaction)

To synthesise Co_xP by the thermal phosphidation reaction, the precursor of cobalt hydroxide $Co(OH)_2$ was made first by a precipitation method. Therefore, a buffer solution of 1.7×10^{-3} M sodium citrate dihydrate $C_6H_5Na_3O_7$. $2H_2O$ (>99%, Fisher Scientific) was prepared in 100 mL deionised water. Then, 200 mg of cobalt nitrate hexahydrate $Co(NO_3)_2\cdot 6H_2O$ (>98%, Fisher Scientific) was added into the solution, which stirred for 15 min. This solution was treated as a titrate. For the titrant, a solution of 0.5 M sodium hydroxide was prepared in 100 mL deionised water using NaOH pellets (>98%, Sigma Aldrich). The titrant solution was added dropwise to the titrate solution until pH rise of 14 to ensure cobalt hydroxide precipitants were fully formed (at the excess of NaOH) as:

$$\mathrm{CO(NO_3)_2 + 2\,NaOH \rightarrow CO(OH)_2 + 2\,NaNO_3} \quad (3\text{-}3)$$

The precipitated $Co(OH)_2$ was then centrifuged, the solution decanted, and the solid powders dried in a vacuum oven. To synthesise cobalt phosphide, 50 mg of the formed $Co(OH)_2$ and 250 mg of sodium hypophosphite monohydrate NaH_2PO_2. H_2O powder (>99%, Sigma Aldrich) were ground by pestle and mortar and then transferred to a crucible and inserted into a tube furnace for annealing time of 1h in an argon atmosphere (gas flow rate 30 mL/min) and temperature of 300 °C using a ramp up rate of 2 °C·min^{-1}, see arrangement in Fig 3.3. At the annealing step, the

thermal phosphidation reaction occurred, where NaH_2PO_2 was decomposed to produce phosphine PH_3 and Na_2HPO_4 and where this short-lived gaseous intermediate of phosphine quickly reacted with $Co(OH)_2$ in an acid-base reaction to form CoP, as:

$$2\,NaH_2PO_2 \rightarrow Na_2HPO_4 + PH_3 \quad \text{(decomposition reaction)} \quad (3\text{-}4)$$

$$PH_3 + Co(OH)_2 \rightarrow CoP(s) + H_2O \quad \text{(acid-base reaction)} \quad (3\text{-}5)$$

The formed black solid CoP was then washed subsequently by water/ethanol mixture (molar ratio of 3:7) three times and dried in a vacuum oven.

Figure 3. 3 Experimental set-up for the solution phase synthesis of CoP in an argon purging tube furnace with PID temperature controller.

3-2-3-2 Solution phase synthesis (organometallic reaction)

To synthesise Co_xP by the organometallic reaction, 5 ml of 15.7 mmol 1-octodecene and 5 ml of 15.2 mmol oleylamine and 257 mg $Co(acac)_2$ were added into a 100 ml three-necked round-bottom flask, equipped with a reflux condenser, thermocouple, bubbler and a heating mantle, see Fig 3.4. First, the reaction mixture was heated under argon to 120 ^oC and kept at this temperature for 1 h in order to remove oxygen, water and low boiling point impurities. Then, the reaction temperature was further raised to 320 ^oC under argon atmosphere and allowed to equilibrate for 10 min. Following the temperature equilibrium, 2 ml trioctylphosphine (TOP) was slowly injected into the reaction mixture and the reaction was kept at this temperature for 1 h and 12 h. After that, the flask was allowed to cool down to room temperature by

removing the heating mantle. The resulting suspension was then cleaned by the addition of 50 ml isopropyl alcohol to the reaction mixture, followed by centrifugation at 4000 rpm for 10 min. Then, the precipitate was suspended in the mixture of 15 ml hexane and 25 ml ethanol. Washing process with the mixture of hexane and ethanol and then centrifugation at 4000 rpm was repeated for 6 times to assure all oily residues were removed and the dried CoP powders retained at the bottom of the tube vials.

Figure 3. 4 Experimental set-up for the solution phase synthesis (organometallic reaction) of CoP.

3-2-3-3 Solution phase synthesis (hydrothermal reaction)

Synthesis of Co_xP was also undertaken by a hydrothermal method, where 1 mmol (291 mg) of cobalt nitrate hexahydrate $Co(NO_3)_2 \cdot 6H_2O$ (>98%, Fisher Scientific) and 10 mmol (310 mg) of red phosphorous P (>97%, Sigma Aldrich) were added into 30 mL deionised water. Then, the solution was mixed for 30 min (with 100 rpm mixing speed). To form crystalline Co_xP, the mixture was reacted hydrothermally at 473 K for 18 h in a 250 mL Teflon-lined stainless-steel autoclave (Lab Glassware and Equipment). After cooled to room temperature, the final product was collected by vacuum filtration. The product then washed three times with deionised water and finally dried in a vacuum oven at 60 °C for 3 hours.

3-2-3-4 Loading of Co_xP on CdS

For the loading of the cocatalyst Co_xP onto the CdS particles, different methods of grinding, sonication and in-situ hydrothermal treatment were tested and compared. In the grinding method, certain amount of synthesised Co_xP and CdS powders were dispersed in 1 ml ethanol (for making 5 wt. % Co_xP /CdS) and then thoroughly ground by the pestle and mortar to increase their contact area. After volatilisation of ethanol, an extra 1 ml ethanol was added and the grinding was repeated. This grinding procedure was conducted three times to ensure good loading of Co_xP on the CdS surface sites.

In the sonication method, certain amount of the synthesised Co_xP powder and the CdS filtrate (before drying the final particles) were weighted first, for making 2, 5 and 10 wt. % Co_xP /CdS, and then added into the 20 ml deionised water. Next, the solution was allowed for the 2 h sonication to assure all the Co_xP particles were loaded on the CdS surface sites. The resulting solution was then transferred to a watch glass, where the particles were dried naturally in an ambient temperature.

In the in-situ hydrothermal treatment method, certain amount of the pre-synthesised Co_xP powder and the CdS filtrate were weighted first, for making 2, 5 and 10 wt. % Co_xP /CdS, and then transferred into 160 ml deionised water for a hydrothermal treatment at 473 K for 72 h, using a 250 mL Teflon-lined stainless-steel autoclave. After cooled to room temperature, the catalyst-cocatalyst product was filtered (8 μm filter paper) and washed with 3:7 water/ethanol mixture at least three times and dried in a vacuum oven at ambient temperature.

3-3 Instrumental analysis

3-3-1 XRD analysis

To analyse the crystalline structure and estimate the particle size of the synthesised particles, a high-resolution X-ray diffraction (XRD) apparatus was used with the X-ray diffractometer of MiniFlex Rigaku and an X-ray source of CuKα (λ=1.54056 A and power of 600W). The diffraction spectra is generated when the X-ray light at certain wavelength (λ) is scattered by the sample and detected [108]. Different materials give different diffraction patterns depending on their crystal structure and the

different spacing between crystal layers (*d*). The principle of obtaining the diffraction peaks can be described using the Bragg's law[120];

$$n\lambda = 2d\ sin\theta \tag{3-6}$$

where λ is the wavelength of the incoming radiation, d is the interplanar spacing within the crystal, n is a positive integer and θ is the angle between the incoming and scattered X-ray beam, see Fig 3.5.

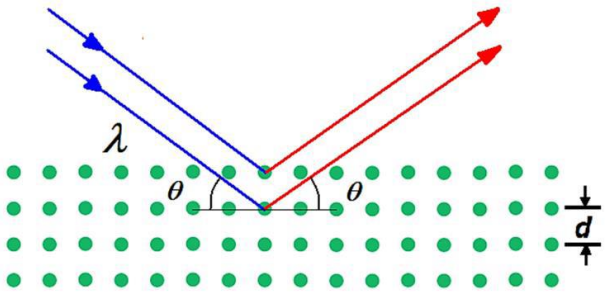

Figure 3. 5 Working principle of XRD with incoming radiation,λ, with an angle, θ,and same angle scattering towards the detector ,with each crystal plan has a defined spacing of, *d*, [120]**.**

The X-ray spectrums in this thesis were collected between 20 -2θ -100 and analysed by a commercial software (X'Pert Plus) and a published database within the software (ICSD reference database). For this thesis, all thermal analysis were undertaken externally at University of Nova Gorica, Slovenia.

3-3-2 TGA/DSC Analysis

To understand thermodynamics of the reactions and obtain correct temperature settings to drive the reactions, thermogravimetric analysis (TGA) coupled with the differential scanning calorimetry (DSC) were used. The TGA measures mass loss or gain over a defined temperature rise in the apparatus. The gas environment can be chosen as air, oxygen, argon, nitrogen. Mass changes observed in the thermogravimetric analysis could be corresponding to decomposition of the sample, water evaporation or as a result of oxidation [115]. A typical thermogravimetric analyser consists of a precision balance with a sample pan that is located inside a

closed furnace chamber with a programmable control temperature setting. Inside the furnace the temperature is increased and the change in the mass of the sample is recorded [121]. The thermogravimetric data at the corresponding temperature are often presented in plots of mass % (of initial mass) versus temperature. The DSC part of the thermal analysis measures amount of heat changes (as heat flux) of the same sample set up i.e. sample pan and a reference pan inside the furnace chamber, see Fig 3.6. The reference sample should have a well-defined heat capacity (C_p) over the range of measuring temperatures.

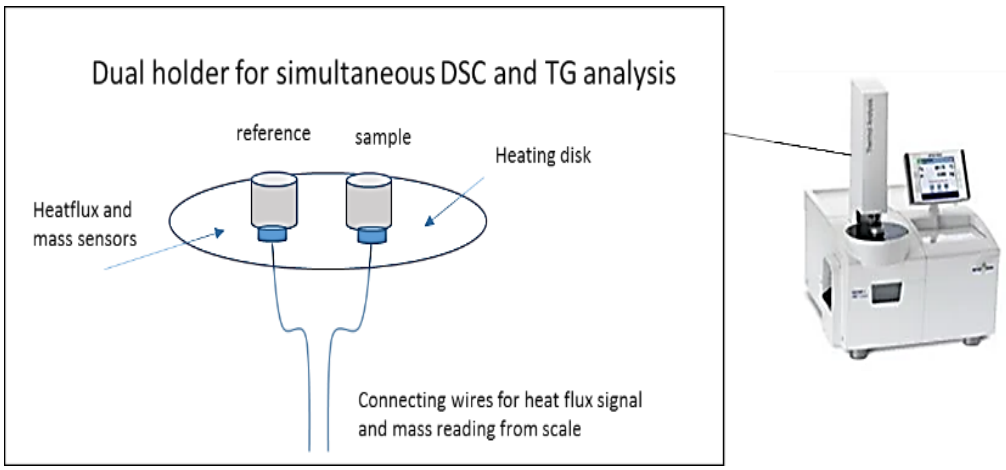

Figure 3. 6 Working principle of TG-DSC analysis set up [115]**.**

When a sample undergoes a phase transition, heat is consumed by the sample (for an endothermic phase transition) or given off from the sample (for an exothermic phase transition). This is latent heat and is not associated to a mass change. For this thesis, all thermal analysis were undertaken externally at University of Nova Gorica, Slovenia using a TGA/DSC analyser (Mettler Toledo 2), where the particle samples were analysed at air in a heating rate of 10°C/min up to 700 °C. For the reference a well dried corundum crucible was used as well as the powder sample that was weighted carefully on a high precision scale in the corundum sample holder.

3-3-3 SEM/EDS analysis

To analyse chemical composition and morphology of the synthesised samples, a scanning electron microscope (SEM) (JSM7100f TTLS, JEOL, Japan) equipped with an energy dispersive X-ray spectroscopy (EDS) detector (X-Max80, Oxford) was used.

The EDS enable analysis of (majority) surface elemental compositions of the powder sample, hence when such analysis was needed, the sample was pressed prior inserting into the microscope chamber.

To produce an image, a focused beam of high-energy electrons is generated by an electron gun. The SEM uses an anode (which is positively charged), a magnetic lens (which generates a magnetic field) and a specific set of coils (which scans the electron beam in a raster-like pattern) to direct the generated electron beam to the sample. After the sample is bombard by the electron beam, the secondary electron signals are generated (the atoms of the sample that have absorbed energy of electron beam give off their own electrons). These secondary electrons that are knocked off the near-surface region of a sample will enter to a secondary electron detector (300 V) where the signals are converted to create an image. Since the wavelength of electrons is much smaller than the wavelength of light, the resolution of SEM image is far better than an optical microscope. The working principle of a SEM instrument is shown in Fig 3.7, where it can be seen that the sample specimen is placed inside a vacuum evacuated chamber and bombarded with the highly focused electron beam, created by the electron gun. The returning electron signals from the sample surface are then entered into the SEM detector.

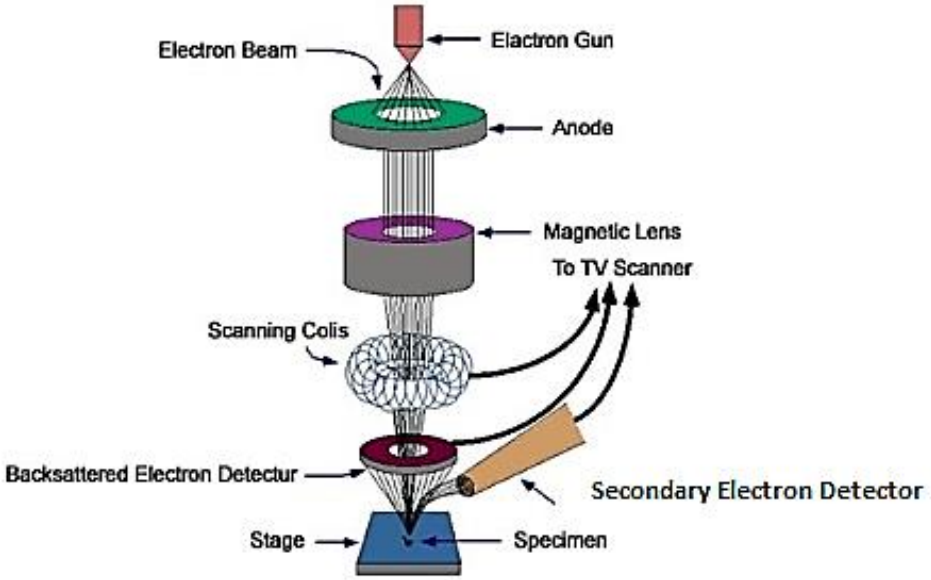

Figure 3. 7 Working principle of a typical scanning electron microscope analysis[122]**.**

For the elemental analysis an additional EDS detector needs to be activated inside the chamber and used instead. Therefore, in addition to the secondary electron signals generated from the sample surface for image analysis, the EDS detects the formed X-rays from the back scattered electrons that trapped inside the sample. The X-rays are produced by inelastic collisions of the incident electrons with electrons in discrete orbitals, shells, of the sample atoms. The produced X-rays are then emitted in all directions and so they can escape the sample and thus be detected by the dedicated EDS detector [123]. The number and energy of the X-rays emitted from the sample are measured by EDS. The elemental analysis is undertaken by comparing the peak of signals and its energy with known standards, which are part of the microscope software package. The SEM/EDS analysis could therefore produce both chemical compositional information, purity information as well as size, plus shape information of the synthesised nanoparticles.

2-3-4 UV-Vis spectroscopy analysis

The UV-Vis spectroscopy was used for both qualitative analysis of compounds in reaction solution and optical properties of the catalyst sample.

For molecular analysis of the reaction solutions specimen, the UV-visible light would have enough energy to promote bonding and non-bonding electrons of the molecules to a higher electronic state (which can be bonding and anti-bonding molecular orbitals). The difference between these energy states of the orbitals is called “band gap”, where the energy of the photon must exactly match the band gap to be absorbed. Molecules with different chemical structures have different energy band gaps, as they all have different atoms and bonding, and therefore all will show different absorption spectra.

The working principle of the UV/Vis spectrophotometer with dual beam is shown in the Fig 3.8. First a light source (Xenon arc lamp covering 160 to 2000 nm) passes through a scanning monochromator (including two slits and a prism), which filters the light so only light of a single wavelength enters the instrument at a time. This is necessary to see the samples response at specific wavelengths. Then the single

wavelength light is split into two beams with equal intensities before reaching to the detector (if dual beam set up is used). One beam is used for a reference and the other beam is used for the sample. The reference beam intensity is taken as 100 % transmittance (zero absorbance), and the measurement displayed is the ratio of the two beam intensities. Therefore, if sample absorbs the light, the intensity of the sample decreases compared to the reference intensity (100% transmittance), which leads to a decrease in the ratio of the two beam intensities and subsequently a decrease in its transmittance (an increase in absorption). The UV-Vis detector presents the measured data based on transmittance % (or absorbance %) over the wavelength (nm).

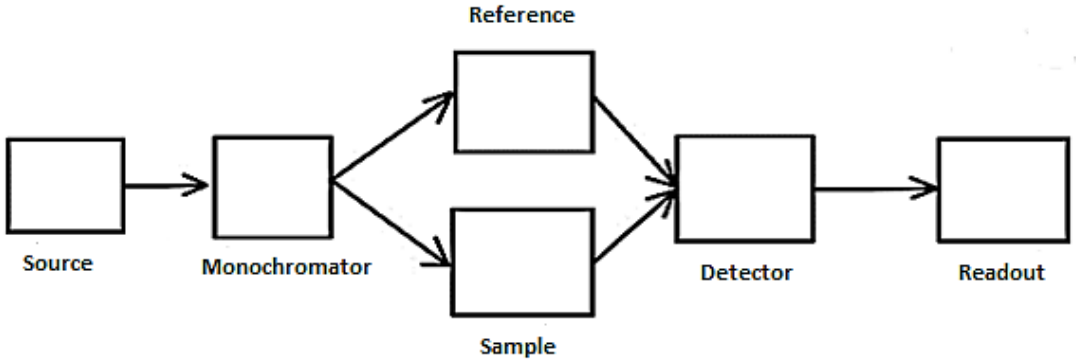

Figure 3. 8 Flow sheet of a typical dual beam UV-Vis spectroscopy analysis [124]**.**

For the optical analysis of the catalyst sample an externally placed spectrometer was used at University of Nova Gorica, where an integrating sphere attachment (ISR-3100) was mounted into the spectrophotometer (Shimadzu, UV-Vis 3100) to measure diffuse transmittance and reflectance of the powders. The powder sample was placed at the front or at the back of the sphere depending on if transmittance (and absorbance) or reflectance was measured. The principle of measuring the diffuse reflectance can be seen in Fig 3.9 where the sample is placed opposite the incoming incident light and then the sphere concentrates the light reflected from the sample on the detector. The obtained value is read as the reflectance with respect to the reflectance of the white board standard (here barium sulphate with 100 % reflectance).

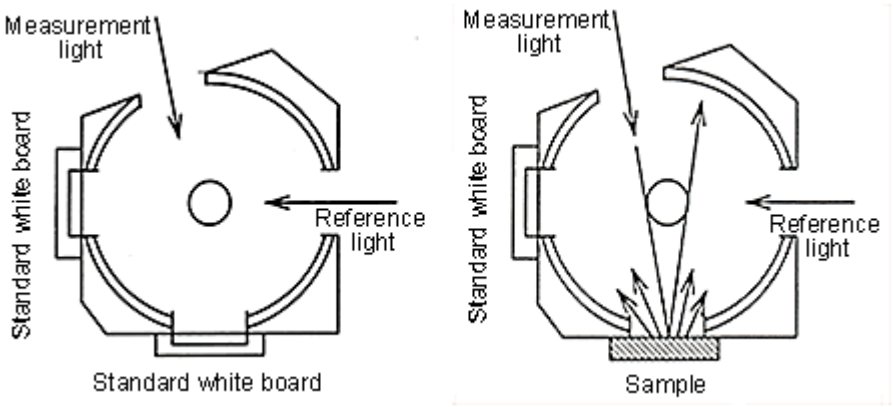

Figure 3. 9 A typical working principle of a UV-Vis diffuse reflectance analysis when using an integrated sphere, where the sample is placed at the back of the sphere and reading compared with a standard white board [124]**.**

For the photocatalyst band gap calculation, the Tauc relations were used together with the measurements obtained from the integrated sphere. The Kubelka-Munk function, F(R), was also used to approximate the optical absorbance and scattering of a sample from its reflectance as; $F(R) = (1-R)^2 / 2R$. The Tauc plot is then created by taking the function of F(R) and photon energy ($h\nu$) and use of a correct exponent ,*n*, (for direct semiconductors n= 0.5 and for indirect semiconductor n=2) as; $[F(N) \times (h\nu)]^n$. For a direct band gap semiconductor (as expected for CdS), the Tauc plot will show a linear Tauc Region just above the optical absorption edge. Extrapolation of this line to the photon energy x-axis can then be read as the semiconductor band gap in eV. More details about the bang gap calculation will be presented in in the Result Chapters.

3-3-5 Fourier transform infrared spectrometer (FTIR) analysis

Fourier transform infrared spectrometer (FTIR) was used to analyse the reaction molecules, where molecular structural information originates from the molecules' characteristic absorption of an incoming infrared radiation. When the molecules are exposed to the infrared radiation, they can selectively absorb the IR radiation of specific wavelengths, which causes a vibrational energy levels transfer from ground state to the excited state. The resultant absorption spectrum indicates presence of various chemical bonds and functional groups present in the sample. The background

emission spectrum of IR source is first recorded to create a baseline and then followed by the emission spectrum of the sample. The ratio of the sample spectrum to the background spectrum is directly related to the sample's absorption spectrum, representing a molecular 'fingerprint' of the sample and shown in % transmittance per wavelength number (cm^{-1}). Fig 3.10 shows a block flow diagram of a typical FTIR, consisting of the IR source, a collimator (causing direction of beams to become more aligned), interferometer, sample compartment and the signal detector. A typical interferometer used in FTIR, consists of two perpendicular mirrors (one stationary and one movable) and a beam splitter.

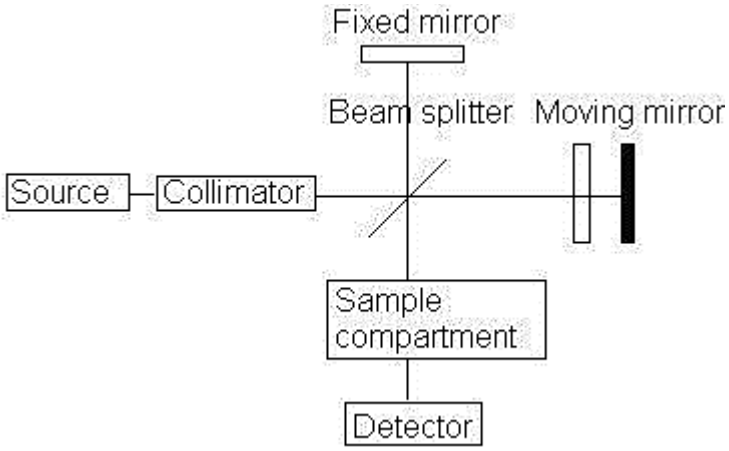

Figure 3. 10 Block flow diagram showing a typical work principle of a FTIR analysis [125]**.**

First, the source generating the IR radiation is passed through the sample (some radiation is absorbed by the sample and some passes through), and then through the interferometer and reaches the detector. The beam splitter is designed to transmit half of the light and reflect half of the light. Subsequently, the transmitted light and the reflected light strike the stationary mirror and the movable mirror respectively. When reflected back by the mirrors, two beams (with different path) of light recombine with each other at the beam splitter and conducted into the detector, where the difference of the intensity of these two beams are measured as a function of the difference of the paths.

In this research, FTIR (Shimadzu, IR Tracer-100) was used to analyse adsorption of lactic acid on 5 wt.% of Pt/CdS system and ammonium sulphite on 5 wt.% of CoP/CdS.

First the catalyst powders were immersed in the photolyte solutions long time enough to assure maximum adsorption on the particles. Then the samples were washed with deionised water and then dried in the vacuum oven before analysis. The 10 mg dried solid sample was pressed into a pellet (using FTIR dedicated die and press) and transferred to the FTIR sample holder. For the liquid samples (the various solution specimens), small drops on the sample holder were used for the FTIR analysis.

3-3-6 Ion chromatography (IC) analysis

To measure concentration of anion species in the reaction solution, such as SO_3^{2-} and lactate, ion chromatography (IC) was used. In a typical ion exchange chromatography analysis, the dissolved charged ions bind to the oppositely charged functional groups that have been bound covalently on the matrix of the column resin and then eluted by changing the ionic environment using a mobile phase. The mobile phase (eluent) which runs through the column, consists of another specific ionisable functional group that can bind to the targeted charged ions on the column wall and then separate them (by ion exchange function). This means ions will have different affinity to the column wall and therefore different mobility through the column. The ions with high affinity for the functional groups of the column will have a lower separation, a lower mobility, and consequently a longer retention time. The eluent fluid, which now contains new ion complexes(after the ion exchange) will have ions with different retention time depending on their respectively time of ion exchange, and therefore will finally pass the detector for the specimen analysis. The different retention peaks obtained by the separated ions, can be used to determine type and the concentrations, if a calibration curve has been created first.

The working principle of a typical ion chromatography is shown in Fig 3.11. First the eluent is delivered to the system using a high-pressure pump. Then, the sample is introduced and flows into the analytical ion-exchange columns where the ion-exchange separation occurs. The eluent both carries the sample through the ion chromatography system and separates the sample ions. Then the separated sample ions are introduced to a suppressor, where the high conductivity ions are removed

and replaced with low conductivity ions. This process not only reduces the background conductivity, but also reduces the associated noise while simultaneously increase the conductivity response of the low concentration analytes. An eluent regeneration system as a fundamental part of the suppressor system, also facilitates the recycling of the eluent and only causing a water-based eluent waste. Finally, the ions are introduced to a conductivity detector, which detects ions based on a change in their conductivities. The detector is connected to a data recorder to acquire and process the data and show peaks in the chromatogram.

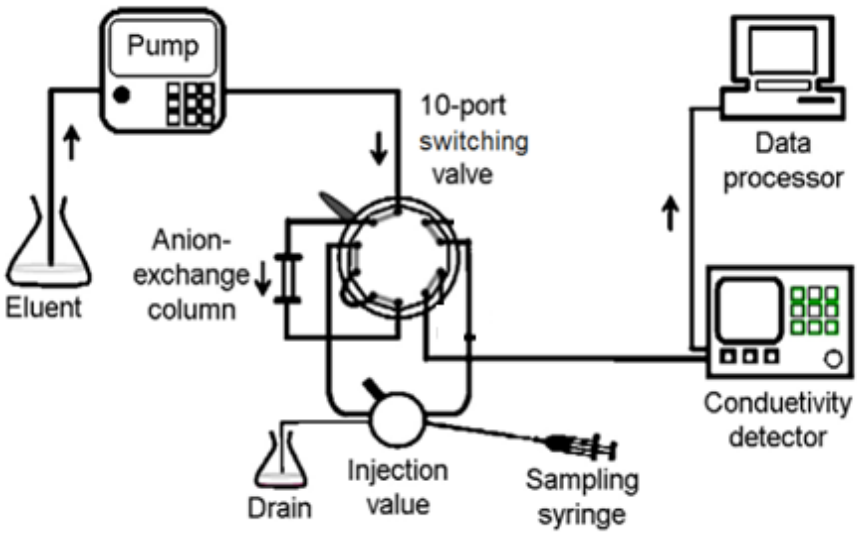

Figure 3. 11 Working principle of an anion IC analysis using a conductivity detector [126]**.**

The analysis of concentration of different ions of sulphite and lactate in this research was carried out by an ion chromatograph (Dionex IC-25 system, Thermo Fisher) equipped with an isocratic pump (ICS-5000 system). The pump had a high accuracy performance to maintain a controlled rate and pressure for the eluent. The eluent was a mixture of sodium carbonate (Na_2CO_3) and sodium bicarbonate ($NaHCO_3$) that continuously ran through the separation ion-exchange column (LC30). The column contained amino-ethyl functional group which suited best for the detection of the anionic species in this research . A suppressor (Dionex, micromembrane MMS 300) in combination with an eluent regeneration system (Dionex, ERS™ 500) were used for the chemically regeneration of the eluent. A detector (Dionex, ICS-4000 CD) was used for the high-performance conductivity detection of the targeted ions. The

obtained information from the IC will be used in the reaction kinetic studies that will be presented in the Result Chapters.

3-3-7 Gas chromatography (GC) analysis

To identify the level of purity of the formed gas, gas chromatography (GC) with a thermal conductivity detector (TCD) was used. The working principle of a GC is shown in Fig 3.12, where a gas sample is first injected into the injector port and is heated assuring all volatile specimens are vaporised prior entering the column. A thermal conductivity detector consists of two parallel tubes; one tube for the sample and the carrier gas and the other one is for the carrier gas only (which was helium gas in this research).

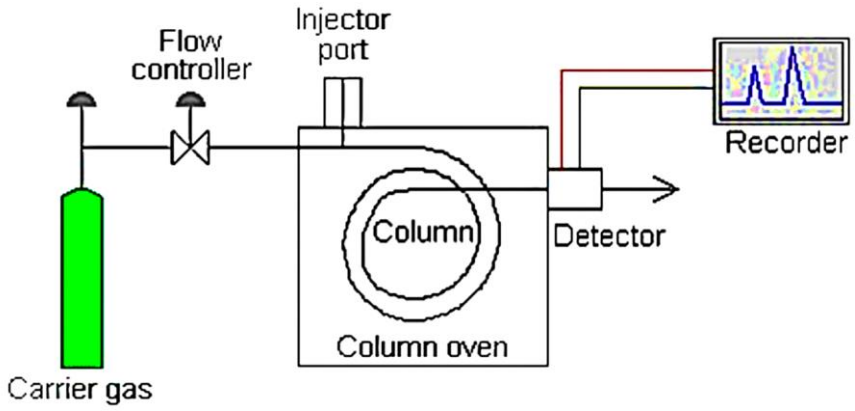

Figure 3. 12 Working principle of gas chromatography[127]**.**

A thermal conductivity detector senses changes in the thermal conductivity of the column effluent and compares it to a reference flow of carrier gas. A gas with high conductivity will therefore produce a different heat transfer rate than a gas with lower conductivity. Temperature sensors pick up these changes and convert them to digital signals. A GC chromatogram is a plot of gas retention peaks against time where each different gas specimen produces a distinct peak which can be compared to the known standards. The retention time depends on the duration of travel through the column. The height of the peaks (or area under the peaks) can be used to evaluate the concentrations.

The gas analysis in this research work was carried out using a gas chromatograph (TRACE 1310 Gas Chromatograph, Thermo Scientific), equipped with a TCD (Instant Connect Thermal Conductivity Detector, Thermo Scientific™) for the specimen analysis and a column chosen for the light gases such as hydrogen (Trace plot TG-Bond M sieve 5 Å) of approximate dimensions of 30 m x 0.53 mm x 50 µm. The 5 Å molecular sieve for the column was chosen to provide good separation of the expected light gas peaks and produce well-defined peaks. For manual injection of the gas samples, a dedicated GC syringe (10 µl, Hamilton™ 700 tight syringe) was used. The injection port temperature was kept at 250 °C and the thermal conducting detector at 200 °C for most of the analysis. A selection of high purity gases was employed for calibration of the GC instrument, as listed in Table 3.1, plus the calibration sheets from Fisher Scientific.

Table 3. 1 Gases used as the standards.

Gases	Purity (%)	Supplier
Hydrogen (H_2)	99.999	BOC
Nitrogen (N_2)	99.999	BOC
Oxygen (O_2)	99.999	BOC
Argon (Ar)	99.999	BOC

3-4 Reactor design

For the photocatalytic experiments, a water-jacketed Pyrex glass photoreactor was designed and benchmarked. The vessel was supplied with four ports; one for pre-purging with argon gas, one for the produced gas outlet, one for photolyte and catalyst input and one for gas sampling, see Fig 3.13. The cylindrical photoreactor had a volume of 1.57 litre with an inner diameter of 10 cm (ID) and height of 20 cm (h). The reactor temperature was controlled by an isothermal water jacketed reservoir with a PID temperature controller. A magnetic stirrer was placed at the bottom of the reactor to provide sufficient agitation.

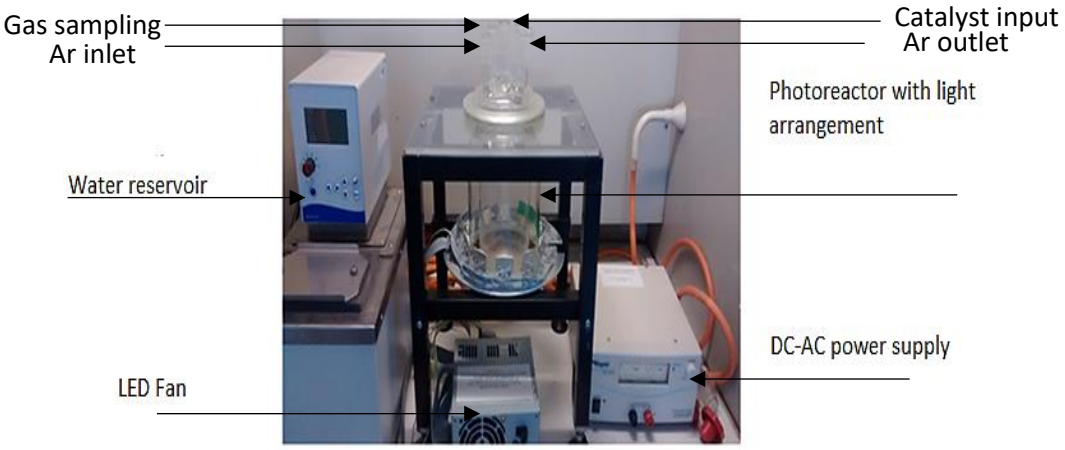

Figure 3. 13 Jacketed Pyrex photoreactor set-up with a LED arrangement , the four ports, and the additional LED fan and power supply.

A cool white-LED light arrangement was designed and attached to the outside of the reactor, see Fig 3.13. For the reactor light source (LED) appropriate factors such as great irradiation area, uniform light distribution throughout the reactor and adequate light intensity for the electron-hole generations were considered. Based on these factors the first LED unit was designed, as shown in Fig 3.14, which included 10 LEDs (10 W cool white LED) in a parallel connection configuration that was wrapped around the outside of the Pyrex reactor. As the LED unit would be very hot when driven at maximum power, a metallic heat sink was attached to the light configuration. A thermocouple was attached to the back of the light assembly to record the temperature. An additional fan (LED fan) for removing the heat from LEDs back surface was placed outside the reactor vessel, as seen in Fig 3.13. A gap of 2 mm between the LED front surfaces and the outside of the Pyrex® glass reactor was made to assure direct contact and for easy removal of the reactor vessel if need be.

The arrangement of light in the LED unit was done after spectral analysis of one LED, see section 3-4-1, and then arranged in a manner so that the intensity of the irradiation could be met by a power control. To drive the LEDs, a DC power supply, with variable output (max 15 V DC) and current capability up to 10 A was used, see Fig 3.13. A setting of 15 V and 10 A, would provide the maximum power for the 10 x 10 W LED's. To ensure that the maximum power was provided inside the reactor, a digital hand-held light meter (Voltcraft MS-1300) was used to register the exact level

of illumination used in the photocatalytic reactions. The device measured 700,000 lux, which corresponded to 0.0102 W/cm^2 (102 W/m^2).

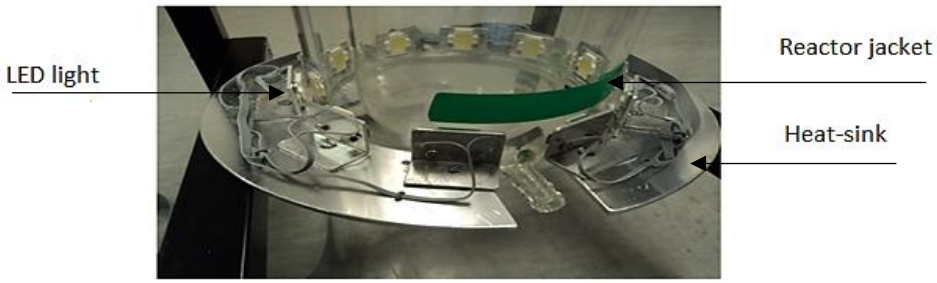

Figure 3. 14 The 10 x 10W cool white-LED arrangement at the outside of Pyrex glass reactor vessel with additional metal heat sink.

3-4-1 Hydrogen collection

To collect the produced hydrogen, an inverted water-filled measuring cylinder or burette was used, where the volume of the collected hydrogen was determined by the volume of the water displaced, see Fig 3.15. The accuracy and reproducibility of the water displacement method was tested using a syringe. Before the start of the test, the plunger was pushed outwards to be filled with air and then pressed fully into the barrel to expel any air present into the syringe and therefore into the measuring cylinder. Then, the volume of the air which was displaced by water, was measured using a balance scale. The accuracy and reproducibility (experimental errors) of the water displacement set-up was recorded within $\pm$ 0. 1 ml based on the standard deviation of 3 tests.

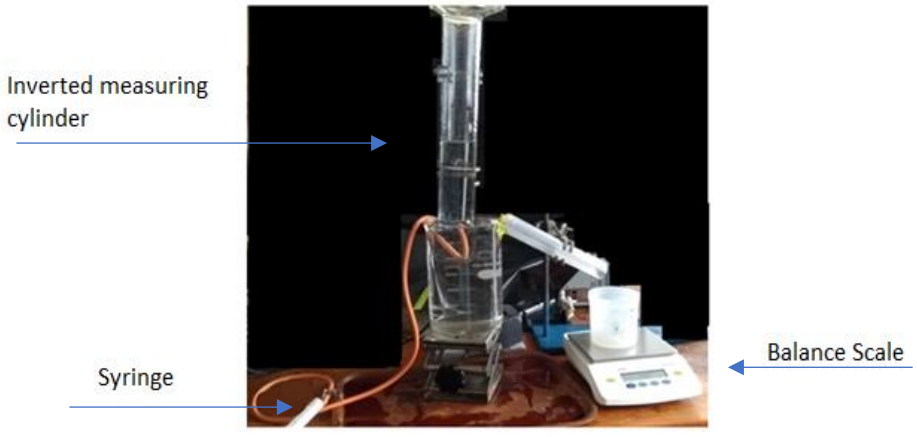

Figure 3. 15 Inverted column hydrogen collection set-up.

3-4-2 Photonic energy conversion efficiency

The energy conversion efficiency for the photoreactor used in this research was defined as the ratio of the chemical energy of the photogenerated hydrogen per unit of time, to the irradiation energy absorbed by the photocatalyst particles per unit of time as:

$$\eta = \frac{rH_2 \times 286}{I_{abs}} \times 100\% \quad (3\text{-}7)$$

,where rH_2 is the rate of hydrogen production (mol/min), multiplier 286(KJ/mol) is the higher heating value of H_2 (HHV) and I_{abs} is the radiation power absorbed by the photocatalyst (KJ/min). It will be shown later in Fig 7.15 that the rate of hydrogen production for the 1.57 Litre photoreactor with 300 ml ammonium sulphite (2.66 M) using 0006 g/cm^3 CoP/CdS catalyst and two rows of cool white LED arrays (2 x 10 W, total of 200 W) will be 0.8 µmol/s. The maximum total radiative flux received by the photocatalyst particles will be shown later in Fig 7.14, to be around 1 W/m^2 at the absorption band of the photocatalyst (CoP/CdS). Therefore, the energy conversion efficiency used in this research was calculated as:

$$\eta = \frac{0.8\times10^{-6}\left(\frac{mol}{s}\right)\times60\left(\frac{s}{\min}\right)\times286\left(\frac{kj}{mol}\right)}{0.001\left(\frac{kj}{s}\right)\times60\left(\frac{s}{\min}\right)} \times 100\% \approx 22.88\% \quad (3\text{-}8)$$

3-4-3 Photocatalytic hydrogen experiment

The photoreactor compartments for the photocatalytic hydrogen production were put together according to Fig 3.16. For this photoreactor, (i) an argon gas was supplied to assure oxygen free reaction conditions, (ii) a water reservoir was used to control the temperature, (iii) a LED unit (with the power supply and a fan) was used to provide the required light intensity, and (iv) a hydrogen collection part was attached to collect and measure the produced hydrogen.

Figure 3. 16 The connected compartments for a typical photocatalytic hydrogen production.

Prior to the hydrogen production tests, the solution mixture, including photolyte and the photocatalyst particles, was purged with argon gas for 45 min to assure the reaction system to be oxygen free. Then photocatalytic reactor was then exposed to the maximum LED light intensity at the start of the photocatalytic reaction. The temperature for the photocatalytic reactor could be varied and majority of the lactic acid solution runs where at 25°C and majority of the ammonium sulphite solutions at 60°C.

3-5 Conclusion

In this chapter, all experimental procedures were presented and the basic principles of XRD, SEM/EDS, UV-Vis, FTIR, TG/DSC, IC and GC were clarified. The details of the reactor design, analysis of the light intensity, hydrogen collection, photonic energy conversion efficiency and hydrogen experiment were also explained.

Chapter 4 Results and Discussion: Photocatalyst Characterisation

4-1 Introduction

In this Chapter, the synthesised photocatalyst is analysed. First, the CdS characterisation is given in section 4-2, followed by the co-catalyst Pt synthesis and loading on the CdS synthesis and analysis in section 4-3. After that the co-catalyst Co_xP synthesise through a solid-phase reaction is presented in section 4-4-1, followed by the two types of solution-phase synthesis in section of 4-4-2.

4-2 CdS processing

The cadmium sulphide nanoparticles were synthesised by a hydrothermal method. First, a sulphuric precursor of Na_2S was added slowly to a cadmium precursor solution of $Cd(CH_3CO_2)_2$ by titration to form an amorphous CdS precipitate that was hydrothermally annealed. To investigate the effect of oxygen in the titration step, two different samples were synthesised; one inside an oxygen free glove box and one outside in air, see Fig 4.1.

Figure 4. 1 Comparison of CdS powders prepared in air and in oxygen free environment.

From the image, there is no indication of any interferer cadmium oxide formed for the sample that synthesised in air, as it would have produced a darker coloured

powder. The two synthesised samples were then analysed by XRD, where two identical overlapping pattern were obtained, both matching perfectly with the CdS standard data (JCPDS, File No. 41-1049), Fig 4.2. There was also no identified peak shift or peak broadening in any of the two spectra. This confirms that oxygen did not affect the CdS synthesis and therefore both synthesised CdS samples can be assigned to a highly crystalline hexagonal cadmium sulfide phase with the lattice parameters of a= 4.1360 $\mathring{A}$, b=4.136 $\mathring{A}$, and c=6.713 $\mathring{A}$, which is in agreement with the published data [128,129].

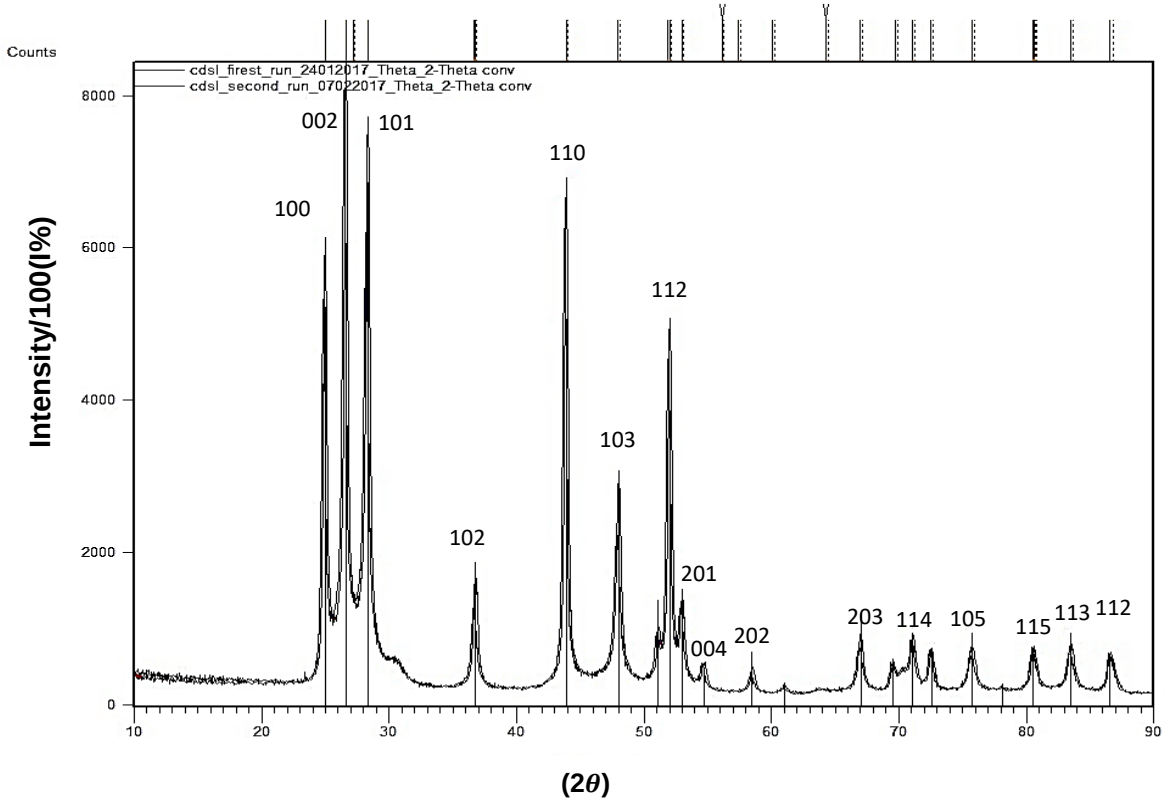

Figure 4. 2 Comparison of the two synthesised CdS XRD pattern ; in oxygen free atmosphere ("first run") and in presence of air ("second run") as compared against CdS standard data (JCPDS, 41-1049).

From the full width at half maximum (FWHM) of the most intense peak, particle size for both samples were calculated by Scherrer equation [130], as:

$$D = \frac{0.9\lambda}{\beta \cos\theta} \qquad (4\text{-}1)$$

, where λ is the wavelength of X-ray diffraction (Cu K-alpha), β is FWHM in radians of the XRD peak and θ is the angle of diffraction. The obtained values can be seen in Table 4.1, leading to the calculated crystalline mean size in a range of 18 nm.

Table 4. 1 Parameters used for the Scherrer formula.

FWHM (°)	β (rad)	λ (Å)	2θ	θ	COS θ	D (nm)
0.5	0.008	0.154	45	22.5	0.92	18.060

It should be noted that the high crystallinity of the synthesised CdS particles would mean a reduced amount of defects in the crystal structure and therefore promotion of an efficient movement of the photogenerated electrons and holes to the CdS surface, as reported by the researchers[131–135]. For photocatalysis, hexagonal-CdS is preferred as its electron band structure configuration promotes a higher photocatalytic activity compared with the cubic CdS crystal structure. The small nanostructured size of the synthesised CdS particles will also promote a faster electron and hole diffusion to the catalyst surface and as a result, will lead to a higher efficient photocatalytic yield. To investigate the optical absorption performance of the synthesised CdS samples, UV-Vis spectroscopy of the powders was conducted, see Fig 4.3.

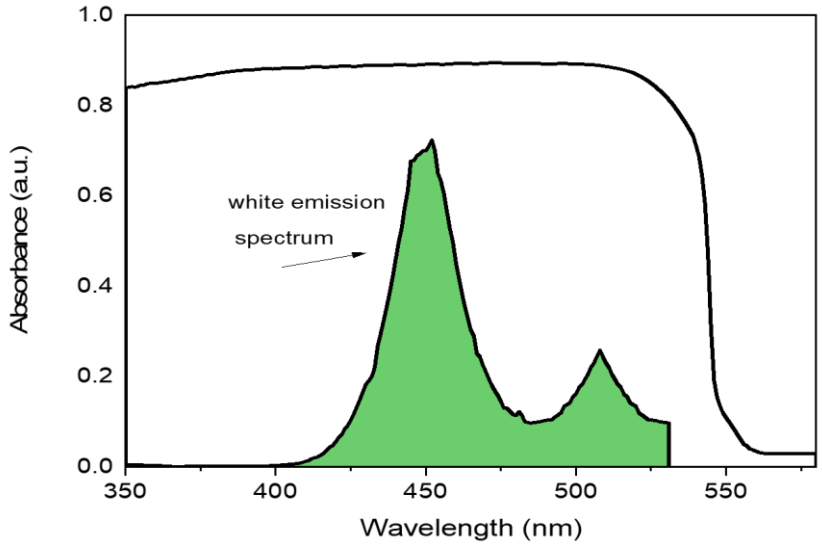

Figure 4. 3 Light absorbance of the synthesised CdS sample compared with radiation from the10 W cool white LED.

It should be pointed out that the absorption and reflection spectra of the two types of synthesised CdS powders were identical, which further proves that a successful CdS synthesis does not need to be conducted in an oxygen free environment. In Fig 4.3, it can be seen that the CdS sample exhibits an absorption edge in the visible light region between 512–555 nm, which is attributed to the CdS intrinsic band gap. This optical absorption profile matches with the emission spectrum of the cool white LED lamps used in the photoreactor, suggesting that the CdS photocatalyst can be successfully photoactivated inside the LED-driven photoreactor.

The optical band gap of the synthesised CdS nanoparticles was calculated using the Tauc relation [131,136] as:

$$(\alpha' hv)^{1/n} = A(hv - Eg) \quad (4\text{-}2)$$

, where α' is the absorption coefficient, hv is the photon energy (eV) where $hv = \frac{1240}{\lambda}$, A is the proportionality constant and Eg is the energy of the optical band gap. In the above equation, exponent n dictates the characteristics of the transition in the semiconductor [131], i.e. n = 1/2 for the direct band gap transition and n = 2 for the indirect band gap transition. The absorption coefficient α' was obtained using the diffuse reflectance measurements, R, as:

$$\alpha' = (1 - R)^2/2R \quad (4\text{-}3)$$

CdS is regarded as a direct transition semiconductor by most authors [131,137]. A direct band gap transition is when the energy changes, but the momentum is conserved and it is formed between the lowest energy point of a conduction band and the highest energy point of a valence band. The indirect transition is when both the energy and the momentum change and is formed between the lowest energy point of a conduction band and the highest energy point of a valance band [138]. A schematic showing the difference can be seen in Fig 4.4. By plotting the values of $(\alpha' hv)^{1/n}$ on the y-axis versus the hv on the x-axis, the corresponding direct band gap of the synthesised crystalline CdS sample was obtained from extrapolating the straight part of the graph on the hv-axis, as shown in Fig 4.5. The extrapolation of the straight line that intercepted the hv -axis gave the value of 2.3 eV for the optical band gap, which was consistent with reported results[129,137,139].

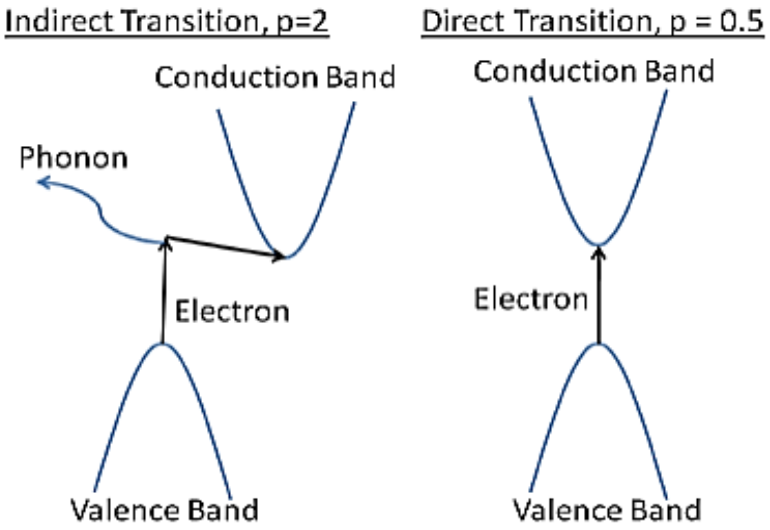

Figure 4. 4 Comparison between indirect and direct bandgap transitions [138]**.**

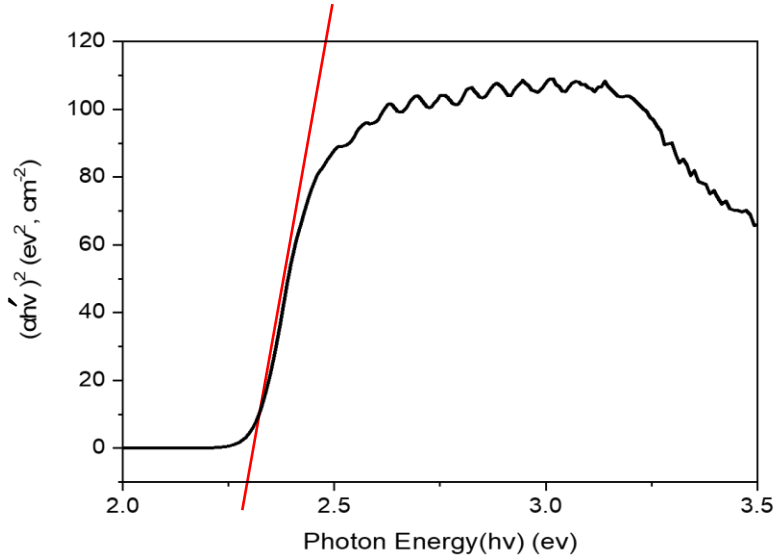

Figure 4. 5 Tauc plot based on the UV-Vis diffuse reflectance analysis to obtain optical bandgap value for CdS.

4-3 Pt synthesis

Platinum nanoparticles were synthesised by the reduction of $PtCl_6^{2-}$ ions to elemental Pt^0 by sodium citrate at 80°C. The citrate ions are used as both reducing agent and capping agent. As a reducing agent, it transforms the metal ions into the elemental metal which then grows into a Pt particle. As a capping agent, it prevents the Pt particle from growing beyond the nanometric size. To investigate the course of

reduction of $PtCl_6^{2-}$ to Pt^0, UV-Vis spectroscopy analysis of the reaction solution at various reaction times between 0 to 120 minutes were conducted, see Fig 4.6. The figure shows that before the reaction starts at t=0 min (before addition of sodium citrate), a peak at 264 nm attributed to $PtCl_6^{2-}$ (Pt^{IV}) is observed, which is consistent with literature [140]. The 264 nm peak gradually diminishes with time and completely disappears after t=120 min. This indicates a gradual formation of platinum nanoparticles in the reaction mixture has occurred, where Pt^0 exhibits broad but very weak absorbance band. The solution also shifted in colour from a pale yellow to dark brown, which is also consistent with previous published data [141,142]. For all Pt synthesis in this research, the reduction reaction was undertaken at a minimum of 120 minutes to assure complete Pt formation.

To investigate the success of Pt loading on CdS two distinct experiments were conducted; one where the CdS particles added at the end of the Pt reduction procedure (t=120 min) and one at the beginning of the reaction, before sodium citrate addition (t= 0 min). The theoretical aim was a 7 wt. % loading of Pt on CdS. The final products were analysed by SEM/EDS, see Fig 4.7 (a, b and c).

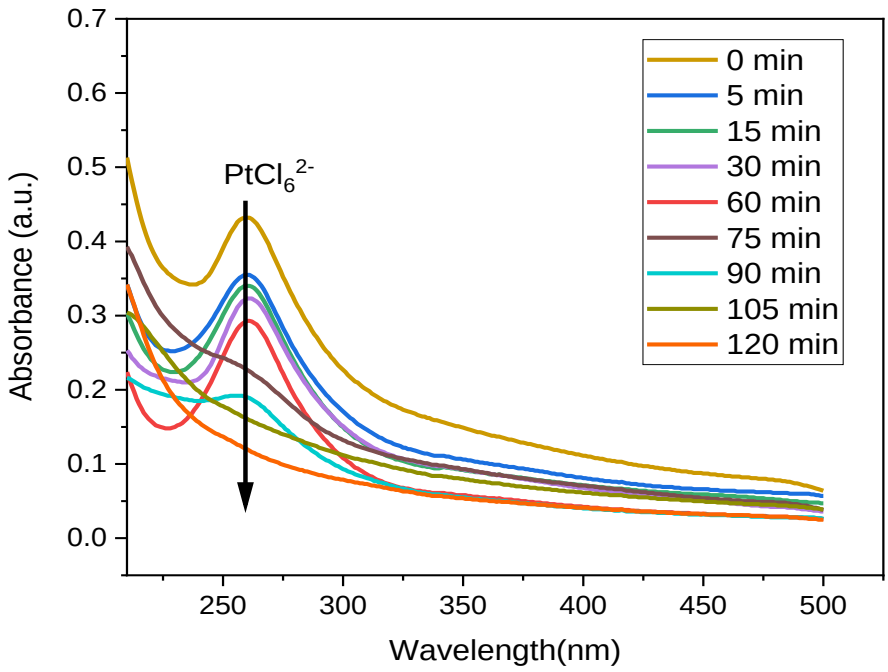

Figure 4. 6 UV-Vis absorption analysis on the reduction of $PtCl_6^{2-}$ ion to Pt^0.

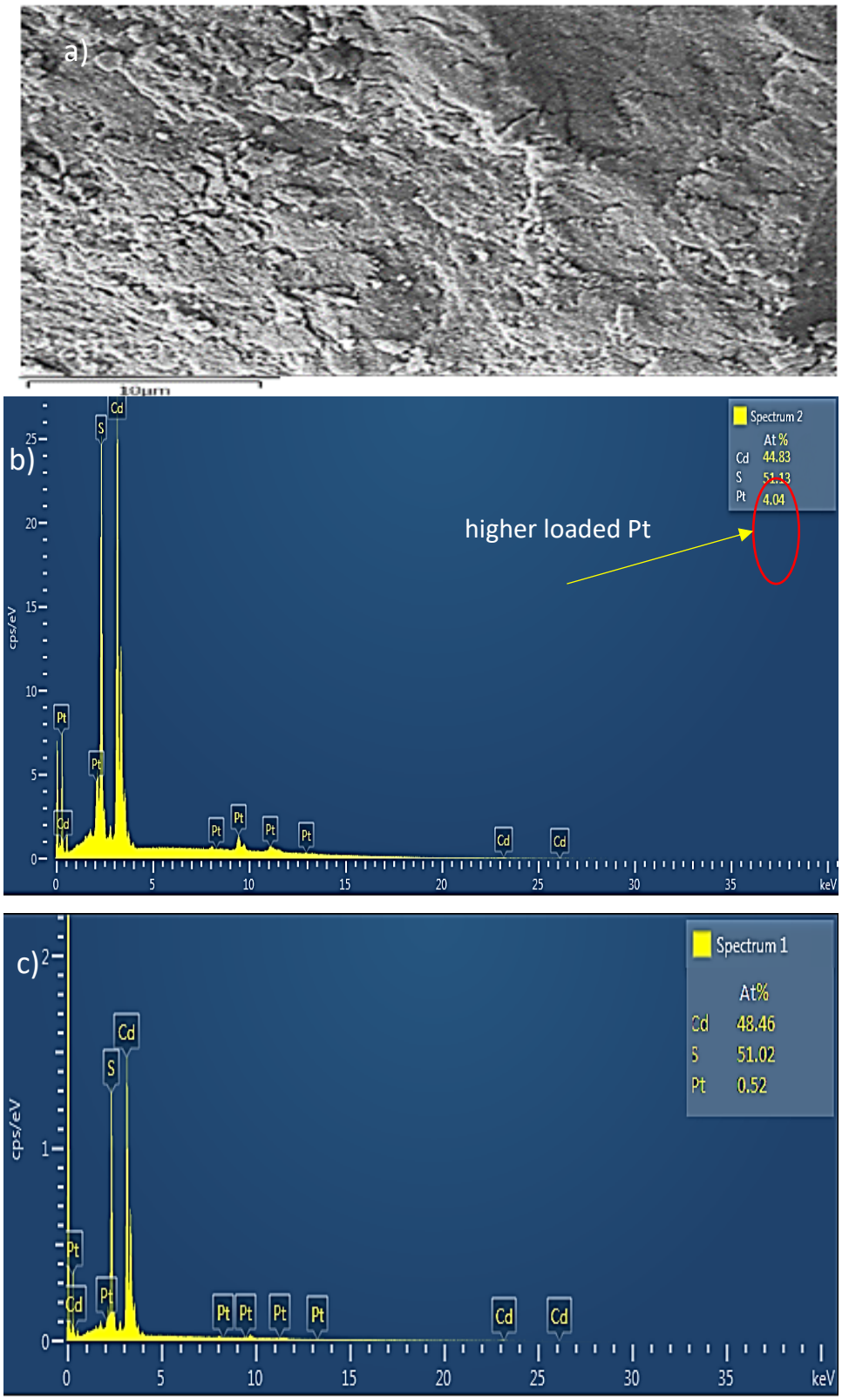

Figure 4. 7 (a) A typical SEM sample area of the 7 wt.% Pt/CdS sample, and (b) the representative EDS spectrum when CdS added at t= 0 min and (c) when CdS added at t=120 min in the Pt on CdS loading experiment.

In Fig 4.7 (a), a typical SEM sample area (11200 μm^2) of a compressed powder can be seen, whereas Fig 4.7 (b) shows the corresponding EDS analysis of a 7 wt. % Pt/CdS sample when CdS was added at t=0 min and when CdS was added at t=120 min is shown in Fig 4.7 (c) . In both EDS, it can be seen that CdS and Pt are the main elements present. The molar ratio of Cd : S is also very close to the expected 1:1 stoichiometry for the both cases of (b) and (c). However, the EDS in (b) shows 4 atm. % Pt (corresponding to 7.5 wt. %) when CdS was added at t=0 min, while the EDS in (c) shows only 0.5 atm. % Pt (corresponding to 0.7 wt. %) when CdS was added at t=120 min. This suggests higher possibility of loading of Pt particles on the CdS surface when CdS is added at the beginning of the Pt reduction, due to the greater chance of $PtCl_6^{2-}$ to occupy binding sites of CdS as being reduced to Pt^0. At t=120 min, there is a smaller chance for the Pt growth site on the CdS surface ("seeding sites") and therefore majority of the Pt particles would be dispersed in the solution. To precisely characterise the actual loading of Pt on the CdS, supporting analysis technologies would be needed such as Transition Electron Microscope (TEM) or even a High Resolution SEM (HR-SEM).

To further analyse the 7 wt. % Pt/CdS sample when the CdS was added at t=0 min, XRD analysis of the powder was conducted, see Fig 4.8. No peak shift or peak broadening of the CdS was observed after deposition of Pt, indicating that the Pt loading did not alter the phase structure or crystallinity of the hexagonal CdS particles. Due to the low loading of Pt, which was below the detection limit of the XRD, no distinct Pt peaks were observed. Three Pt peaks at 2θ values of 42.9°(111), 46.4°(200) and 67.9° (220), consistent with previous reported data [143], are shown in Fig 4.8.

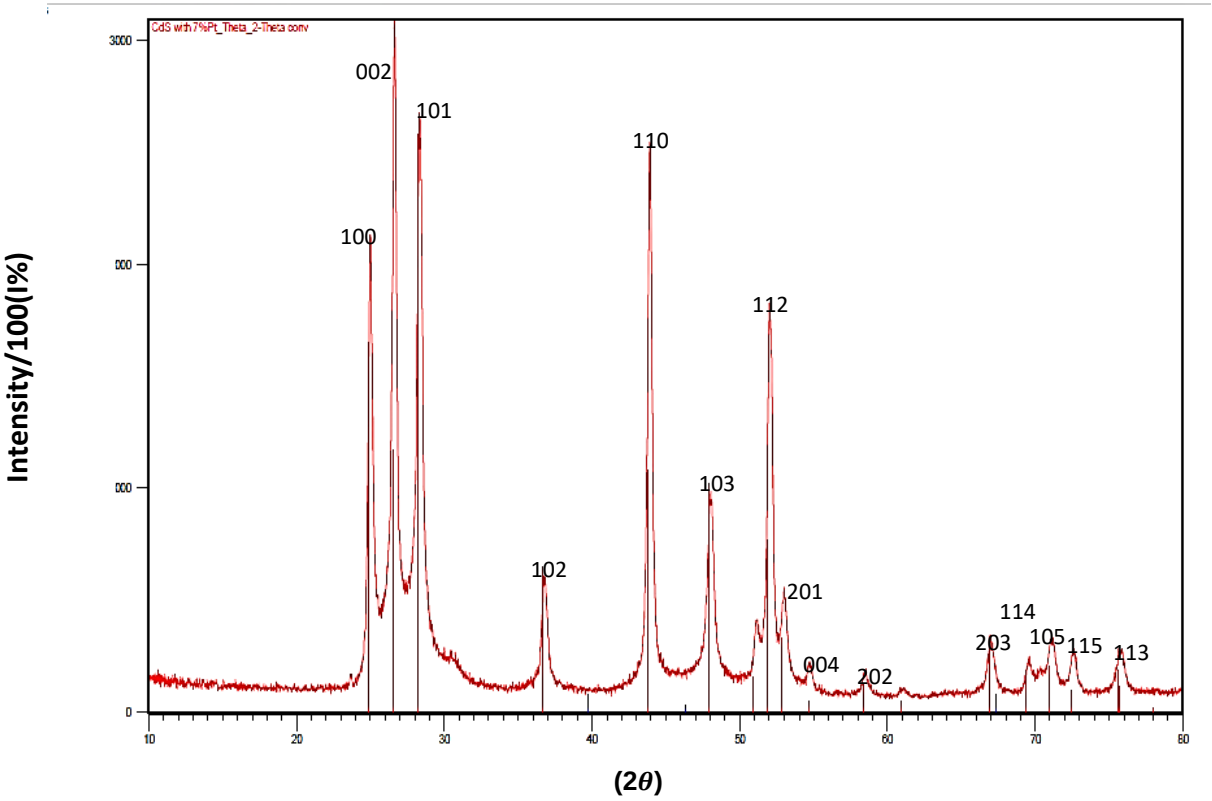

Figure 4. 8 XRD of 7 wt.% Pt/CdS prepared at t=0 min of the Pt on CdS loading experiment, compared with CdS standard data (JCPDS, 41-1049) and Pt standard data (JCPDS, 87-0647).

4-4 Co_xP processing

4-4-1 Solid phase synthesis

In the solid phase synthesis (phosphidation reaction) of cobalt phosphide (CoP), the phosphor precursor of $NaH_2PO_2.H_2O$ was thermally decomposed, producing an short lived intermediate PH_3 gas which immediately reacted with the nearby cobalt precursor, $Co(OH)_2$, inside a closed crucible in the furnace. The $Co(OH)_2$ precursor was synthesised by a titration reaction, by slowly adding 0.5 M NaOH to a solution of $Co(NO_3)_2$ until a precipitate of $Co(OH)_2$ was formed when reaching pH 14, see more details in Chapter 3.

The success of the CoP synthesis depends on: (i) successful pre-synthesis of $Co(OH)_2$, and (ii) the correct temperature and annealing time for the thermal decomposition of NaH_2PO_2. The XRD result of the synthesised CoP did not show any diffraction peaks

matching with a CoP standard data (JCPDF, File No. 29-0497) and therefore the results are not reported in this thesis. This result suggested either not high enough furnace temperature to drive decomposition of NaH_2PO_2, or too-short annealing time, or the possibility of a poorly $Co(OH)_2$ synthesis. To evaluate the optimal decomposition temperature of the NaH_2PO_2, thermal analysis of the $NaH_2PO_2.H_2O$ powder was undertaken by TGA/DSC, as seen in Fig 4.9. The TGA plot shows that the first weight losses occur at 83° C and 132° C respectively, corresponding to the water loss (non-bonded and bonded humidity) with the associated endothermic DSC peaks. At 255° C, an endothermic DSC peak is observed with no associated weight loss, contributed to a phase transition (melting point). However, the main decomposition occurs at 320° C, where the PH_3 is formed, which is associated with a large, 12 %, weight loss and an exothermic DSC peak.

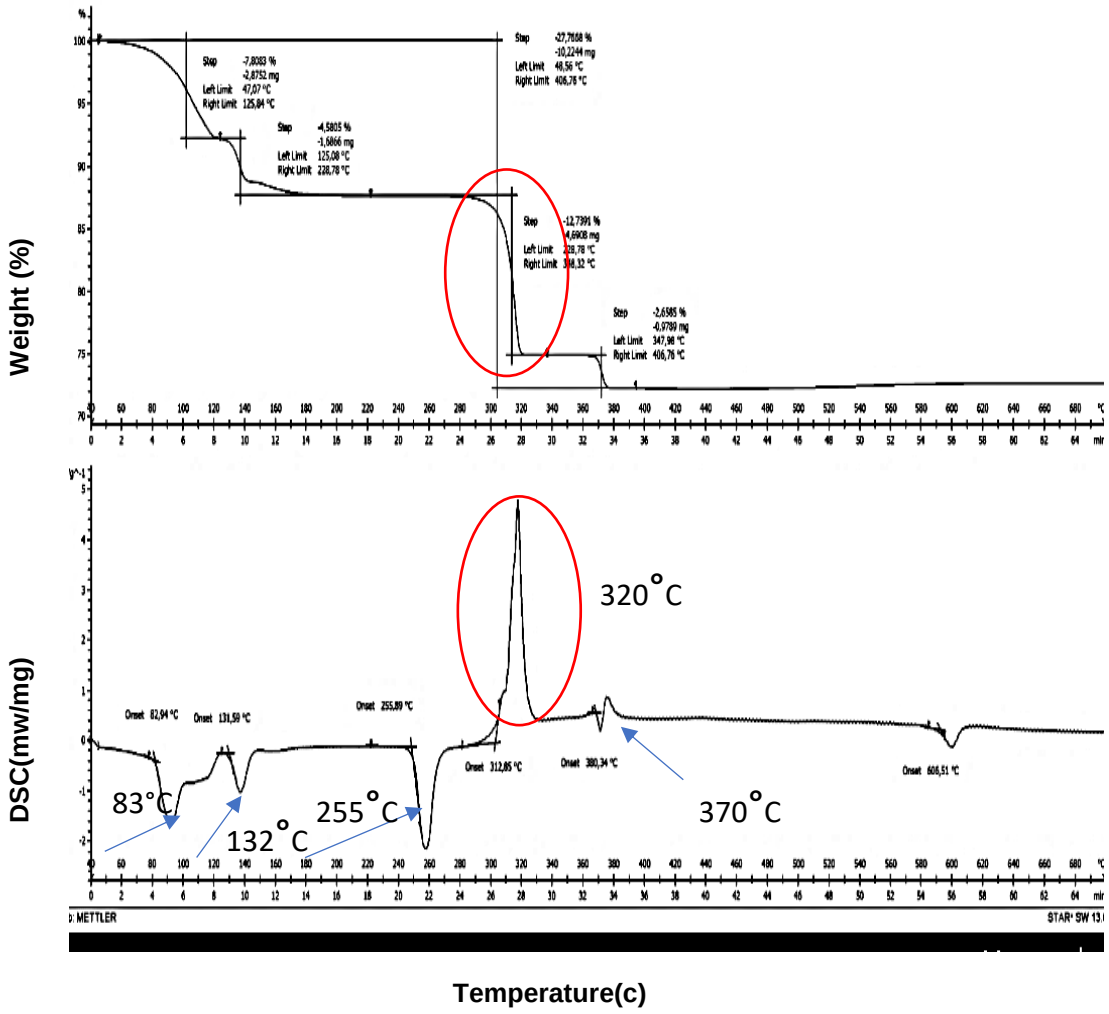

Figure 4. 9 Thermal analysis (TGA/DSC) of $NaH_2PO_2.H20$, where the major decomposition at 320° C is marked with red circles.

Another weight loss occurs around 370 ° C with a small exothermic DSC peak, associated with the further decomposition of the solids. From the thermal analysis, it was therefore concluded that the furnace temperature for the successful phosphidation reaction ought to be at 320° C for 1 hour (this annealing -time is enough for the decomposition). Next step was to assure that the synthesis of the precursor $Co(OH)_2$ was successful, which was done by the XRD analysis. The first batch of the synthesised $Co(OH)_2$ did not show any XRD peak matching with the $Co(OH)_2$ standard data (JCPDF, File No.74-1057) (results are not shown here), indicating that the $Co(OH)_2$ particles were amorphous and not crystallised. To improve crystallinity of the $Co(OH)_2$ particles, the synthesised $Co(OH)_2$ powder was heated up in an air-filled tube furnace at 600° C, 10° C /min ramp up, for 5 hours annealing. The XRD of the post annealed $Co(OH)_2$ powder, as seen in Fig 4.10, showed additional diffraction peaks of Co_3O_4 formed by the following equation:

$$6\ Co(OH)_2 + O_2 \rightarrow 2\ Co_3O_4(s) + 6\ H_2O \qquad (4\text{-}4)$$

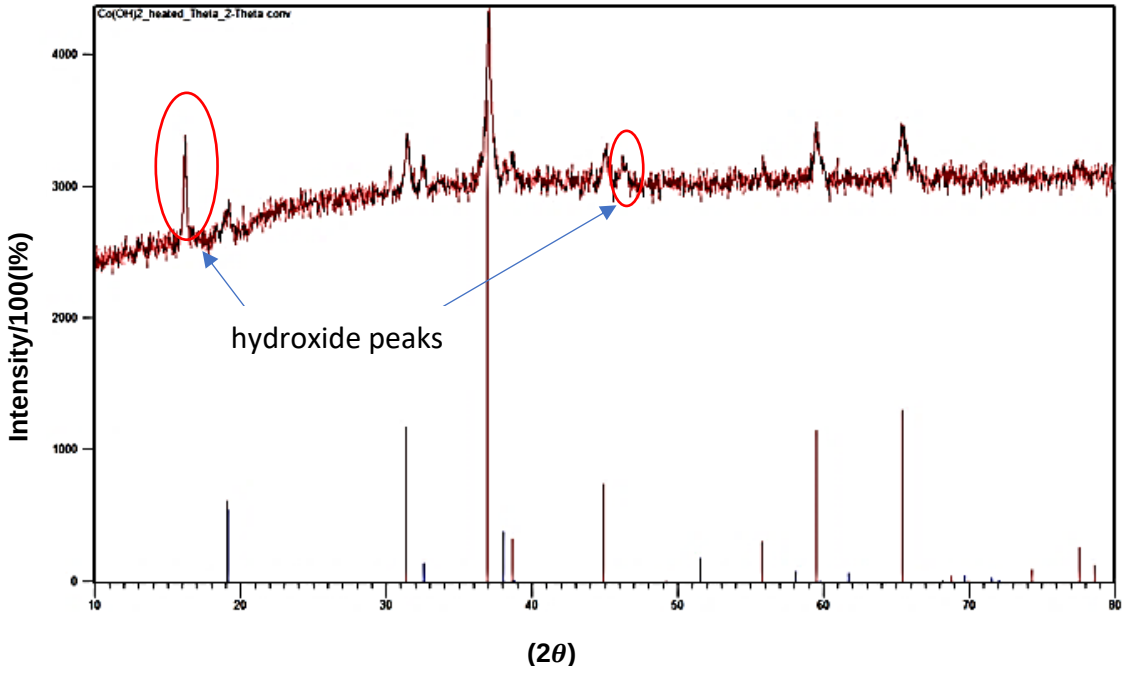

Figure 4. 10 XRD pattern of the post-annealed $Co(OH)_2$ sample in air, 600°C for 5 hours, against Co_3O_4 standard peaks (JCPDS 74-1657). The hydroxide peaks are marked as red cycles.

However, the formed Co_3O_4 is not considered as a suitable alternative Co source in the phosphidation reaction of producing CoP, due to being more stable than $Co(OH)_2$, hence preventing a rapid and low temperature CoP synthesis. Due to the difficulty in controlling the synthesis of $Co(OH)_2$, commercially available $Co(OH)_2$ (Sigma, fine particles, 99.9% purity) was purchased. Then, the phosphidation reaction was conducted at 360° C /1 hr to ensure complete decomposition of NaH_2PO_2 and formation of CoP. Fig 4.11 shows the XRD pattern of the formed product compared with a CoP standard data (JCPDS, 29-0497), where only a few of the peaks can be assigned to CoP. The rest of the peaks are associated with various phosphate and sodium compounds according to the XRD software (High Score X'Pert).

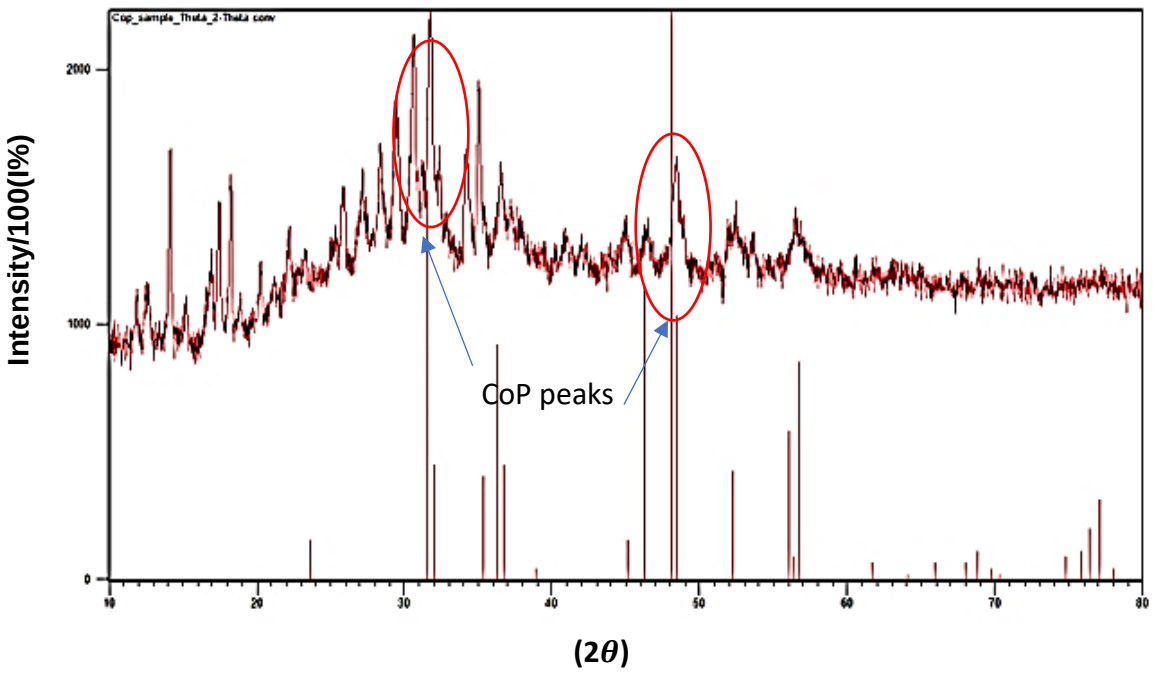

Figure 4. 11 XRD of synthesised CoP sample (in argon at 360° C /1 hr) , using commercial $Co(OH)_2$, against CoP standard peaks (JCPDS 29-0497). The CoP peaks are marked as red cycles.

The presence of these phosphate and sodium compounds suggests non-stoichiometric environment and that some part of the produced PH_3 gas may have escaped with the purging argon gas inside the furnace, which might have hindered a complete reaction with the $Co(OH)_2$. Another reason why such high content of phosphate and sodium compounds are observed in the XRD could be due to

ineffective washing of decomposition residues of Na_2HPO_4 prior to XRD analysis, see further details in Chapter 3 Methodology. To further investigate the phosphidation synthesis, the prepared CoP sample was analysed by SEM/EDS for the elemental analysis, Fig 4.12 . The results reveal that C, O, P, Co and Na are the main elements present for all spectrums in a spot analysis of the powder. However, Co : P ratio indicates very little CoP formation. This observation further confirms an incomplete reaction between PH_3 and $Co(OH)_2$ in addition to an ineffective removal of the decomposition products of Na_2HPO_4.

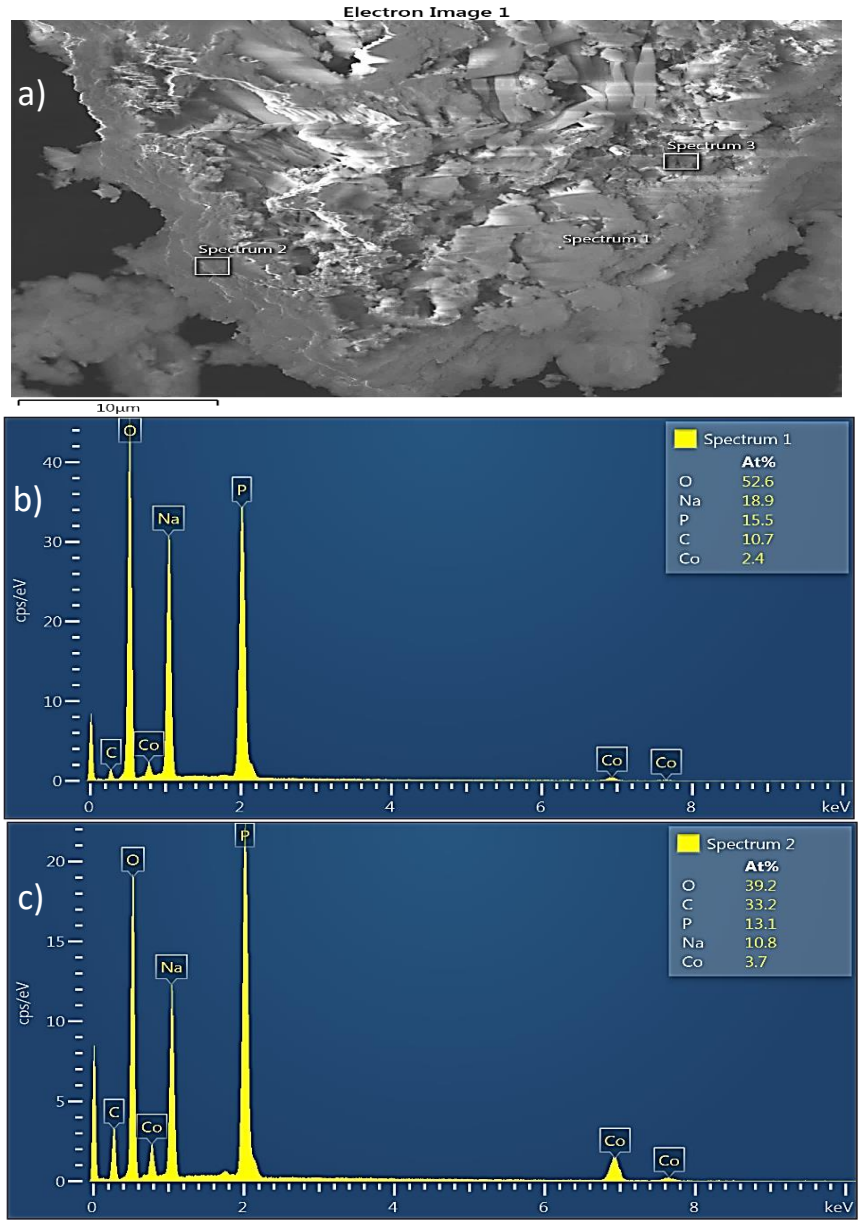

Figure 4. 12 (a) A typical SEM sample area (11200 µm^2)of the synthesised CoP sample and (b) and (c) EDS analysis on two spectrums of the SEM image.

Based on these results, it was concluded that the solid phase synthesis of CoP was not suitable due to the associated difficulties in the synthesis process and in addition the disadvantage of producing the intermediate PH_3 gas, which was extremely toxic and lethal even at a few ppm.

4-4-2 Solution phase synthesis

4-4-2-1 Organometallic reaction

One of the solution phase synthesis of cobalt phosphide (Co_xP) was undertaken by the so-called "organometallic reaction" method. Cobalt acetylacetonate $Co(C_5H_7O_2)_2$, referred as $Co(acac)_2$, was the source of cobalt and trioctylphosphine $P(C_8H_{17})_3$, referred as (TOP), was the phosphor source. The $Co(acac)_2$ precursor, which uses the bidentate ligand to form a large chelated compound, was used to control the Co_xP nanoparticle size. To further control the nanoparticle synthesis, the $Co(acac)_2$ was mixed with the solvent oleylamine ($C_{18}H_{35}NH_2$). As well as a solvent for the reaction mixture, the oleylamine acted as a coordinating agent and a stabiliser. The schematic of the involved molecules can be seen in Fig 4.13.

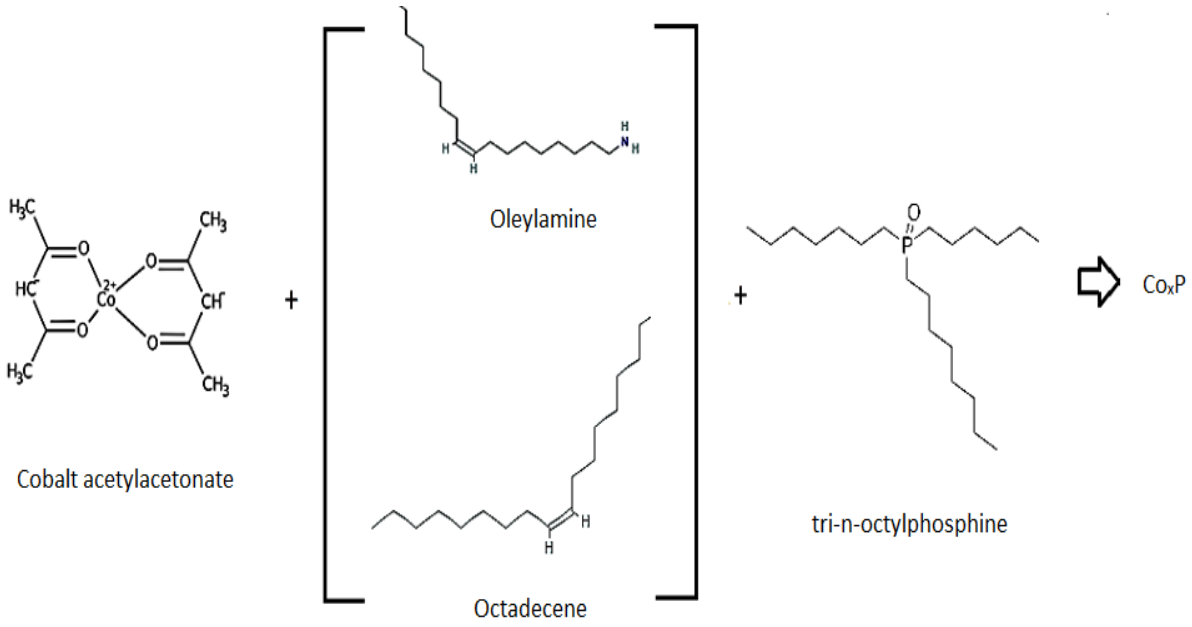

Figure 4. 13 Schematic of the molecular structures for all components involved in the organometallic reaction synthesis of cobalt phosphide (Co_xP).

As a coordinating agent oleylamine formed more stable chelates with the cobalt ions inside the $Co(acac)_2$ and as a stabilising agent, it reduced the growth rate of the formed Co nanoparticles via the prevention of a nuclei agglomeration. The stabilisation proceeds as the amines ($-NH_2$) of the oleylamine bind to the formed particles surface and lead to a particle repulsion and therefore a stabilisation of particle growth in the solution. This stabilisation mechanism can therefore be used to control the formation kinetics during the synthesis (particle growth rate control). The amine group in the oleylamine that binds to transition Co metal, plus its long hydrocarbon chain make the oleylamine molecule as an ideal surfactant to control nanoparticle growth. Oleylamine can also function as a weak reducing agent at high temperatures of solution phase syntheses, hence serving many roles such as; the solvent, surfactant, stabilising agent *and* reducing agent in the Co_xP nanoparticle synthesis.

To further facilitate the reduction of Co in the $Co(acac)_2$ chelate while slowing down the growth rate of the formed nanoparticles, the non-coordinating, nonpolar solvent octadecene as was added to the oleylamine and $Co(acac)_2$, as shown in Fig 4.13. The reduced concentration of oleylamine by increasing the amount of non-polar octadecene narrows down the size distribution of the particles. This is another mechanism used to control the particle growth rate, as a very small size was aimed for. Then after the initial solution mixing at 120° C for 1h to remove low boiling point impurities, the solution temperature was raised to 320°C. At this point, the phosphor precursor (TOP) was introduced very slowly into the, now destabilised, $Co(acac)_2$ chelates to continuously deliver a Co–TOP complex and gradually transform it to the Co_xP phases during 12 h reaction time at 320°C. The phosphor precursor, TOP , also acted as a coordinating agent which provided better size control and surface passivation. The phase evolution of the final Co_xP nanoparticles was monitored at t=1 h and t=12 h. Fig 4.14 shows the XRD result of the formed products at t=1 h with only one matching peak with a Co_2P standard data (JCPDF, File No. 89-3030) at 2θ value of 43.5°(121), where the signal to noise ratio was low. To improve crystallinity of the

synthesised particles, the powders were post-annealed in an argon filled tube furnace at 450° C, 10° C/min ramp rate , for 2 hours.

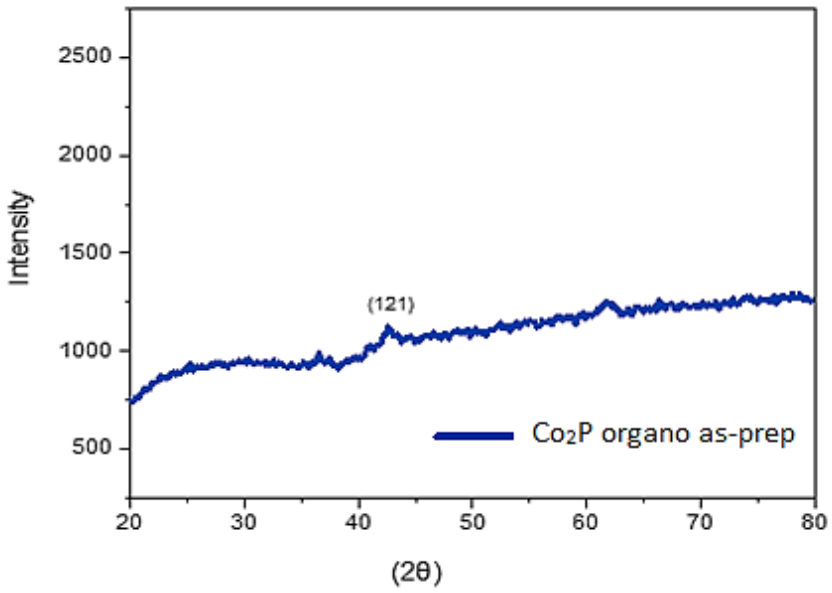

Figure 4. 14 XRD pattern of the organometallicly synthesised Co_xP sample at t=1h.

However, the post annealing treatment did not show any improvement of the XRD peaks (results are not shown here), assuming the majority of the particles were still amorphous. Fig 4.15 shows the XRD result of the formed products at t=12 h with the matching peaks with an orthorhombic CoP standard data (JCPDS, 29-0497) at 2θ values of 31.7°(011), 36.5°(111), 46.3°(112), 48.4°(211)and 56.61°(103). From the full width at half maximum (FWHM) of the most intense peak, size of the CoP particles was calculated to be 5 nm using the Scherrer equation, see Table 4.2. However, the signal to the noise ratios, as seen in Fig 4.15, were all low. This indicates that the synthesised CoP particles were only partly crystallised, and therefore majority of particles were still amorphous. To improve crystallinity of the synthesised particles, again a post-annealing treatment of the particles was undertaken in an argon atmosphere at 450° C, 10° C/min ramp rate, for 2 hours.

Table 4. 2 Parameters used for the Scherrer formula.

FWHM (°)	β (rad)	λ (Å)	2θ	θ	COS θ	D (nm)
19.44	0.33	0.15	48	24	0.91	5.01

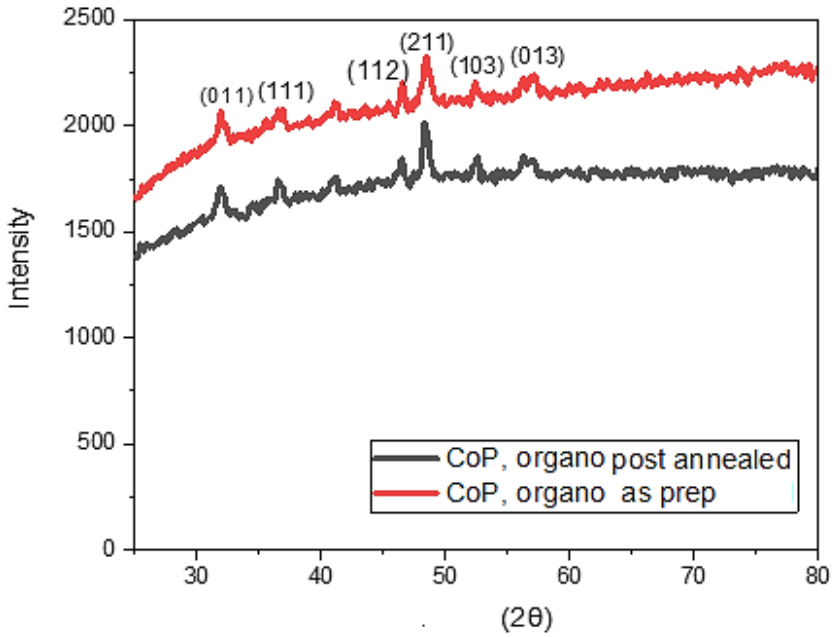

Figure 4. 15 XRD pattern of the organometallicly synthesised Co_xP sample at t= 12 h when; as-prepared (black) and post-annealed at 450 °C (red).

The post-annealing treatment showed once again nearly the same XRD pattern regarding the peak positions and intensities compared to that as-prepared sample, with a slight improvement in the baseline drift for the post annealed samples. This indicates that the post-annealing neither affected the crystal structure of the formed particles, nor dramatically improved the detectable (within the sensitivity range of XRD analysis) crystallinities. It should be pointed out here that such small nanoparticles indeed contained a large amount of defects and broken bonds at the surface versus a very small bulk interior. To further support the analysis of the post annealing step, thermal analysis of as-prepared and post-annealed CoP samples was undertaken by TGA/DSC at the heating rate of 10 °C/min in argon, as seen in Fig 4.16. The TGA plot for the as-prepared sample showed a gradual mass loss (8%) when heated up to 360 °C, followed by a sudden weight loss when further heated up to 450 °C, where the sample had 18% mass loss. The initial gradual weight loss is attributed to the atmospheric moisture and organic solvents present in the sample, while the high-temperature weight loss with a corresponding exothermic DSC peak at 380° C is probably due to some phase changes in the sample.

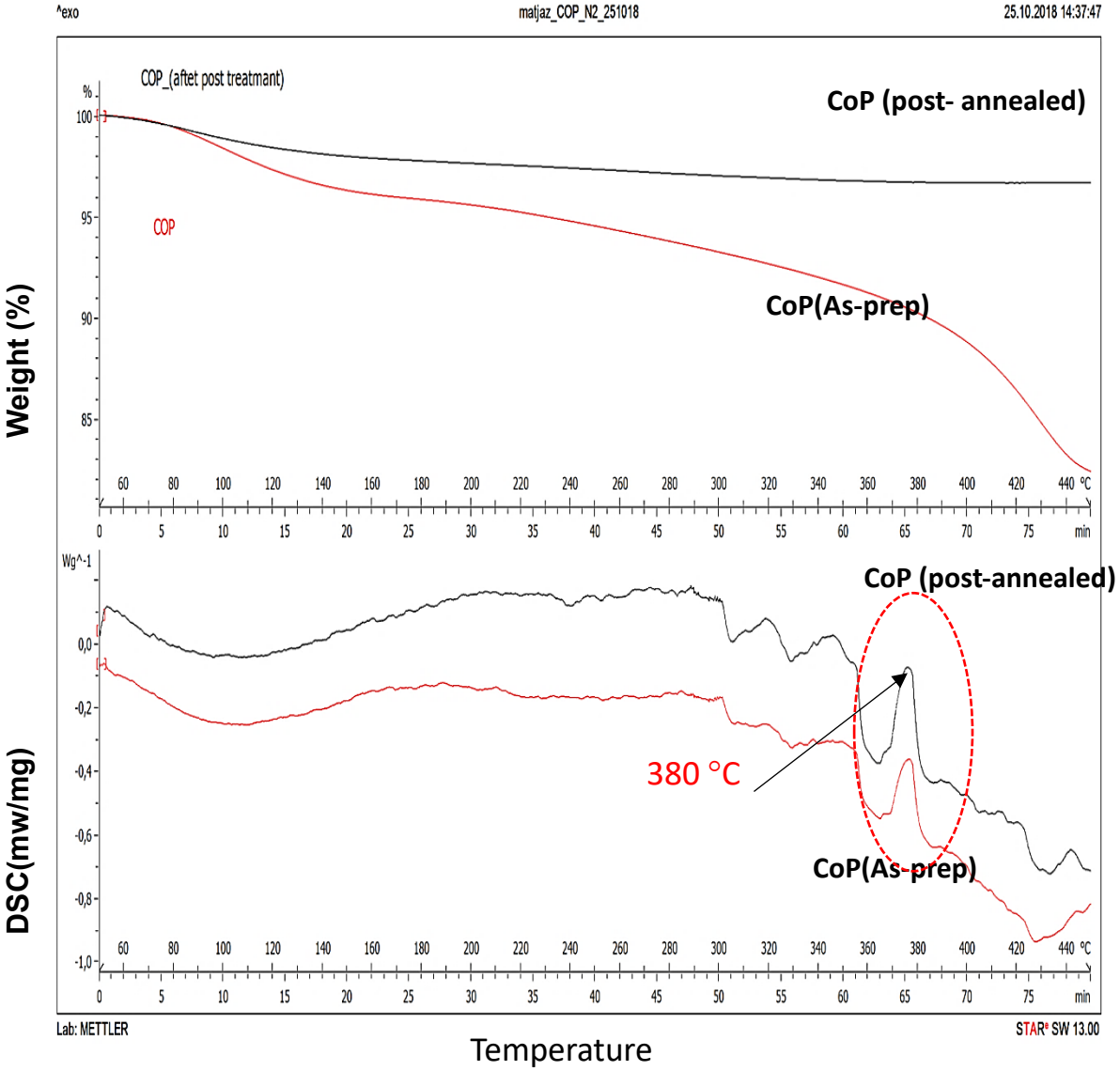

Figure 4. 16 Thermal analysis (TGA) of Co_xP at t=12 h when as-prepared (red) and post-annealed in argon at 450 ° C (black).

In a related study, Yang et al. [37] reported that at 380° C, probably a part of the particles was converted into the carbon as a result of carbonisation of the organic solvent residue. The TGA curve for the post-annealed sample showed only 3% mass loss when heated up to 440 °C as the post-annealing process had already caused removal of the moisture and organic solvents present in the sample. However, the corresponding DSC curve of the post-annealed sample exhibited again the same exothermic peak at 380° C. This surprisingly indicates some reversible phase changes at this temperature.

These post annealing observations will be further discussed in Chapter 5, where a reduced hydrogen performance for the post-annealed Co_xP in the Co_xP/CdS composites compared with those using as-prepared Co_xP was obtained. This may be because of carbonisation as explained by Yang et al. [37], which in this case would reduce the Co_xP electroconductivity for the hydrogen production. Only a few researchers [30,144] reported the hydrogen performance of similar Co_xP/CdS composites but in the electrochemical cells, stating the hydrogen performances were not dependent on the Co_xP crystallinity, but on the high electronegativity of the P atoms to attract electrons from the metal (Co) atom. Therefore, the phosphorus becomes a negatively charged centre attracting the positively charged H^+ in solution. This will be further explained in Chapter 5.

The phase transformation from metallic Co to Co_2P and then finally to CoP, has been reported by some researchers [98,145,146], see Fig 4.17, which would further explain the reaction time and temperature in this research. For the transformation from Co to Co_2P, two diffusion mechanisms are considered; one is inward diffusion of phosphorus into the Co matrix, forming an initial Co-rich Co_2P shell with negligible movement of cobalt and the another one is an outward diffusion of cobalt from the Co_2P region, leaving a hollow particle structure through an Kirkendall mechanism.

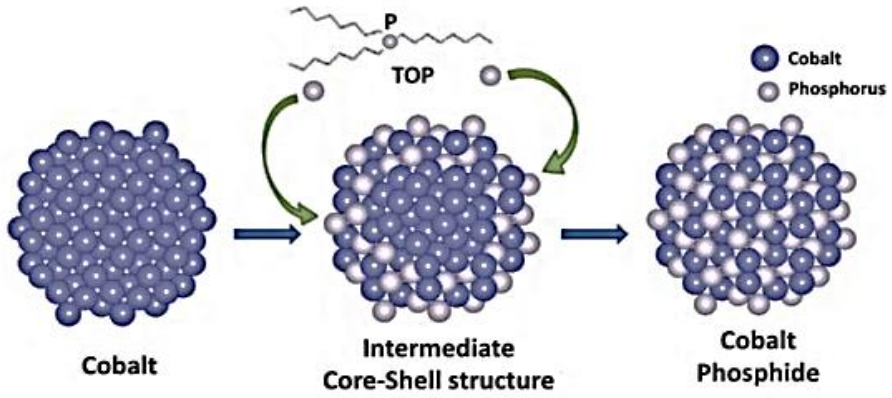

Figure 4. 17 Schematic of the formation transition from metal cobalt (left hand) to a Co_2P shelled cobalt particle (middle) to a CoP particle (right hand), where a phosphor precursor TOP added to the cobalt metal [139].

The Kirkendall diffusion mechanism (a defect supported diffusion) can explain how initially the phosphorus atoms diffuse much faster than the cobalt atoms into the cobalt matrix, where they form an amorphous shell of Co–P around the Co nanoparticles that is gradually transformed to more crystalline Co_2P. This is followed by a change in the diffusion mechanism, causing a "Kirkendall hollowing" effect, where the outward diffusion of the Co from the formed Co_2P core becomes faster than the inward diffusion of P.

The transformation process from Co_2P to CoP is different from that of Co metal to Co_2P. The cobalt-rich inner region of the initial formed Co_2P causes further Kirkendall hollowing with an increased void size, at the increased time and temperature. This would explain the difference between sample t=1 and t=12, producing Co_2P and CoP respectively. However, at some point fracturing of hollow particles is expected, leading to a decrease in the number of particles that are hollow. From above results, it was found that a longer reaction time caused crystallographic transformation towards the more thermostable CoP, see Fig 4.18 , which was confirmed by the XRD results in Fig 4.14 and 4.15.

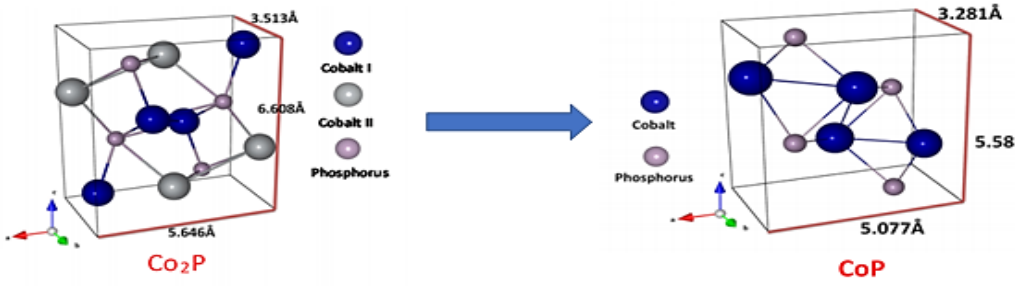

Figure 4. 18 Thermo-stability transformation of Co_2P to CoP structure [145].

To investigate the success of Co_xP loading on CdS, the loading methods of grinding and sonication were conducted, and their results were compared. The theoretical aim was a 5 wt. % loading of Co_xP on CdS. The final products were analysed by SEM/EDS and XRD, see Figures of 4.19 (a, b and c), 4.20, 4.21 and 4.22. In Fig 4.19 (a), a typical SEM sample area of a 5 wt. % ground CoP (as-prepared)/CdS composite can be seen while Fig 4.19 (b) and (c) show the corresponding EDS analysis of the sample.

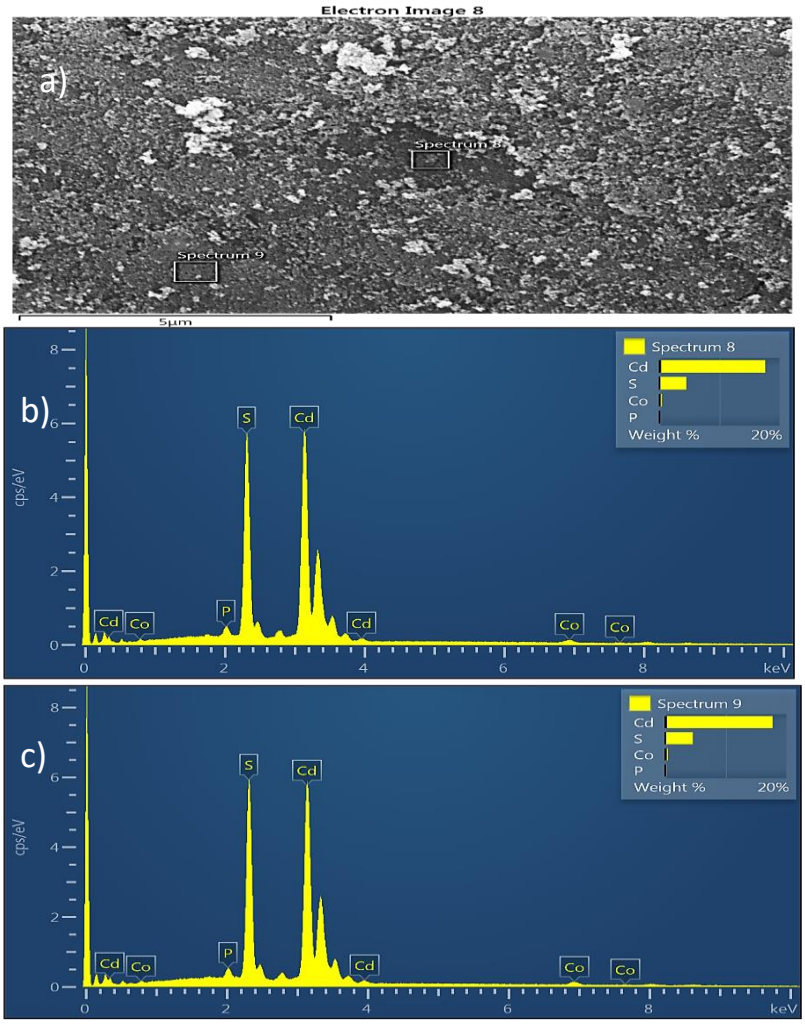

Figure 4. 19 (a) A typical SEM sample area of a 5 wt.% ground CoP (as-prepared) /CdS composite and EDS analysis on the two spectrums of the SEM image in (b) and (c).

For both EDS spectra, the elements detected were Cd, S, Co and P with the molar ratio of Cd : S very close to the expected 1:1 stoichiometry (corresponding to 45.9 wt. % Cd and 44.1 wt. % S). Further SEM imaging of the sample, see Fig 4.20, showed no segregation of CoP clusters, indicating the CoP particles nicely covered the CdS surface with a very uniform distribution. However, the CdS particles had large size variation of agglomerates (> 50 nm), implying only the outside exposed surface of the CdS agglomerates were covered by the CoP and for those CdS particles trapped inside the agglomerates there was a limited chance of physical contact with the CoP particles. This issue will be further reflected in the hydrogen performance of the composite catalysts (see Chapter 5), where the 5 wt. % ground CoP (as-prepared)/CdS performed far less hydrogen evolution than the Pt/CdS system.

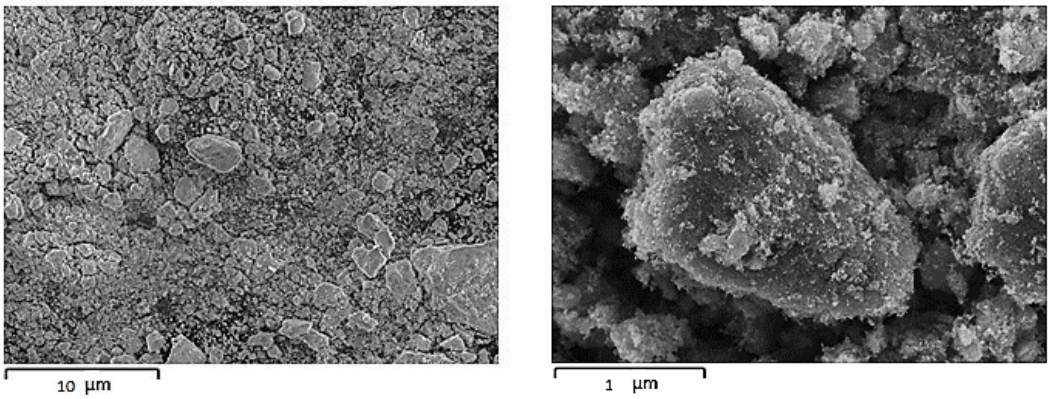

Figure 4. 20 SEM images of the 5 wt. % ground CoP (as-prepared)/CdS.

The loading of 5 wt. % Co_2P (as-prepared) on CdS by the grinding method showed the same SEM/EDS results as 5 wt. % ground CoP (as-prepared)/CdS sample (results are not presented here). The results again showed large CdS agglomerates, providing a little chance for the Co_2P particles to cover all available surfaces of CdS particles. The effect of the grinding method will be further reflected in the hydrogen performance of the composite catalysts in Chapter 5. Based on these results, it was concluded that the Co_xP loading on CdS by grinding was not a suitable method if an increased physical contact between the photocatalyst and cocatalyst is aimed for, and therefore loading by the sonication method was investigated.

In Fig 4.21 (a), a typical SEM sample area of a 5 wt. % sonicated CoP (as-prepared)/CdS composite can be seen. The corresponding EDS result of the sample can also be seen in Fig 4.21 (b). From the EDS result, Cd, S, Co and P were the main elements present with the Cd : S molar ratio nearly equal to 1:1 (corresponding to 45.96 At. % Cd and 44.15 At. % S) and the CoP content (corresponding to 5.21 At. % or 5.4 wt.% Co and 4.96 At. % or 3.4 wt.% P), which was close to what was theoretically expected from a 5 wt. % CoP loading in the sonication solution. From the SEM image, no segregation of CoP clusters was observed but instead breakage of the large CdS agglomerates to the smaller sizes (< 50 nm) was observed. This is due to the forceful sonication energy input which produced less CdS particle agglomerates and separation into very small fractured CdS particles with a high-volume ratio of broken bonds and vacancies close to its surface, where the cocatalyst CoP particles more successfully adhered.

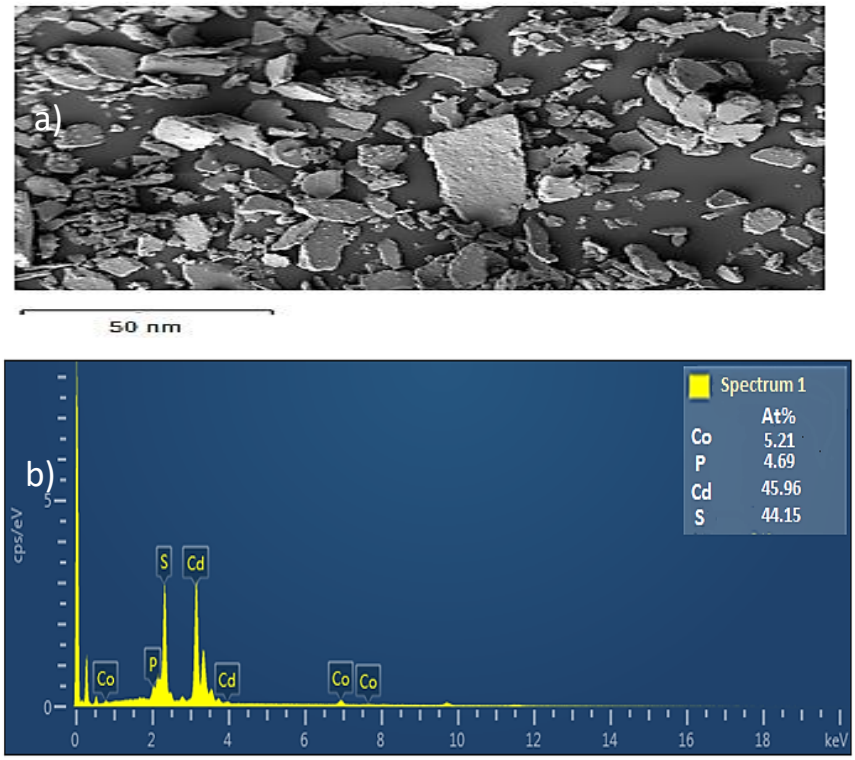

Figure 4. 21 (a) A typical SEM sample area of a 5 wt.% sonicated CoP (as-prepared) /CdS composite, and (b) the representative EDS spectrum of the SEM image.

The XRD analysis of the 5 wt. % sonicated CoP (as-prepared)/CdS sample was also conducted, see Fig 4.22, showing no peak shift or peak broadening of the CdS after energetic deposition of CoP. Due to the low loading of CoP, which was below the detection limit of the XRD, no distinct CoP peaks were observed (the standard marked in black in Fig 4.22).

The photocatalytic hydrogen generation of the sonicated CoP/CdS sample was later conducted, where an incredible H_2 evolution was obtained compared to the more common Pt/CdS system, see Chapter 5. As a conclusion, the SEM/EDS and XRD analysis of 5 wt. % sonicated CoP (as-prepared)/CdS sample together with its hydrogen performance test confirmed an improved CoP loading on the CdS by using the sonication method compared to more commonly published grinding methods, despite lack of actual proof from supporting material analysis such as TEM or HR-SEM.

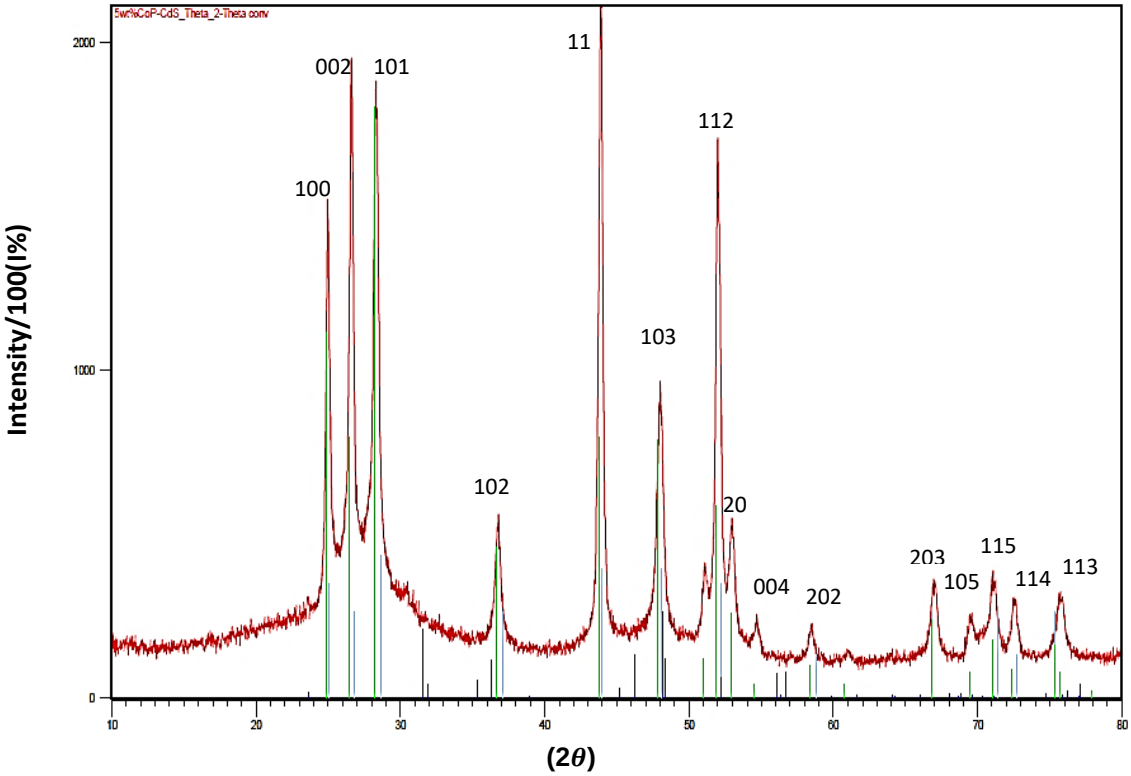

Figure 4. 22 XRD pattern of a 5 wt.% sonicated CoP (as-prepared)/CdS composite, against CdS standard peaks (JCPDS, 41-1049) (green) and CoP standard peaks (JCPDS 29-0497) (black).

4-4-2-2 Hydrothermal reaction

The other solution phase synthesis of cobalt phosphide (Co_2P) was by a hydrothermal method, where a cobalt precursor $Co(NO_3).6H_2O$ was added to a phosphor precursor (red phosphorus), and then the solution mixture was hydrothermally annealed at 200° C for 18 h. Figure 4.23 shows the SEM/EDS analysis of the Co_2P hydrothermally processed sample, where the Co and P with an atomic ratio close to the expected 2:1 stoichiometry was observed, see Fig 4.23.(b) and (c). Figure 4.24 shows the XRD analysis of the above sample (black spectra, "Co_2P hydro 200°C 18hr"), where the peaks were matched with an orthorhombic Co_2P standard data (JCPDS file no. 89-3030) with 2θ values of 41°(121), 43.5°(211), 44°(130), 52.5°(002). From the full width at half maximum (FWHM) of the most intense peak, the size of the Co_2P particles was calculated to be 2 nm by Scherrer equation, see Table 4.3. However, the signal to the noise ratios were rather low. This may indicate that the synthesised

Co_2P particles were only partly crystallised, and majority of particles were still amorphous.

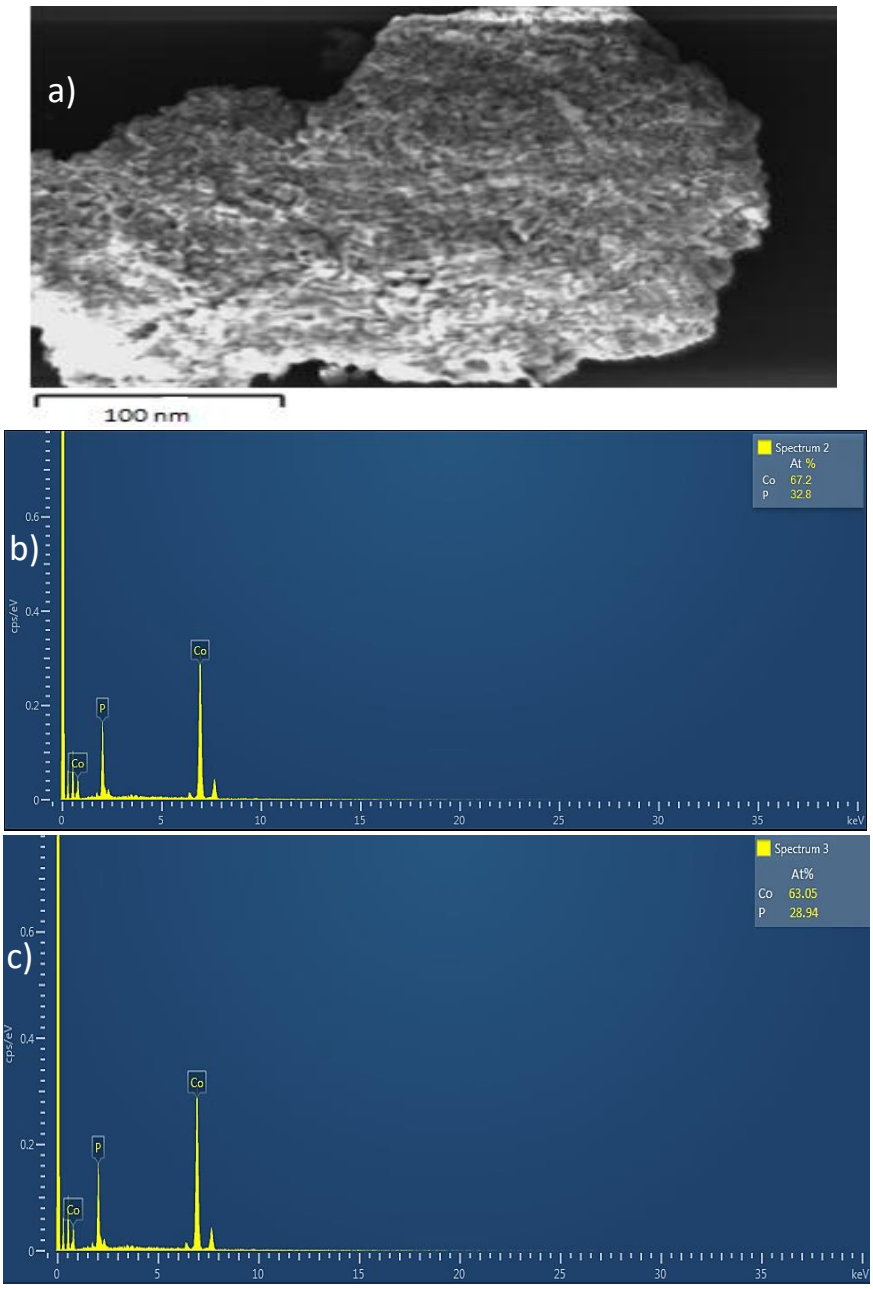

Figure 4. 23 (a) A typical SEM sample area of a compressed hydrothermally synthesised Co_2P sample, and (b) and (c) the corresponding EDS analysis of the two spectrums in the SEM image.

Table 4. 3 Parameters used for the Scherrer formula.

FWHM (°)	β (rad)	λ (Å)	2θ	θ	COS θ	D (nm)
18.44	0.31	0.15	41	20.5	0.93	2

To increase crystallinity of the particles, a change of annealing condition from 200 °C /18 h to 220 °C /24 h was conducted. Fig 4.24 shows the XRD results of this change, where nearly the same XRD pattern with the same peak positions and similar intensities were observed. The aluminium peak (artefact) in the pattern was from the microscopes sample holder. Also, in Fig 4.24 the two different hydrothermal annealing condition samples were compared with the organometallic synthesised Co_2P sample at t= 1h "Co_2P organo" in blue. Improved Co_2P XRD peaks can be seen in both the hydrothermally synthesised samples when comparing with the organometallic ones. It should be pointed out here that the expected Kirkendall diffusion would not be applied to the hydrothermal annealing conditions as the hollow Co_xP structured were only reported where organometallic methods were used [29,32,37,116]. However, as explained before and will be shown later in Chapter 5, the hydrogen performance of Co_2P/CdS composite was not dependent on the level of the cocatalyst crystallinity, as only Co_2P (organometallic-as prep)/CdS composites appeared to have the highest hydrogen evolution rate than the rest.

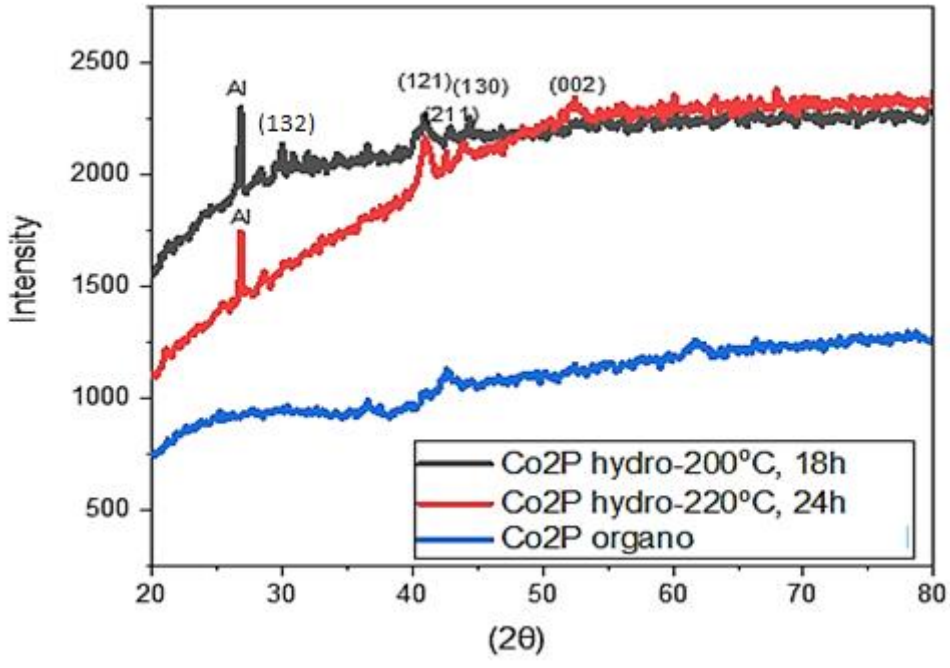

Figure 4. 24 XRD pattern comparison of different synthesised Co_2P samples when; hydrothermally annealed at 200 °C for 18 h (black), hydrothermally annealed at 220 °C for 24 h (red) and organometallically synthesised at t=1h (blue).

To load Co_xP on the CdS surfaces, the grinding method was found inefficient here whereas loading by a high energy input of sonication for 2 hours proved efficient for breaking the large CdS agglomerates into smaller fractured particles and providing a better scenario for the cocatalyst affinity for adhering to the exposed surfaces.

4-5 Conclusion

The synthesis and characterisation of the visible light absorbing semiconductor CdS was presented alongside its different co-loaded catalysts. An investigation was also undertaken to find a suitable cocatalyst loading method. The XRD analysis of the CdS sample showed that nanoparticles with a highly crystalline hexagonal phase were successfully synthesised. The UV-Vis analysis of the CdS sample indicated the particles' optical absorption matched with the emission spectrum of cool white LEDs that will be used in the photoreactor. This means that majority of the received visible fluxes can successfully activate the particles. Then, a UV-Vis analysis on the reduction reaction of $PtCl_6^{2-}$ ion → Pt^0 was conducted, where it was found that Pt^{IV} was reduced to elemental platinum. The SEM/EDS analysis of Pt/CdS sample showed that a successful Pt loading would be only achieved if CdS was added at t=0 min of the Pt reduction reaction. XRD analysis of the same sample showed that the Pt loading process did not affect the hexagonal CdS particles.

Initially the Co_xP synthesised through a solid phase reaction (thermal phosphidation reaction) did not show any XRD diffraction peaks matching with any corresponding standard data. This was followed by a thermal decomposition study of the $NaH_2PO_2.H_2O$ precursor using TGA/DSC , which revealed correct furnace settings for a successful phosphidation reaction: 320^o C for 1 h. This deviated from the published data. Further, the other precursor $Co(OH)_2$, which was synthesised in the laboratory and analysed by the XRD, indicated that the $Co(OH)_2$ particles were still amorphous and not fully crystallised. The $Co(OH)_2$ particles were then post-annealed at higher temperature and longer time, with the aim of increasing the crystallinities, but XRD showed additional diffraction peaks from a Co_3O_4 formation. This oxide was concluded not to be suitable as a Co-precursor in the phosphidation reaction. To assure pure stoichiometric $Co(OH)_2$, a commercial nanostructured powder was used

instead which showed a better CoP synthesis. However due to the high toxicity of PH_3, it was concluded the solid phase reaction was not suitable to be used in this research. This leaded the research into a safer option where next Co_xP synthesis was conducted by an organometallic synthesis reaction. The first XRD of the synthesised Co_xP sample (t=1 h) showed some peaks that partly matching with the orthorhombic Co_2P phase, and that majority of the sample were amorphous. Then, a sample post-annealing step was introduced, which did not improve the crystallinity of the particles. The XRD of the formed products at t=12 h showed some orthorhombic CoP phase XRD peaks, but with low peak-to-noise ratios, meaning the majority of the particles were still amorphous. Again, a post-annealed step was introduced, but the CoP sample (t=12 h) showed the same peak position and intensities than the as-prepared sample. The thermal analysis of the organometallically synthesised Co_xP samples by TG/ DSC indicated that a post aneling step probably only converted a part of the particles into the carbon as a result of carbonisation of the organic solvent residue, and did not improve crystallinities. This conversion effect will be seen in the hydrogen performances of the corresponding Co_xP/CdS composites in Chapter 5. The SEM/EDS analysis of the organometallic Co_xP loading on CdS also showed that the grinding loading method was not suitable but instead the sonication method was the most efficient one.

The other synthesis method of Co_xP was by a hydrothermal reaction. The first XRD analysis showed peaks corresponding to orthorhombic Co_2P. However, once again the background noise was high, suggesting that the particles were only partly crystallised, and majority still amorphous. Here no post-annealing was introduced but an alteration in the hydrothermal annealing condition was done by increasing from 200 ^oC/18h to 220 ^oC/24 h, where it did not show any major effect on the XRD analysis. However, both the two different hydrothermal annealing condition samples showed better XRD peaks when compared with the post-annealed organometallic synthesised Co_2P sample (t= 1h). Therefore, it was concluded that hydrothermal method was better for Co_2P and organometallic better for CoP. Finally, the SEM/EDS analysis of Co_2P (hydro) loading on CdS showed that only the sonication loading method was suitable. The hydrogen performance of all Co_xP/CdS composites will be compared later in the following chapters.

Chapter 5 Results and Discussions: Photocatalytic Hydrogen Generation

5-1 Introduction

In this Chapter, the different photocatalytic hydrogen reactions inside the photoreactor is presented. First, the various CdS-composite catalytic particles were tested in a simultaneous hydrogen generation and lactic acid degradation photocatalytic reaction system in section 5-2. This is followed by variations of reaction operational parameters and usage of different sacrificial reagents (hole donors), but keeping the catalyst composite material constant in section 5-3 and 5-4 respectively. Then, different catalytic material choices and comparison of their impact on the reaction kinetics are presented in section 5.5 and 5.6, followed by a stability and recycling test of the chosen heterogeneous CoP/CdS composite catalyst in section 5-7.

5-2 Photocatalytic hydrogen reactions in lactic acid solution

Lactic acid is a commonly used chemical in food, cosmetics and bioplastic industries, which can therefore be found in industrial waste streams [147]. Lactic acid has also been used as a sacrificial reagent (hole donor), for the visible light driven hydrogen generation using CdS photocatalyst [148–150]. For a simultaneous water reduction and lactic acid oxidation by a CdS photocatalyst, there are four important steps to fulfil; (i) absorption of photons with energy equal or higher than the CdS electron band gap (ii) dissociation of the formed excitons and their diffusion to the catalyst surface (iii) lactic acid adsorption on CdS surface, and (iv) desorption of the formed products. For a successful photocatalytic degradation of lactic acid, it is important to assure it does not absorb the incoming photons, and for the reaction kinetics, it is important to understand that the surface adsorbance and reaction products

desorption occur. To investigate if lactic acid absorbs photons, a 10 mM aqueous solution of lactic acid was analysed in a UV-Vis spectroscopy between 190-800 nm. It was found that lactic acid only absorbs UV light < 250 nm, with an absorption peak at 200 nm, see Fig 5.1.

As a visible light driven reactor was used in this research, it was concluded that no direct photo reaction of the lactic acid occurred, and that all incoming photons energy would be only absorbed by the CdS particles.

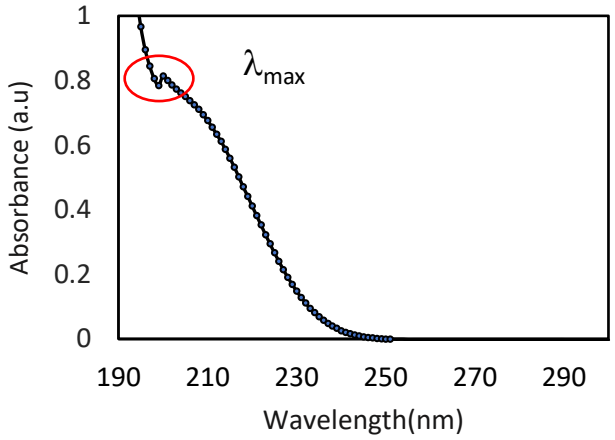

Figure 5. 1 UV-Vis absorption spectrum of lactic acid.

To investigate lactic acid adsorption on the surface of CdS , FTIR spectroscopy was used. Catalytic particles (5% Pt/CdS) that was newly made was compared with catalyst particles that had been immersed in 2.67 M lactic acid solution, washed and dried and both particle sets were then compared with neat lactic acid (> 90% purity), which can be seen in Fig 5.2.

For the 5% Pt/CdS sample, the bands located at 642, 974 and 1040, 1402 cm^{-1} are ascribed to the vibrational modes from the Cd–S bond [151–153]. The peak at 1566 cm^{-1} attributed to a O-H bending vibration from adsorbed H_2O [151]. For the 5% Pt/CdS sample pre-immersed in lactic acid (black spectra in Fig 5.2), additional bands at 1227, 1392, 1430 and 1650 cm^{-1} corresponding to the lactic acid are now observed. The lactic acid vibrational mode at 1640 was not, however, observed in this sample. This is because this vibration corresponds to the free lactic acid's strong C=O stretching vibration at 1640 cm^{-1} will disappear or be shifted, if the lactic acid is adsorbed, particularly chemisorbed on a surface, as reported by Susai

Rajendran[154]. The small peak at 2334 cm^{-1} corresponds to adsorbed CO_2 [152]. From the FTIR study it was concluded that lactic acid bond strongly (chemisorbed) to the Pt/CdS surface as the 1640 cm^{-1} peak disappeared.

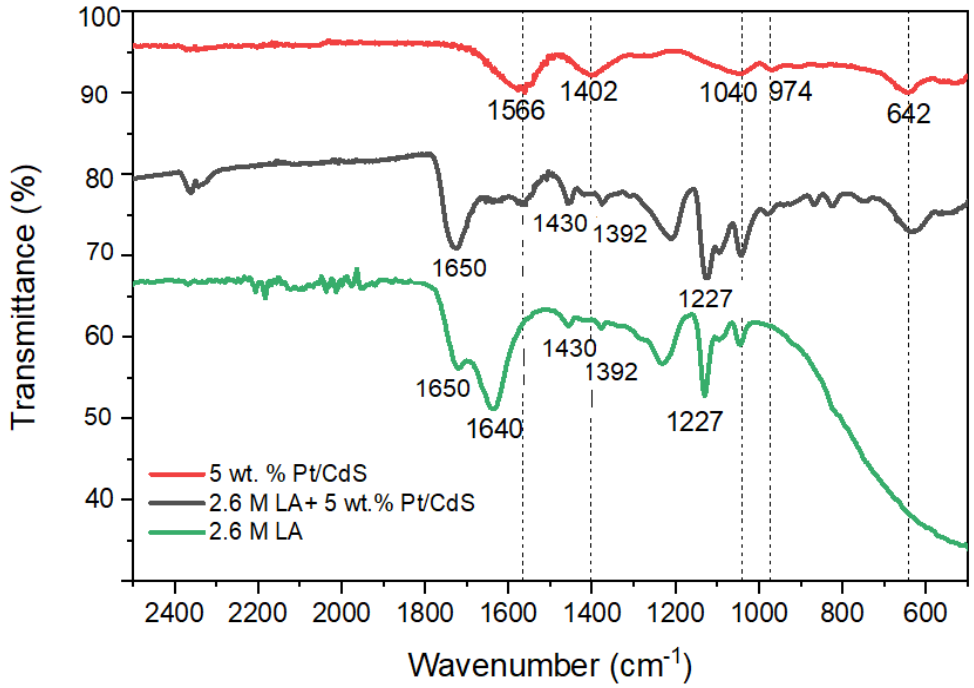

Figure 5. 2 FTIR spectrum of newly made 5 wt. % Pt/CdS (red), same particles pre-immersed lactic acid (black) and pure lactic acid (green). The dotted lines correspond to particle Pt/CdS's vibration peaks.

Suggested lactic acid surface adsorption can be seen in Fig 5.3, where the strongly adsorbed lactic acid molecule would rapidly facilitate an electron transfer for the necessary photocatalytic reaction. In the figure it can be seen a lactic acid molecule to the left, followed by the chemisorption of the free lactic acid and then the desorption of the formed pyruvic acid as the reaction product. Further investigation on the photooxidation of lactic acid will be presented at below.

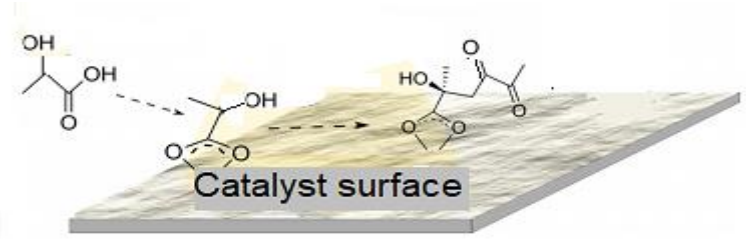

Figure 5. 3 Suggested lactic acid surface chemisorption and desorption of the pyruvic acid product on a Pt/CdS surface.

Also, discussion on the photooxidation reaction will be seen in the reaction kinetic modelling in Chapter 6, where the *k* and K values for the Langmuir Hinshelwood contribution to the model, will be obtained by fitting of the model and validation.

Researchers have reported that the only immediate photocatalytic oxidation product when using lactic acid solution is pyruvic acid (PA) [24,39]. However, it should be pointed out that molecular pyruvic acid is in equilibrium with the pyruvate ion, as it is a weak acid with pK_a=2.39. Also, it is assumed that lactic acid with pK_a=3.8, is in the neutral form (molecular rather than ionic form) at these low solution pH. From above conclusions, the initial oxidation pathway on the CdS surface can be proposed as Fig 5.4. By looking at this pathway, it would be expected that the pH of the reaction solution would experience a significant drop over time (as more and more H^+ is formed) or that additional H_2 gas would be formed.

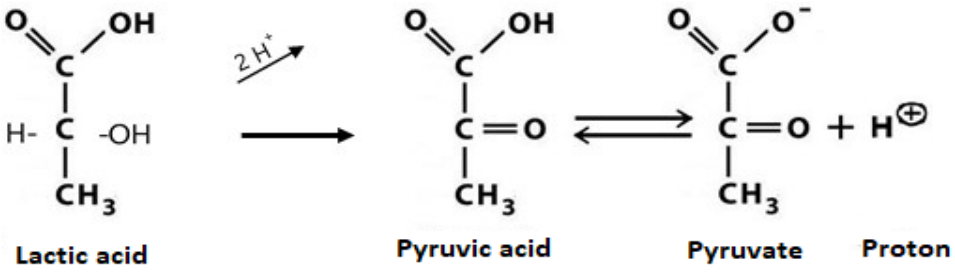

Figure 5. 4 Suggested initial oxidation pathway of lactic acid.

To investigate these assumptions, pH measurement was done over a 4 hours reaction run alongside a complementary IC-measurement of the lactic acid concentration change, as seen in Fig 5.5. According to this figure, the initial pH was 1.05 and after 4 hours it dropped down to 0.87 (corresponding to a small H^+ change from 0.089 M to 0.13 M), whereas the lactic acid concentration dropped from 2.6 M to 1.6 M. The conclusion here was that the pyruvic acid ↔ pyruvate equilibrium, was heavily left shifted towards pyruvic acid ($CH_3(CO)COOH$) at these low pH as part of the lactic acid oxidation route. In fact, the slight decrease in pH (as a result of increased H^+), corresponded to the increase in the pyruvic acid formation and therefore reduction of lactic acid in the solution. Also, it was further concluded that the two protons (2

H^+) released from the lactic acid oxidation would not contribute into the increase of pH nor additional of H_2 formation (this will be confirmed in the kinetic modelling section in Chapter 6, where the experimental H_2 rate matches with the model predicted H_2 rate). The two released protons would therefore form water with the formed hydroxyl ions from the photoreduction of water.

The photocatalytic reactions on the surface can therefore be proposed as:

$$2\,H_2O + 2\,e^- \rightarrow H_2 + 2\,OH^- \quad \text{water reduction} \quad (5\text{-}1)$$

$$CH_3CH(OH)COOH + 2\,h^+ \rightarrow CH_3(CO)COOH + 2\,H^+ \quad \text{lactic acid oxidation} \quad (5\text{-}2)$$

If further reaction time elapsed, demineralisation of pyruvate would have possibly occurred, forming acidic acid and CO_2. However, no CO_2 was detected in the GC analysis up to 4 hours reactor run suggesting that this will be after much longer reaction runs.

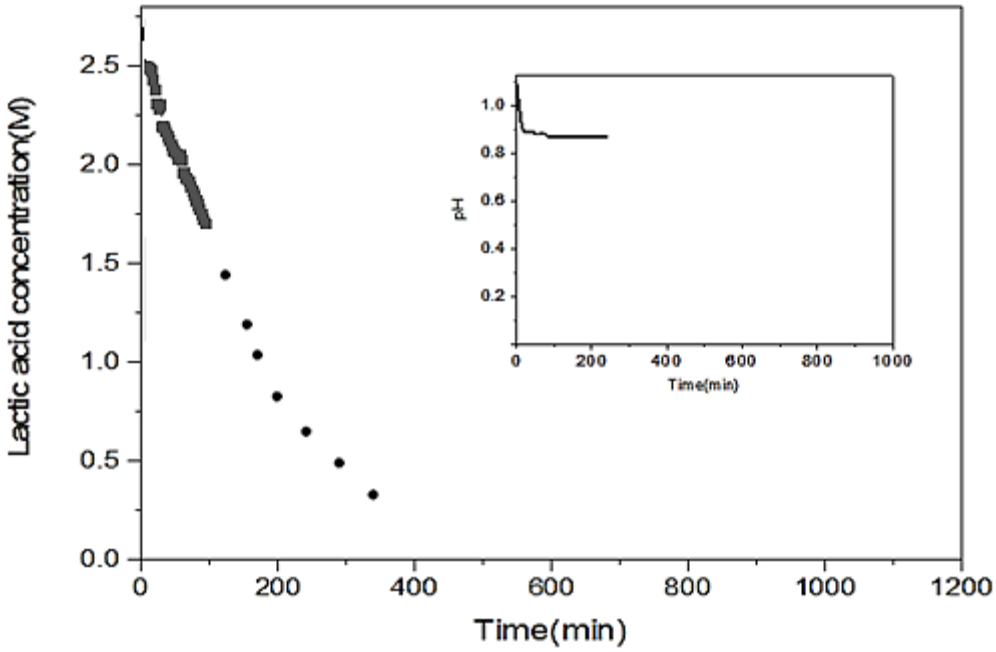

Figure 5. 5 Lactic acid degradation over 3 h measured by IC (black squares■). The black dots ● show the predicted reducing trend for the lactic acid toward its proven complete depletion at the end of the photocatalytic reaction. The Insert shows pH variation over a 4 h reaction run.

As the same time lactic acid was oxidised, water was reduced and formed hydrogen gas. To evaluate the purity of the produced hydrogen, gas chromatography analysis was conducted where gas samples from the reactor were taken and injected manually into the GC apparatus. The GC analysis, Fig 5.6 and the corresponding retention times and full peak widths at half maximum (FWHM) of the detected gases and the matching standards, Table 5.1, shows three peaks corresponding to hydrogen, oxygen and nitrogen.

Table 5. 1 The detected retention times and peak widths by the GC.

Peak name	Reaction time (min)	FWHM (min)
Hydrogen	2.26	0.035
Oxygen	3.10	0.040
Nitrogen	5.32	0.033
Standard Gases		
Hydrogen (99%)	2.12	0.027
Oxygen(99%)	3	0.033
Nitrogen(99%)	5.26	0.030

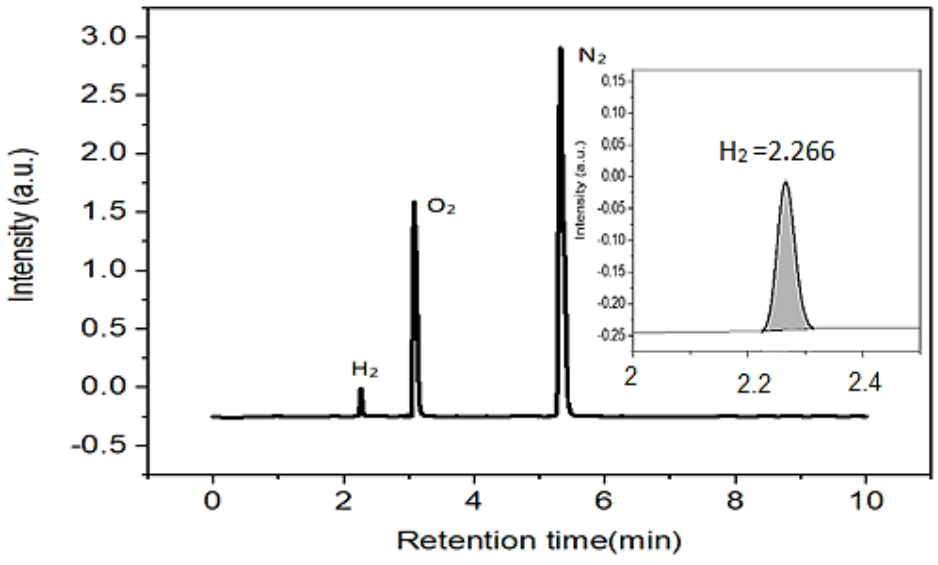

Figure 5. 6 GC analysis of a photocatalytic gas product sample, showing only H_2 peak as the liberated reaction product (see insert).

The oxygen and nitrogen peaks originated from air due to the off-line sampling technique and therefore the only gas evolved from the photocatalytic reaction was

pure hydrogen (R=2.26 ,FWHM = 0.035) as no other peaks were observed . The air presence was further confirmed by a “dry run” using the same gas-tight syringe, that showed no hydrogen but only oxygen and nitrogen peaks with retention times and peak heights that matched that of the air signatures recorded during the photocatalytic gas product analysis (results are not presented here).

5-3 Effect of operational parameters on the hydrogen evolution

The photocatalytic hydrogen experiments were conducted at various cocatalyst Pt-loading on CdS, Pt/CdS photocatalyst loading in the reactor, incident flux intensity, lactic acid concentration and reaction temperature to investigate the effect of these operational parameters on the hydrogen evolution. Fig 5.7 shows the experimental set-up of the small scale photocatalytic reaction system, where a 60 ml quartz photoreactor (inner diameter 2 cm) was used with one outlet for the hydrogen gas (which was measured by the inverted burette method) and one inlet for the argon pre-purging (to assure oxygen free reaction conditions). The reactor was externally irradiated by a 10 LED lamp arrangement (10 x 10 W cool white LED) with a LED lights to reactor wall distance of 4 cm, as seen in Fig 5.7.

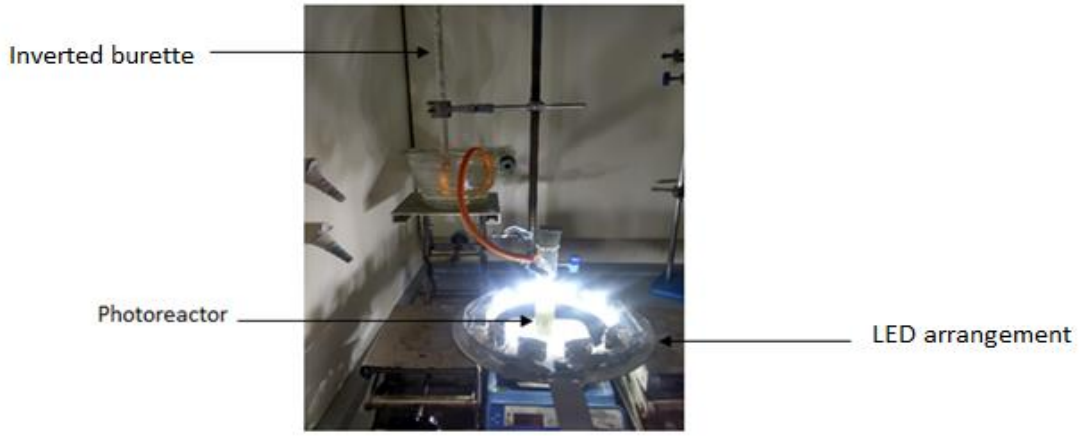

Figure 5. 7 Experimental set-up of the small-scale photocatalytic reactor.

For the LED lights to be used in the photoreactor, the choice of the LED power and the distance of the lights from the reactor wall was made by conducting the light intensity analysis. It should be noted that the lights should be powerful enough to

excite the photocatalyst particles in the photoreactor within the suitable emitted wavelengths. To measure light intensity and light spectra of the LEDs, a light meter spectrometer (GL Spectis 1.0) device was utilised. The GL Spectis 1.0 device uses a CMOS image sensor in the range of 340-780 nm which can be visualised by connecting to a PC. Figure 5.8 shows the conducted experiment in the dark room for the light measurement of two types of LEDs; (0.3 W cool white and 10 W warm white, Deal Extreme) at different distances (6, 4 and 2 cm) from the sensor. The variation of distances was done to place the LEDs at an appropriate distance from the photocatalytic reactions.

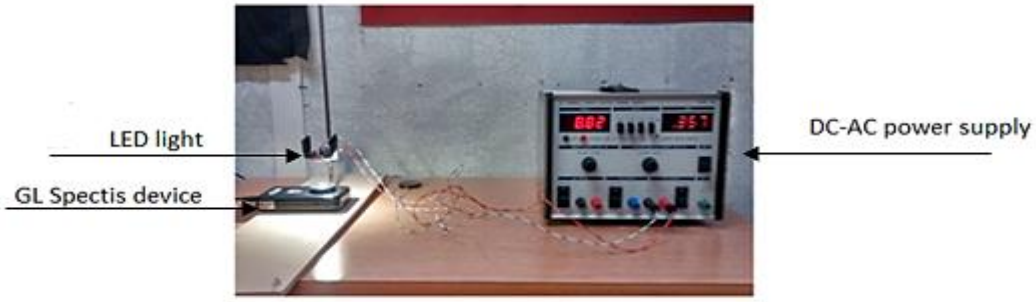

Figure 5. 8 The light spectrophotometric analysis conducted on the LEDs in a dark room.

The device measured the spectral irradiance as power per area for each wavelength (mW/m^2nm). The effect of light distance for the two types of LEDs, 0.3 W cool and 10 W warm white LED, when running at the highest power is presented in Fig 5.9 (a, b, c) and Fig 5.9 (d, e, f) respectively. For the 0.3 W cool white LEDs, the maximum intensity peak was found at 455 nm (visible region), followed by a lower broad peak between 500-700 nm, see Fig 5.9 (a, b, c). The maximum peak (suitable for CdS absorbance) was used for the intensity analysis at the distances of 6, 4 and 2 cm, where their values increased from 48 mW/m^2nm to 114 mW/m^2nm and to 328 mW/m^2nm respectively. This indicates when the distance to the sensor decreases, the light intensity significantly increases. However, these measured intensities for 0.3W would not be enough to mimic solar radiation intensities in the photocatalytic reaction, therefore the higher intensities, 10 W warm LEDs, were analysed at the same distances. Fig 5.9 (d, e, f) shows the spectrum for the 10 W warm LED. For all warm LEDs, two strong peaks were observed; one at 455 nm and the other one at

600 nm. Both peaks are the same as the cool LED's spectra, but the second peak at 600 nm (IR region) have a much higher intensity when using warm LEDs than the cool LEDs, which could lead to an undesirable heat generation if used in the photoreactor. For the peak at 455 nm, the measured values of intensity for the distances of 6, 4 and 2 cm increased from 733 mW/m^{2}nm to 1434 mW/m^{2}nm and to 3333 mW/m^{2}nm respectively and for the peak at 600 nm from 1056 mW/m^{2}nm to 2252 mW/m^{2}nm and to 4561 mW/m^{2}nm.

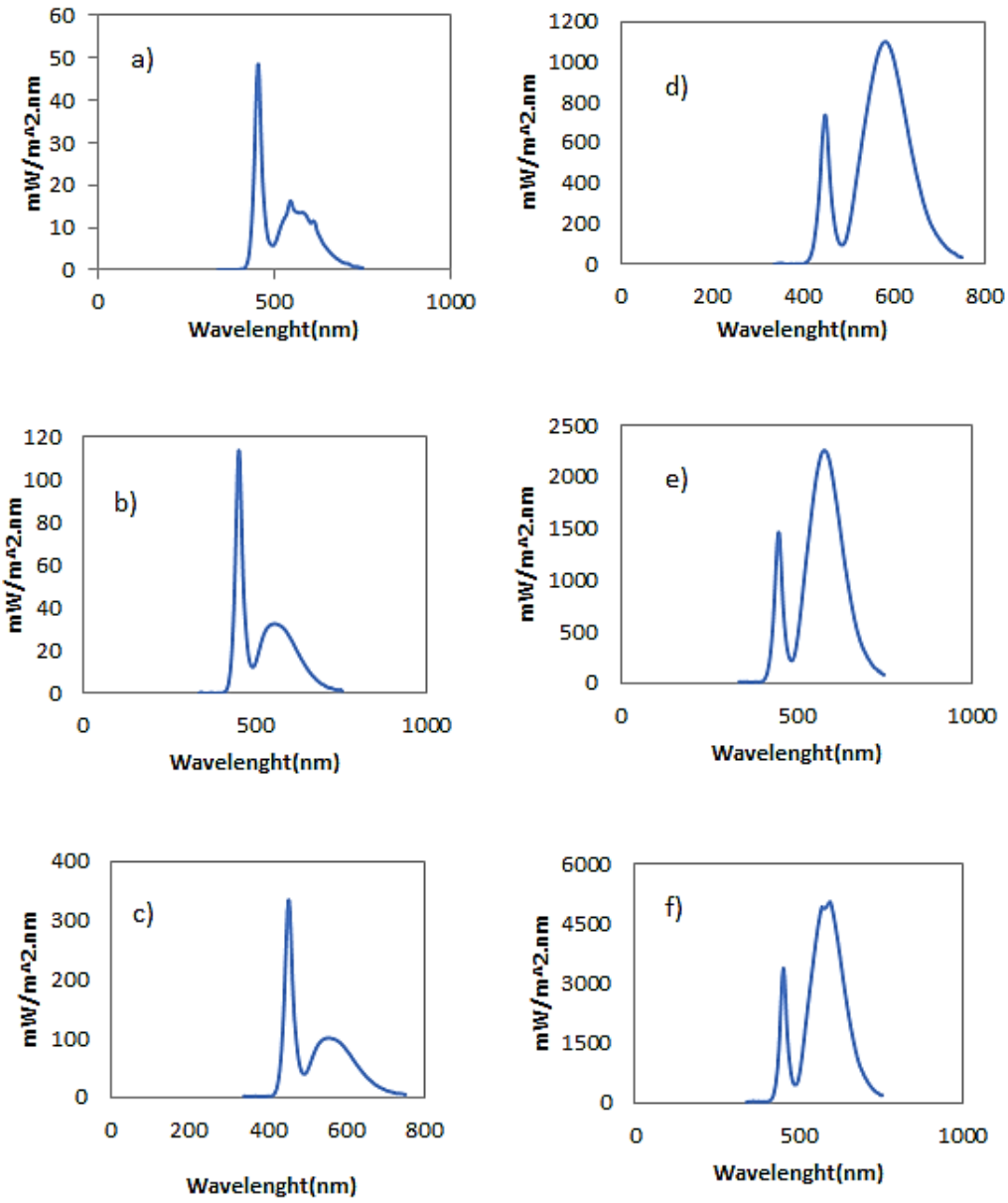

Figure 5. 9 Light intensity analysis for a 0.3 W cool white LED at distance of; a) 6 cm, b) 4 cm and c) 2 cm and for a 10 W warm LED at distance of; d) 6 cm, e) 4 cm and f) 2 cm from the GL Spectis light spectrometer surface.

For the photocatalytic purposes, the warm LED lights possessed sufficient visible light intensities, but they were not suitable to be used in the photoreactor as the heat build-up in the reactor would jeopardise the study of reaction kinetics later. For such analysis, the reactor needs to have a controlled and stable temperature. Therefore, 10 W cool white LED was considered instead of 10 W warm white LED, which would surely prevent the unnecessary heat build-up in the reactor.

The different hydrogen generation response by varying the amount of Pt-loading on CdS can be seen in Fig 5.10 (a). The Pt-loading is expressed as the weight % of Pt to CdS powder. The theoretical aim was to have 2, 5, 7 and 10 wt. % Pt/CdS, despite the actual supporting material analysis proof such as TEM or HR-SEM for the real loading of Pt on the CdS . The accuracy and reproducibility (experimental errors) of the hydrogen generation of Pt/CdS at different Pt loading of 2, 5, 7 and 10 wt.% was also recorded within $\pm$ 0.5 ml based on the standard deviation of 3 tests. After each run, the composite catalyst was immediately washed and then dried and used again for the next run. This indicated validity of the hydrogen tests and stability of the composite catalyst of Pt/CdS (with different Pt loading of 2, 5, 7 and 10 wt.%) that caused nearly similar hydrogen evolution at each run.

For the hydrogen generation tests here, the lactic acid concentration was 2.67 M, the incident flux intensity was 2.6 W/m^2 per LED, temperature was 25°C and catalytic reactor loading (Pt/CdS) was 0.0002 g/cm^3. Note that the incident flux intensity of 2.6 W/m^2 was measured on the reactor wall for one LED light and with the maximum allowed voltage of the power unit. According to Fig 5.10 (a) an increase from 2 wt.% to 5 wt.% Pt-loading shows more than a 3-fold increase in the cumulative hydrogen production, reaching to 1100 μmol H_2 after 240 min. However, a further increase to 7 wt.% or even 10 wt.% Pt loading, resulted in a significant drop of the cumulative H_2. This observed trend can be explained by an initial advantageous excited electron trapping in the Pt (from a photoexcited CdS) until a point where the increased co-catalyst loading on the CdS starts blocking the incoming photons and promote scattering and reflection of the incoming light. Therefore, the optimum Pt-loading of 5 wt.% was considered throughout the hydrogen evolution experiments in this research.

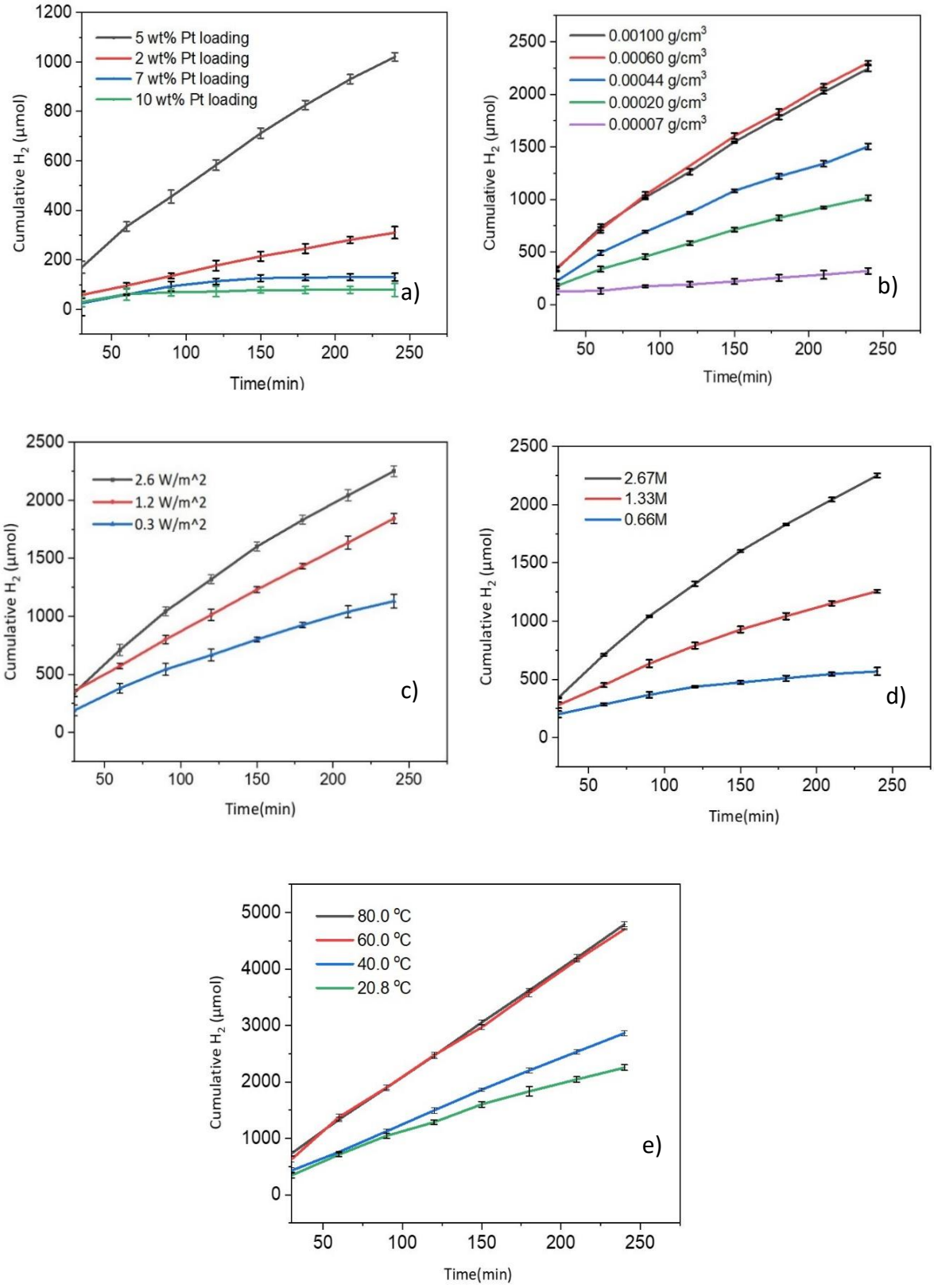

Figure 5. 10 Effect of reaction variables on the cumulative H_2 evolution by variation of; (a) cocatalyst Pt-loading on CdS, (b) photocatalyst loading in reactor, (c) light intensity, (d) lactic acid concentration and (e) reaction temperature.

The effect of catalyst particle loading can be seen in Fig 5.10 (b). Here the initial lactic acid concentration was 2.67 M, the incident flux intensity was 2.6 W/m^2 per LED, temperature was 25°C and the Pt loading on CdS was 5 wt.%. As the catalyst loading was increased from 0.00007 g/cm^3 to 0.00060 g/cm^3, the evolved hydrogen was increased from 318.9 to 2300 μmol, respectively, after 4 hours irradiation. A further loading increase to 0.00100 g/cm^3, did not significantly change the cumulative evolved hydrogen after 4 hours irradiation. This implies that there is an upper limit for the catalyst loading, where the H_2 production rate remains practically unchanged, as a result of shielding effect of the incoming light. Thus, the photocatalyst reactor loading of 0.0006 g/cm^3 was used as the baseline in the most of the H_2 experiments. The effect of incident light intensity on the cumulative H_2 evolution can be seen in Fig 5.10 (c). The lactic acid concentration was 2.67 M, photocatalyst loading was 0.0006 g/cm^3 with Pt loading of 5 wt.%, reaction temperature was 25 °C and light intensity per LED variation was between 0.3 to 2.6 W/m^2. According to the figure, an increase in the light intensity improved linear the amount of evolved hydrogen from 1058 to 2300 μmol after 4 hours irradiation. This means at the higher intensity, the more photon absorption and therefore more electron-hole generation, leading to an enhanced redox-reaction rate. A further increase of light intensity was limited due to the power restriction. Note that the upper limit of 2.6 W/m^2 was the maximum driven intensity of one LED light.

The effect of lactic acid concentration is shown in Fig 5.10 (d), where an increased lactic acid concentration from 0.66 M to 2.67 M, also increased the hydrogen evolution, from 729 to 2300 μmol respectively, after 4 hours irradiation at a fixed incident flux of 2.6 W/m^2, a photocatalyst loading of 0.0006 g/cm^3 with Pt loading of 5 wt.% and a reaction temperature of 25 °C. This means that at higher lactic acid concentration, the more lactic acid is surface adsorbed, where the photogenerated holes can oxidise more lactic acid to pyruvic acid. This hole reaction will therefore improve simultaneous the water reduction to hydrogen by the photogenerated electrons. A further increase in lactic acid concentration beyond 2.67 M did not cause a further increase in the hydrogen production (the result is not presented here), which is indicating an upper limit with the change of lactic acid concentration.

Finally, the effect of reaction temperature on the H_2 evolution was analysed, as seen in Fig 5.10 (e). Here the incident flux was 2.6 W/m^2, lactic acid concentration was 2.67 M, and photocatalyst loading was 0.0006 g /cm^3 and the temperature varied between 20.8 °C and 80.0 °C. The H_2 evolution increased with increasing reaction temperature, reaching a maximum of 4780 μmol at 60 °C after 4 hours irradiation. However, further increase to 80 °C did not significantly change the H_2 evolution. There are many reasons for this temperature dependency. The initial increase is directly related to the adsorption isotherm between the catalyst surface and water/lactic acid, where the higher temperatures facilitate a higher mass diffusion i.e. adsorption and desorption rates. Also, the lower viscosity of the solution at the elevated temperature can facilitate detachment of the H_2 bubbles (gas desorption) and contribute to an apparent increased hydrogen production. In addition, the band-gap of CdS will slightly decrease with the increasing temperature due to an increase in thermally excited electrons (a response by the increase of CdS lattice vibrations and therefore change in the phonon density of state). Furthermore of the CdS state change, the potential of the conduction band may therefore vary in these temperature variations and/or the electron transfer to the Pt where the water reduction occurs may be affected. These CdS alterations with the temperature are beyond the scope of this thesis and only briefly speculated here and therefore is not explored further here. For the majority of the photocatalytic reactions in this thesis, room temperature of 25°C was used.

5-4 Effect of sacrificial reagents on the hydrogen generation by Pt/CdS

In Fig 5.11 the comparison of hydrogen generation performances in various hole donor solutions using a 5 wt.% Pt/CdS catalyst loading can be seen. The solutions of choice were 2.6 M lactic acid (which was thoroughly studied earlier in this chapter) and 2.6 M ammonium sulphite with the sodium sulphide variation between 0.5-1.5 M. The cumulative H_2, normalised to mg catalyst, were measured at 1 h, 2.5 h and 4 h irradiation, at a fixed incident flux of 2.6 W/m^2 per LED, a photocatalyst loading of 0.0006 g/cm^3 and a temperature of 25°C. As seen in Fig 5.11, the Pt/CdS system showed far higher hydrogen evolution per mass of catalyst in the lactic acid solution

compared to any of the ammonium sulphite + sodium sulphide solutions. Moreover, the Pt/CdS system performed almost identical when 1 M sodium sulphide and 1.5 M sodium sulphide were separately used in ammonium sulphite solution, where both showed slightly higher hydrogen evolution than the solution with 0.5 M sodium sulphide.

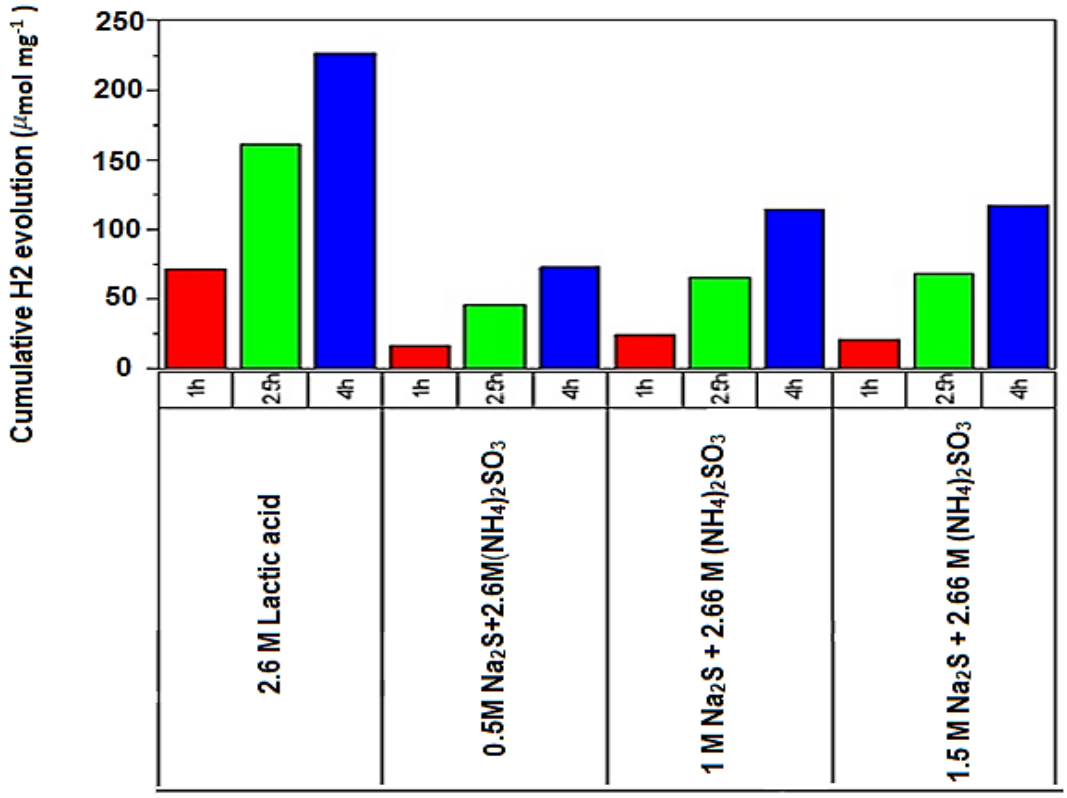

Figure 5. 11 Effect of sacrificial reagents on the cumulative H_2 evolution after 1 h, 2.5 h and 4 h irradiation when using 5 wt.% Pt/CdS loading.

The reason why Pt/CdS showed such a high activity in lactic acid compared to the ammonium sulphite + sodium sulphide solutions could be due to a range of factors. One important factor is that the surface potential of the trapped excited electrons in the Pt cocatalyst versus the half potential of reducing water scenario, which varies at different pH, see Fig 5.12. Another is the difference between the electron potential of CdS (c. b.) and both the potential of the water reduction and the Pt co-catalyst, that both change with change of pH. The water reduction is assumed to proceed as a result of trapped electrons in the co-catalyst which involves an initial efficient electron transfer from the CdS (c. b.) to the cocatalyst (Pt), before the final electron

transfer necessary to reduce the water. According to Fig 5.12, at low pH (as found in the lactic acid solution), the electron potential for Pt is only -0.04 eV [155], compared to the necessary water reduction potential of H^+/H_2 = 0 eV and the CdS (c. b.) potential of -0.7 eV [149]. At high pH (as found in the ammonium sulphite - sodium sulphide solutions) the electron potential for Pt is now -0.4 eV and the water reduction potential changed to -0.3 eV [155], on the contrary, the CdS (c. b.) potential marginally changes with pH changes [156].

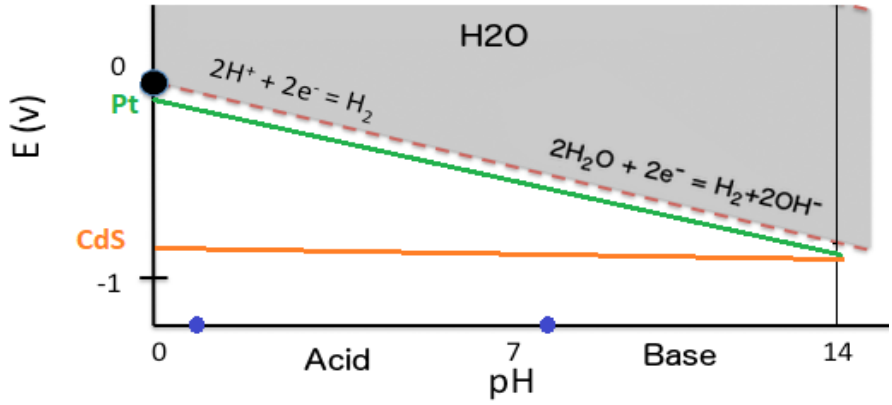

Figure 5. 12 pH dependency of the potentials driving the water reduction. The blue dots ● show pH in the lactic acid solution (pH=1.1) and in the ammonium sulphite -sodium sulphide solution (pH=8.7).

The higher pH also decreases slightly the electron bandgap of CdS, which will also affect both the reduction and oxidation reactions potentials [156]. Moreover, the pH changes will also change the zeta potential of the CdS, which will then affect the surface adsorption and repulsion mechanisms (both are important for a high level of electron transfer) [157]. Conclusion is that the needed electron transfer from CdS to Pt and from Pt to the solution specie will all be affected by the pH variation, in addition to the ability for the surface adsorption by the photolyte .

In the results shown in Fig 5.11, an addition of sodium sulphide in the 2.6 M ammonium sulphite was used, where the concentration of sulphide (S^{2-}) ions varied from 0.5 M to 1.5 M. This addition of S^{2-} was aimed to improve the electron donation of the already physiosorbed SO_3^{2-} ions (as will be shown in Chapter 7) on the CdS surface as a result of the difference in the oxidation potentials of SO_3^{2-}/SO_4^{2-}=+0.92

eV [104] and S^{2-}/S_2^{2-} = +0.57 eV [104] compared to the CdS valence band potential of +1.68 eV [156]. According to the figure, an increase of S^{2-} from 0.5 M to 1 M, showed a slight improvement in the cumulative hydrogen evolutions after 1 h, 2.5 h and 4 h irradiations, but when 1.5 M S^{2-} concentration was used no further improvement was observed. This indicates an exceeded concentration of the oxidation product disulphide ions (S_2^{2-}) on the catalyst surface, which probably acted as an optical filter (absorbs incoming light) or competed the photocatalytic reactions. Previously, Bao et al.[158] described the negative effect of this disulphide ion when sulphite ions were photo-oxidised and also reported a suggested reaction mechanisms. The investigation of using the sodium sulphide- ammonium sulphite mixture was not explored further here, as the final working fluid of the sulphur ammonia thermochemical cycle is aimed to be only ammonium sulphide.

As final conclusion, the chemosorbed lactic acid proved to more efficiently donated electrons to the valance band of CdS than the physiosorbed S^{2-} + SO_3^{2-} ions. Also, it was concluded that the presence of S^{2-} in a SO_3^{2-} containing solution did not significantly improve the photocatalytic reaction. Therefore, as presence of S^{2-} is not needed in a thermochemical cycle fluid, it was abandoned for the continuation of the research.

5-5 Hydrogen generation of Co_xP/CdS photocatalysts

The hydrogen generation using different synthesised Co_xP/CdS composite photocatalysts ,and with or without post-annealing of Co_xP, were compared with Pt/CdS , as seen in Fig 5.13. The cumulative H_2 evolution values are per mg catalyst loading and measured after 1 h, 2.5 h and 4 h reactor irradiation, at a fixed incident flux of 2.6 W/m^2 per LED, a lactic acid concentration of 2.67 M, a photocatalyst loading of 0.0006 g/cm^3 (with 5 wt.% cocatalyst) and 25°C. The cocatalyst loadings were all done by the grinding method except for Pt (which was done by a reduction reaction). The results show that Pt/CdS produced a higher hydrogen evolution per mass of catalyst than the other composites, reaching 71.6 μmol mg^{-1}, 183.5 μmol mg^{-1} and 226.3 μmol mg^{-1} after 1 h, 2.5 h and 4 h irradiation respectively. These results are comparable to reported data [29]. The CoP/CdS synthesised via the organometallic method, appeared to be the second most active composite with a H_2

evolution of 173.5 μmol mg^{-1} after 4 h irradiation. The third active composite was Co_2P/CdS, also synthesised by the Co_xP organometallic method, which displayed a H_2 evolution of 137.4 μmol mg^{-1} after 4 h irradiation.

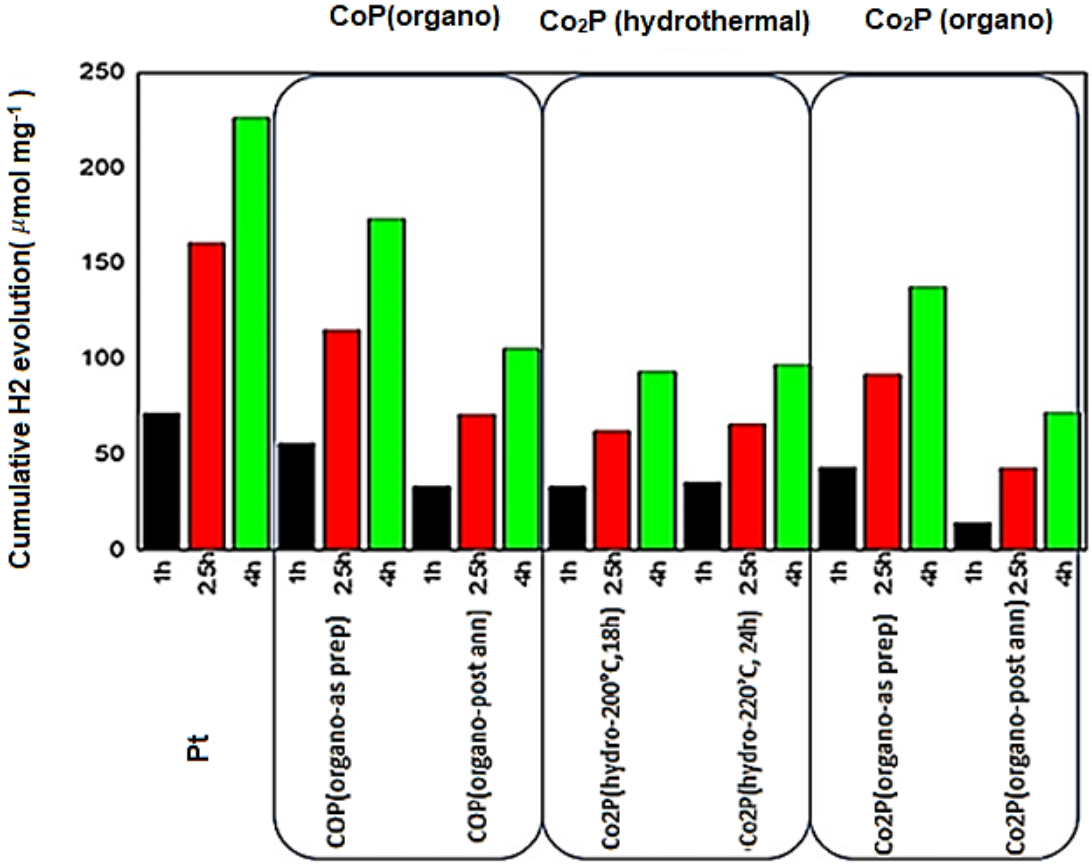

Figure 5. 13 Hydrogen performance of synthesised photocatalyst composites, with and without post annealing of their cocatalysts, compared with Pt/CdS after 1 h, 2.5 h and 4 h irradiation.

The least active composite was hydrothermally synthesised Co_2P/CdS, where Co_2P was synthesised at 200 °C for 18 h. This catalyst displayed a H_2 evolution of only 85.3 μmol mg^{-1} after 4 h irradiation.

None of synthesised Co_xP/CdS composites performed as much as the Pt/CdS system. This could be either due to low crystallinity of the synthesised Co_xP or inefficient grinding loading efficiency for the Co_xP on the CdS particles. To increase the crystallinity of Co_xP, a post-annealing step was introduced to the organometallic synthesis of the Co_xP particles and for the hydrothermal method, higher and longer temperature setting was introduced. The hydrogen generations were compared under identical conditions with those of the as-prepared samples, see Fig 5.13. However, the post-annealing step adversely affected the hydrogen evolutions of

Co_xP/ CdS composites. For the hydrothermal synthesis of Co_2P, the longer and higher process temperature did not cause any significant enhancement of the H_2 evolution of its composites either. Previous, in Chapter 4, it was shown that one negative effect of the organometallic synthesis post-annealing was carbonisation on the particle surfaces and not improved crystallinities, which is the main reason for a reduced hydrogen evolution for these composites. Shi et al. [30] claimed in a related electrochemical study that the good hydrogen producing performance of organometallically synthesised Co_xP was by the high electronegativity of the P atoms creating a polar particle, which would enhance the H^+ affinity to the P sites of the Co_xP particle. This confirms the insignificant role of crystallinity in the hydrogen evolutions using the organometallic synthesised Co_xP particles. On the other hand, the reason why minimum hydrogen evolution activity was obtained for the hydrothermally Co_2P synthesised composites, even with the change of hydrothermal condition, may come down to the charge transfer between the Co_2P particles and the CdS nanoparticles at the interfaces.

In Chapter4, it was shown that the hydrothermally synthesised CdS particles contained a high level of large agglomerates (> 50 nm particles). Therefore, the cocatalyst loading by the grinding method would provide only a small probability for the Co_xP particles to cover all exposed CdS surfaces. The conclusion was therefore that for a more trustworthy comparison, an improved cocatalyst adhering process were needed. In the following section, the hydrogen evolutions between different loading methods will be shown.

5-6 Hydrogen evolution comparison between different cocatalyst loading methods

In Fig 5.14, the hydrogen generation of CoP /CdS (with organometallicly synthesised CoP) and Co_2P/CdS (with the hydrothermally synthesised Co_2P), before and after loading improvements (i.e. grinding vs sonication loading), are compared with Pt/CdS. For the hydrothermal Co_2P/CdS, an additional loading improvement named “in situ” was also conducted (route explained in Chapter 3). In Fig 5.14 the cumulative H_2 evolution values are by µmol per mg catalyst loading and read after 1

h, 2.5 h and 4 h irradiation, at a fixed reactor incident flux of 2.6 W/m^2 per LED, a lactic acid concentration of 2.67 M and a photocatalyst loading of 0.0006 g/cm^3 and a temperature of 25°C.

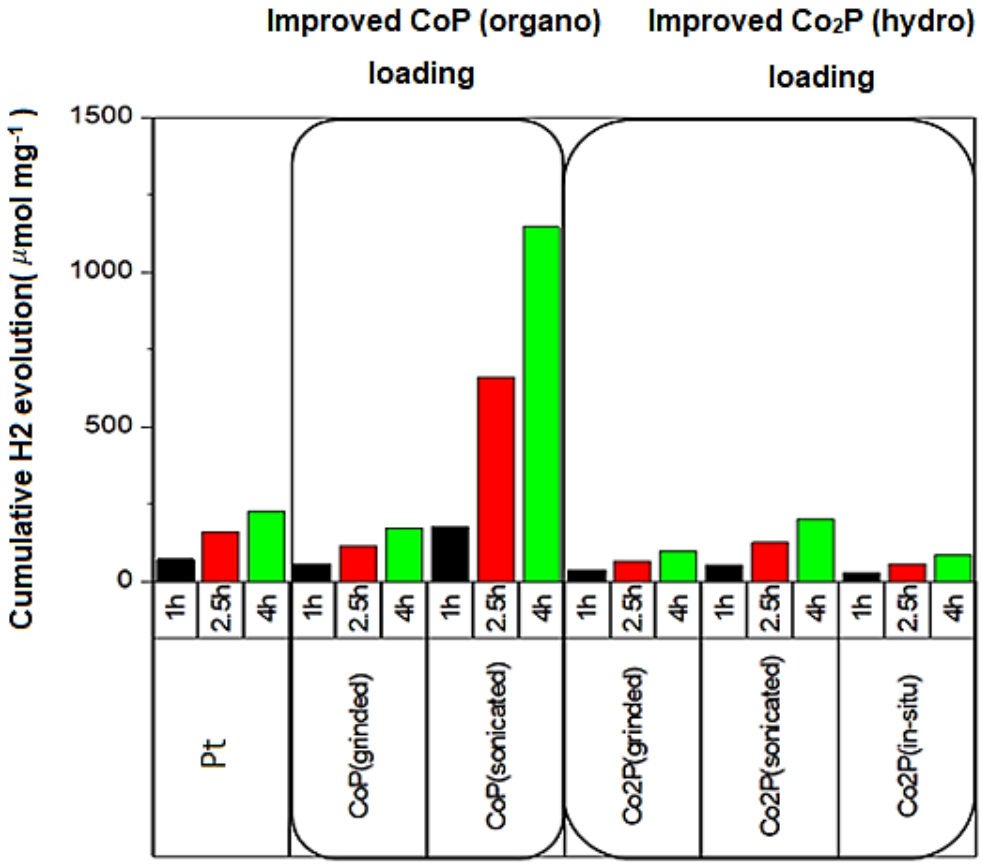

Figure 5. 14 Hydrogen generation of Co_xP/CdS photocatalyst before and after cocatalyst loading improvements and compared with Pt/CdS.

The main observation from these results is the outstanding hydrogen generation for the CoP/CdS photocatalyst when the organometallic CoP was loaded by the sonication method, reaching 1150 μmol mg^{-1} after 4 h irradiation, which is about 5 times more than Pt/CdS. This observation is consistent with the results of a comparative study in 2015 by Shuang Chao et al. [29] on the hydrogen evolution of composite catalysts using metal phosphides co-catalyst (especially cobalt phosphide) against Pt-based photocatalytic systems of CdS. In that study it was concluded that the CoP was the only metal phosphide that held an exceptional potential to serve as a cheaper alternative cocatalyst, than the other metal phosphide catalyst systems

and therefore could acceptably replace the noble metal Pt nanoparticles for the practical photocatalytic applications, due to its incredible hydrogen evolution.

The impressive hydrogen evolution of CoP/CdS system in Fig 5.15 was mainly due to an improved loading caused by the energetic sonication forces when CoP was added to CdS. Another important factor to mention again is the surface potential of the trapped excited electrons in the cocatalyst (CoP or Pt) versus the half potential of reducing water at low solution pH (as in 2.67 M lactic acid). As the water reduction is assumed to proceed by the trapped electrons in the co-catalyst, it involves an initial efficient electron transfer from the CdS(c. b.) to the cocatalyst (CoP or Pt) before the final water reduction reaction. Callejas et al. in 2015[32], compared the estimated overpotentials needed in a Ti-Pt and Ti-CoP electrochemical cell to produce a cathodic current of –10 mA cm^{-2} (Co_xP catalysts were organometallically synthesised). The study was conducted at a low solution pH (H_2SO_4) and aimed to find cheaper alternatives than noble metals for driving hydrogen evolution reactions (HER). In that study the cobalt phosphide cathode of Ti-CoP required an overpotential of -75 mV for a -10 mA/cm^2 current, compared with -19 mA/cm^2 for Pt. From the overpotential study the ranking order was as; Pt>CoP, however their hydrogen evolution reaction study (HER) showed a raking order as; CoP >Pt (in low pH). In addition, the researchers observed an excellent acidic stability of the cobalt phosphides with high hydrogen evolution after long and repeated tests. Their final conclusion of why CoP worked well for HER activity was due to the dynamic relation of transitional metal ion (Co) and phosphorous (P) for the surface reactions rather than the expected work potentials. Relating Callejas et al. [32] study with what was observed in Fig 5.14, it can be concluded that indeed CoP exhibited better HER activity than Pt at low solution pH.

Another observation from the results illustrated in Fig 5.14, is that only a marginal hydrogen evolution improvement of 0.4% for the hydrothermal Co_2P was seen when using sonication loading rather than the grinding loading. Also, the in-situ hydrothermal method of Co_2P loading did not show any significant improvement when compared to the grinding method. The sonication loading was used to deliver ultrasonic energy to particles at a defined time (2h), where a change of the surface characteristics of particles (e.g. size related surface area, surface defects and

dissolution of surface bound contaminants) would be expected and therefore be a route to change the interaction with other particles or specimens. However, the sonication loading method did not cause a significant change in the surface characteristics of the hydrothermally synthesised Co_2P particles, and only caused less CdS agglomerates (as confirmed in Chapter 4), resulting in only margin improvement in the hydrogen evolutions, seen in Fig 5.14. The in-situ hydrothermal loading method that included an additional hydrothermal step for the Co_2P in-situ synthesis showed very poor performance and it was therefore suggested that this route would need further optimisation, see Future Work.

From these results, it was concluded that only the CoP/CdS composite (with the organometallically synthesised CoP and loaded by sonication) was the best performing photocatalyst and surprisingly far better than the Pt/CdS photocatalyst which is more understood and elaborated in literature. This massive improvement after sonication was not only because of the reduced agglomerates (as this would be the same for the hydrothermal process comparison), but by the fact that the solvent residues after the organometallic synthesis, will be dissolved or "cleaned" during the sonication method. Further studies to appreciate the extent of such sonicating cleansing effect on the organometallic CoP particles were suggested, see Future Work. The optimised synthesised CoP/CdS photocatalyst was therefore chosen to be used for the hydrogen producing step of the proposed solar driven sulphur ammonia thermochemical cycle, as will be presented in Chapter 7.

5-7 Stability of the optimised CoP/CdS composite

The stability and reusability of the optimised CoP(organo)/CdS composite was evaluated through six consecutive runs under the same experimental conditions; fixed incident flux of 2.6 W/m^2 per LED, a lactic acid concentration of 2.67 M and a photocatalyst loading of 0.0006 g/cm^3 and a temperature of 25°C, as seen in Fig 5.15. Each run was performed for 2.5 h, where the catalyst was immediately washed afterward and then dried and used again. The figure shows that there was no significant decrease in the H_2 evolution activity after each cycle.

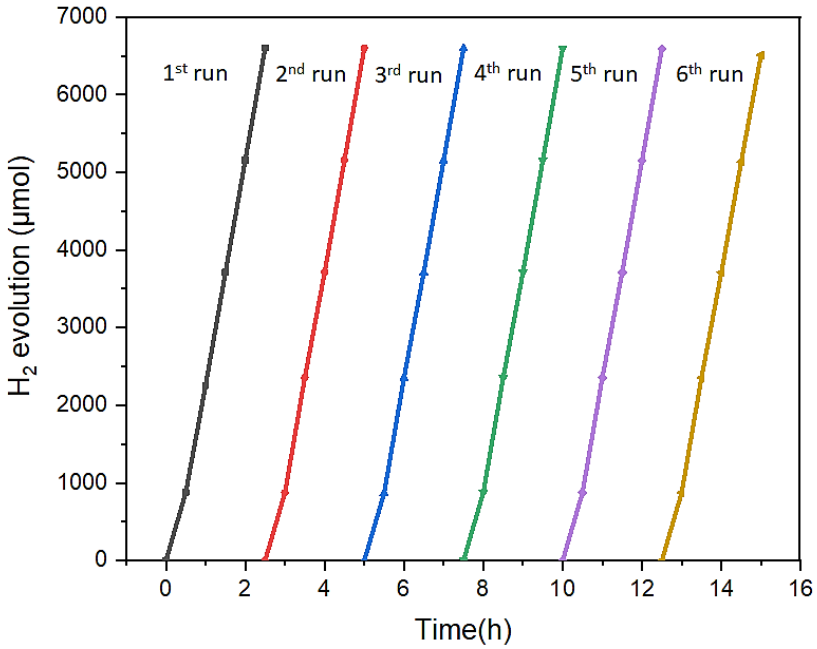

Figure 5. 15 Stability test of the CoP(organo)/CdS catalyst in a use-wash-dried-and use again cycle repeatability test.

It was therefore concluded that the optimised photocatalyst could maintain the similar photocatalyst activity for at least 12 hours and probably more. As a conclusion, the optimised CoP(organo)/CdS catalyst showed both an excellent hydrogen production in addition to an excellent stability for the photocatalytic hydrogen production. The photocatalytic stability of the optimised compote catalyst of CoP(organo)/CdS is also consistent with the reported results by Shuang Chao et al. [29] in 2015, where they found incredible photocatalytic activity even after 100 h of light irradiation.

5-8 Conclusion

In this chapter a comprehensive investigation of the photocatalytic hydrogen evolution with different synthesised particles and different reaction conditions was presented. First the different photocatalytic reactions when using lactic acid solution was investigated. A preliminary UV-Vis analysis of the solution showed that no direct photodissociation of the lactic acid would be possible and therefore the visible

photon energy would only be received by the CdS particles. The FTIR results showed that lactic acid was probably chemisorbed on the Pt/CdS photocatalyst particles as the typical vibrations of a “free molecule” disappeared. This finding will play an important role in the hydrogen rate model development in Chapter 6, where the surface adsorption/desorption and surface reaction rates observed, were found to have an impact on of the amount of formed H_2. The GC analysis of the evolved gas proved it was 100% hydrogen and no inferior gas was formed in the reactor. All these analytical methods plus a pH measurement during the reaction, enhanced the understanding of photooxidation mechanism of the lactic acid while water was photoreduced. The primary oxidation pathway was found through oxidation of lactic acid to pyruvic acid, which was normally in an equilibrium with a pyruvate ion and one proton. The two released protons from the lactic acid oxidation would only form water with the hydroxyl ions produced from the photoreduction of water molecules and not contribute to the hydrogen production. When using Pt/CdS photocatalyst in the lactic acid, the best performing operational parameters were; photocatalyst loading of 0.0006 g/cm^3 (with the cocatalyst content of 5 wt.%), incident flux of 2.6 W/m^2 per LED, lactic acid concentration of 2.67 M and with temperatures in the range of 60 °C -80 °C. The comparison of the different sacrificial reagents effect (hole donor solutions) when using Pt/CdS (at these optimised operating conditions) indicated that the chemosorbed lactic acid on the catalyst surface would more efficiently donate electrons to the valance band of CdS than when compared to the weakly physiosorbed S^{2-}+ SO_3^{2-} ions. Further it was concluded that the presence of S^{2-} in the SO_3^{2-} solution did not significantly improve the reactivity. When comparing all synthesised catalysts while using 2.67 M lactic acid , a decreasing order of ; Pt/CdS > CoP(organo)/CdS > Co_2P(organo)/CdS > Co_2P(hydro)/CdS was found, when the simple grinding loading method was used. By introduction of a post-annealing step in the organometallic synthesis of CoP and by changing the hydrothermal synthesis conditions of Co_2P, no major improved hydrogen evolution of the same catalysts systems was found. Therefore, a change of cocatalyst loading method on the CdS surface was seen as the only route for improvement. By using a sonication-assisted loading method which could also dissolve surface bound contaminants, an exceptional photocatalytic activity for the CoP(organo)/CdS was obtained. The

amount of hydrogen after 4 hours run was significantly higher than other composite photocatalysts, especially the more elaborated and previous published Pt/CdS composite. The stability test of the optimised CoP (organo)/CdS catalyst indicated it had excellent photocatalytic stability and repeatability, and for more 6 x 2 hours run with a use-wash-dry-use again cycle in a lactic acid solution. As the final conclusion the optimised CoP(organo)/CdS composite where CoP was loaded by a sonication-assisted method, was the best photocatalyst composite to substitute Pt/CdS for photocatalytic hydrogen reactions in ammonium sulphate solutions and therefore to be used in the hydrogen producing step of a suggested solar driven sulphur ammonia thermochemical cycle.

Chapter 6 Results and Discussions: Hydrogen Photoreactor Modelling

6-1 Introduction

In this Chapter a descriptive mathematical model to predict the hydrogen production rate is presented. First, surface reaction kinetics for adsorption of lactic acid on Pt/CdS catalyst surface based on Langmuir Hinshelwood adsorption is presented in section 6-2, followed by the radiation field model explanation in section 6-3. Then in Section 6-4, the complete model and results will be discussed, where the model will be validated against the empirical data at various operating conditions.

6-2 Surface reaction kinetics

The hydrogen generation reaction can be described as a joint event of the formed electrons and holes in the CdS after absorbing a photon. When the electron and holes have diffused to the surface, it is assumed that simultaneous reduction/oxidation reactions occur on the particle surface. In the cathodic reduction step, hydrogen gas is formed via reduction of adsorbed water molecules by the excited electrons that transferred from CdS to the Pt co-catalyst surface. Therefore the driving potentials is that of the Pt co-catalyst which is -0.04 eV[32], and is less negative than flat band potential of CdS, -0.7 eV, but more negative than redox potential of H^+/H_2 = 0 eV. In the anodic step, oxidation of lactic acid is undertaken by the surface trapped-holes on the CdS with the valence band potential of +1.7 eV [159], which is more positive than oxidation potential of lactate/pyruvate, +0.19 eV. It is assumed that lactic acid is not dissociated at the experimental solution of pH 1.20-1.34. It is also assumed that no OH^- radicals taking part of the oxidation, as the formation potential of OH^- radicals is +2.8 eV, which is higher than the valence band potential of CdS. Also, there is no oxidation driven by free O_2 due to the oxygen-free experimental conditions and

therefore the oxidation pathway is by the surface trapped holes only. The anodic and cathodic reactions as already presented in Chapter 5, can be seen in Eq.(6-1) and (6-2).

Cathodic reaction:

$$2\,H_2O + 2\,e^- \rightarrow H_2 + 2\,OH^- \qquad H^+/H_2 = 0\ eV \qquad (6\text{-}1)$$

Anodic reaction:

$$CH_3CH(OH)COOH + 2\,h^+ \rightarrow CH_3(CO)COOH + 2\,H^+$$

lactate/pyruvate = +0.19 eV (6-2)

The rate of hydrogen formation is therefore depending on incoming (and absorbed) radiative flux as well as the rate of surface reactions. The hydrogen production rate can then be expressed as a product of Langmuir Hinshelwood surface reactions with the incorporation of total radiative flux received by all catalyst particles. The equilibrium of adsorption and desorption rate of lactic acid (LA) on CdS surface adsorption sites (S), or the vacant sites, can be expressed as:

$$LA + S \underset{k_{-1}}{\overset{k_1}{\leftrightarrow}} LAS \qquad \text{(reversible adsorption)} \qquad (6\text{-}3)$$

,where LAS is the occupied sites by the lactic acid. The adsorbed lactic then donates electron to the valance band of CdS, (“hole donation”). The holes will therefore oxidise lactic acid to form pyruvic acid (PA) and proton as:

$$LAS + 2\,h^+ \overset{k_2}{\rightarrow} PA + S + 2\,H^+ \qquad \text{(photooxidation reaction)} \qquad (6\text{-}4)$$

The released protons (2 H^+) would not contribute into the increase of pH, as discussed and shown in Chapter 5 , but rather they would form water with the hydroxyl ions produced from the water photoreduction. However, due to the small change in the hydroxyl concentration observed in the pH measurements during the reaction, as shown in Fig 5.6, equation (6-4) can be approximated to a first order reaction

mechanism. If the total amount of available surface adsorption sites by lactic acid is denoted with$[S]_{tot}$, the vacant sites $[S]$ can also be obtained as:

$$[S] = [S]_{tot} - [LAS] \quad (6\text{-}5)$$

A pseudo- steady state hypothesis of the reaction rate is applied to the surface occupied sites by lactic acid (as described by Ollis in 2005 [51]), assuming $\frac{d[LAS]}{dt} = 0$ as:

$$\frac{d[LAS]}{dt} = k_1[LA][S] - k_{-1}[LAS] - k_2[LAS] = 0 \quad (6\text{-}6)$$

, where $k_1[LA][S]$ represents adsorption rate of lactic acid with adsorption constant of $k_1(\mathrm{mol}^{-1}\mathrm{s}^{-1})$, $k_{-1}[LAS]$ represents desorption rate of lactic acid with desorption constant of $k_{-1}(\mathrm{litre}^{-1}\mathrm{s}^{-1})$, and $k_2[LAS]$ represents product rate (pyruvic acid) formation with product formation constant of k_2(is explained in the following section). By substituting Eq. (6-5) into (6-6) and solving for $[LAS]$, we arrive at:

$$[LAS] = \frac{k_1[LA][S]_{tot}}{k_1[LA]+k_{-1}+k_2} \quad (6\text{-}7)$$

Re-arrangement of Eq. (6-7) results in:

$$[LAS] = \frac{\frac{k_1}{k_{-1}+k_2}[LA][S]_{tot}}{1+(\frac{k_1}{k_{-1}+k_2})[LA]} \quad (6\text{-}8)$$

, where $\frac{k_1}{k_{-1}+k_2}$ is termed as $K_{a,app}$. $K_{a,app}$ is the apparent adsorption constant representing that lactic acid adsorption/desorption rate is affected by the product formation. In Eq. (6-8), $[S]_{tot}$ can be approximated to 1, if the equation is expressed by surface coverage of lactic acid, θA, as;

$$[\theta_A] = \frac{\frac{k_1}{k_{-1}+k_2}[LA]}{1+(\frac{k_1}{k_{-1}+k_2})[LA]} = \frac{K_{a,app}\,[LA]}{1+K_{a,app}\,[LA]} \quad (6\text{-}9)$$

As the rate determining step is by the photooxidation step, see Eq. (6-4), the product formation rate from the holes can be described as:

$$r_{product-holes} = k_2[\theta_A] \quad (6\text{-}10)$$

The substitution of Eq. (6-9) in (6-10) results in:

$$r_{product-holes} = k_2\left(\frac{\frac{k_1}{k_{-1}+k_2}[LA]}{1+(\frac{k_1}{k_{-1}+k_2})[LA]}\right) \quad (6\text{-}11)$$

As suggested by Ollis in 1990 [52], the product formation constant k_2 is a function of absorbed radiative flux, I, by the catalyst within the reactor as; $k_2 = k'I^{\alpha}$. The constant of $k'$is the proportionality constant and α is the light absorbing parameter that varies between 0.5 and 1. Therefore, Eq. (6-11) will be presented as:

$$r_{product-holes} = k'I^{\alpha}\left(\frac{[LA]}{\frac{k_{-1}+k'I^{\alpha}}{k_1}+[LA]}\right) \quad (6\text{-}12)$$

It is assumed that the rate of hydrogen production by electrons are equal to the rate of product formation by the holes, therefore $r_{product-holes}$= r_{H2}, where the expression for the rate of hydrogen production will be as:

$$r_{H_2} = k'I^{\alpha}\left(\frac{[LA]}{\frac{k_{-1}+k'I^{\alpha}}{k_1}+[LA]}\right) \quad (6\text{-}13)$$

This expression accounts for the absorbed radiative flux from only one LED light, so incorporation of total received radiative fluxes from all LED lights, G, in this expression will result in the final expression:

$$r_{H_2} = k'G^{\alpha}\left(\frac{[LA]}{\frac{k_{-1}+k'G^{\alpha}}{k_1}+[LA]}\right) \quad (6\text{-}14)$$

,where r_{H_2} is the rate of hydrogen production (µmol/s), $[LA]$ is lactic acid concentration(M), k' is the proportionality constant ($m^2 litre^{-1} J^{-1}$) and G^{α} is the total received radiative fluxes from all lights (W m^{-2} nm^{-1}) and α is the light absorbing parameter. The hydrogen production rate produces two limiting cases; one when the total radiative flux on the reactor wall is high with α =0.5 and one when it is low α =1[51,52]. The total radiative flux, G^{α}, is a function of photocatalyst particles' positions inside the photoreactor and the angle of receiving photons, leading to an inhomogeneous distribution of radiative flux absorbed by the particles inside the reactor, with maximum values near the irradiated wall (where the lights are

positioned) and negligible values towards the centre. This issue will elaborate in the following section.

6-3 Radiation field modelling

The radiation distribution in the photoreactor system with 10 visible LED lights is modelled by the approach previously developed by G. Palmisano [62] but for 6 UV-lights. The LED lights surrounding the reactor vessel were placed on a level that a complete coverage of the reaction solution occurred. Therefore, there is no gradients in the radiative flux in the vertical direction and change of flux is only considered in the cross-section of the cylindrical reactor. For each particle positioned in that area, contribution of the radiative flux from all 10 LED lights accounts for the total received fluxes. The radiative flux from each LED absorbed by an irradiated particle is evaluated by the radiative transfer equation (RTE), which expresses the radiation energy balance at a certain wavelength (λ) and given propagation direction (Ω). The RTE gives information of how the spatial intensity variation depends on the particle light absorption, particle emission and the two types of particle scattering (in-scattering and out-scattering). The complete form of the RTE can be seen in Eq. (6-15)

$$\frac{dI_{\Omega,\lambda}}{dx} = -k_\lambda I_{\Omega,\lambda} + \varepsilon I_{bb,\lambda} - sI_{\Omega,\lambda} + \frac{S}{4\pi}\int I_{\Omega,\lambda}\phi(\Omega',\Omega)\,d\Omega' \quad (6\text{-}15)$$

RTE = - (absorption) + (emission) - (out-scattering) + (in-scattering)

, where $\frac{dI_{\Omega,\lambda}}{dx}$ describes changes of light intensity (which is directional and wavelength dependant) over dx (which is the spatial coordinate along Ω). In Eq. (6-15), the first term represents absorption of the particle with light absorption coefficient k (cm^{-1}) and the second term represents emission of the particle, with emissivity of ε (unit less) and black body light intensity $I_{bb,\lambda}$ ($W\ m^{-2}\ nm^{-1}$). The third term represents light scattering from the particle with scattering coefficient s (cm^{-1}), which takes away photon energy from the propagation direction. The last term, in-scattering, describes the probability of light absorption and then its scattering in a particular direction

originating from scattering from other particles within the reactor with $\phi(\Omega', \Omega)$ as a scattering phase function that is angular distribution of scattered radiation [47]. The complete form of the RTE involves a set of integrated-differential equations, where rigorous numerical procedures are required for obtaining the solution. The numerical solution of RTE can be eased if it is considered with specific assumptions such as negligible emission contribution, as the emission would have too high wavelengths to excite any of the particles. The final RTE approximation based on the Schuster-Schwarzschild isotropic scattering approach [160], consists of dividing the radiation field of two oppositely directed radiation fluxes; I_λ (in the positive propagation direction) and J_λ(in the negative propagation direction), where the effect of absorption and scattering terms of the RTE (Eq. (6-15)) can be described as:

$$\frac{dI_\lambda}{dx} = -(k_\lambda + s_\lambda)I_\lambda + s_\lambda J_\lambda \tag{6-16}$$

$$\frac{dJ_\lambda}{dx} = -(k_\lambda + s_\lambda)J_\lambda + s_\lambda I_\lambda \tag{6-17}$$

If it is assumed that the radiation flux in the negative propagation direction, J_λ, is negligible, an approximate solution to Eq. (6-16), as suggested by Palmisano et al.[62], can be presented as:

$$\frac{I_\lambda}{I_0} = \left(1 - {R_\infty}^2\right)\exp\left(-2bs^*C_{cat}L\right) \tag{6-18}$$

,where I_0 is the incident radiative flux density at the reactor wall (W m^{-2} nm^{-1}), R_∞ is the diffuse reflectance of the catalyst (Pt/CdS)(dimensionless), C_{cat} is the catalyst concentration (g cm^{-3}), s^* is scattering coefficient per unit catalyst concentration (cm^2 g^{-1}), L is the light path length (cm) and b is $\sqrt{\left(1 + \frac{k^*}{s^*}\right)^2 - 1}$.

The wavelength-dependent diffuse reflectance, R_∞, and the scattering coefficient of the particles, s^*, are determined from spectrophotometric measurements at the absorption band of the photocatalyst (Pt/CdS), coinciding with the reactor LED's output. Here R_∞ was in a range of 0.16-017, s^* was in a rage of 1-2 ×10^4 cm^2 g^{-1} and k^* was in the range of 0.16-0.17×10^4 cm^2 g^{-1}. The light path length, L, of each LED to a photocatalyst particle positioned in the cross-section of the reactor, is obtained by

deriving the geometrical position of the particle in the reactor with regards to the other lights. If a particle is positioned in the reactor with radius R, where the reactor itself is positioned in the distance r_0 from one LED light, the particle coordinate $(L_i\,,\theta_i)$ can be defined as seen in Fig 5.1. For that particle coordinate, $i = 1\ldots10$ denotes number of lights, θ_i denotes the angle of receiving photons to the particle by the light i, which varies between $-\theta_0$ and $+\theta_0$, and L_i is the corresponding distance between the particle and the reactor wall. The geometrical derivation of all θ_i and L_i , for $i = 2\ldots10$ are presented in Appendix (A), where $(L_1\,,\theta_1)$ is chosen as the reference point.

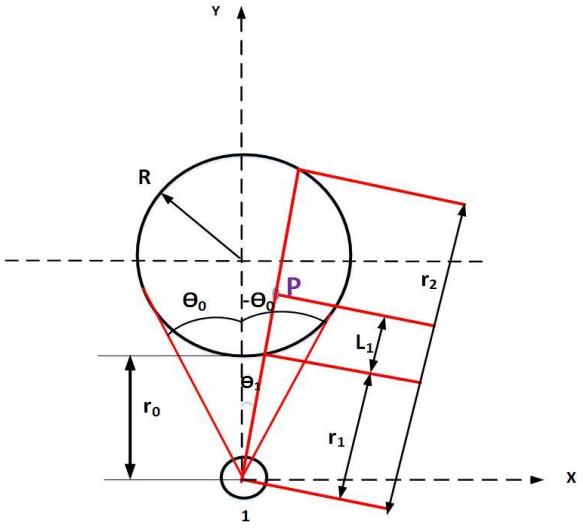

Figure 6. 1 Derivation of the geometrical coordinate $(L_i\,,\theta_i)$ for particle, P, inside a reactor with radius, R, irradiated by one lamp.

Therefore, the radiative flux density of Eq. (6-18) for light i and a particle with coordinate $(L_i\,,\theta_i)$ at wavelength (λ), is evaluated using Eq. (6-19):

$$I_\lambda\,(L_i\,,\theta_i)\;=I(0,\theta_i)\left(1-{R_\infty}^2\right)\exp\,(-2bs^*C_{cat}L_i) \qquad (6\text{-}19)$$

, where $I(0,\theta_i)$ is the radiative flux density on the reactor wall in the direction of radiation. The term $I(0,\theta_i)$ can be substituted with the term $I(0{,}0)\frac{r_0}{r_i}$ to adjust for the radiation intensity at r_i [160], where the radiative flux density at coordinate (0, 0), $I(0{,}0)$, was measured by the spectrometer (GL Spectis 1.0). In Fig 6.2 (A), the 3D-representation of the radiative flux density distribution by one LED light on a particle with the coordinate $(L_1\,,\theta_1)$ can be seen as $I_\lambda(L_i\,,\theta_i)$, where the maximum flux is

observed closest to the LED lamp position. To obtain the overall radiative flux density from all 10 LED lights on that chosen particle, the individual contributions from all lights are added up, $G_\lambda(L_1, \theta_1)$, as seen in Fig 6.2(B).

Having calculated $G_\lambda(L_1, \theta_1)$ and substituted its values into Eq.(6-14), the theoretical hydrogen rate expression results in:

$$r_{H_2} = k' G_\lambda (L_1, \theta_1)^{\alpha} \left(\frac{[LA]}{\frac{k_{-1} + k' G_\lambda (L_1, \theta_1)^{\alpha}}{k_1} + [LA]} \right) \tag{6-20}$$

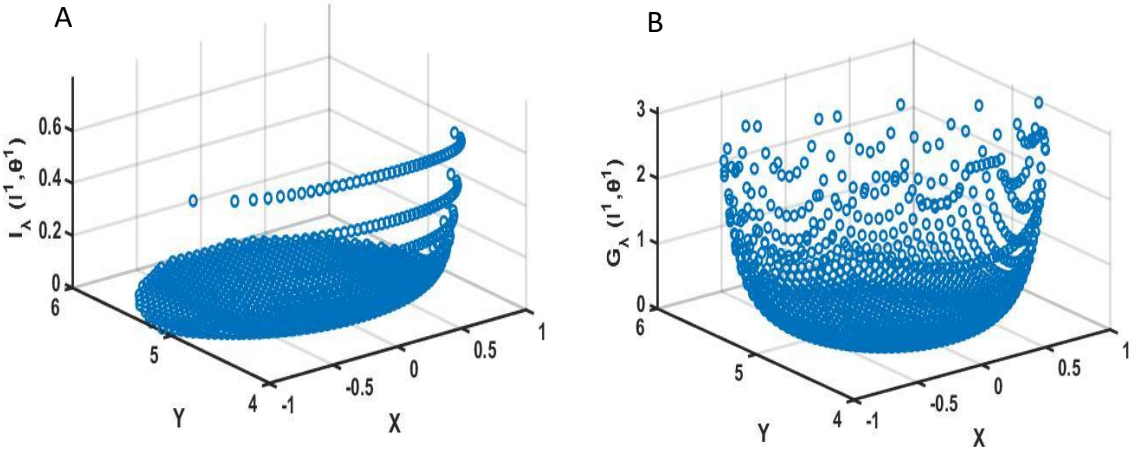

Figure 6. 2 Three-dimensional representation of the radiative flux density distribution created by MATLAB at coordinate (L_1, θ_1) for; (A) 1 LED light and (B) 10 LED lights.

Note that the experimental rates of hydrogen production were obtained for the entire reactor volume, whereas Eq. (6-20) represents the theoretical rate of hydrogen for a cross-section of the reactor at the coordinate (L_1, θ_1), and therefore Eq. (6-20) was integrated over the whole reactor volume as:

$$r_{H_2}{}^{v} = k' k_1 [LA] \int G_\lambda (L_1, \theta_1)^{\alpha} \left(\frac{1}{k_{-1} + k' G_\lambda (L_1, \theta_1)^{\alpha} + k_1 [LA]} \right) dv \tag{6-21}$$

By substituting dv with $dS.h$, where $dS = (r_1 + L) dL\, d\theta$ is the area of the cross-section and h is the reactor solution height within the reactor, we have:

$$r_{H_2}{}^{v} = k' k_1 [LA] h \int_0^{r_2 - r_1} \int_{-\theta_0}^{+\theta_0} G_\lambda (L_1, \theta_1)^{\alpha} \left(\frac{1}{k_{-1} + k' G_\lambda (L_1, \theta_1)^{\alpha} + k_1 [LA]} \right) (r_1 + L) dL\, d\theta \tag{6-22}$$

,where the angle θ_0 and path length, L_1 , seen in Fig 5.1, can be expressed as [62]:

$$\theta_0 = cos^{-1}\left(\frac{\sqrt{2Rr_0+{r_0}^2}}{R+r_0}\right) \quad (6\text{-}23)$$

and the boundary conditions of L_1 varies between r_1 and $r_2$as:

$$r_1 = cos\theta_1(R+r_0) - \sqrt{cos^2\theta_1(R+r_0)^2 - r_0^2 - 2Rr_0} \quad (6\text{-}24)$$

$$r_2 = cos\theta_1(R+r_0) + \sqrt{cos^2\theta_1(R+r_0)^2 - r_0^2 - 2Rr_0} \quad (6\text{-}25)$$

The rate of hydrogen production from Eq. (6-22) needs to be converted to μmol/s to be consistent with the empirical rate.

6-4 Model results

The variable parameters in the 64 experimental runs, as shown in Table 6.1, were different catalyst loadings (5% Pt-CdS), different lactic acid concentrations and various incident flux intensities during the reaction. All experimental runs were previously presented in detail in Chapter 5. The theoretical hydrogen rate from the model, Eq. (6-22), was fitted to the experimental H_2 rate to obtain α, k_1, k_{-1} and k', by a least-square best fitting procedure, using a non-linear derivative-free optimization method in MATLAB. The objective function ($O.F.$), which is the sum of squared difference between the experimental and the calculated values of H_2 production rate, was then minimised as:

$$O.F. = \sum_1^{64}(H_2^{exp} - H_2^{cal})^2 \quad (6\text{-}26)$$

The obtained parameters for the 64 reaction runs are shown in Table 6.2. The comparisons between the empirical and predicted H_2 rates at different lactic acid concentrations, incident flux intensities and catalyst loadings can be seen in Fig 6.3 (a, b, c). The cumulative hydrogen for the same reaction conditions are presented in Fig 6.4 (a, b, c). Both set of figures show a satisfactory agreement between the model and the experimental data points. In Fig 6.3 (a), the model is compared with the experimental results when the initial concentration of lactic acid varied between 0.66-3 M at a fixed incident flux of 2.6 W/m^2 and a catalyst loading of 0.0006 g/cm^3.

Table 6. 1 Photocatalytic reaction runs at different catalyst loadings, lactic acid concentrations and incident fluxes.

Run	Cat. loading (g/cm^3)	[LA] (M)	Incident flux at $I(0,0)$ (W/m^2)	Run	Cat. loading (g/cm^3)	[LA] (M)	Incident flux at $I(0,0)$ (W/m^2)
1	0.00060	2.64	2.60	33	0.00060	2.64	1.20
2	0.00060	2.41	2.60	34	0.00060	2.42	1.20
3	0.00060	2.04	2.60	35	0.00060	2.03	1.20
4	0.00060	1.80	2.60	36	0.00060	1.90	1.20
5	0.00060	1.74	2.60	37	0.00060	1.80	1.20
6	0.00060	1.60	2.60	38	0.00060	1.74	1.20
7	0.00060	1.64	2.60	39	0.00060	1.68	1.20
8	0.00060	1.51	2.60	40	0.00060	1.58	1.20
9	0.00044	2.65	2.60	41	0.00060	2.31	0.30
10	0.00044	2.43	2.60	42	0.00060	2.22	0.30
11	0.00044	2.02	2.60	43	0.00060	2.12	0.30
12	0.00044	1.94	2.60	44	0.00060	2.00	0.30
13	0.00044	1.81	2.60	45	0.00060	1.93	0.30
14	0.00044	1.70	2.60	46	0.00060	1.65	0.30
15	0.00044	1.64	2.60	47	0.00060	1.43	0.30
16	0.00044	1.56	2.60	48	0.00060	1.41	0.30
17	0.00020	2.55	2.60	49	0.00060	1.30	2.60
18	0.00020	2.44	2.60	50	0.00060	1.28	2.60
19	0.00020	2.04	2.60	51	0.00060	1.01	2.60
20	0.00020	1.91	2.60	52	0.00060	0.98	2.60
21	0.00020	1.84	2.60	53	0.00060	0.91	2.60
22	0.00020	1.72	2.60	54	0.00060	0.86	2.60
23	0.00020	1.64	2.60	55	0.00060	0.85	2.60
24	0.00020	1.49	2.60	56	0.00060	0.70	2.60
25	0.00007	2.55	2.60	57	0.00060	0.63	2.60
26	0.00007	2.45	2.60	58	0.00060	0.62	2.60
27	0.00007	2.22	2.60	59	0.00060	0.5	2.60
28	0.00007	2.04	2.60	60	0.00060	0.48	2.60
29	0.00007	1.94	2.60	61	0.00060	0.44	2.60
30	0.00007	1.83	2.60	62	0.00060	0.42	2.60
31	0.00007	1.74	2.60	63	0.00060	0.30	2.60
32	0.00007	1.44	2.60	64	0.00060	0.25	2.60

Table 6. 2 Obtained model parameters.

k_1	0.0907
k_{-1}	0.0877
k'	0.1596
α	0.52

The experimental rate of H_2 production increases non-linearly with increasing lactic acid concentration and starts to levelling-out at 2.66 M with a H_2 generation rate of 0.12 µmol/s. The model prediction agrees well with the experimental non-linear behaviour, implying that the adsorbed lactic acid on the catalyst surface sites reaches a limit value where no more adsorption sites would be available by the increased lactic acid concentration (as reflected in the developed Langmuir Hinshelwood adsorption mechanism above).

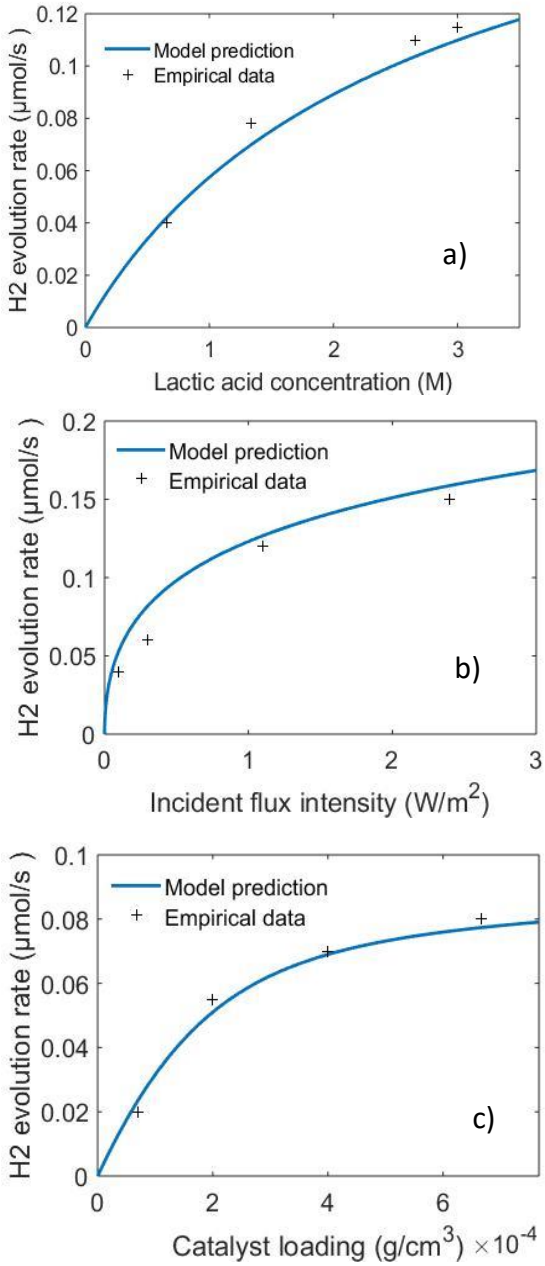

Figure 6. 3 Model predicted H_2 rate (blue line) vs. experimental rate (+), when lactic acid concentration (a), incident flux intensity (b) and loading of catalyst (c) were varied.

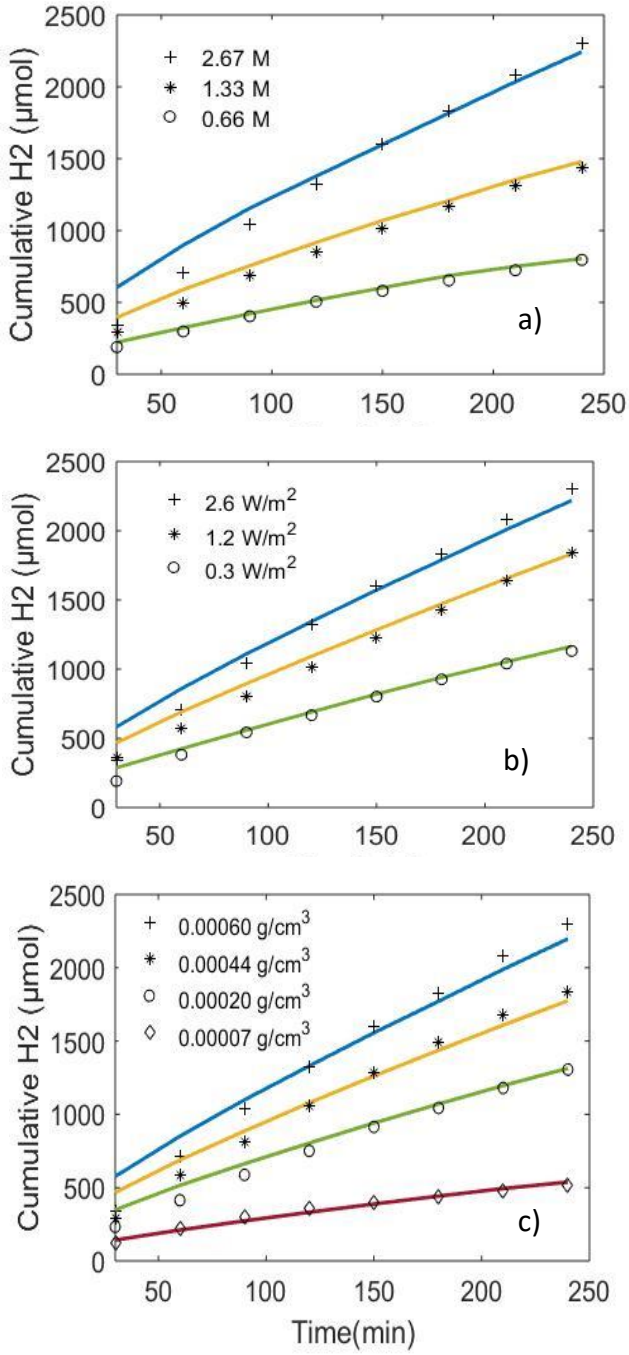

Figure 6. 4 Model predicted cumulative H_2 production (solid lines) vs. experimental H_2 production after 4 hours irradiation by varying lactic acid concentration (a), incident flux intensity (b) and catalyst loading (c).

Lactic acid did not absorb radiation from the LED (as shown in UV-Vis in Chapter 5) and therefore did not affect the irradiation model segment. The cumulated H_2 over time at various lactic acid concentrations, seen in Fig 6.4 (a), shows a gradual non-linear increase in the cumulative hydrogen production from 729 µmol to 2300 µmol H_2 after 4 hours irradiation. In Fig 6.3 (b), the model was compared with

experimental data when the incident flux varied between 0.2 W/m^2 to 2.6 W/m^2 at a fixed initial lactic acid concentration of 2.66 M and a catalyst loading of 0.0006 g/cm^3. According to this figure, the hydrogen generation rate is proportional to the incident flux until levelling out at the higher incident fluxes of 2.6 W/m^2, where maximum rate of hydrogen production of 0.15 µmol/s was obtained. The levelling-out of the reaction rate by the increased flux was probably due to the absorption limit of photocatalytic slurry at maximum incident flux of the light, beyond which no further absorption by the catalyst particles was observed. The results are completely in accordance with cumulative H_2 generation, Fig 6.4 (b), where rate of H_2 production also undergoes a gradual increase.

Figure 6.3 (c) compares the model predictions with the experimental results when the catalyst loading varied between 0.0006 to 0.00007 g/cm^3 at a fixed incident flux of 2.6 W/m^2 and an initial lactic acid concentration of 2.66 M. The model agrees satisfactory with the experimental results and shows clearly a levelling-out toward higher particle loadings. This might be due to two factors; one is an exceeded vacant photocatalyst adsorption site limit for the lactic acid (as seen in the Langmuir Hinshelwood adsorption), and the other is the shielding effect which does not allow all particles to be evenly irradiated. The gradual increase in the hydrogen production rate is also confirmed in the cumulated hydrogen data over time, Fig 6.4 (c), where the maximum of 2300 µmol H_2 after 4 hours irradiation was obtained for the catalyst loading of 0.0006 g/cm^3.

6-5 Conclusion

A descriptive hydrogen mathematical model including both adsorption and irradiation mechanisms for an externally LED-driven photoreactor was presented and validated against experimental results. The batch slurry photoreactor was externally irradiated by 10 visible light-emitting diodes (LED), surrounding the circumference of the cylindrical reactor. The irradiation mechanism part of the model was based on an approximate solution of the Radiative Transport Equation (RTE) with the derivation of the geometrical position of the particles in the cross-section of the reactor with regards to the lights. This enabled the calculation of the

total visible radiative flux density received from all 10-LEDs by the Pt/CdS particles positioned in that special area of the reactor. Integration of total calculated radiative flux density over the whole reactor volume accounted for the total received photon fluxes of the particles positioned in the said reactor volume. The irradiation mechanism of the descriptive model further increased its accuracy by incorporating the spectrophotometric experimental measurements of the Pt/CdS' scattering and absorption coefficients within the LED's output range of 410-500 nm. The adsorption mechanism of the model was based on a pseudo-steady state Langmuir-Hinshelwood adsorption mechanism, where the surface adsorbed lactic acid was oxidised to pyruvic acid (via electron transfer) while simultaneously the adsorbed water was reduced to hydrogen (via electron transfer).

The developed hydrogen model was then successfully validated against experimental measured rate of hydrogen production using different catalyst loadings, lactic acid concentrations, and incident radiation fluxes. The unknown model parameters of α, k_1, k_{-1} and k' were obtained by a least-square fitting procedure using a non-linear derivative-free optimization method in MATLAB. All experiments were conducted to their limiting values which could be concluded well by the mathematical model. The satisfactory agreement between the model and empirical results showed the model capability to predict behaviour of any photocatalytic reactor in a wide range of operating conditions. The model also allowed analysis of flux distribution depending on the number of switched-on lamps being used, as long as their position was not changed. The main advantage of the developed mathematical model was to predict reaction results with minor computational effort, without employing any commercial software. The information obtained from the model could be used for design and scale-up of any photocatalytic batch reactor system regardless of type of radiation or reactor size.

Chapter 7 Results and Discussions: Photocatalytic Hydrogen Production in the Sulphur-Ammonia Thermochemical Cycle

7-1 Introduction

In this Chapter, a comprehensive investigation on the photocatalytic hydrogen producing step of the sulphur–ammonia thermochemical cycle is presented. The aim here was to realistically investigate a replacement of the traditional electrolyser unit with a solar driven hydrogen generation unit in a solar driven thermochemical cycle using ammonium sulphite as the working fluid. The chapter will draw conclusion from previous result chapters (Chapter 4, 5 and 6) and bring forward a plausible suggestion for this replacement.

First the reaction mechanism of photocatalytic degradation of ammonium sulphite is described in detail in section 7-2. Then the various operational parameters using the novel CoP/CdS catalyst for the hydrogen part in the cycle will be evaluated in section of 7-3. Next, in section 7-4, the H_2 performance of CoP/CdS and Pt/CdS composites will be compared when using the cycle fluid ammonium sulphite solution. This will be followed by an adapted hydrogen prediction model in section 7-5, using ammonium sulphite as the photolyte together with CoP/CdS as the photocatalyst in an upscaled reactor size with a relevant visible light arrangement. Finally, a feasibility study for the upscaling the thermochemical cycle using the suggested hydrogen producing step will be presented in section 7-6.

7-2 Photocatalytic degradation of ammonium sulphite

In the photocatalytic step of the sulphur–ammonia thermochemical cycle, hydrogen gas is produced on the catalyst surface upon absorption of incoming photon energy with the simultaneous oxidation of ammonium sulphite. For a simultaneous water

reduction and ammonium sulphite oxidation, there are four important rate determining steps; (i) absorption of photons with energy equal or higher than the CdS electron band gap (ii) dissociation of the excitons and their diffusion to the surface (iii) ammonium sulphite adsorption on CdS surface, and (iv) desorption of the formed products. For the successful redox reactions on the photocatalyst surface, initial experiments were undertaken to assure ammonium sulphite did not absorb the incoming light inside the reactor, ammonium sulphite was pre-adsorbed on the catalyst surface and the successful desorption of the reaction products occurred.

First UV-Vis spectroscopy was used to investigate the ammonium sulphite light absorption between 190-800 nm using an initial 2.6 M aqueous solution in a cuvette; at 0 h, 3 h and 25 h reaction time, as seen in Fig 7.1. At 0 h, the predominating spectra showed the signature of the SO_3^{2-} absorbance spectra which absorbs UV light < 275 nm. However, some traces of SO_4^{2-} was observed in the ammonium sulphite solution due to the partly oxidation of ammonium sulphite during solution preparation and storage, which was also shown in the ion chromatography section that follows. According to Huang et al. [90], who compared 0.5 M Na_2SO_4 with 0.5 M Na_2SO_3 in a UV-Vis study, SO_4^{2-} ions absorbed only at high energetic UV light <200 nm. At 3 h of reaction time, the absorbance spectra was blue-shifted with a more distinct slope and a reduced absorption intensity, excepting toward 200 nm. This indicates an oxidation to SO_4^{2-} as well as some formed intermediates, which will be discussed in the following section.

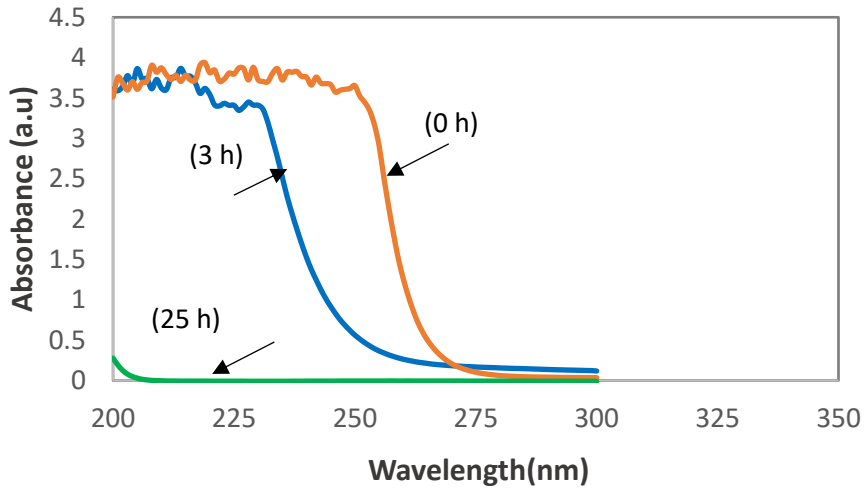

Figure 7. 1 UV-Vis absorption spectra of the ammonium sulphite photocatalytic degradation, at 0 h(orange), 3 h (blue) and 25 h (green) reaction time.

At the end of the reaction, 25 h, (green spectra in Fig 7.1), only the signature of SO_4^{2-} was observed, indicating that all 2.6 M SO_3^{2-} was consumed and oxidised. It was therefore concluded that no compounds in the solution would absorb the LED (or visible) light and that no direct photolysis would occur. To support this finding, Ion chromatographic (IC) measurement was conducted before (0 h) and after (25 h) of the photocatalytic reaction to further investigate the photoreaction path of ammonium sulphite. In Fig 7.2, both SO_3^{2-} and SO_4^{2-} ions are shown with R=12.08 and R=13.12 respectively before the photocatalytic reaction (0 h).

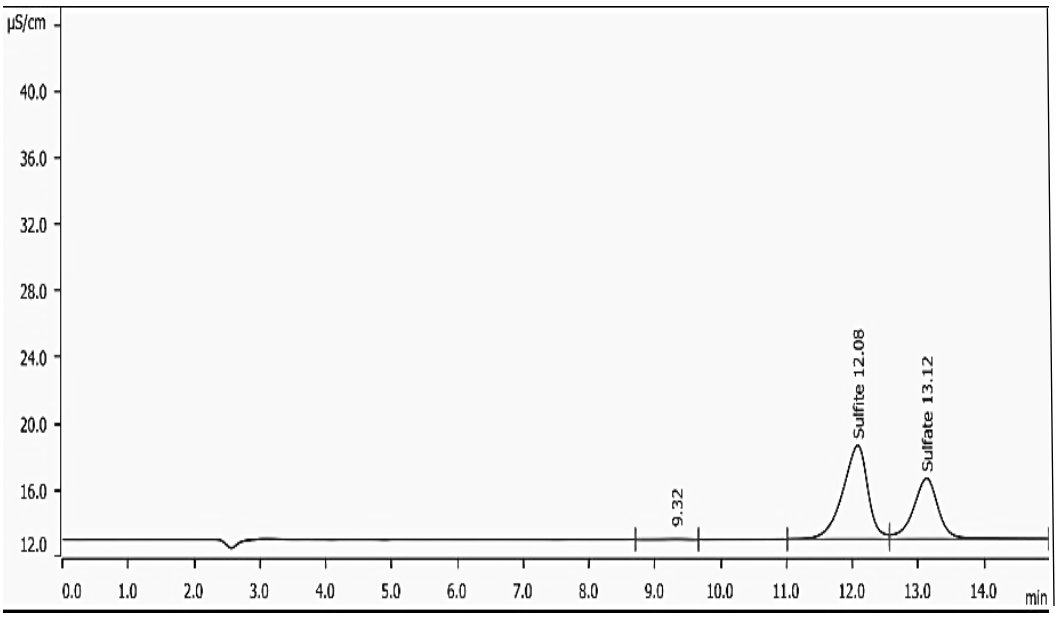

Figure 7. 2 Ion chromatogram of 2.66 M of aqueous solution at pH =8.7 taken before the photocatalytic reaction (0 h).

This further supports the fact that some SO_3^{2-} are converted to SO_4^{2-} when preparing the solution or as an effect to air exposure, as also reported by Huang et al. [90]. However, at the end of the photocatalytic reaction, only the SO_4^{2-} peak was detected, as shown in Fig 7.3, which is in an agreement with the UV-Vis findings. To investigate the ammonium sulphite adsorption on the CoP/CdS surface, FTIR spectroscopy was used. In Fig 7.4, a bare CdS sample was first compared with a 5 wt. % CoP loaded CdS sample and then the same CoP/CdS sample was immersed in 2.67 M ammonium sulphite solution, washed and dried prior the FTIR measurements. For the bare CdS sample, the bands located at 642, 974, 1040 and 1402 cm^{-1} can be ascribed to the vibrational modes from the Cd–S bond, with a broad band at 1566 cm^{-1} as a result of the adsorbed surface water, see more in Chapter 5.

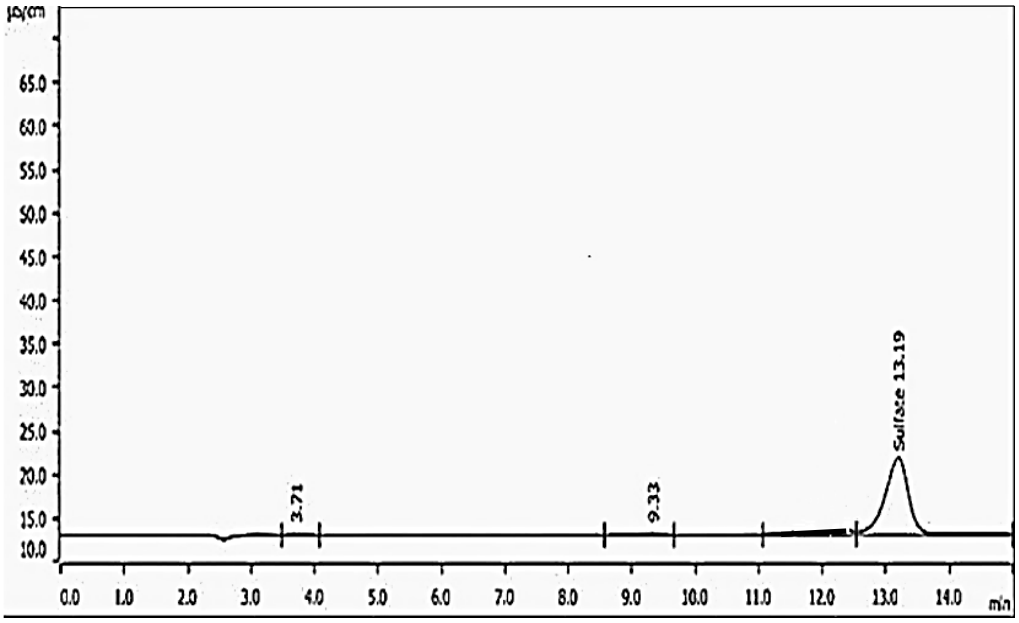

Figure 7. 3 Ion chromatogram of 2.66 M of aqueous solution at pH =8.9 taken after the photocatalytic reaction (25 h).

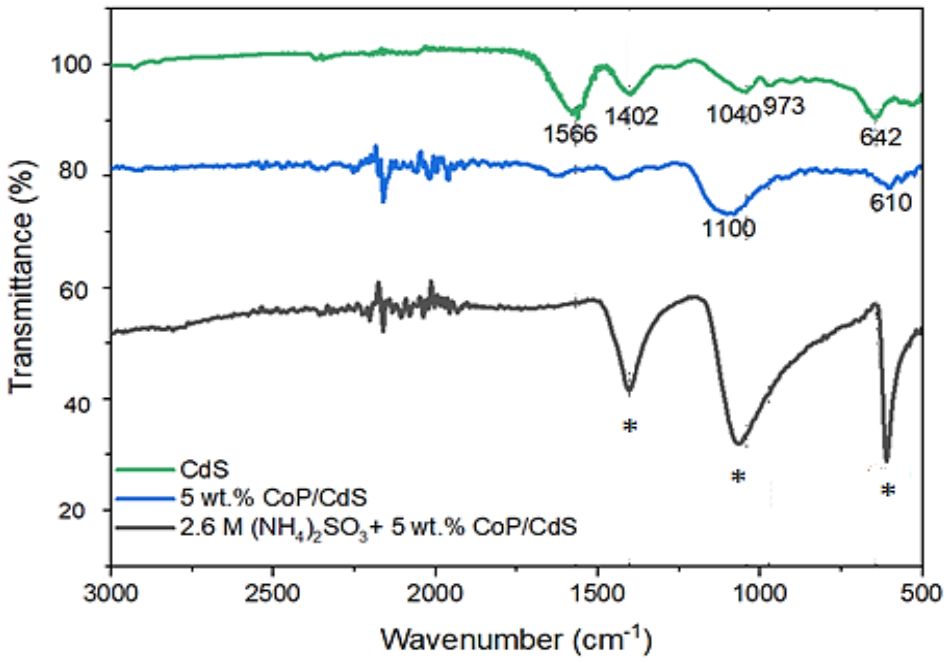

Figure 7. 4 FTIR spectrum of pure CdS (green), 5 wt. % CoP/CdS (blue) and 5 wt. % CoP/CdS pre exposed to 2.67 M ammonium sulphite (black). The asterisks (*) show ammonium sulphite IR bands.

For the 5% CoP/CdS sample, the CdS peaks were found to be slightly shifted and got broader. This might be due to the effect of the forceful sonication when adding the CoP co-catalyst to CdS. The energetic sonication will produce less particle agglomerates and then separation (or liberate) into very small sub 17 nm CdS particles (as determined from the XRD) ,with a high-volume ratio of broken bonds and vacancies close to its surface, where the CoP particles are adhered during the sonication. The black spectra in Fig 7.4 was for the 5% CoP/CdS particles exposed to the ammonium sulphite. Mattias Hallquist [161] reported that free ammonium sulphite had four distinctive features in the IR spectrum; two sulphite bands at 620 cm^{-1} and 1115 cm^{-1}, one N-H bending vibration at 1400 cm^{-1} and one N-H stretching vibration at 2500 cm^{-1}, where the first three are marked with an asterisk(*) in Fig 7.4. From the FTIR study it was concluded that the ammonium sulphite was physisorbed on the surface not chemisorbed as the peaks of the sample immersed in the ammonium sulphite corresponded to free ammonium sulphite species. This can be compared with the chemisorbed lactic acid discussed in Chapter 5, where the free lactic acid peak completely disappeared.

To evaluate purity of the produced hydrogen, gas chromatography was conducted. Gas samples from the reactor were taken and injected manually into the GC apparatus. Fig 7.5 shows the result of the GC analysis and Table 7.1 shows the corresponding retention times and full peak widths at half maximum (FWHM) of the detected gases and the matching standards. Three peaks corresponding to hydrogen, oxygen and nitrogen were detected in this analysis, where the oxygen and nitrogen peaks originated from the air due to the off-line sampling. Therefore, the only gas evolved from the reaction was pure hydrogen with the retention time of 2.26 min and FWHM of 0.030 min. The detected air presence was further confirmed by a dry run using the same gas-tight syringe, where it showed that no hydrogen peak and only peaks of oxygen and nitrogen with the retention times and peak heights matched that of the air signatures recorded during the H_2 gas analysis (results are not presented here). Therefore, it was finally concluded that only hydrogen gas was liberated from the photocatalytic reaction.

Table 7. 1 The detected retention times and peak widths by the GC.

Peak name	Reaction time (min)	FWHM (min)
Hydrogen	2.26	0.030
Oxygen	3.10	0.035
Nitrogen	5.32	0.033
Standard Gases		
Hydrogen (99%)	2.12	0.027
Oxygen(99%)	3	0.033
Nitrogen(99%)	5.26	0.030

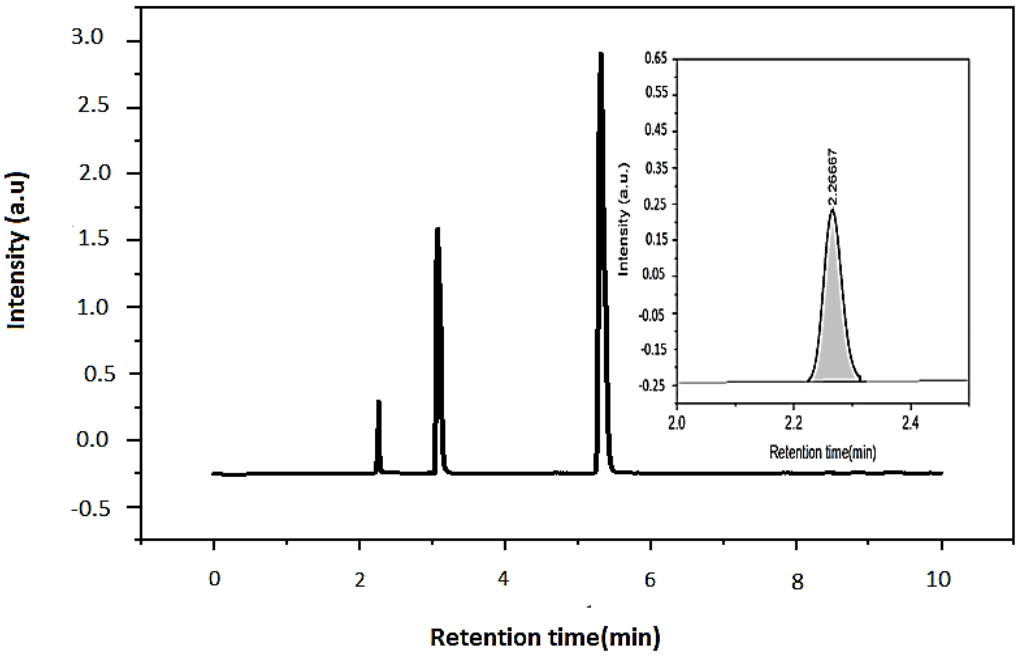

Figure 7. 5 GC analysis of a photocatalytic gas product sample, showing only H_2 peak as the liberated product (see insert) when 5 wt. % CoP/CdS was used in ammonium sulphate photocatalytic reaction.

To understand chemistry of the reaction, all possible reactions and dissociations were identified as:

$$(NH_4)_2SO_3 \leftrightarrow {NH_4}^+ + {SO_3}^{2-} \quad (7\text{-}1)$$

The water molecules were also dissociated as:

$$2H_2O \leftrightarrow OH^- + H_3O^+ \quad (7\text{-}2)$$

Therefore, the possible reactions between the available ions in the photocatalytic solution were proposed as:

$$SO_3^{2-} + H_3O^+ \leftrightarrow HSO_3^- + H_2O \quad (7\text{-}3)$$

$$HSO_3^- + H_3O^+ \leftrightarrow SO_2(g) + 2H_2O \quad (7\text{-}4)$$

$$NH_4^+ + OH^- \leftrightarrow NH_3(g) + H_2O \quad (7\text{-}5)$$

Eq. (7-4) and (7-5) are less likely to proceed as the GC analysis of the gaseous products only confirmed H_2 formation (at the detection level of the GC technique). This can be related to a study by Muradov et al. [162] who analysed the gaseous products from an ammonium sulphide photocatalytic reaction by in-situ GC analysis and also found no traces of SO_2(g) or NH_3 (g). This means the equilibrium of Eq. (7-3) was heavily left-shifted towards SO_3^{2-}. Earlier it was confirmed by the IC measurements that SO_4^{2-} was present alongside SO_3^{2-} in the solution prior to the photocatalytic reaction. Here, the suggested conversion pathways of SO_3^{2-} to SO_4^{2-} are explained and shown in Fig 7.6. In the figure, the pathway (1), it can be seen how the SO_3^{2-} ions react with the hydroxyl ions (from the water photoreduction or water dissociation) and then subsequently produce sulphate (SO_4^{2-}) ions and water in the solution. This reaction explains why small amount of SO_4^{2-} are present in the water solution *before* the reaction. In pathway (2), the weakly physiosorbed SO_3^{2-} ions (at high concentration) donate electrons to the valence band of the CdS to form SO_3^{2-} radicals. The half potential to for the SO_3^{2-}/SO_4^{2-} is +0.92 eV, which is less positive the valence band potential (hole potential) of CdS (+1.65 eV[156]), making an electron transfer from SO_3^{2-} possible, forming a reactive $\cdot SO_3^{2-}$ radical which would rapidly form $S_2O_6^{2-}$ as:

$$2\,SO_3^{2-} + 2h^+ \rightarrow 2\cdot SO_3^{2-} \quad (7\text{-}6)$$

$$2\cdot SO_3^{2-} \rightarrow S_2O_6^{2-} \quad (7\text{-}7)$$

The dithionate ($S_2O_6^{2-}$) ions would further react with the surface adsorbed hydroxyl ions and produce sulphate (SO_4^{2-}) ions and proton as:

$$S_2O_6^{2-} + 2\,OH^- \rightarrow 2\,SO_4^{2-} + 2\,H^+ \quad (7\text{-}8)$$

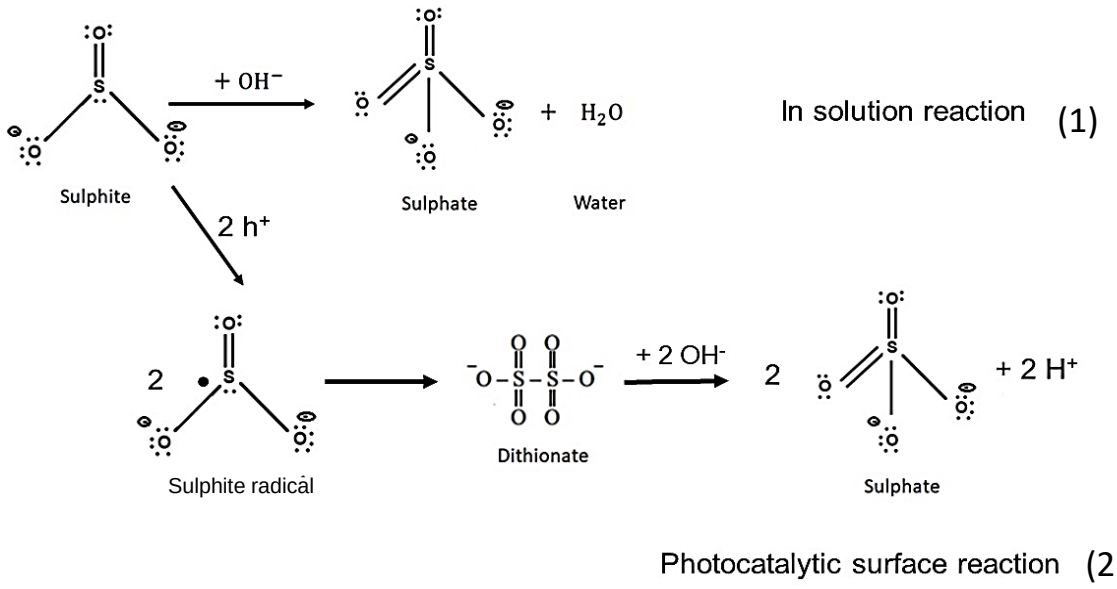

Figure 7. 6 Suggested SO_3^{2-} to SO_4^{2-} conversion reactions.

These suggested pathways are in an agreement with the related previous studies [90,163], where Ali T-Rassi's group in Florida analysed the photocatalytic oxidation of ammonium sulphite by HPLC and UV-Vis and found traces of dithionate ions as a suggested intermediate before the complete conversion to SO_4^{2-}. By looking at these two pathways, a pH drop over time is expected by both pathways. To investigate this, pH measurement was performed in a 25 h reaction run, alongside measurements of sulphite degradation and H_2 generation (at the incident flux of 6.5 W/m^2, initial ammonium sulphite concentration of 2.67 M, photocatalyst loading of 0.0006 g/cm^3 and temperature of 60 °C). According to Fig 7.7, the H_2 generation rate for the first 1300 min of photocatalytic reaction was a linear function of time, yielding a constant production rate of 55.39 μmol/min, followed by a levelling-off until 1500 min when the hydrogen production completely stopped. From the pH result, the insert in Fig 7.7, it can be seen that the initial pH of 8.7 increased with a high rate at the first 100 min, corresponding to a higher rate of sulphite degradation for the same time, and then stabilised at 8.87 > 16 hours run (1000 min). Despite the fact that the IC measurement was not continuously taken for the whole 25 h (1500 min), the IC measurement until 3 h and extrapolated to the one single measurement at 25 h, with the previous described UV-Vis analysis indicated that there were no sulphite ions present in the solution after 25 hours reactor run.

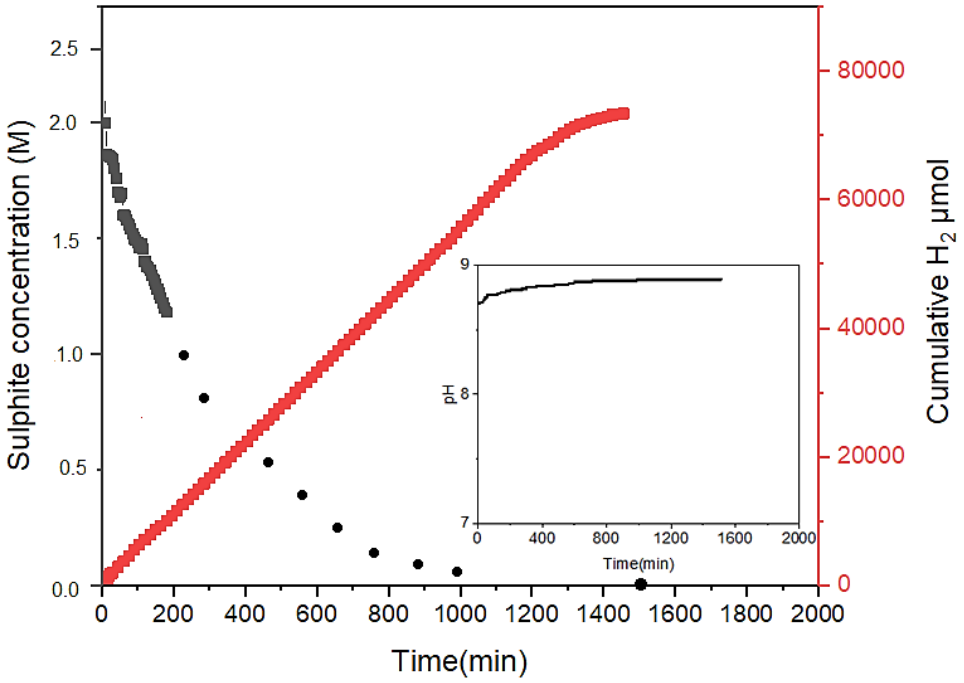

Figure 7. 7 Hydrogen generation over 25 h (red), compared with the IC measured sulphite concentration over 3 h(black). The black dots show predicted reducing trend for the sulphite ions toward its complete depletion, where at 25 h the concentration was measured by IC . The insert shows pH variation over a 25 h reaction run.

The increase of pH corresponded to a H^+ concentration change from 1.99 $\times 10^{-9}$ M to 1.58 $\times 10^{-9}$ M, where it remained constant after 1000 min until 1500 min measured reactor run time. The sulphite concentration dropped 0.8 M, from 2.6 M to 1.8 M during 3 h (180 min) of the reaction, and then to zero after 25 h. The 0.8 M (0.21 mol) drop for the first 3 h corresponded to a simultaneous H^+ decrease from 1.99 $\times 10^{-9}$ M to 1.94 $\times 10^{-9}$ M.

As a conclusion, the slight initial increase in the pH (increase of hydroxyl ions) proves a very fast water reduction rate $H_2O + 2e^- \rightarrow H_2 + 2\ OH^-$, as water (in the dissociated forms at pH 8.7) is readily adsorbed on the catalyst surface, promoting an efficient electron transfer straight from the start. On the contrary, sulphite ions are not strongly adsorbed on the surface, in addition that hole diffusion to the surface tend to be slower than the electrons, meaning that the photocatalytic oxidation route is expected to be apparently slower than the water reduction. These expected different reaction rates would therefore explain the small pH increase (up to 1000 min reaction run) before it stabilises, which is coincidence with the completion of the photocatalytic reaction and complete depletion of SO_3^{2-}. Note that the protons (2

H^+) released from the pathway (2) would not contribute into the change of pH or additional formation of H_2 gas (this will be confirmed in the kinetic modelling section, where experimental H_2 rate matches with the predicted H_2 rate), but rather they would form water with the hydroxyl ions produced from the photoreduction of water molecules.

The proposed overall photocatalytic reactions on the CdS-CoP catalyst surface, which will be used in the kinetic modelling section 7-5, are:

$$2\,H_2O\,(\leftrightarrow 2\,H^+ + 2\,OH^-) + 2\,e^- \rightarrow H_2 + 2\,OH^- \quad \text{water reduction} \qquad (7\text{-}9)$$

$$2\,SO_3{}^{2-} + 2\,OH^- + 2\,h^+ \rightarrow 2\,SO_4{}^{2-} + 2\,H^+ \quad \text{sulphite oxidation} \qquad (7\text{-}10)$$

7-3 Effect of operational parameters on the hydrogen generation

The photocatalytic hydrogen experiments were conducted at various CoP/CdS photocatalyst loading in the reactor, incident flux intensity, ammonium sulphite concentration and reaction temperature to investigate the effect of these operational parameters on the hydrogen evolution. Fig 7.8 shows the experimental set-up of the scaled-up photocatalytic reaction system, where a 1.57 Litre photoreactor (inner diameter 10 cm) was used with one outlet for the hydrogen gas (which was measured by the inverted burette), one outlet for the gas-sampling, one inlet for the argon pre-purging to assure oxygen free reaction conditions and one inlet for photolyte and catalyst input.

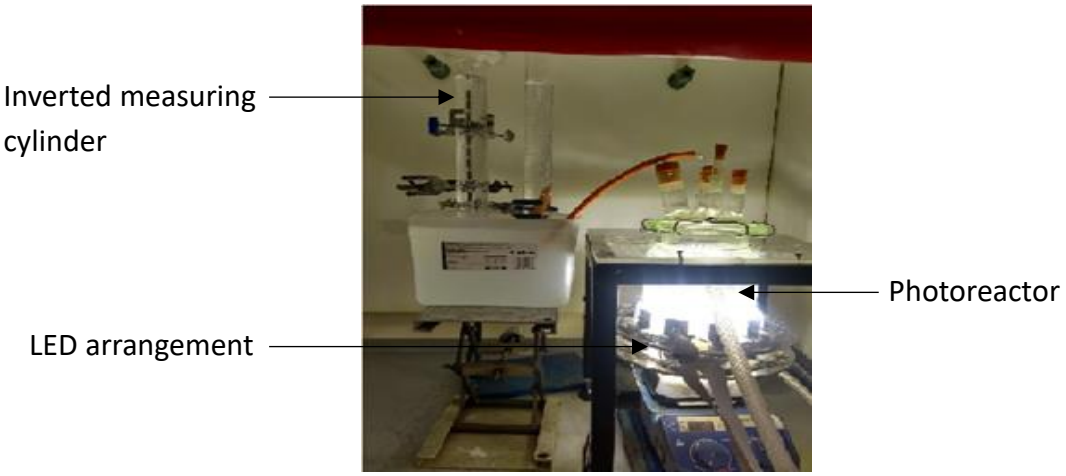

Figure 7. 8 Experimental set-up for the scaled-up photocatalytic reactor using 20 x 10W LED arrangement.

The reactor was externally irradiated by two rows of 10 W cool white LED lamp surrounding the outside of the reactor to assure an efficient hydrogen evolution. The result of the hydrogen evolution using this reactor system when varying the catalyst loading can be seen in Fig 7.9 (a). The initial ammonium sulphite concentration was 2.67 M, the incident flux intensity 6.5 W/m^2 per LED, temperature 60 °C and the CoP loading on CdS was 5 wt.%. Note that the incident flux intensity of 6.5 W/m^2 was measured on the reactor wall for one LED light and with the maximum allowed voltage of the power unit. As the particle loading was increased from 0.00007 g/cm^3 to 0.00060 g/cm^3, the evolved hydrogen increased from 3216.2 to 9965.9 μmol after 3 hours irradiation respectively.

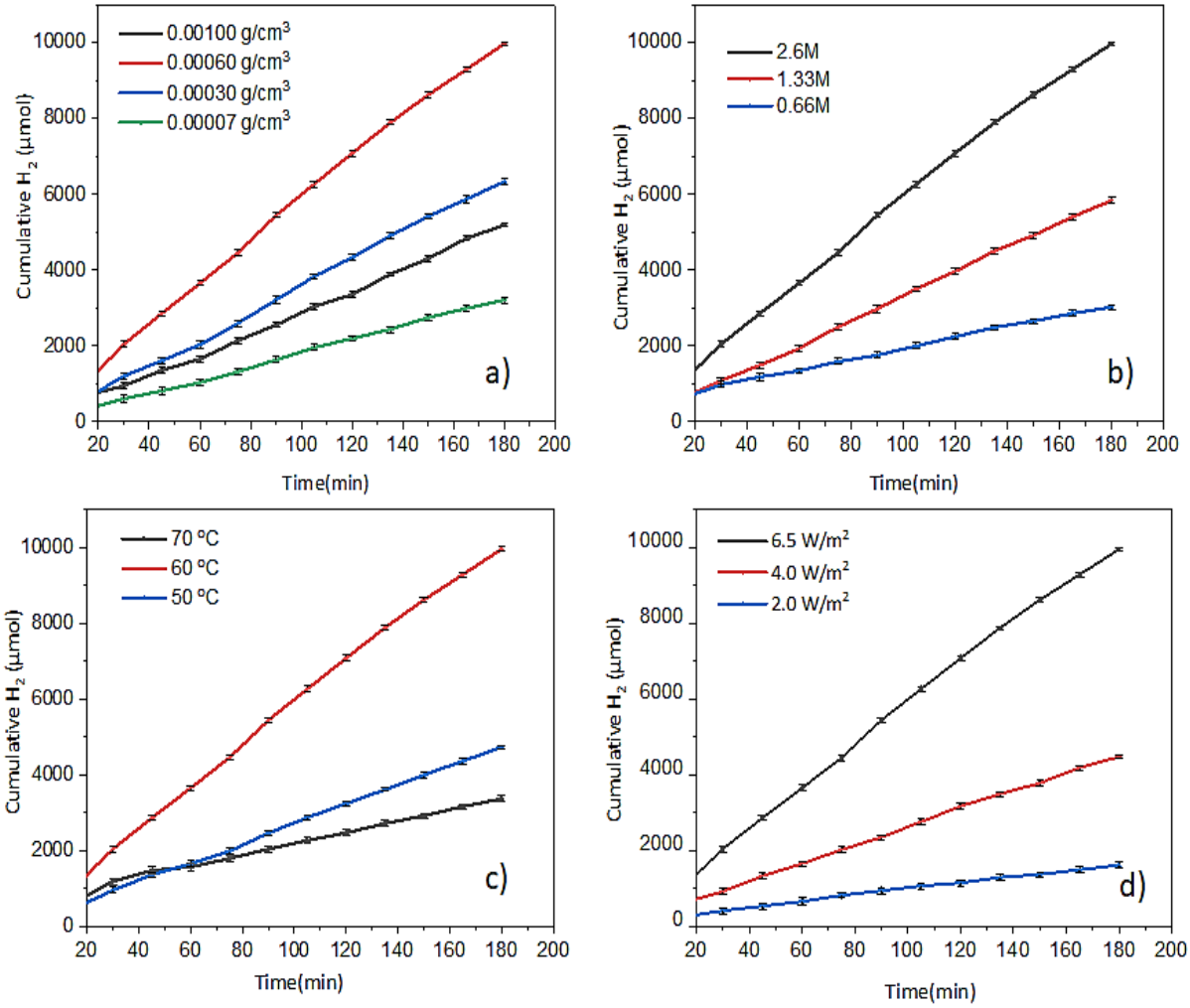

Figure 7. 9 Effect of process parameters on the cumulative H_2 evolution of CoP/CdS composite catalyst; when photocatalyst loading (a), ammonium sulphite concentration (b), reaction temperature (c) and incident flux intensity (d) are varied.

A further increase in loading to 0.00100 g/cm^3 reduced the cumulative evolved hydrogen after 3 hours run. This decrease with increased catalyst loading was due to the shielding effect of the incoming light. Thus, the photocatalyst loading of 0.0006 g/cm^3 was used as the baseline in the rest of the scaling-up study.

The effect of ammonium sulphite concentration variation where an increase in ammonium sulphite concentration from 0.66 M to 2.67 M increased the hydrogen evolution from 3024.5 to 9965.9 μmol respectively , after 3 hours reaction at a fixed incident flux of 6.5 W/m^2, a photocatalyst loading of 0.0006 g/cm^3 with CoP loading of 5 wt.% and a reaction temperature of 60 °C , seen in Fig 7.9 (b). This means that with more concentrated solution, the more sulphite ions are adsorbed on the surface sites of the catalyst, where the photogenerated holes on the CdS surface can oxidise more sulphite to sulphate. Further increase in the ammonium sulphite concentration beyond 2.67 M, did not cause any further increase in the hydrogen production (the result is not presented here), indicating an upper limit for the hydrogen production with the increase of ammonium sulphite concentration. The surface adsorption of sulphite showed different behaviour when comparing with lactic acid, which adsorbed more strongly to the catalyst, in Chapter 5. Therefore, the next study shows a concentration dependency comparison when using lactic acid and ammonium sulphate in Fig 7.10. It is clear that the evolved hydrogen was more depending on the variation of lactic acid concentration than when using ammonium sulphite. This fact will be further shown in the reaction kinetic modelling section in this Chapter.

The H_2 evolution variation with different reaction temperature was then analysed and shown in Fig 7.9 (c). Here the incident flux was 6.5 W/m^2, initial ammonium sulphite concentration 2.67 M, photocatalyst loading 0.0006 g/cm^3 and the temperature varied between 50 °C to 70 °C. As it can be seen in Fig 7.9 (c), the rate of H_2 evolution was the fastest at 60 °C with 55.39 μmol/min, when comparing with 50 °C and 70 °C with the rates of 25.94 μmol/min and 16.79 μmol/min respectively.

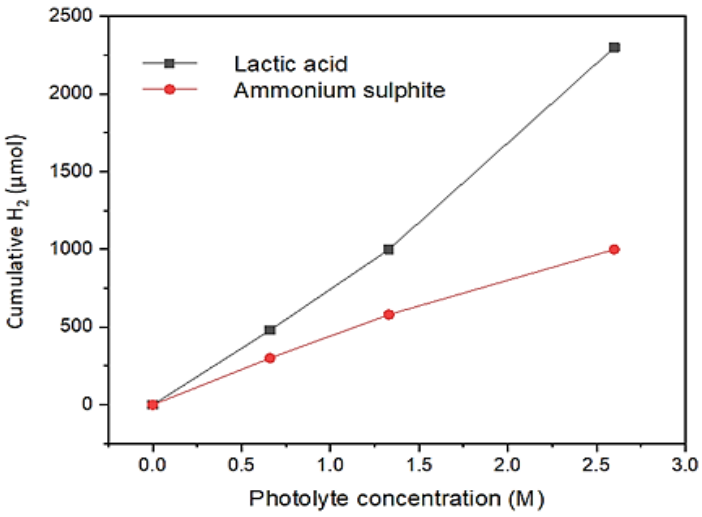

Figure 7. 10 Comparison of concentration dependency between lactic acid and ammonium sulphite.

The dramatic improvement around 60 °C was assured by repeating 3 reaction runs with a SDS of $\pm$ 0.4-0.8 μmol. This temperature depending trend was different than when using lactic acid, see in Chapter 5. The initial rate increase from 50°C to 60 °C may be related to the adsorption isotherm effect between the catalyst surface and water/sulphite, where the higher temperatures facilitate a higher mass diffusion i.e. adsorption and desorption rates, just like what observed for the lactic acid in Chapter 5, but the dramatic drop in rate for 70 °C reflects that what was previous thought of temperature depending factors for lactic acid, certainly is not applied for ammonium sulphite.

Here it is possible that the spontaneous oxidation of SO_3^{2-} to SO_4^{2-} in water, as shown in the reaction pathway (1) in Fig 7.6, is highly temperature dependant, meaning less amount of SO_3^{2-} to participate in the photocatalytic reaction and therefore less hydrogen evolution. It is also possible that pH of the solution was varied by the temperature changes due to several possible dissociation, resulting in a lower hydrogen evolution at higher temperature. The same result in this unexpected temperature trend was observed earlier by Huang et al. [163], who found a maximum hydrogen evolution at 70°C before the rate dropped towards 90°C in a similar photocatalytic system. They did not elaborate further the reason but only assumed a connection with pH variation with temperature. For the photocatalytic H_2 scale-up

experiments in this thesis aimed for a solar driven thermochemical cycle, a reactor temperature of 60°C was considered as the optimum operating temperature when working with ammonium sulphite cycle fluid.

The effect of the incident light intensity on the cumulative H_2 evolution then evaluated for this reactor system and can be seen in Fig 7.9 (d). Here the initial ammonium sulphite concentration was 2.67 M, photocatalyst loading was 0.0006 g/cm^3 with CoP loading of 5 wt.% , and the reaction temperature was set at 60 °C while the light intensity per LED was varied between 2 to 6.5 W/m^2. According to the figure, an increase in the light intensity improved the amount of evolved hydrogen from 1614.4 (2 W/m^2) to 9965.9 μmol (6.5 W/m^2) after 3 hours irradiation in a linear response. These results are comparable with lactic acid in Chapter 5, meaning that hydrogen evolution is proportional to the activity of the catalyst itself, i.e. higher intensity leading to more photon absorption and therefore more electron-hole generation. A further increase of light intensity was limited due to the power restriction. Note that the upper limit of 6.5 W/m^2 was the maximum driven intensity of one LED light.

7-4 Comparison of hydrogen generation of CoP/CdS and Pt/CdS composites

As the aim of this research study was to find the best photocatalytic system to be incorporated into a solar driven sulphur ammonia thermochemical cycle, the final examination was to compare two different visible light CdS photocatalyst composites; one as the most common but more expensive Pt/CdS and one as the novel and less expensive CoP/CdS. In Fig 7.11(a) a comparison of the two catalyst systems' hydrogen performances in lactic acid is shown. It can be seen in the figure how differently the two photocatalysts systems produce hydrogen per mg catalyst loading after 1 h, 2.5 h and 4 h irradiation in a reactor system of; 2.6 M lactic acid, with an incident flux of 2.6 W/m^2 and a temperature of 25°C. The novel and far cheaper CoP/CdS system showed a higher hydrogen generation per mass of catalyst than the Pt/CdS when lactic acid was used. In Figure 7.11 (b) a comparison between the two composite systems but in a 2.67 M ammonium sulphite is seen with the only

difference is the reaction temperature of 60 °C and incident flux of 6.5 W/m^2 per LED is used here (larger reactor system). Here the CoP/CdS performed almost the same as the more understood and elaborated Pt/CdS system.

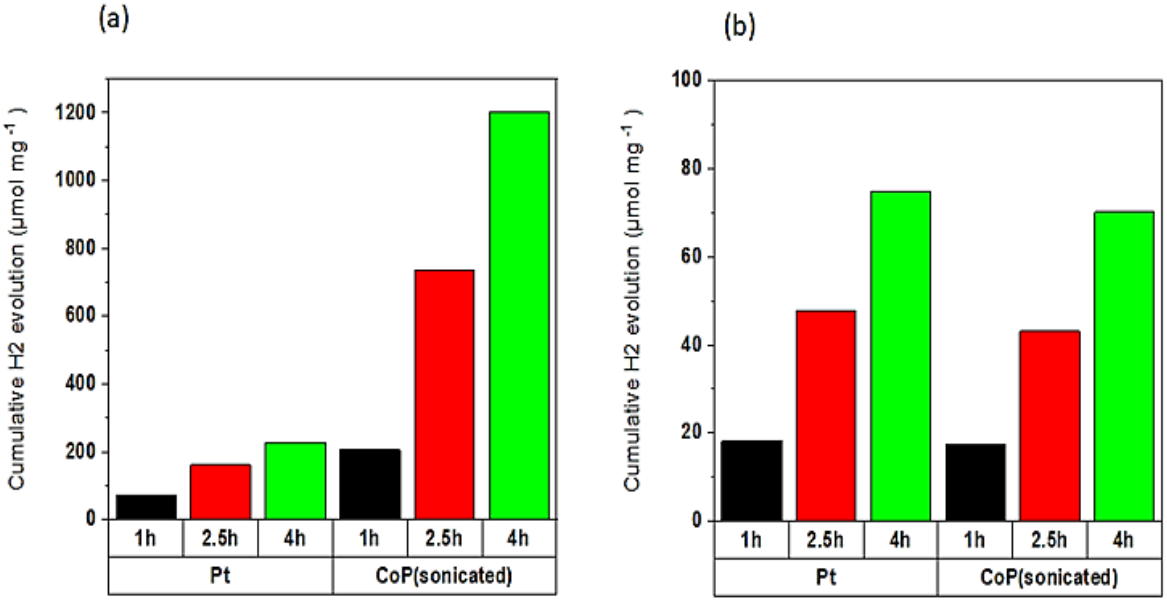

Figure 7. 11 (a) Hydrogen performance of composites of CoP/CdS and Pt/CdS in 2.6 M lactic acid solution after 1 h, 2.5 h and 4 h irradiation in the small reactor and (b) same composite comparison but in 2.6 M ammonium sulphite solution in the scaled-up reactor.

In both (a) and (b) the photocatalyst loading was the same with 0.0006 g/cm^3 (with a co-catalyst loading of 5 wt.%). The reason why CoP/CdS showed such a high activity improvement in lactic acid solution could be due to a range of factors that was previously explained in detail in Chapter 5. One important factor to mention here is the surface potential of the trapped excited electrons in the cocatalyst (Co_xP or Pt) versus the half potential of reducing water, which all will vary with different solution pH. Earlier in a study by Callejas et al. [32] the evaluated over-potentials in a hydrogen cell when using these cocatalysts materials, had the ranking order as; Pt>CoP. However their observed hydrogen evolution reaction study (HER) showed a different raking order as; CoP>Pt (in low pH), where it was finally concluded that the dynamic relation of transitional metal ion (Co) and phosphorous (P) for the surface reactions (rather than the work potentials) caused cobalt phosphides Co_xP performing well for the HER activity. Relating Callejas et al. [32] study with what was observed in 7.11(a), it can be concluded that indeed CoP exhibits better HER activity

than Pt at low solution pH. With the change of pH in the solution, as seen in Fig 7.11(b), the potentials driving the reactions will be altered with pH, seen in Fig 5.10, Chapter 5. The difference between the electron potential of CdS (c. b.) and both potentials of water reduction and the co-catalyst potential, will change with changing of pH. According to Fig 5.10, at low pH (lactic acid solution), the electron potential for Pt is only -0.04 eV [155], compared to the necessary water reduction potential of H^+/H_2 = 0 eV. At high pH (ammonium sulphite solution) the electron potential for Pt changes to -0.4 compared with the water reduction potential that changes now to -0.3 eV [155], whereas the CdS (c. b.) potential marginally changes with pH[156]. The higher pH also decreases the electron bandgap of CdS, which will then affect both the reduction and oxidation reactions potentials [156]. Moreover, at high pH(ammonium sulphite solution) , the zeta potential of the CdS will also change, which will affect the surface adsorption and repulsion mechanisms [157]. Therefore, all necessary electron transfer from the parent CdS to co-catalyst and from co-catalyst to the solution will all be affected by the pH variation, in addition to the ability for the surface adsorption by the photolyte that will vary with pH. Another factor to highlight here is the surface adsorption varies with temperature too, where the temperature was different for lactic acid (T=25°C) compared to ammonium sulphite solutions (T=60°C). As a conclusion ammonium sulphite as the working fluid of the thermochemical cycle showed the great performance using CoP/CdS composite catalyst instead of Pt/CdS for the hydrogen production. The main advantage of the CoP/CdS composite catalyst is its low-cost and earth-abundant nature compared to the more expensive Pt/CdS composite, which would lead to an improved hydrogen economy for the cycle. Furthermore, the CoP/CdS showed good initial stability and repeatability results.

7-5 Hydrogen production modelling (surface reaction kinetics and irradiation modelling) in ammonium sulphite solution

To understand the development of the mathematical prediction model applied to be used in ammonium sulphite it is important to review the necessary charge transfer

from the photon absorbed particle to the catalyst surface, with the simultaneous reduction/oxidation reactions that will occur on the catalyst and cocatalyst surface, as shown in Fig 7.12. In the cathodic reduction step, hydrogen gas is formed via reduction of adsorbed water molecules (they are in the dissociate form at pH 8.7) by the excited electrons transferred to the CoP cocatalyst. The driving reduction potential of the CoP co-catalyst is assumed to be -0.5 eV at pH 8.7, (taken as an approximate from the reported data[164]), which is less negative than the flat band potential of CdS, -0.68 eV[156], but more negative than the water reduction potential at this pH; H^+/H_2 = -0.3 eV[155].

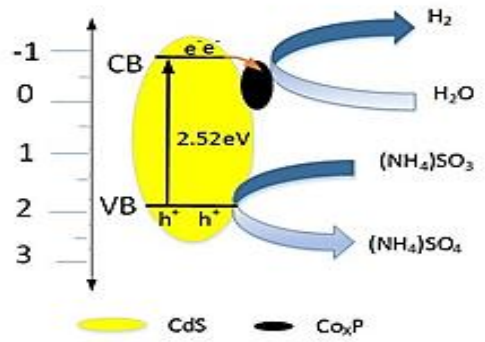

Figure 7. 12 Schematic of the photocatalytic redox reactions of CoP/CdS in ammonium sulphite solution.

In the anodic step, the oxidation of sulphite ions are undertaken by the surface trapped-holes on the CdS, with the assumed valence band potential of +1.68 eV [156], which is more positive than the oxidation potential of SO_3^{2-}/SO_4^{2-},+0.92 eV[104]. It is also assumed that no OH^- radicals taking part of the oxidation, as the formation potential of OH^-radicals is +2.8 eV, which is higher than the valence band potential of CdS. Moreover, there is no oxidation driven by any free O_2 due to the oxygen-free experimental conditions and therefore the oxidation pathway is by the surface trapped holes only. The anodic and cathodic reactions are presented in Eq. (7-9) and (7-10). The equilibrium of adsorption and desorption rate of sulphite on the CdS surface adsorption sites (S) based on the Langmuir Hinshelwood surface adsorption isotherm, can then be expressed as:

$$\text{Sulphite} + \text{S} \underset{k_{-1}}{\overset{k_1}{\leftrightarrow}} (\text{Sulphite} - \text{S}) \qquad \text{(reversible adsorption)} \qquad (7\text{-}11)$$

,where $(\text{Sulphite} - \text{S})$ is the occupied sites by the sulphite ions, S is the vacant sites, k_1 $(\mu\text{mol}^{-1}\text{s}^{-1})$ is the adsorption constant and k_{-1} $(\text{litre}^{-1}\text{s}^{-1})$ is the desorption constant. The adsorbed sulphite ions react with the hydroxyl ions, adsorbed on the different surface sites, and then donate electron to the valance band of CdS ("hole donation"). The holes will therefore oxidise sulphite to sulphate and proton at the end as:

$$2\,(\text{Sulphite} - \text{S}) + 2\,\text{OH}^- + 2\,\text{h}^+ \xrightarrow{k_2} 2\,\text{Sulphate} + \text{S} + 2\,\text{H}^+$$

(photooxidation reaction) (7-12)

,where k_2($\text{m}^2\text{litre}^{-1}\text{J}^{-1}$) is the product formation constant. Hydroxyl ions are produced from both the water reduction and the self-dissociation of water molecules in the solution (pH>8). However, due to the small change in the hydroxyl concentration observed in the pH measurements during the reaction, as shown in Fig 7.7, equation (7-12) can be approximated to a first order reaction mechanism.

If the total amount of available surface adsorption sites is denoted with$[S]_{tot}$, the vacant sites $[S]$ can be obtained as:

$$[S] = [S]_{tot} - [Sulphite - S] \qquad (7\text{-}13)$$

A pseudo-steady state hypothesis of the surface reaction rate is applied to the surface occupied sites by the sulphite ions (as described by Ollis in 2005 [51]), assuming $\frac{d[Sulphite-S]}{dt} = 0$ as:

$$\frac{d[Sulphite-S]}{dt} = k_1[Sulphite][S] - k_{-1}[Sulphite - S] - k_2[Sulphite - S] = 0 \qquad (7\text{-}14)$$

, where $k_1[Sulphite][S]$ represents adsorption rate of sulphite ions, $k_{-1}[Sulphite - S]$ represents desorption rate of sulphite ions and $k_2[Sulphite -$

$S]$ represents product formation rate for sulphate ions. By substituting Eq. (7-13) into (7-14) and solving for $[Sulphite - S]$, we arrive at:

$$[Sulphite - S] = \frac{k_1[Sulphite][S]_{tot}}{k_1[Sulphite]+k_{-1}+k_2} \quad (7\text{-}15)$$

Re-arrangement of Eq. (7-15) results in:

$$[Sulphite - S] = \frac{\frac{k_1}{k_{-1}+k_2}[Sulphite][S]_{tot}}{1+(\frac{k_1}{k_{-1}+k_2})[Sulphite]} \quad (7\text{-}16)$$

, where $\frac{k_1}{k_{-1}+k_2}$ is termed as $K_{a,app}$. $K_{a,app}$ is the apparent adsorption constant representing that the sulphite adsorption/desorption rates are affected by the product formation. In Eq. (7-16), $[S]_{tot}$ can be approximated to 1, if the equation is expressed by the surface coverage of sulphite ions, θA, as:

$$[\theta_A] = \frac{\frac{k_1}{k_{-1}+k_2}[Sulphite]}{1+(\frac{k_1}{k_{-1}+k_2})[Sulphite]} = \frac{K_{a,app}\,[Sulphite]}{1+\,K_{a,app}\,[Sulfite]} \quad (7\text{-}17)$$

As the rate determining step is by the photooxidation step, see Eq. (7-12), the product formation rate from the holes can be described as:

$$r_{product-holes} = k_2[\theta_A] \quad (7\text{-}18)$$

The substitution of Eq. (7-17) in (7-18) results in:

$$r_{product-holes} = k_2\left(\frac{\frac{k_1}{k_{-1}+k_2}[Sulphite]}{1+(\frac{k_1}{k_{-1}+k_2})[Sulphite]}\right) \quad (7\text{-}18)$$

As suggested by Ollis in 1990 [52], the product formation constant k_2 is a function of absorbed radiative flux, I, by the catalyst within the reactor as; $k_2 = k'I^{\alpha}$. The constant of $k'$is the proportionality constant and α is the light absorbing parameter that varies between 0.5 and 1. Therefore, Eq. (7-18) will be presented as:

$$r_{product-holes} = k'I^{\alpha}\left(\frac{[Sulphite]}{\frac{k_{-1}+k'I^{\alpha}}{k_1}+[Sulphite]}\right) \quad (7\text{-}19)$$

It is assumed that the rate of hydrogen production by electrons are equal to the rate of product formation by the holes, therefore $r_{product-holes}$= r_{H_2}, where the expression for the rate of hydrogen production will be as:

$$r_{H_2} = k' I^{\alpha} \left(\frac{[Sulphite]}{\frac{k_{-1}+k' I^{\alpha}}{k_1}+[Sulphite]} \right) \quad (7\text{-}20)$$

This expression accounts for the absorbed radiative flux from only one LED light, so incorporation of total received radiative fluxes from all lights, G, in this expression will result in the final expression as:

$$r_{H_2} = k' G^{\alpha} \left(\frac{[Sulphite]}{\frac{k_{-1}+k' G^{\alpha}}{k_1}+[Sulphite]} \right) \quad (7\text{-}21)$$

,where r_{H_2} is the rate of hydrogen production (μmol/s) in the cross-section of the reactor, $[Sulphite]$ is the sulphite ions concentration(M), k' is the proportionality constant ($\mathrm{m^2 litre^{-1} J^{-1}}$) and G^{α} is the total received radiative fluxes from all LED lights (W m^{-2} nm^{-1}) and α is the light absorbing parameter. The hydrogen production rate produces two limiting cases; one when the total radiative flux on the reactor wall is high with α =0.5 and one when it is low with α =1 [51,52]. The total radiative flux, G^{α}, is a function of the CoP/CdS photocatalyst particles' positions inside the photoreactor together with the angle of the receiving photons, leading to an inhomogeneous distribution of the radiative flux absorbed by the particles inside the reactor, with maximum values near the irradiated wall (where the lights are positioned) and negligible values towards the centre of the reactor.

The radiative flux distribution here, in the photoreactor with 20 LED lights, was obtained by the irradiation modelling approach developed in Chapter 6 and by adjusting the corresponding equations to the reactor size, light arrangement and now with the CoP/CdS photocatalyst's optical scattering and absorption coefficients. Fig 7.13 (A) and (B) show the radiative flux density distribution obtained by the MATLAB for; one LED light and for all LED lights on a CoP/CdS particle with the coordinate (L_1 , θ_1), where the maximum flux is observed closest to the LED lamp positions.

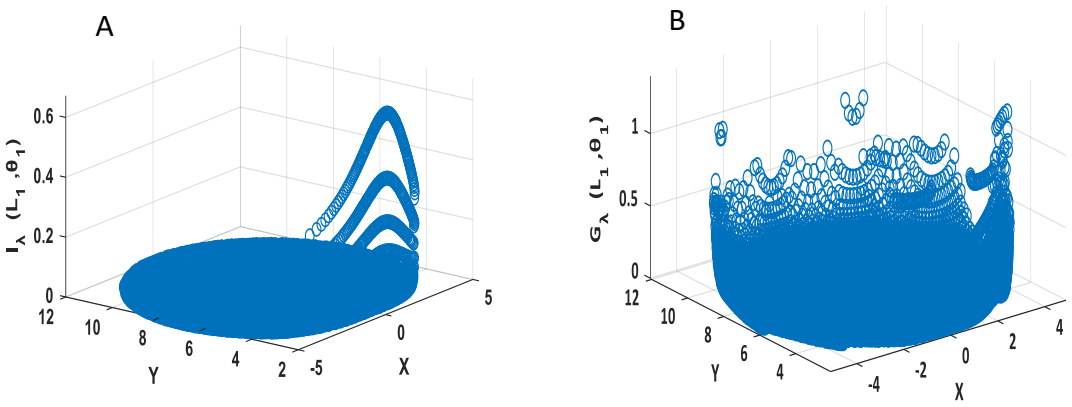

Figure 7. 13 Three-dimensional representation of the radiative flux density distribution at coordinate (L_1 , θ_1) for (a) one LED light as $I_\lambda(L_1$, $\theta_1)$ and for (b) all 20 LED lights as $G_\lambda(L_1$, $\theta_1)$, as simulated by MATLAB.

In the calculation of overall radiative flux density on one particle, as shown in Fig 7.13 (B), the individual contributions from all 20 lights were added up as $G_\lambda(L_1$, $\theta_1)$. Then, by substituting the calculated values of $G_\lambda(L_1$, $\theta_1)$ into Eq. (7-21), the theoretical rate of hydrogen production at the cross-section of the reactor at the particle coordinate (L_1 , θ_1) was obtained. Since, the experimental rates of hydrogen production were obtained for an entire used reactor solution volume, the theoretical hydrogen rate was integrated over the whole used reactor volume as:

$$r_{H_2}{}^{v} = k'k_1[Sulphite]h \int_0^{r_2-r_1} \int_{-\theta_0}^{+\theta_0} G_\lambda\,(L_1\,,\theta_1)^\alpha \left(\frac{1}{k_{-1}+\,k'G_\lambda\,(L_1\,,\theta_1)^\alpha+k_1[Sulphite]}\right)(r_1 + L)dL\,d\theta \quad (7\text{-}22)$$

, where h is the reactor solution height within the reactor, angle θ_0 and path length L_1 were obtained as:

$$\theta_0 = cos^{-1}\left(\frac{\sqrt{2Rr_0+r_0{}^2}}{R+r_0}\right) \quad (7\text{-}23)$$

the boundary conditions of L_1 varied between r_1 andr_2 as:

$$r_1 = cos\theta_1(R+r_0) - \sqrt{cos^2\theta_1(R+r_0)^2 - r_0^2 - 2Rr_0} \quad (7\text{-}24)$$

$$r_2 = cos\theta_1(R+r_0) + \sqrt{cos^2\theta_1(R+r_0)^2 - r_0^2 - 2Rr_0} \quad (7\text{-}25)$$

Finally, the rate of hydrogen production from Eq. (7-22) was converted to μmol/s to be consistent with the empirical rate.

In Table 7.2 the experimental conditions for all 84 reactor runs conducted at different catalyst loading of the 5 wt.% CoP/CdS, different ammonium sulphite concentration and various incident flux intensity used during all the photocatalytic reaction can be seen. The theoretical rate of hydrogen production from Eq. (7-22) was then fitted to the experimental rate of hydrogen production to obtain the α, k_1, k_{-1} and k' by a least-square best fitting procedure, using a non-linear derivative-free optimization method in MATLAB. The objective function ($O.F.$), which was the sum of squared difference between the experimental and the calculated values of H_2 production rate, was then minimised as:

$$O.F. = \sum_1^{84} (H_2^{exp} - H_2^{cal})^2 \quad (7\text{-}26)$$

The obtained fitted parameters for the 84 reactor runs are shown in Table 7.3. In Fig 7.14 (a, b and c) the comparisons between the empirical and predicted rate of hydrogen production at different initial ammonium sulphite concentrations, incident flux intensities and catalyst loadings are shown. The empirical rate for the cumulative formed hydrogen, at the same conditions, is presented in Fig. 7.15 (a, b and c). Both set of figures show a satisfactory agreement between the model and the experimental data points. In Fig 7.14 (a), the model and the empirical hydrogen rate are compared when the initial concentration of ammonium sulphite varied between 0.66-3 M at a fixed incident flux of 6.5 W/m^2, a catalyst loading of 0.0006 g/cm^3 and a reaction temperature of 60 °C. The empirical rate of H_2 production increases non-linearly with increasing ammonium sulphite concentration, fitted as Y= k$^{0.5}$ [Ammonium Sulphite], and starts to levelling-out at 2.66 M with a H_2 generation rate of 0.9 µmol/s. In Fig 7.15 (a) the corresponding cumulated H_2 over time at various concentrations increased linearly from 3024.5 µmol (50 min) to 9965.9 µmol H_2 (180 min). The rate model agrees well with the empirical non-linear behaviour, implying that the adsorbed ammonium sulphite on the catalyst surface sites reached a limiting value where no more adsorption sites were available for the increased ammonium sulphite concentration (as reflected in the adsorption mechanism), hence the non-linear behaviour.

Table 7. 2 Photocatalytic reaction runs at different CoP/CdS catalyst loadings, ammonium sulphite concentrations and incident fluxes.

Run	Cat. loading (g/cm^3)	[Am-sulphite] (M)	Incident flux at $I(0,0)$ (W/m^2)	Run	Cat. loading (g/cm^3)	[Am-sulphite] (M)	Incident flux at $I(0,0)$ (W/m^2)
1	0.00060	2.65	6.5	43	0.00060	1.1	6.5
2	0.00060	2.43	6.5	44	0.00060	1.05	6.5
3	0.00060	2.35	6.5	45	0.00060	1.0	6.5
4	0.00060	2.3	6.5	46	0.00060	0.98	6.5
5	0.00060	2.3	6.5	47	0.00060	0.95	6.5
6	0.00060	2.25	6.5	48	0.00060	0.9	6.5
7	0.00060	2.2	6.5	49	0.00060	0.64	6.5
8	0.00060	2.25	6.5	50	0.00060	0.63	6.5
9	0.00060	2.2	6.5	51	0.00060	0.6	6.5
10	0.00060	2.1	6.5	52	0.00060	0.58	6.5
11	0.00060	2	6.5	53	0.00060	0.54	6.5
12	0.00060	1.8	6.5	54	0.00060	0.53	6.5
13	0.00033	2.65	6.5	55	0.00060	0.52	6.5
14	0.00033	2.43	6.5	56	0.00060	0.51	6.5
15	0.00033	2.35	6.5	57	0.00060	0.5	6.5
16	0.00033	2.3	6.5	58	0.00060	0.48	6.5
17	0.00033	2.3	6.5	59	0.00060	0.45	6.5
18	0.00033	2.3	6.5	60	0.00060	0.42	6.5
19	0.00033	2.25	6.5	61	0.00060	2.55	4
20	0.00033	2.2	6.5	62	0.00060	2.45	4
21	0.00033	2.2	6.5	63	0.00060	2.2	4
22	0.00033	2.1	6.5	64	0.00060	2.04	4
23	0.00033	2	6.5	65	0.00060	1.94	4
24	0.00033	1.8	6.5	66	0.00060	1.83	4
25	0.00007	2.55	6.5	67	0.00060	1.74	4
26	0.00007	2.44	6.5	68	0.00060	1.44	4
27	0.00007	2.42	6.5	69	0.00060	1.3	4
28	0.00007	2.42	6.5	70	0.00060	1.2	4
29	0.00007	2.4	6.5	71	0.00060	1.1	4
30	0.00007	2.4	6.5	72	0.00060	1	4
31	0.00007	2.35	6.5	73	0.00060	2.64	2
32	0.00007	2.3	6.5	74	0.00060	2.42	2
33	0.00007	2.3	6.5	75	0.00060	2.03	2
34	0.00007	2.25	6.5	76	0.00060	1.9	2
35	0.00007	2.2	6.5	77	0.00060	1.8	2
36	0.00007	2.2	6.5	78	0.00060	1.74	2
37	0.00060	1.31	6.5	79	0.00060	1.68	2
38	0.00060	1.3	6.5	80	0.00060	1.57	2
39	0.00060	1.27	6.5	81	0.00060	1.5	2
40	0.00060	1.25	6.5	82	0.00060	1.4	2
41	0.00060	1.20	6.5	83	0.00060	1.3	2
42	0.00060	1.15	6.5	84	0.00060	1.2	2

Table 7. 3 Obtained model parameters

k_1	1.3
k_{-1}	1.73
k'	0.35
α	0.5

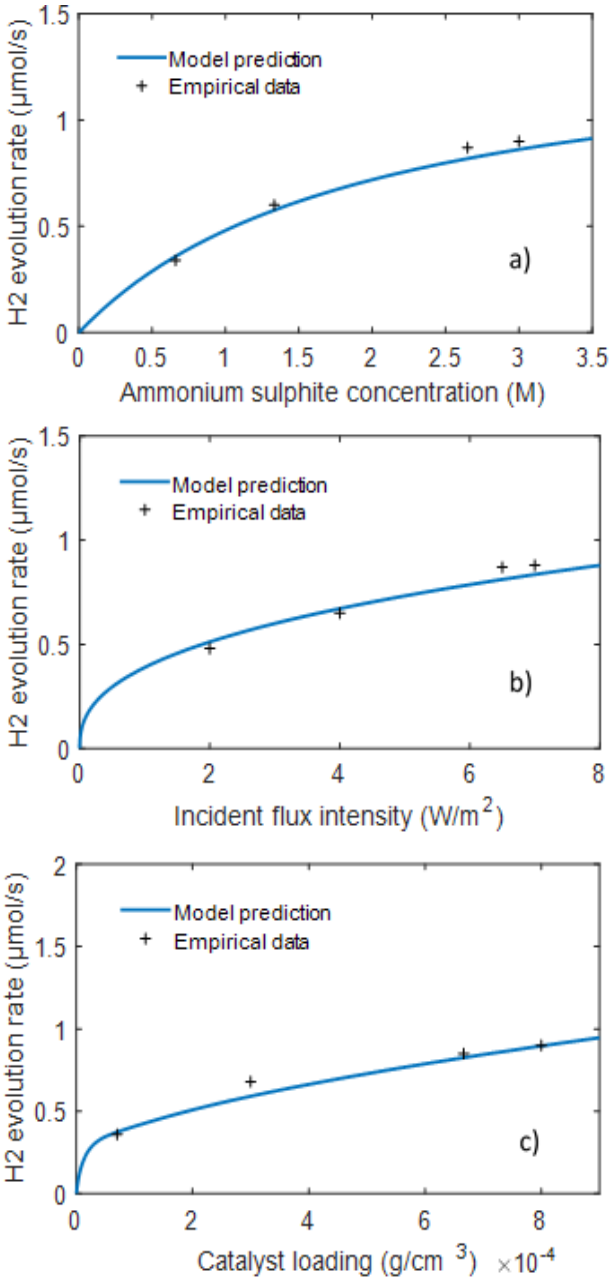

Figure 7. 14 Model predicted H_2 rate (blue line) vs. experimental rate (+), when the ammonium sulphite concentration (a), the incident flux intensity (b) and the loading of catalyst (c) are varied.

It is important to point out here that the ammonium sulphite did not absorb any radiation from the LED (as confirmed by the UV-Vis results in Fig 7.1) and therefore did not affect the irradiation segment in the model. In Fig 7.14 (b), the hydrogen rate comparison between the empirical data and the model can be seen, where the incident flux varied between 2 W/m^2 to 6.5 W/m^2 at a fixed initial ammonium sulphite concentration of 2.66 M, a catalyst loading of 0.0006 g/cm^3 and a reaction temperature of 60 °C. According to the figure, the hydrogen generation rate is proportional to the incident flux until a distinct levelling out at higher incident fluxes of 6.5 W/m^2, where a maximum rate of hydrogen production of 0.87 µmol/s was obtained. The levelling-out of the hydrogen rate by the increased flux, was probably due to the absorption limit of photocatalyst slurry at the maximum incident light flux, beyond which no further light absorption by the particles are observed. The rate results when varying the light intensities are in agreement with the corresponding cumulative hydrogen seen in Fig 7.15 (b), where the cumulative H_2 generation undergoes a small but a gradual non-linear trend with increasing light intensity.

In Figure 7.14 (c) the model is compared with the empirical hydrogen rate when the catalyst loading was varied between 0.0006 to 0.00007 g/cm^3 at a fixed incident flux of 6.5 W/m^2, an initial ammonium sulphite concentration of 2.66 M and a reaction temperature of 60 °C. The model agrees satisfactory with the empirical results and shows a gradual levelling-out of the hydrogen evolution rate with higher catalyst loading. The gradual increase in the hydrogen production rate by the increased loading was also confirmed in the corresponding cumulated hydrogen over time, as seen in Fig 7.15 (c), where a maximum of 9965.9 µmol H_2 after 3 hours irradiation was obtained using a catalyst loading of 0.0006 g/cm^3. This limiting catalyst loading effect might be due to two factors; one is an exceeded vacant surface adsorption site limit for the ammonium sulphite (as seen in the Langmuir Hinshelwood adsorption part of the model), and the other is the shielding effect, which does not allow all particles to be evenly irradiated with high loading.

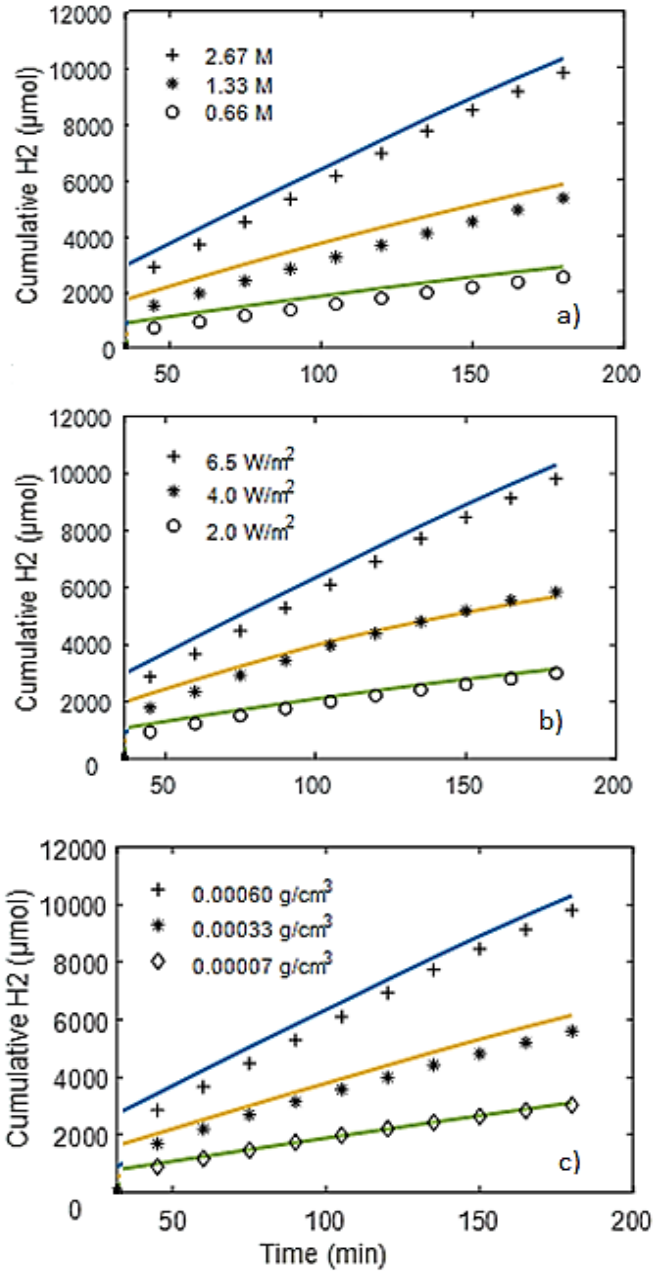

Figure 7. 15 Model predicted cumulative H_2 production (solid lines) vs. experimental H_2 production after 3 hours irradiation; at varying ammonium sulphite concentration (a), incident flux intensity (b) and catalyst loading (c).

From these results, it was concluded that the developed hydrogen rate model successfully predicted the hydrogen production even in the scaled-up photocatalytic reaction where ammonium sulphite was used. The results were then critically compared with the hydrogen rate model for lactic acid, which was undertaken in a smaller volume reactor (30 ml vs 1.57 lire) and using Pt/CdS. Therefore, it was concluded that the developed hydrogen rate model has enough strength to be used

for a scale-up of a H_2 photocatalytic reactor system to incorporated into a large-scale sulphur–ammonia thermochemical cycle.

7-6 Feasibility of upscaling (towards fully working of solar driven thermochemical cycle)

One of the main objectives in this research was to provide a suggestion for a fully working solar driven thermochemical cycle to support large scale hydrogen production and the development of hydrogen fuel cell technology. Furthermore, the findings will support the development of a pilot plant design for the hydrogen production segment.

The LED-driven photoreactor in this research was a 1570 ml stirred jacketed Pyrex reactor, where 300 ml ammonium sulphite produced 75000 µmol hydrogen in 25 hours, corresponding to 0.0728 Litre/h (or 0.0048 kg/h) using a CoP/CdS catalyst loading of 0.0006 g/ml. The reactor light arrangement consisted of two parallel rows of LEDs (2 x 10 W, total of 200 W), surrounding the reactor. However, to utilise the maximum capacity of the photoreactor, a 1000 ml of ammonium sulphite photolyte is suggested (allowing 30% of argon filled headspace), where a theoretically 246000 µmol (0.21 Litre/h or 0.014 kg/h) of hydrogen could be obtained after 30 hours irradiation. When using this maximum capacity, an increased LED arrangement is also needed to accommodate the increase of the reaction solution volume bringing it to 6 x 10 W, total of 600 W. Fig 7.16 shows an schematic of a photoreactor aimed for the capacity increase from 300 ml to 1000 ml (corresponding to 0.0728 l/hr and 0.2100 l/h respectively). For the 1000 ml Pyrex photoreactor capacity, the following instalments are suggested; a suitable agitation system (containing an agitator and baffles), argon gas purging, appropriate hydrogen collection unit, temperature control, pH monitor and corresponding light arrangement (6 rows arrays). After each completed reaction in a thermochemical cycle, a separation of the used cycle fluid from the catalyst particles is needed. Therefore, a purpose made system including a sparge and a drain, is suggested, as seen in Fig 7.16.

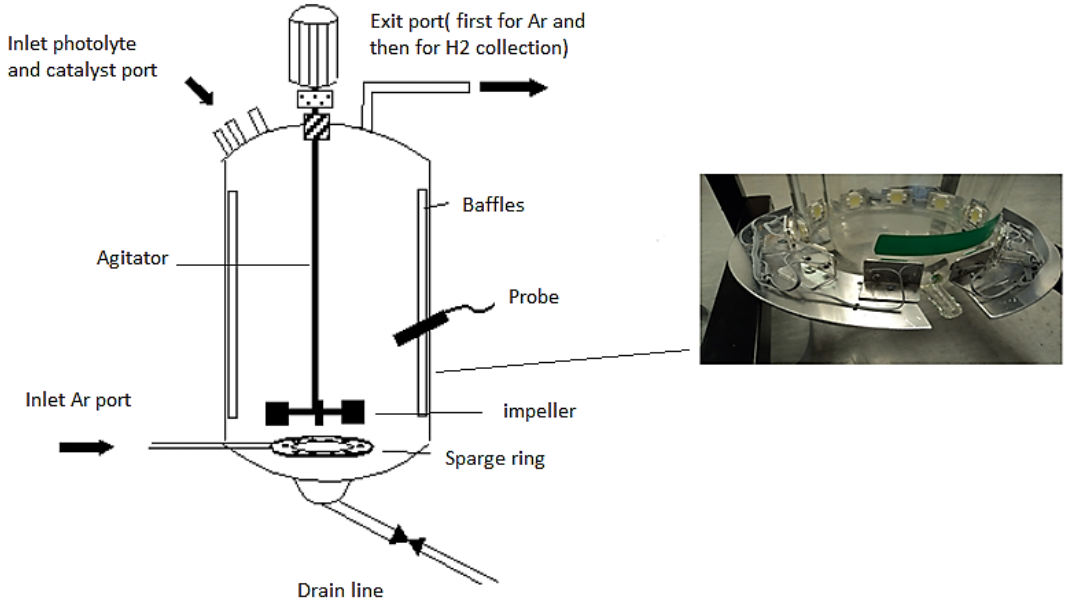

Figure 7. 16 Schematic of a stirred jacketed Pyrex reactor for the hydrogen scale-up.

To incorporate a hydrogen producing reactor into a sulphur ammonia thermochemical cycle, the suggested reactor arrangement should be in a parallel set-up, as seen in Fig 7.17 where a network of parallel semi-continuous photoreactors are shown. The water and ammonium sulphite cycle fluid will be the only inputs to the reactors and hydrogen gas and ammonium sulphate the only outputs.

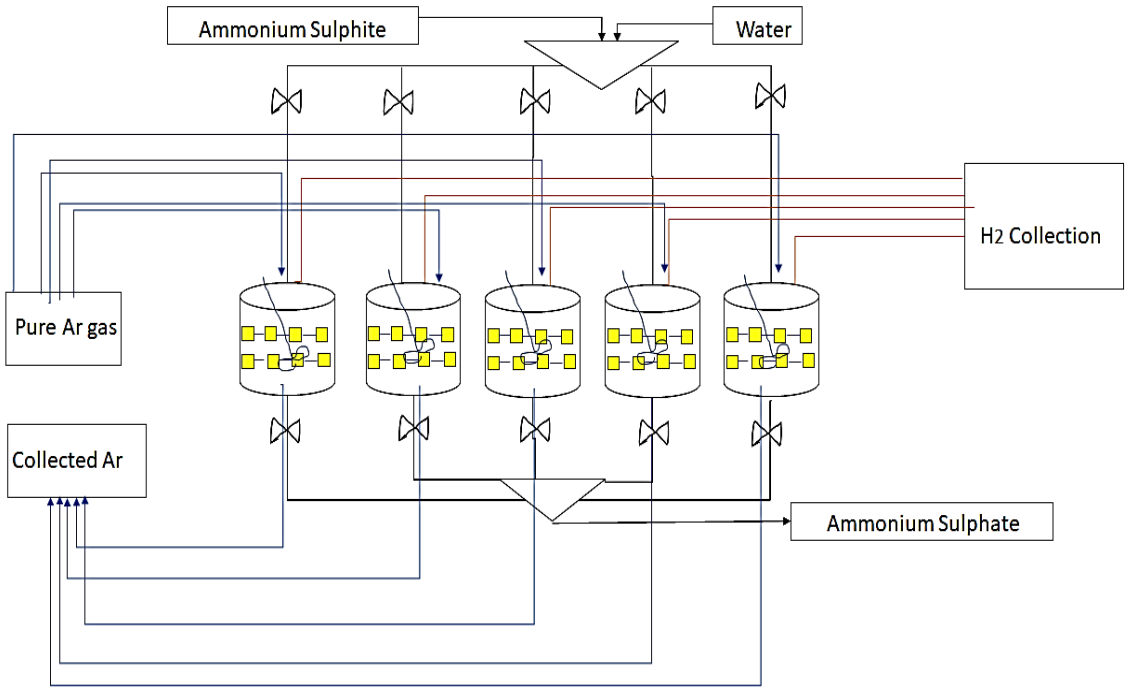

Figure 7. 17 Schematic of the suggested photocatalytic reactor configuration in an ammonium sulphate thermochemical cycle.

The reason why several parallel reactors is favoured instead of one single photoreactor is due to a range of factors. One is to easily accommodate a hydrogen generation capacity increase of an existing hydrogen plant as a result of increasing the mass flow rates of ammonium sulphite in the cycle. A single reactor would not be able to accommodate such increase due to the residence time needed in the reactor. A parallel configuration allows more flexibility of capacity increase, considering the same catalyst loading and the same average light input. In addition, a reduced solar to hydrogen conversion would be expected for the cycle if only one single photoreactor is used, depending on solar light energy and not LEDs. Another advantage of a parallel configuration is the maintenance effectiveness without jeopardising operation of the working reactors, where one or two reactors can be closed while margin allowance can still accommodate the increased production need. According to a process simulation of the sulphur ammonia thermochemical cycle conducted by Ali T-Rassi's group in Florida [75], the obtained hydrogen production rate when using electrolysers was 2.24 kg/s , with the specification seen in Table 7.4.

Table 7. 4 Specification of an suggested electrolyser used in a solar thermochemical cycles from Ref [75]**.**

Reactor temp (°C)	140
Reactor pressure (bar)	9
Required power (MW)	172
Conversion (%)	98

To achieve the same hydrogen production capacity of 2.24 kg/s using the above suggested reactor configuration, 5 groups of parallel photoreactors would be needed, where 5 x reactors are located in each group as seen in Fig 7.17 where each reactor having 1500 Litre capacity. To meet the 2.24 kg/s capacity as Ref 55 , all 5 parallel reactors in each group must be in the full working operation, hence one extra reactor per group would be needed for the maintenance purpose or for a breakdown back-up. These photoreactors will operate at a reduced temperature and pressure (T= 60 °C and P =1 bar) compared with Ali T-Rassi's electrolysers (T=140 °C and P=9 bar) in Ref 55. Furthermore, as the photoreactors are aimed to be fully solar-driven,

the power consumption will be significantly reduced, compared to the 172 MW power consumption by the electrolyser (see Table 7.4). The photonic energy conversion efficiency of the photoreactors with the maximum working volume of each reactor of 1500 ml, was calculated 25% (as explained in Chapter 3), which is 9% higher than the photonic energy conversion efficiency of a CdS coloaded with 0.5 w.t % Pt/Pd/Ru system that was reported by Ali T-Rassi's group in Florida [7]. The high cost of their photoreactor system is not suitable for scaling up purposes due to the use of expensive noble metal catalyst and a as they used a 1000 W (high energy demanding) solar simulator to irradiate their photoreactor. One of the uniqueness of this suggested photoreactor configuration, is the use of earth-abundant *and* inexpensive CoP/CdS photocatalyst system for the hydrogen evolution, with a proven high stability and reproducibility for the extended and repeated reactor runs. This reactor system showed no disadvantage when using ammonium sulphite , which is suggested as the cycle working fluid. The final advantage to put forward is the material of construction of the photoreactors, which is Pyrex, that has a low refractive index and relatively low cost compared to the proposed solar-simulated driven stainless steel photoreactor used by Ali T-Rassi's group in Florida [7].

All these advantages will result in; an increased hydrogen efficiency (due to an increased photonic energy conversion) and an improved hydrogen economy (due to use of cheaper catalyst & reactor materials and the power consumption reduction).

It is finally concluded that a hydrogen generating photocatalytic step for the sulphur ammonia cycle with groups of (solar or LED driven) parallel reactors configuration can be fully implemented and be successfully operational. For complete investigation of electrolyser to photoreactor replacement, a cost study with more accurate capital cost estimations (mainly the photoreactors cost) and operating cost (photocatalyst regeneration and power) would need further elaboration.

7-7 Conclusion

A comprehensive investigation of replacing the traditional electrolyser unit with a solar driven hydrogen generation unit using the working fluid ammonium sulphite in

a thermochemical cycle was presented. First, the reaction mechanism of photocatalytic conversion of ammonium sulphite was investigated. UV-Vis analysis of the reaction solution showed how the initial dominating SO_3^{2-} ions oxidised to SO_4^{2-} in 25 hours reaction time . After 25 hours, only SO_4^{2-} was detected, indicating this ion was not photocatalytically active. The UV-Vis analysis also confirmed that none of the dissolved ions in the working fluid absorbed any of the incoming LED light. The Ion chromatography analysis of the reaction solution further confirmed the UV-Vis results, describing how the SO_3^{2-} was oxidised to SO_4^{2-}. The FTIR analysis showed that ammonium sulphite was weakly physiosorbed on the CoP/CdS photocatalyst particles, compared with the adsorption of lactic acid, where lactic acid showed much higher surface adsorption affinity than the ammonium sulphite. This finding played an important role in the development of the hydrogen production model where surface adsorption/desorption and surface reaction rates were found to have an impact on the amount of formed H_2. GC analysis of the evolved gas proved it was 100% hydrogen and no inferior gas was formed in the reactor. All these analytical methods plus pH measurement during the reaction, enhanced the understanding of photooxidation mechanism of ammonium sulphite while water was photoreduced. The main photooxidation pathway was through oxidation of SO_3^{2-} ions, forming first SO_3^{2-} radicals and very rapidly $S_2O_6^{2-}$, where $S_2O_6^{2-}$ ions further reacted with the surface adsorbed hydroxyl ions and produced SO_4^{2-} ions and two protons. A very fast water reduction rate that promoted an efficient electron transfer straight from the start was also found, compared to the slower photooxidation rate with the slower hole diffusion to the surface (sulphite ions were not strongly adsorbed on the surface).

One of the main finding of this research was that the novel and far cheaper CoP(organo)/CdS system performed almost the same as the more understood and elaborated Pt/CdS system in ammonium sulphite. This confirmed that ammonium sulphite as the working fluid of the cycle had the potential using CoP/CdS catalyst instead of Pt/CdS for a successful hydrogen evolution. The main advantage of the CoP/CdS composite was its low-cost and earth-abundant nature compared to the expensive and more elaborated Pt/CdS composite. Evaluation of various operational parameters on the H_2 generation of the most suitable composite catalyst (CoP/CdS)

for the cycle, suggested the optimised parameters as; photocatalyst loading of 0.0006 g/cm^3 (with the CoP content of 5 wt.%), incident flux of 6.5W/m^2 per LED, ammonium sulphite concentration of 2.67 M and temperature of 60 °C.

An adapted hydrogen prediction model, based on Chapter 5 lactic acid Pt/CdS model, was then developed using ammonium sulphite as a photolyte, CoP/CdS as the photocatalyst and an upscaled reactor size with a suitable visible light arrangement. The irradiation mechanism of the model incorporated the optical properties of the photocatalytic (CoP/CdS), measured in the LED output range of 410-500 nm by spectrophotometric measurements to improve its accuracy. The adsorption segment of the model which was based on a pseudo-steady state Langmuir-Hinshelwood adsorption mechanism, assumed that the adsorbed sulphite on the particles was oxidised to sulphate while simultaneously adsorbed water was reduced to hydrogen. The adopted model was successfully validated against the experimentally measured rate of hydrogen production at different photocatalyst loadings, photolyte concentrations, and incident radiation fluxes. The parameters of α, k_1, k_{-1} and k' were obtained by a least-square fitting procedure using a non-linear derivative-free optimization method in MATLAB. The developed model allowed analysis of flux distribution for number of the switched-on lamps. The model results confirmed the model strength and consistency for a H_2 photocatalytic reactor scale-up, which could potentially be used in a large-scale sulphur–ammonia thermochemical cycle.

The feasibility of upscaling towards fully working of solar driven thermochemical cycle was also conducted, where the use of a group of parallel hydrogen photoreactors instead of a traditional electrolyser in the hydrogen step of the cycle was evaluated. The parallel photoreactors showed that they can be successfully implemented and operationally efficient, resulting in an increased hydrogen efficiency (due to an increased photonic energy conversion) and an improved hydrogen economy of the cycle (due to use of cheaper catalyst & reactor materials and the power consumption reduction).

Chapter 8 Conclusions and Future Work

8-1 Conclusion

In this thesis a solar driven sulphur ammonia thermochemical cycle for hydrogen (g) and oxygen (g) production has been presented. Until today, there are only a few published reports of this type cycle[7,63,64], however it is clear that further improvement is needed until this technology can be considered as both safe for large scale production purpose and low in energy consumption. To make this type of thermochemical cycle completely solar driven, a suggestion of harvesting both the thermal and quantum components of solar irradiation should be aimed for, where the thermal part and quantum component (in the visible region) would drive the oxygen and the hydrogen productions respectively. By introducing a photocatalytic reactor for the hydrogen generation, and thereby replacing the energy demanding electrolytic step of the cycle, the target of lower energy consumption would be met. In this research all aspects of the photocatalytic step were investigated with the aim of industrial implementation and scaling-up purpose.

The first stage of this research was to find a best photocatalyst system for the photocatalytic hydrogen step in a sulphur ammonia thermochemical cycle. To be solar driven, a photocatalyst that could be driven by the visible light was aimed for. CdS was the choice of material as CdS absorb visible light and because the bandgap potentials seemed to match what would drive the requested redox reactions needed for the thermochemical cycle's purpose. The aim was to synthesise a novel and less expensive cocatalyst/CdS photocatalyst that could substitute the more common but more expensive visible light driven Pt/CdS system. Initially, the CdS particles were successfully synthesised to the desired hexagonal crystal structure by a hydrothermal method. After a thorough research, it was found that a metallic phosphide could

possibly replace the noble metal Pt or Pd for an effective photocatalytic hydrogen generation. Then the first trial of Co_xP synthesis was by a solid phase reaction. However, the synthesis of the cobalt precursor $Co(OH)_2$ was challenging plus the phosphidation reaction in the furnace did not lead to a successful formation of Co_xP in addition to the formation of toxic intermediate products inside the furnace.

Due to the challenges in the solid phase synthesis of Co_xP, a solution phase synthesis through an organometallic reaction was studied next. Here, depending on the addition of the phosphor precursor TOP and 1 h or 12 h reaction time, either Co_xP or CoP could be formed through the organometallic route. The formed particles of Co_xP were mainly amorphous for the both reaction times, where post-annealing treatment was used to improve the crystallinity. The effect of post-annealing on the crystallinity of Co_xP samples was, however, insignificant for both cases. In a thermal analysis of the as-made Co_xP samples it was shown that the argon gas post-annealing treatment above 380° C, converted parts of the particles into carbon as a result of a carbonisation mechanism. This high level of carbon originates from the solvents used in the synthesis, in particular cyclohexane.

The next solution phase synthesis of Co_xP was by a hydrothermally method, where partly crystallised Co_2P nanoparticles with an orthorhombic crystal structure were found. A change of hydrothermal annealing condition to higher and longer temperature settings did not improve the particle crystallinities much. However, both the two different hydrothermal annealing conditioned samples had better crystallinity when compared with the organometallic synthesised Co_2P sample (at t= 1h).

Following the synthesis of the cocatalyst, loading of the Co_xP on CdS was needed. The Pt/CdS had also been made as to compare the developed Co_xP/CdS photocatalytic activity. In Pt/CdS, the Pt was adhered on the CdS particle by metal salt reduction, hence assuring a good connectivity between the cocatalyst and semiconductor particle. Unfortunately, such deposition method could not be adapted for the Co_xP. Instead two other methods of grinding and sonication were investigated as several related articles had reported that thorough grinding of the nanoparticles could produce effective photocatalyst composites. However, the grinding method turned out to be unsuitable due to large CdS agglomerates being formed with less

possibilities of surface covering of the Co_xP , while the sonication method turned out to be the most efficient method, as a mean of reducing the large CdS agglomerates and working in a favour for dissolution of surface bound contaminants on the organometallic Co_xP.

After a selection cocatalyst/CdS were synthesised, the photocatalytic hydrogen evolution was investigated. The aim was to understand the photocatalytic reaction, and find the optimal operational parameters to be able to compare the hydrogen performance of differently synthesised Co_xP/CdS composites with the model catalyst Pt/CdS system in a LED-driven photoreactor.

The reactor was designed around the purpose of an oxygen free atmosphere inside the vessel, and with a good illumination of all particles in the slurry which would need some form of agitation and temperature control. Further all ports for sampling, purging and connectors needed to be fitted. Instead of using an expensive and energy demanding solar simulator, low energy LED's with visible light output was searched for in an arrangement that would provide comparable light intensities of a commercial solar simulator in the visible region. An arrangement of connected white cool LED's surrounding the cylindrical reactor was the final choice. Optical analysis of the LED lights indicated that an initial arrangement of 20 × 10 W cool white LED lights were powerful enough to excite efficiently the CdS photocatalyst in the photoreactor without a heat build-up in the reactor due to a designed heat sink arrangement and external LED fan. Finally, a 1.57 Litre water-jacketed photoreactor with an inner diameter 10 cm was successfully benchmarked with four ports and a 20 x LED light arrangement (each 10 W cool white LED) which was attached to the outside of the reactor, where the reactor was externally irradiated. The reactor temperature was controlled by an isothermal water reservoir and the temperature of light arrangement was controlled by a thermocouple attached outside the reactor.

For the photocatalytic reaction, initially a lactic acid solution, as a most common photolyte, was studied, where no direct photodissociation of the lactic acid in LEDs' visible region was found, suggesting majority of visible photon energy was only

received by the CdS particles. The characteristics of the lactic acid at high concentrations (and low pH) were investigated. It was found that the lactic acid was chemisorbed to the catalyst surface in its molecular form and its possible oxidation route, via the holes (electron transfer to the CdS) ,was also investigated. The main oxidation pathway was through the oxidation of the surface adsorbed lactic acid molecules, forming pyruvic acid and two protons.

The Pt/CdS composite, which was the reference catalyst, was used to determine the optimised operational parameters for the H_2 evolution in lactic acid and the following was found; a photocatalyst loading of 0.0006 g/cm^3 (with a cocatalyst content of 5 wt.%), incident flux of 2.6 W/m^2 per LED and a lactic acid concentration of 2.67 M at room temperature. At these conditions, the lactic acid was found to efficiently donate electrons to the valance band of CdS while water was simultaneously reduced by an electron transfer at Pt.

The photocatalytic H_2 performance of the different synthesised Co_xP/CdS composites (using grinding loading method) in lactic acid compared with Pt/CdS at the optimised conditions followed the order of; Pt/CdS > CoP(organo as-prep)/CdS > Co_2P(organo as-prep)/CdS > CoP(organo-anneal)/CdS > Co_2P(hydro as-prep)/CdS ≥ Co_2P(hydro-with a change of condition)/CdS > Co_2P(organo-anneal)/CdS.

It was found that the post- annealing step in the organometallic synthesis of Co_xP caused a reduced hydrogen evolution compared to the as-prepared Co_xP, due to the partly carbonisation of the Co_xP surface. Also, a reduced hydrogen performance for the hydrothermal Co_2P compared to the organometallic Co_2P was found. This was surprising as the improved particle crystallinity was found for the hydrothermal synthesis Co_2P particles compared with the highly amorphous crystal structure in the organometallic route.

Then, a change of cocatalyst loading method was investigated to the sonication-method that resulted dissolution of surface bound contaminants. Here an exceptional photocatalytic activity for the CoP(organo)/CdS was obtained which was significantly higher than other composite photocatalysts, especially the more understood Pt/CdS composite, maintaining its photocatalytic activity very well in a repeatability test. This indicated that the hydrogen performances may be driven differently as initial though, where the work potentials of the Co_xP was seen as the

driving potential for the water splitting. However, the numbers of these work-potentials were found in the literature and were determined for the bulk single crystals. Instead in the highly amorphous CoP, the high electronegativity P atoms in the amorphous structure created a dipole moment which facilitated an effective hydrogen generation from the water splitting attracting. CoP has a higher ratio of P than in Co_2P. Another reason for this high performance when organometallic synthesised CoP was used, was originated from the sonicating loading method where not only the large CdS agglomerates were separated to smaller (and surface exposed) particles but also the residual organic solvents (which caused carbonisation in the post annealing) where cleaned away from the CoP surfaces, which now created a better foundation for electron transfer from the excited CdS to the CoP cocatalyst. As a result, CoP(organo)/CdS composite (with the sonication loading) was chosen as the best photocatalyst composite to substitute the more commonly used Pt/CdS in a sulphur ammonia thermochemical cycle.

The CoP(organo)/CdS catalyst was further tested at different operational conditions, confirming the potential of developing a robust and quantitative assessment of photocatalytic reactions to be implemented into a thermochemical cycle using ammonium sulphite solution rather than lactic acid. The optimised reaction parameters determined as; CoP(organo)/CdS photocatalyst loading of 0.0006 g/cm^3 (with the CoP content of 5 wt.%), incident flux of 6.5 W/m^2 per LED, ammonium sulphite concentration of 2.67 M and temperature of 60 °C.

The analysis of the reaction solution showed small amount of SO_4^{2-} ions alongside SO_3^{2-} ions before the photocatalytic reaction, however no direct photodissociation of any of the compounds in the LEDs' visible region was found, suggesting all visible photon energy would be absorbed by the CdS particles only. The main photooxidation pathway was suggested through the oxidation of SO_3^{2-} ions, forming first SO_3^{2-} radicals and then a short lived intermediate $S_2O_6^{2-}$, where these $S_2O_6^{2-}$ ions further reacted with the surface adsorbed hydroxyl ions and produced SO_4^{2-} ions and two protons. By FTIR it was concluded that the SO_3^{2-} was weakly physiosorbed to the

catalyst surface (and not the SO_4^{2-}) . This was different compared with lactic acid where the lactic acid molecule was chemisorbed on the particle surface. The only gas formed when using either lactic acid or ammonium sulphite as a photolyte was pure hydrogen, according to GC analysis. As ammonium sulphite and its dissociated ions, did not adsorb so strong, a very fast water reduction rate by an efficient electron transfer was observed straight from the start, compared to a slower photooxidation rate caused by a slower hole diffusion rate to the surface and sulphite ions that not strongly adsorbed on the surface.

When using ammonium sulphite solution and comparing it with lactic acid a range of new factors turned out to play a big part in the reaction, such as the pH dependency which caused changes the driving potentials and changes of the zeta potential. The needed electron transfer from the parent CdS to co-catalyst and from co-catalyst to the solution and how it varied between high and low pH was investigated, in addition to the ability for the surface adsorption by the sulphite that also varied with both pH and temperature. Consequently, using ammonium sulphite as the working fluid of the cycle was found to work well with the visible light driven photocatalytic CoP/CdS instead of Pt/CdS for the hydrogen step in a suggested thermochemical cycle. The main advantage of choosing the more effective CoP/CdS composite was its low-cost and earth-abundant nature compared to the expensive Pt/CdS composite, leading to an improved hydrogen economy for the cycle.

The fourth stage was to develop a descriptive mathematical model for the LED-driven H_2 photoreactor and validate it against the experimental data. The obtained data can then be used for a scale-up purpose of the sulphur ammonia thermochemical cycle and easily be linked to complete process flow diagrams (PFD) in Aspen Plus. First the hydrogen production rate using the small photoreactor (irradiated by 10 LEDs) and Pt/CdS in lactic acid solution was used for the development of the model. Then the basis of the same model for an up-scaled reactor (irradiated by 20 LEDs) was used but using CoP/CdS photocatalyst in the ammonium sulphite solution instead. The surface reaction mechanism of the developed model was based on a pseudo-steady

state Langmuir-Hinshelwood adsorption isotherm which incorporated the total radiative flux effect. The irradiation mechanism of the model was based on an approximate solution of the RTE together with the derivation of geometrical position of particles in the cross-section of the small reactor. The total received photon fluxes by all particles in the cross section of the reactor then were obtained, followed by an additional integration over the longitudinal reaction depth to account for the total received photon fluxes inside the whole slurry photoreactor by integration.

To improve the accuracy of the model, measurements of the photocatalyst's optical properties such as absorbance, reflectance and transmittance were made, and then integrated into the model, with increments of 1 nm within the LED output range of 410-500 nm. The developed model was then successfully validated against experimental measured rate of hydrogen production when using different catalyst loadings, different photolyte concentrations, and different incident light intensity. The unknown model parameters of α, k_1, k_{-1} and k' were obtained by a least-square fitting procedure using a non-linear derivative-free optimization method in MATLAB. A satisfactory agreement between the model and empirical results indicated the model's capability to predict the behaviour of any photocatalytic reactor in a wide range of operating conditions, regardless of the radiation type or reactor size, with minor computational effort. The model also allowed analysis of flux distribution depending on the number of switched-on lamps around the reactor vessel. To take the model from a small sized reactor (Pt/CdS and lactic acid in room temperature and 10 x LED), to the large reactor (using CoP/CdS and ammonium sulphate at 60^{o}C and 20 x LED (and more)), some adjustments were made and then solved. The final descriptive mathematical model again confirmed the model strength and consistency to provide a coherent framework for a LED-photoreactors scale-up that would predict the hydrogen production satisfactory in a visible light driven sulphur ammonia thermochemical cycle.

The final stage was a technological feasibility study towards a fully working large scale solar driven thermochemical cycle, where a group of parallel hydrogen photoreactors instalments was suggested to replace the traditional electrolyser in

the hydrogen step of the cycle. The suggested parallel group photoreactors configuration showed that they can be easily implemented and being operationally efficient, while providing an increased hydrogen efficiency and most importantly; an improved the hydrogen economy of the cycle (due to use of cheaper catalyst & reactor materials and power consumption reduction).

8-2 Future work

The range of ideas that could be further carried out for this research project are suggested in this section. The recommendations for the future work include:

1- Evaluating the effect of different loading methods of Co_xP on the CdS nanoparticles: understanding the sonicating cleansing effect on the organometallic CoP particles and optimising the in-situ loading methods.
2- Evaluating the regeneration of the spent composite catalyst of CoP/CdS.
3- Synthesising CdS nanorods: CdS nanorod structures could overcome the slow hole diffusion and reduce photooxidation of CdS and therefore improve the photocatalytic reaction rates.
4- Evaluating photocatalytic hydrogen evolutions and other redox reactions where CdS nanorods are used and compare it with the CdS composite photocatalysts as undertaken in this research.
5- Evaluating CdS nanorod based particles in ammonium sulphite solution or any other thermochemical cycle fluid to be used in the hydrogen producing step of a cycle.
6- Development of how to incorporate the photocatalytic hydrogen data into a computer process simulation such as Aspen Plus of the sulphur ammonia thermochemical cycle to evaluate the overall process efficiency. An initial process flow diagram of the sulphur ammonia cycle was implemented in this study as seen in Fig 8.1. However, the efficiency of the whole cycle needs further elaboration.
7- A full investigation of the cycle, including the cost analysis where accurate estimation of capital cost and operating cost to be implemented in the computer process simulation such as Aspen Plus.

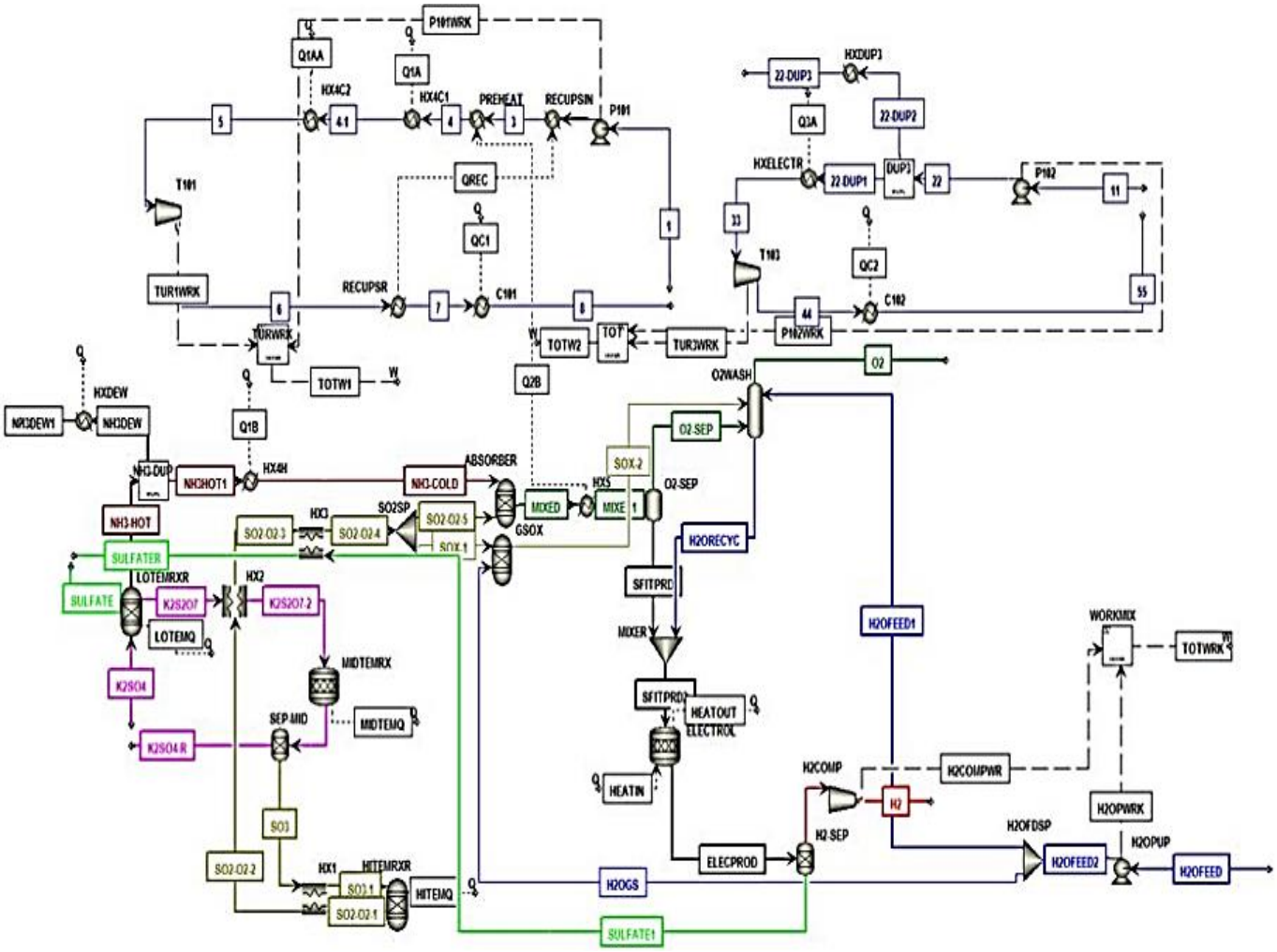

Figure 8. 1 Initial full process flow diagram representing a sulphur ammonia thermochemical cycle obtained in Aspen Plus.

REFRENCES

[1] S. Dutta, A review on production, storage of hydrogen and its utilization as an energy resource, J. Ind. Eng. Chem. 20 (2014) 1148–1156.

[2] Z. Xing, X. Zong, J. Pan, L. Wang, On the engineering part of solar hydrogen production from water splitting: Photoreactor design, Chem. Eng. Sci. 104 (2013) 125–146.

[3] N. Muradov, A.T. -Raissi, N. Qin, K. Kakosimos, O16 -SOLAR HYBRID PHOTO-Thermochemical water- splitting cycle with in-situ themal enrgys storage, Hydrog. Power Theor. Eng. Solut. Int. Symp. 6 (2015).

[4] N. Muradov, A. T-Raissi, S. Fenton, Solar hybrid water splitting cycle with integrated thermal storage, 3 (2014) 2070–2074.

[5] L. BRECHER, S. SPEWOCK, C. WARDE, The Westinghouse Sulfur Cycle for the thermochemical decomposition of water, Int. J. Hydrogen Energy. 2 (1977) 7–15.

[6] W. Yao, C. Huang, N. Muradov, A. T-Raissi, A novel Pd–Cr2O3/CdS photocatalyst for solar hydrogen production using a regenerable sacrificial donor, Int. J. Hydrogen Energy. 36 (2011) 4710–4715.

[7] C. Huang, W. Yao, A.T. -Raissi, N. Muradov, Development of efficient photoreactors for solar hydrogen production, Sol. Energy. 85 (2011) 19–27.

[8] A. T-raissi, C. Huang, L. Mao, N. Muradov, A new solar metal sulphate–ammonia based thermochemical water solitting cycle for the production of hydrogen, Mater Issues in Hydrog. Econ. 34(2009)15–45.

[9] R. Taylor, R. Davenport, J. Talbot, R. Herz, W. Luc, D. Genders, P. Symons, L. Brown, Status of the Solar Sulfur Ammonia Thermochemical Hydrogen Production System for Splitting Water, Energy Procedia. 49 (2014) 2047–2058.

[10] X. Zong, Photocatalytic water oxidation on F, N co-doped TiO2 with dominant exposed facets under visible light, Chem. Commun. 47 (2011) 11742.

[11] W. Jiang, W. Luo, J. Wang, M. Zhang, Y. Zhu, Enhancement of catalytic activity and oxidative ability for graphitic carbon nitride, J. Photochem. Photobiol. C Photochem. Rev. 28 (2016) 87–115.

[12] L.J. Zhang, S. Li, B.K. Liu, D.J. Wang, T.F. Xie, Highly Efficient CdS/WO3 Photocatalysts: Z-Scheme Photocatalytic Mechanism for Their Enhanced Photocatalytic H2 Evolution under Visible Light, ACS Catal. 4 (2014) 3724–3729.

[13] X.-J. Lv, W.-F. Fu, H.-X. Chang, H. Zhang, J.-S. Cheng, G.-J. Zhang, Y. Song, C.-Y. Hu, J.-H. Li, Hydrogen evolution from water using semiconductor nanoparticle/graphene composite photocatalysts without noble metals, J. of Mater. Chem 22.4 (2012): 1539-1546

[14] J. Yu, Y. Yu, B. Cheng, Enhanced visible-light photocatalytic H2-production performance of multi-armed CdS nanorods, RSC Adv. 2 (2012) 11829–11835.

[15] Y. Wang, Y. Wang, R. Xu, Photochemical Deposition of Pt on CdS for H_2

Evolution from Water: Markedly Enhanced Activity by Controlling Pt Reduction Environment, J. Phys. Chem. C. 117 (2013) 783–790.

[16] J. Yang, H. Yan, X. Wang, F. Wen, Z. Wang, D. Fan, J. Shi, C. Li, Roles of cocatalysts in Pt–PdS/CdS with exceptionally high quantum efficiency for photocatalytic hydrogen production, J. Catal. 290 (2012) 151–157.

[17] H. Wang, W. Chen, J. Zhang, C. Huang, L. Mao, Nickel nanoparticles modified CdS – A potential photocatalyst for hydrogen production through water splitting under visible light irradiation, Int. J. Hydrogen Energy. 40 (2015) 340–345.

[18] J. Ran, J. Yu, M. Jaroniec, Ni(OH)2 modified CdS nanorods for highly efficient visible-light-driven photocatalytic H2 generation, Green Chem. 13 (2011) 2708-2013.

[19] J. Jie, W. Zhang, I. Bello, C.-S. Lee, S.-T. Lee, One-dimensional II–VI nanostructures: Synthesis, properties and optoelectronic applications, Nano Today. 5 (2010) 313–336.

[20] A. Pareek, A. Gopalakrishnan, P.H. Borse, Efficiency and stability aspects of CdS photoanode for solar hydrogen generation technology, in: J. Phys. Conf. Ser., IOP Publishing, 2016: p. 12006.

[21] V. Preethi, S. Kanmani, Photocatalytic hydrogen production using Fe2O3-based core shell nano particles with ZnS and CdS, Int. J. Hydrogen Energy. 39 (2014) 1613–1622.

[22] L. Zou, H. Wang, X. Wang, High Efficient Photodegradation and Photocatalytic Hydrogen Production of CdS/BiVO4 Heterostructure through Z-Scheme Process, ACS Sustain. Chem. Eng. 5 (2017) 303–309.

[23] X. Zong, H. Yan, G. Wu, G. Ma, F. Wen, L. Wang, C. Li, Enhancement of Photocatalytic H 2 Evolution on CdS by Loading MoS 2 as Cocatalyst under Visible Light Irradiation, J. Amer. Chemi. Soci. 130.23 (2008): 7176-7177..

[24] W. Zhang, Highly efficient and noble metal-free NiS/CdS photocatalysts for H2 evolution from lactic acid sacrificial solution under visible light, Chem. Commun. 46 (2010) 7631-7633.

[25] J. Wang, B. Li, J. Chen, N. Li, J. Zheng, J. Zhao, Z. Zhu, Enhanced photocatalytic H2-production activity of CdxZn1−xS nanocrystals by surface loading MS (M=Ni, Co, Cu) species, Appl. Surf. Sci. 259 (2012) 118–123.

[26] S. Cao, Highly efficient photocatalytic hydrogen evolution by nickel phosphide nanoparticles from aqueous solution, Chem. Commun. 50 (2014) 10427.

[27] H. Cheng, X.-J. Lv, S. Cao, Z.-Y. Zhao, Y. Chen, W.-F. Fu, Robustly photogenerating H2 in water using FeP/CdS catalyst under solar irradiation., Sci. Rep. 6 (2016) 19846.

[28] Q. Yue, Y. Wan, Z. Sun, X. Wu, Y. Yuan, P. Du, MoP is a novel, noble-metal-free cocatalyst for enhanced photocatalytic hydrogen production from water under visible light, J. Mater. Chem. A. 3 (2015) 16941–16947.

[29] S. Cao, Y. Chen, C.-J. Wang, X.-J. Lv, W.-F. Fu, Spectacular photocatalytic hydrogen evolution using metal-phosphide/CdS hybrid catalysts under sunlight irradiation, Chem. Commun. 51 (2015) 8708–8711.

[30] Y. Shi, B. Zhang, Recent advances in transition metal phosphide nanomaterials: synthesis and applications in hydrogen evolution reaction, Chem. Soc. Rev. 45 (2016) 1529–1541.

[31] P. Jiang, Q. Liu, C. Ge, W. Cui, Z. Pu, A.M. Asiri, X. Sun, CoP nanostructures with different morphologies: synthesis, characterization and a study of their electrocatalytic performance toward the hydrogen evolution reaction, J. Mater. Chem. A. 2 (2014) 14634–14640.

[32] J.F. Callejas, C.G. Read, E.J. Popczun, J.M. McEnaney, R.E. Schaak, Nanostructured Co2P Electrocatalyst for the Hydrogen Evolution Reaction and Direct Comparison with Morphologically Equivalent CoP, Chem. Mater. 27 (2015) 3769–3774.

[33] J. Su, J. Zhou, L. Wang, C. Liu, Y. Chen, Synthesis and application of transition metal phosphides as electrocatalyst for water splitting, Sci. Bull. 62 (2017) 633–644.

[34] M. Luo, W. Yao, C. Huang, Q. Wu, Q. Xu, Shape effects of Pt nanoparticles on hydrogen production via Pt/CdS photocatalysts under visible light, J. Mater. Chem. 3.26 (2015): 13884-13891.

[35] J.F. Callejas, C.G. Read, C.W. Roske, N.S. Lewis, R.E. Schaak, Synthesis, characterization, and properties of metal phosphide catalysts for the hydrogen-evolution reaction, Chem. Mater. 28 (2016) 6017–6044.

[36] H. Huang, X. Huang, Z. Zhu, J. Dai, Hydrothermal synthesis of cobalt phosphide nanoparticles, Ceram. Int. 38 (2012) 1713–1715.

[37] D. Yang, J. Zhu, X. Rui, H. Tan, R. Cai, H.E. Hoster, D.Y.W. Yu, H.H. Hng, Q. Yan, Synthesis of cobalt phosphides and their application as anodes for lithium ion batteries, ACS Appl. Mater. Interfaces. 5 (2013) 1093–1099.

[38] J. Su, J. Zhou, L. Wang, C. Liu, Y. Chen, Synthesis and application of transition metal phosphides as electrocatalyst for water splitting, Sci. Bull. (2016).

[39] S. Guan, X. Fu, Y. Zhang, Z. Peng, β-NiS modified CdS nanowires for photocatalytic H2 evolution with exceptionally high efficiency, Chem. Sci. 9 (2018) 1574–1585.

[40] Y. Xu, Y. Huang, B. Zhang, Rational design of semiconductor-based photocatalysts for advanced photocatalytic hydrogen production: the case of cadmium chalcogenides, Inorg. Chem. Front. 3 (2016) 591–615.

[41] R.J. Braham, A.T. Harris, Review of major design and scale-up considerations for solar photocatalytic reactors, Ind. Eng. Chem. Res. 48 (2009) 8890–8905.

[42] K. Deng, L. Li, CdS Nanoscale Photodetectors, Adv. Mater. 26 (2014) 2619–2635.

[43] A.A. Ismail, D.W. Bahnemann, Photochemical splitting of water for hydrogen production by photocatalysis: A review, Sol. Energy Mater. Sol. Cells. 128 (2014) 85–101.

[44] S. Kohtani, E. Yoshioka, H. Miyabe, Photocatalytic Hydrogenation on Semiconductor Particles, in: Hydrogenation, InTech, 2012.

[45] D. Meissner, R. Memming, B. Kastening, D. Bahnemann, Fundamental problems of water splitting at cadmium sulfide, Chem. Phys. Lett. 127 (1986) 419–423.

[46] J. Marugán, R. van Grieken, A.E. Cassano, O.M. Alfano, Intrinsic kinetic modeling with explicit radiation absorption effects of the photocatalytic oxidation of cyanide with TiO2 and silica-supported TiO2 suspensions, Appl. Catal. B Environ. 85 (2008) 48–60.

[47] G. Palmisano, V. Loddo, V. Augugliaro, M. Bellardita, G. Camera Roda, F. Parrino, Validation of a two-dimensional modeling of an externally irradiated slurry photoreactor, Chem. Eng. J. 262 (2015) 490–498.

[48] J. Sabaté, S. Cervera-March, R. Simarro, J. Giménez, Photocatalytic production of hydrogen from sulfide and sulfite waste streams: a kinetic model for reactions occurring in illuminating suspensions of CdS, Chem. Eng. Sci. 45 (1990) 3089–3096.

[49] H.M.G. Tambago, R.L. De Leon, Intrinsic Kinetic Modeling of Hydrogen Production by Photocatalytic Water Splitting Using Cadmium Zinc Sulfide Catalyst, Int. J. Chem. Eng. Appl. 6 (2015) 220–227.

[50] S.Y. Ryu, J. Choi, W. Balcerski, T.K. Lee, M.R. Hoffmann, Photocatalytic Production of H2 on Nanocomposite Catalysts, Ind. Eng. Chem. Res. 46 (2007) 7476–7488.

[51] D.F. Ollis, Kinetics of Liquid Phase Photocatalyzed Reactions: An Illuminating Approach, J. Phys. Chem. B. 109 (2005) 2439–2444.

[52] C.S. Turchi, D.F. Ollis, Photocatalytic degradation of organic water contaminants: Mechanisms involving hydroxyl radical attack, J. Catal. 122 (1990) 178–192.

[53] C. Casado, R. Timmers, A. Sergejevs, C.T. Clarke, D.W.E. Allsopp, C.R. Bowen, R. van Grieken, J. Marugán, Design and validation of a LED-based high intensity photocatalytic reactor for quantifying activity measurements, Chem. Eng. J. 327 (2017) 1043–1055.

[54] A.E. Cassano, O.M. Alfano, Reaction engineering of suspended solid heterogeneous photocatalytic reactors, Catal. Today. 58 (2000) 167–197.

[55] R.J. Brandi, M.A. Citroni, O.M. Alfano, A.E. Cassano, Absolute quantum yields in photocatalytic slurry reactors, Chem. Eng. Sci. 58 (2003) 979–985.

[56] G. Li Puma, Modeling of Thin-Film Slurry Photocatalytic Reactors Affected by Radiation Scattering, Environ. Sci. Technol. 37 (2003) 5783–5791.

[57] G. Li Puma, J.N. Khor, A. Brucato, Modeling of an Annular Photocatalytic Reactor for Water Purification: Oxidation of Pesticides, Environ. Sci. Technol. 38 (2004) 3737–3745.

[58] O. Alvarado-Rolón, R. Natividad, R. Romero, L. Hurtado, A. Ramírez-Serrano, Modelling and Simulation of the Radiant Field in an Annular Heterogeneous Photoreactor Using a Four-Flux Model, Int. J. Photoenergy. 3(2018) 104-134.

[59] M. Motegh, J. Cen, P.W. Appel, J.R. van Ommen, M.T. Kreutzer, Photocatalytic-reactor efficiencies and simplified expressions to assess their relevance in kinetic experiments, Chem. Eng. J. 208 (2012) 607–615.

[60] P.J. Valades-Pelayo, J. Moreira, B. Serrano, H. de Lasa, Boundary conditions and phase functions in a Photo-CREC Water-II reactor radiation field, Chem. Eng. Sci. 107 (2014) 123–136.

[61] A.L.L. Zazueta, H. Destaillats, G. Li Puma, Radiation field modeling and optimization of a compact and modular multi-plate photocatalytic reactor (MPPR) for air/water purification by Monte Carlo method, Chem. Eng. J. 217 (2013) 475–485.

[62] Two-Dimensional Modeling of an Externally Irradiated Slurry Photoreactor , Int. J. Chem. React. Eng. . 11 (2013) 675.

[63] W. Yao, C. Huang, N. Muradov, A.T. -Raissi, A novel PdeCr 2 O 3 /CdS photocatalyst for solar hydrogen production using a regenerable sacrificial donor, Int. J. Hydrogen Energy. 36 (2011) 4710–4715.

[64] C. Huang, O. Odebiyi, N. Muradov, A.T. Raissi, Hydrogen production via photocatalytic oxidation of aqueous ammonium sulfite solutions, Proceedings, WHEC. 16 (2006) 591–599.

[65] A. FUJISHIMA, K. HONDA, Electrochemical Photolysis of Water at a Semiconductor Electrode, Nature. 238 (1972) 37–38.

[66] S. Licht, B. Wang, S. Mukerji, T. Soga, M. Umeno, H. Tributsch, Over 18% solar energy conversion to generation of hydrogen fuel; theory and experiment for efficient solar water splitting, Int. J. Hydrogen Energy. 26 (2001) 653–659.

[67] Y. Horiuchi, T. Toyao, M. Takeuchi, M. Matsuoka, M. Anpo, Recent advances in visible-light-responsive photocatalysts for hydrogen production and solar energy conversion - from semiconducting TiO2 to MOF/PCP photocatalysts,

Phys. Chem. Chem. Phys. 15 (2013) 13243–13253.

[68] M.S. Prévot, K. Sivula, Photoelectrochemical Tandem Cells for Solar Water Splitting, J. Phys. Chem. C. 117 (2013) 17879–17893.

[69] C. Perkins, A.W. Weimer, Likely near-term solar-thermal water splitting technologies, Int. J. Hydrogen Energy. 29 (2004) 1587–1599.

[70] A. Steinfeld, Solar thermochemical production of hydrogen—a review, Sol. Energy. 78 (2005) 603–615.

[71] S. Abanades, P. Charvin, G. Flamant, P. Neveu, Screening of water-splitting thermochemical cycles potentially attractive for hydrogen production by concentrated solar energy, Energy. 31 (2006) 2805–2822.

[72] T. Nakamura, Hydrogen production from water utilizing solar heat at high temperatures, Sol. Energy. 19 (1977) 467–475.

[73] L. Xiao, S.-Y. Wu, Y.-R. Li, Advances in solar hydrogen production via two-step water-splitting thermochemical cycles based on metal redox reactions, Renew. Energy. 41 (2012) 1–12.

[74] R. Palumbo, J. Léde, O. Boutin, E. Elorza Ricart, A. Steinfeld, S. Möller, A. Weidenkaff, E.A. Fletcher, J. Bielicki, The production of Zn from ZnO in a high-temperature solar decomposition quench process—I. The scientific framework for the process, Chem. Eng. Sci. 53 (1998) 2503–2517.

[75] R. Perret, Solar Thermochemical Hydrogen Production Research (STCH) Thermochemical Cycle Selection and Investment Priority, (2011)1-16.

[76] M. Sturzenegger, J. Ganz, P. Nüesch, T. Schelling, T. Schelling, Solar hydrogen from a manganese oxide based thermochemical cycle, Le J. Phys. IV. 09 (1999) Pr3-331-Pr3-335.

[77] P.B. Kreider, H.H. Funke, K. Cuche, M. Schmidt, A. Steinfeld, A.W. Weimer, Manganese oxide based thermochemical hydrogen production cycle, Int. J. Hydrogen Energy. 36 (2011) 7028–7037.

[78] A. Steinfeld, Solar hydrogen production via a two-step water-splitting thermochemical cycle based on Zn/ZnO redox reactions, Int. J. Hydrogen Energy. 27 (2002) 611–619.

[79] T. Kodama, N. Gokon, Thermochemical cycles for high-temperature solar hydrogen production, Chem. Rev. 107 (2007) 4048–4077.

[80] M.A. Rosen, G.F. Naterer, C.C. Chukwu, R. Sadhankar, S. Suppiah, Nuclear-based hydrogen production with a thermochemical copper-chlorine cycle and supercritical water reactor: equipment scale-up and process simulation, Int. J. Energy Res. 36 (2012) 456–465.

[81] G. Naterer, S. Suppiah, M. Lewis, K. Gabriel, I. Dincer, M.A. Rosen, M. Fowler, G. Rizvi, E.B. Easton, B.M. Ikeda, M.H. Kaye, L. Lu, I. Pioro, P. Spekkens, P.

Tremaine, J. Mostaghimi, J. Avsec, J. Jiang, Recent Canadian advances in nuclear-based hydrogen production and the thermochemical Cu–Cl cycle, Int. J. Hydrogen Energy. 34 (2009) 2901–2917.

[82] T.A.H. Ratlamwala, I. Dincer, Comparative energy and exergy analyses of two solar-based integrated hydrogen production systems, Int. J. Hydrogen Energy. 40 (2015) 7568–7578.

[83] M. DOKIYA, Y. KOTERA, Hybrid cycle with electrolysis using Cu□Cl system☆, Int. J. Hydrogen Energy. 1 (1976) 117–121.

[84] D. O'Keefe, C. Allen, G. Besenbruch, L. Brown, J. Norman, R. Sharp, K. McCorkle, Preliminary results from bench-scale testing of a sulfur-iodine thermochemical water-splitting cycle, Int. J. Hydrogen Energy. 7 (1982) 381–392.

[85] D. O'Keefe, C. Allen, G. Besenbruch, L. Brown, J. Norman, R. Sharp, K. McCorkle, Preliminary results from bench-scale testing of a sulfur-iodine thermochemical water-splitting cycle, Int. J. Hydrogen Energy. 7 (1982) 381–392.

[86] C. Huang, C.A. Linkous, O. Adebiyi, A. T-Raissi, Hydrogen production via photolytic oxidation of aqueous sodium sulfite solutions, Environ. Sci. Technol. 44 (2010) 5283–5288.

[87] a. T-Raissi, N. Muradov, C. Huang, O. Adebiyi, Hydrogen From Solar Via Light-Assisted High-Temperature Water Splitting Cycles, J. Sol. Energy Eng. 129 (2007) 184.

[88] P. LU, Technological aspects of sulfur dioxide depolarized electrolysis for hydrogen production, Int. J. Hydrogen Energy. 8 (1983) 773–781.

[89] L. Mao, A.T. -Raissi, C. Huang, N.Z. Muradov, Thermal decomposition of (NH 4) 2 SO 4 in presence of Mn 3 O 4 Thermal decomposition, Int. J. Hydrogen Energy. 36 (2011) 5822–5827.

[90] C. Huang, O. Odebiyi, N. Muradov, A.T. -Raissi, Hydrogen production via photocatalytic oxidation of aqueous ammonium sulfite solutions, WHEC. 16 (2006) 13–16.

[91] P.J.V. Pelayo, P.J. Valades-Pelayo, Scale-Up Methodology for Bench-Scale Slurry Photocatalytic Reactors Using Combined Irradiation and Kinetic Modelling, Int. J. Hydrogen Energy. 168–169 (2014) 4850–4856.

[92] H. de Lasa, B. Serrano, M. Salaices, Photocatalytic Reaction Engineering, Springer US, Boston, MA, 2005.

[93] Z. Xing, X. Zong, J. Pan, L. Wang, On the engineering part of solar hydrogen production from water splitting: Photoreactor design, Chem. Eng. Sci. 104 (2013) 125–146.

[94] F.E. Osterloh, Inorganic Materials as Catalysts for Photochemical Splitting of Water, Chem. Mater. 20 (2008) 35–54.

[95] A.L. Linsebigler, G. Lu, J.T. Yates, Photocatalysis on TiO2 Surfaces: Principles, Mechanisms, and Selected Results, Chem. Rev. 95 (1995) 735–758.

[96] W. Wang, Y. Ye, J. Feng, M. Chi, J. Guo, Y. Yin, Enhanced photoreversible color switching of redox dyes catalyzed by barium-doped TiO2 nanocrystals, Angew. Chemie - Int. Ed. (2015).

[97] L. Kuang, W. Zhang, Enhanced hydrogen production by carbon-doped TiO_2 decorated with reduced graphene oxide (rGO) under visible light irradiation, RSC Adv. 6 (2016) 2479–2488.

[98] M. Sun, H. Liu, J. Qu, J. Li, Earth-Rich Transition Metal Phosphide for Energy Conversion and Storage, Adv. Energy Mater. 6 (2016) 1600087.

[99] S. Cao, C. Wang, W. Fu, Y. Chen, Metal Phosphides as Co-Catalysts for Photocatalytic and Photoelectrocatalytic Water Splitting, ChemSusChem. 10 (2017) 4306–4323.

[100] W. Zhao, W. Ma, C. Chen, J. Zhao, Z. Shuai, Efficient degradation of toxic organic pollutants with Ni2O3/TiO(2-x)Bx under visible irradiation., J. Am. Chem. Soc. 126 (2004) 4782–3.

[101] X.-Z. Bu, G.-K. Zhang, Y.-Y. Gao, Y.-Q. Yang, Preparation and photocatalytic properties of visible light responsive N-doped TiO2/rectorite composites, Microporous Mesoporous Mater. 136 (2010) 132–137.

[102] K. Lalitha, J.K. Reddy, V. Durgakumari, M. Subrahmanyam, Enhanced H2 Production Activity Under Solar Irradiation Over N-Doped TiO2 Prepared Using Pyridine as a Precursor: A Typical Sample of N-Doped TiO2 Series, Mater. Tech. 32.1 (2017) 52-63.

[103] L. Yang, H. Zhou, T. Fan, D. Zhang, Semiconductor photocatalysts for water oxidation: current status and challenges, Phys. Chem. Chem. Phys. 16 (2014) 6810.

[104] J.F. Reber, M. Rusek, Photochemical hydrogen production with platinized suspensions of cadmium sulfide and cadmium zinc sulfide modified by silver sulfide, J. Phys. Chem. 90 (1986) 824–834.

[105] L. Shangguan, W. Zhu, Y. Xue, S. Liu, Construction of photoelectrochemical thrombin aptasensor via assembling multilayer of graphene–CdS nanocomposites, Biosens. Bioelectron. 64 (2015) 611–617.

[106] X. Zhou, J. Jin, X. Zhu, J. Huang, J. Yu, W.-Y. Wong, W.-K. Wong, New $Co(OH)_2$ /CdS nanowires for efficient visible light photocatalytic hydrogen production, J. Mater. Chem. A. 4 (2016) 5282–5287.

[107] H. Yu, F. Chen, F. Chen, X. Wang, In situ self-transformation synthesis of g-

C3N4-modified CdS heterostructure with enhanced photocatalytic activity, Appl. Surf. Sci. 358 (2015) 385–392.

[108] G.S. Borghetti, J.P. Carini, S.B. Honorato, A.P. Ayala, J.C.F. Moreira, V.L. Bassani, Physicochemical properties and thermal stability of quercetin hydrates in the solid state, Thermochim. Acta. 539 (2012) 109–114.

[109] M. Wang, S. Shen, L. Li, Z. Tang, J. Yang, Effects of sacrificial reagents on photocatalytic hydrogen evolution over different photocatalysts, J. Mater. Sci. 52 (2017) 5155–5164.

[110] W. Yao, X. Song, C. Huang, Q. Xu, Q. Wu, Enhancing solar hydrogen production via modified photochemical treatment of Pt/CdS photocatalyst, Catal. Today. 199 (2013) 42–47.

[111] I. Vamvasakis, B. Liu, G.S. Armatas, Size effects of platinum nanoparticles in the photocatalytic hydrogen production over 3D mesoporous networks of CdS and Pt nanojunctions, Adv. Funct. Mater. 26 (2016) 8062–8071.

[112] J. Yu, J. Zhang, M. Jaroniec, Preparation and enhanced visible-light photocatalytic H2-production activity of CdS quantum dots-sensitized Zn1-xCdxS solid solution, Green Chem. 12 (2010) 1611–1614.

[113] J. Zang, G. Zhao, G. Han, Preparation of CdS nanoparticles by hydrothermal method in microemulsion, Front. Chem. China. 2 (2007) 98–101.

[114] H. Yang, C. Huang, X. Li, R. Shi, K. Zhang, Luminescent and photocatalytic properties of cadmium sulfide nanoparticles synthesized via microwave irradiation, Mater. Chem. Phys. 90 (2005) 155–158.

[115] A. Broido, A simple, sensitive graphical method of treating thermogravimetric analysis data, J. Polym. Sci. Part A-2 Polym. Phys. 7 (1969) 1761–1773.

[116] W. Bi, L. Zhang, Z. Sun, X. Li, T. Jin, X. Wu, Q. Zhang, Y. Luo, C. Wu, Y. Xie, Insight into Electrocatalysts as Co-catalysts in Efficient Photocatalytic Hydrogen Evolution, ACS Catal. 6 (2016) 4253–4257.

[117] W.-K. Jo, R.J. Tayade, New Generation Energy-Efficient Light Source for Photocatalysis: LEDs for Environmental Applications, Ind. Eng. Chem. Res. 53 (2014) 2073–2084.

[118] M. Khademalrasool, M. Farbod, M.D. Talebzadeh, The improvement of photocatalytic processes: Design of a photoreactor using high-power LEDs, J. Sci. Adv. Mater. Devices. 1 (2016) 382–387.

[119] E. Taylor-Shaw, E. Angioni, N.J. Findlay, B. Breig, A.R. Inigo, J. Bruckbauer, D.J. Wallis, P.J. Skabara, R.W. Martin, Cool to warm white light emission from hybrid inorganic/organic light-emitting diodes, J. Mater. Chem. C. 4 (2016) 11499–11507.

[120] C. Hammond, C. Hammond, The Basics of Cristallography and Diffraction,

Oxford, 2001.

[121] E. Charsley, D. Price, N. Hunter, P. Gabbott, V. Kett, S. Gaisford, I. Priestley, J. Duncan, P. Royall, I. Scowen, Principles of thermal analysis and calorimetry, Royal society of chemistry, 2019.

[122] O.L. Krivanek, T.C. Lovejoy, N. Dellby, T. Aoki, R.W. Carpenter, P. Rez, E. Soignard, J. Zhu, P.E. Batson, M.J. Lagos, Vibrational spectroscopy in the electron microscope, Nature. 514 (2014) 209.

[123] P.D. Ngo, Energy dispersive spectroscopy, in: Fail. Anal. Integr. Circuits, Springer, (1999) 205–215.

[124] H.-H. Perkampus, UV-VIS Spectroscopy and its Applications, Springer Science & Business Media, 2013.

[125] K. Venkateswarlu, A.C. Bose, N. Rameshbabu, X-ray peak broadening studies of nanocrystalline hydroxyapatite by Williamson–Hall analysis, Phys. B Condens. Matter. 405 (2010) 4256–4261.

[126] H. Small, T.S. Stevens, W.C. Bauman, Novel ion exchange chromatographic method using conductimetric detection, Anal. Chem. 47 (1975) 1801–1809.

[127] H.H. Willard, L.L. Merritt Jr, J.A. Dean, F.A. Settle Jr, Instrumental methods of analysis, (1988).

[128] L.A. Silva, S.Y. Ryu, J. Choi, W. Choi, M.R. Hoffmann, Photocatalytic hydrogen production with visible light over Pt-interlinked hybrid composites of cubic-phase and hexagonal-phase CdS, J. Phys. Chem. C. 112 (2008) 12069–12073.

[129] B.S. Rao, B.R. Kumar, V.R. Reddy, T.S. Rao, Preparation and characterization of CdS nanoparticles by chemical co-precipitation technique, Chalcogenide Lett. 8 (2011) 177–185.

[130] B.D. Cullity, Elements of X-ray diffraction. Morris Cohen, editor, (1977).

[131] M. Khatamian, M.S. Oskoui, M. Haghighi, Photocatalytic hydrogen generation over CdS–metalosilicate composites under visible light irradiation, New J. Chem. 38 (2014) 1684–1693.

[132] Y.-J. Yuan, D. Chen, Z.-T. Yu, Z.-G. Zou, Cadmium sulfide-based nanomaterials for photocatalytic hydrogen production, J. Mater. Chem. A. 6 (2018) 11606–11630.

[133] X. Wang, Z. Feng, D. Fan, F. Fan, C. Li, Shape-controlled synthesis of CdS nanostructures via a solvothermal method, Cryst. Growth Des. 10 (2010) 5312–5318.

[134] B. Zhang, W. Yao, C. Huang, Q. Xu, Q. Wu, Shape effects of CdS photocatalysts on hydrogen production, Int. J. Hydrogen Energy. 38 (2013) 7224–7231.

[135] Y. Cao, P. Hu, D. Jia, Phase- and shape-controlled hydrothermal synthesis of

CdS nanoparticles, and oriented attachment growth of its hierarchical architectures, Appl. Surf. Sci. 265 (2013) 771–777.

[136] N. Soltani, E. Saion, M.Z. Hussein, M. Erfani, A. Abedini, G. Bahmanrokh, M. Navasery, P. Vaziri, Visible light-induced degradation of methylene blue in the presence of photocatalytic ZnS and CdS nanoparticles, Int. J. Mol. Sci. 13 (2012) 12242–12258.

[137] J. Barman, J.P. Borah, K.C. Sarma, Synthesis and characterization of CdS nanoparticles by chemical growth technique, Optoelectron. Adv. Mater. Rapid Commun. 2 (2008) 770–774.

[138] A.S. Hassanien, A.A. Akl, Influence of composition on optical and dispersion parameters of thermally evaporated non-crystalline Cd50S50− xSex thin films, J. Alloys Compd. 648 (2015) 280–290.

[139] D.K. Dwivedi, D. Shankar, M. Dubey, Synthesis, structural and optical characterization of CdS nanoparticles, J. Ovonic Res. 6 (2010) 57–62.

[140] S.H. Kaufman, J.M. Weber, M. Pernpointner, Electronic structure and UV spectrum of hexachloroplatinate dianions in vacuo, J. Chem. Phys. 139 (2013) 194310.

[141] S.T. Briskeby, M. Tsypkin, R. Tunold, S. Sunde, Preparation of electrocatalysts by reduction of precursors with sodium citrate, RSC Adv. 4 (2014) 44185–44192.

[142] T. Maji, S. Banerjee, M. Biswas, T.K. Mandal, In situ synthesis of ultra-small platinum nanoparticles using a water soluble polyphenolic polymer with high catalytic activity, RSC Adv. 4 (2014) 51745–51753.

[143] S. Liu, Z. Guo, X. Qian, J. Zhang, J. Liu, J. Lin, Sonochemical deposition of ultrafine metallic Pt nanoparticles on CdS for efficient photocatalytic hydrogen evolution, Sustain. Energy Fuels. (2019).

[144] J. Wang, Z. Liu, Y. Zheng, L. Cui, W. Yang, J. Liu, Recent advances in cobalt phosphide based materials for energy-related applications, J. Mater. Chem. A. 5 (2017) 22913–22932.

[145] D.-H. Ha, L.M. Moreau, C.R. Bealing, H. Zhang, R.G. Hennig, R.D. Robinson, The structural evolution and diffusion during the chemical transformation from cobalt to cobalt phosphide nanoparticles, J. Mater. Chem. 21 (2011) 11498–11510.

[146] A.E. Henkes, Y. Vasquez, R.E. Schaak, Converting metals into phosphides: a general strategy for the synthesis of metal phosphide nanocrystals, J. Am. Chem. Soc. 129 (2007) 1896–1897.

[147] I. Pagana, R. Morawicki, T.J. Hager, Lactic acid production using waste generated from sweet potato processing, Int. J. Food Sci. Technol. 49 (2014) 641–649.

[148] Y. Pellegrin, F. Odobel, Sacrificial electron donor reagents for solar fuel production, Comptes Rendus Chim. 20 (2017) 283–295.

[149] S. Huang, Y. Lin, J.-H. Yang, Y. Yu, CdS-Based Semiconductor Photocatalysts for Hydrogen Production from Water Splitting under Solar Light, in: 2013: pp. 219–241.

[150] M.R. Gholipour, C.-T. Dinh, F. Béland, T.-O. Do, Nanocomposite heterojunctions as sunlight-driven photocatalysts for hydrogen production from water splitting, Nanoscale. 7 (2015) 8187–8208.

[151] H. Li, L. Liu, Z. Wang, X. Zheng, S. Meng, S. Chen, X. Fu, Optimizing the precursor of sulfur source for hydrothermal synthesis of high performance CdS for photocatalytic hydrogen production, RSC Adv. 8 (2018) 11489–11497.

[152] A. Abdolahzadeh Ziabari, F.E. Ghodsi, Influence of Cu doping and post-heat treatment on the microstructure, optical properties and photoluminescence features of sol–gel derived nanostructured CdS thin films, J. Lumin. 141 (2013) 121–129.

[153] K. Kumar, M. Chitkara, I.S. Sandhu, D. Mehta, S. Kumar, Photocatalytic, optical and magnetic properties of Fe-doped ZnO nanoparticles prepared by chemical route, J. Alloys Compd. 588 (2014) 681–689.

[154] P.N. Devi, J. Sathiyabama, S. Rajendran, Study of surface morphology and inhibition efficiency of mild steel in simulated concrete pore solution by lactic acid–Zn 2+ system, Int J Corros Scale Inhib. 6 (2017) 18–31.

[155] M.J.N. Pourbaix, J. Van Muylder, N. De Zoubov, Electrochemical properties of the platinum metals, Platin. Met. Rev. 3 (1959) 47–53.

[156] V. Mohanraj, R. Jayaprakash, J. Chandrasekaran, R. Robert, P. Sangaiya, Influence of pH on particle size, band-gap and activation energy of CdS nanoparticles synthesized at constant frequency ultrasonic wave irradiation, Mater. Sci. Semicond. Process. 66 (2017) 131–139.

[157] P. Baláž, Z. Bujňáková, E. Dutková, M. Baláž, A. Zorkovská, J. Kováč, J. Kováč Jr, M. Kello, G. Mojžišová, J. Mojžiš, Mixed Core CdS@ ZnS Nanocrystals: Synthesis, Cadmium Dissolution and Cancer Cells Management, in: 4th Int. Conf. Res. Front. Chalcogen Cycle Sci. Technol., 2015: p. 11.

[158] N. Bao, L. Shen, T. Takata, K. Domen, Self-Templated Synthesis of Nanoporous CdS Nanostructures for Highly Efficient Photocatalytic Hydrogen Production under Visible Light, J. Chemi. Mater. 20.1 (2008) 110-117.

[159] X. Li, J. Yu, J. Low, Y. Fang, J. Xiao, X. Chen, Engineering heterogeneous semiconductors for solar water splitting, J. Mater. Chem. A. 3 (2015) 2485–9.

[160] M. Tokumura, H. Tawfeek Znad, Y. Kawase, Modeling of an external light irradiation slurry photoreactor: UV light or sunlight-photoassisted Fenton discoloration of azo-dye Orange II with natural mineral tourmaline powder,

Chem. Eng. Sci. 61 (2006) 6361–6371.

[161] M. Hallquist, D.J. Stewart, S.K. Stephenson, R.A. Cox, Hydrolysis of N 2 O 5 on sub-micron sulfate aerosols, Phys. Chem. Chem. Phys. 5 (2003) 3453–3463.

[162] A.E. Kalyva, E.C. Vagia, A.G. Konstandopoulos, A.R. Srinivasa, A. T-Raissi, N. Muradov, K.E. Kakosimos, Hybrid photo-thermal sulfur-ammonia water splitting cycle: Thermodynamic analysis of the thermochemical steps, Int. J. Hydrogen Energy. 42 (2017) 9533–9544.

[163] C. Huang, O. Odebiyi, N. Muradov, A.T. -Raissi, Hydrogen Production via UV Photolysis of Aqueous Ammonium Sulfite Solutions, WHEC. 16 (2006) 13–16.

[164] C. Costentin, D.G. Nocera, Self-healing catalysis in water, Proc. Natl. Acad. Sci. 114 (2017) 13380 LP-13384.

Appendix A: Geometrical derivation of L_i and θ_i for LED-lights

Fig. A1 shows the positions of the lights surrounding the reactor and the corresponding L_i, θ_i. For a particle positioned at a point P with a given θ_1 and L_1, the below trigonometrical relations can be developed for each L_i, θ_i(i=2…) as:

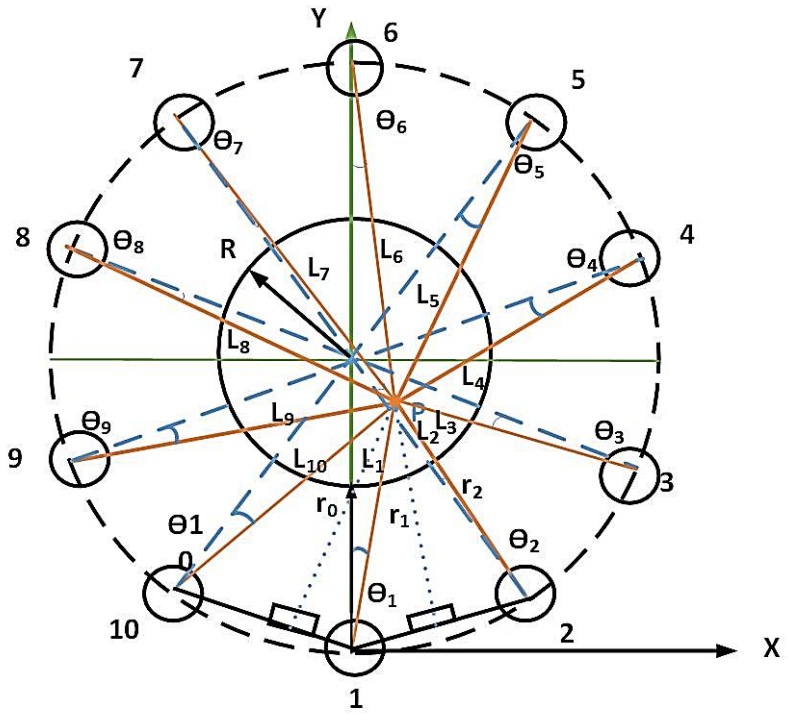

Fig A1. Schematic position of photoreactor and lamps used for the geometrical derivation of L_i, θ_i. r_1 and r_2 indicate distance between random point of P and light of 1 and 2 while r_0 represents the distance between light 1 and the surface of the reactor.

Lamp 2 coordinates:

$$\theta_2 = -\frac{2\pi}{5} + arctan\left[\frac{(L_1+r_1)\,sin\,(\frac{2\pi}{5}-\theta_1)}{2\,(R+r_0)\,cos\,(\frac{2\pi}{5}) - (L_1+r_1)\,cos\,(\frac{2\pi}{5}-\theta_1)}\right] \quad (A_1)$$

$$L_2 = (L_1 + r_1)\,\frac{sin\,(\frac{2\pi}{5}-\theta_1)}{sin\,(\frac{2\pi}{5}+\theta_2)} - cos\,\theta_2(R + r_0) + \sqrt{cos^2\theta_2(R + r_0)^2 - r_0^2 - 2Rr_0} \quad (A_2)$$

Lamp 3 coordinates:

$$\theta_3 = -\frac{2\pi}{5} + arctan\left[\frac{(L_2+r_2)\ sin\ (\frac{2\pi}{5}-\theta_2)}{2\ (R+r_0)\ cos\ (\frac{2\pi}{5}) - (L_2+r_2)\ cos\ (\frac{2\pi}{5}-\theta_2)}\right] \quad (A_3)$$

$$L_3 = (L_2 + r_2)\ \frac{sin\ (\frac{2\pi}{5}-\theta_2)}{sin\ (\frac{2\pi}{5}+\theta_3)} - cos\ \theta_3(R + r_0) + \sqrt{cos^2\theta_3(R + r_0)^2 - r_0^2 - 2Rr_0} \quad (A_4)$$

Lamp 4 coordinates:

$$\theta_4 = -arctan\left[\frac{(L_9+r_9)\ sin\ (\theta_9)}{2\ (R+r_0)\ -(L_9+r_9)\ cos\ (\theta_9)}\right] \quad (A_5)$$

$$L_4 = \frac{2\ (R+r_0)\ -(L_9+r_9)\ cos\ (\theta_9)}{cos\ (\theta_4)} - cos\ \theta_4(R + r_0) + \sqrt{cos^2\theta_4(R + r_0)^2 - r_0^2 - 2Rr_0} \quad (A_6)$$

Lamp 5 coordinates:

$$\theta_5 = -arctan\left[\frac{(L_{10}+r_{10})\ sin\ (\theta_{10})}{2\ (R+r_0)\ -(L_{10}+r_{10})\ cos\ (\theta_{10})}\right] \quad (A_7)$$

$$L_5 = \frac{2\ (R+r_0) - (L_{10}+r_{10})\ cos\ (\theta_{10})}{cos\ (\theta_5)} - cos\ \theta_5(R + r_0) + \sqrt{cos^2\theta_5(R + r_0)^2 - r_0^2 - 2Rr_0} \quad (A_8)$$

Lamp 6 coordinates:

$$\theta_6 = -arctan\left[\frac{(L_1+r_1)\ sin\ (\theta_1)}{2\ (R+r_0)\ -(L_1+r_1)\ cos\ (\theta_1)}\right] \quad (A_9)$$

$$L_6 = \frac{2\ (R+r_0)\ -(L_1+r_1)\ cos\ (\theta_1)}{cos\ (\theta_6)} - cos\ \theta_6(R + r_0) + \sqrt{cos^2\theta_6(R + r_0)^2 - r_0^2 - 2Rr_0} \quad (A_{10})$$

Lamp 7 coordinates:

$$\theta_7 = -arctan\left[\frac{(L_2+r_2)\ sin\ (\theta_2)}{2\ (R+r_0)\ -(L_2+r_2)\ cos\ (\theta_2)}\right] \quad (A_{11})$$

$$L_7 = \frac{2\ (R+r_0)\ -(L_2+r_2)\ cos\ (\theta_2)}{cos\ (\theta_7)} - cos\ \theta_7(R + r_0) + \sqrt{cos^2\theta_7(R + r_0)^2 - r_0^2 - 2Rr_0} \quad (A_{12})$$

Lamp 8 coordinates:

$$\theta_8 = -arctan\left[\frac{(L_3+r_3)\ sin\ (\theta_3)}{2\ (R+r_0)\ -(L_3+r_3)\ cos\ (\theta_3)}\right] \quad (A_{13})$$

$$L_8 = \frac{2\,(R+r_0)\ -(L_3+r_3)\,cos\,(\theta_3)}{cos\,(\theta_8)}\ - cos\,\theta_8(R+r_0) + \sqrt{cos^2\theta_8(R+r_0)^2 - r_0^2 - 2Rr_0}$$

(A14)

Lamp 9 coordinates:

$$\theta_9 = \frac{2\pi}{5} - arctan\left[\frac{(L+r_{10})\,sin\,(\frac{2\pi}{5}+\theta_2)}{2\,(R+r_0)\,cos\,(\frac{2\pi}{5}) - (L_{10}+r_{10})\ cos\,(\frac{2\pi}{5}+\theta_2)}\right] \quad \text{(A15)}$$

$$L_9 = (L_{10}+r_{10})\,\frac{sin\,(\frac{2\pi}{5}+\theta_{10})}{sin\,(\frac{2\pi}{5}-\theta_9)}\ - cos\,\theta_9(R+r_0) + \sqrt{cos^2\theta_9(R+r_0)^2 - r_0^2 - 2Rr_0}$$

(A16)

Lamp 10 coordinates:

$$\theta_{10} = \frac{2\pi}{5} - arctan\left[\frac{(L_1+r_1)\,sin\,(\frac{2\pi}{5}+\theta_1)}{2\,(R+r_0)\,cos\,(\frac{2\pi}{5}) - (L+r_1)\ cos\,(\frac{2\pi}{5}+\theta_1)}\right] \quad \text{(A17)}$$

$$L_{10} = (L_1+r_1)\,\frac{sin\,(\frac{2\pi}{5}+\theta_1)}{sin\,(\frac{2\pi}{5}-\theta_{10})}\ - cos\,\theta_{10}(R+r_0) + \sqrt{cos^2\theta_{10}(R+r_0)^2 - r_0^2 - 2Rr_0}$$

(A18)

Appendix B: MATLAB Program for the hydrogen predication rate

m.file 1

```
% geometrical input

function y = intensity(l1, theta, lnum)
global r0 R;

theta1 = theta;
angel  = deg2rad(72);

r1 = (r0 + R) * cos(theta1)- sqrt((r0 + R) ^ 2 * cos(theta1) ^ 2 - r0
^ 2 - 2 * r0 * R);
theta0 =  acos(sqrt(2 * R * r0 + r0 ^ 2) / (R + r0));
maxl = cos(theta1) * (R + r0) + sqrt(cos(theta1) ^ 2 * ( R + r0) ^ 2
- r0 ^ 2 - 2 * R * r0) - r1;
    if (theta1 > theta0) || (l1 > maxl) || (l1 < 0)
        display("error", theta0, maxl);
        return;
    end

theta2 = atan(((l1 + r1) * sin (angel - theta1)) / (2 * (R + r0) *
cos(angel) - (l1 + r1) * cos(angel - theta1))) - angel;
r2 = (r0 + R) * cos(theta2) - sqrt((r0 + R) ^ 2 * cos(theta2) ^ 2 -
r0 ^ 2 - 2 * r0 * R);
l2 = (r1 + l1) * sin(angel - theta1) / sin(angel + theta2) - r2;

theta3 = atan(((l2 + r2) * sin(angel - theta2)) / (2 * (R + r0) *
cos(angel) - (l2 + r2) * cos(angel - theta2))) - angel;
r3 = (r0 + R) * cos(theta3) - sqrt((r0 + R) ^ 2 * cos(theta3) ^ 2 -
r0 ^ 2 - 2 * r0 * R);
l3 = ((r2 + l2) * sin(angel - theta2)) / sin(angel + theta3) - r3;

theta6 = -atan(((r1 + l1) * sin(theta1)) / (2 * (R + r0) - (r1 + l1)
* cos(theta1)));
r6 = (r0 + R) * cos(theta6) - sqrt((r0 + R) ^ 2 * cos(theta6) ^ 2 -
r0 ^ 2 - 2 * r0 * R);
l6 = (2 * (R + r0) - (r1 + l1) * cos(theta1)) / cos(theta6) - r6;

theta7 = -atan(((r2 + l2) * sin(theta2)) / (2 * (R + r0) - (r2 + l2)
* cos(theta2)));
r7 = (r0 + R) * cos(theta7) - sqrt((r0 + R) ^ 2 * cos(theta7) ^ 2 -
r0 ^ 2 - 2 * r0 * R);
l7 = (2 * (R + r0) - (r2 + l2) * cos(theta2)) / cos(theta7) - r7;

theta8 = -atan(((r3 + l3) * sin(theta3)) / (2 * (R + r0) - (r3 + l3)
* cos(theta3)));
r8 = (r0 + R) * cos(theta8) - sqrt((r0 + R) ^ 2 * cos(theta8) ^ 2 -
r0 ^ 2 - 2 * r0 * R);
l8 = (2 * (R + r0) - (r3 + l3) * cos(theta3)) / cos(theta8) - r8;

theta10 = angel - atan(((l1 + r1) * sin(angel + theta1)) / (2 * (R +
r0) * cos(angel) - (l1 + r1) * cos(angel + theta1)));
```

```
r10 = (r0 + R) * cos(theta10) - sqrt((r0 + R) ^ 2 * cos(theta10) ^ 2
- r0 ^ 2 - 2 * r0 * R);
l10 = ((r1 + l1) * sin(angel + theta1)) / sin(angel - theta10) - r10;

theta9 = angel - atan(((l10 + r10) * sin(angel + theta10)) / (2 * (R
+ r0) * cos(angel) - (l10 + r10) * cos(angel + theta10)));
r9 = (r0 + R) * cos(theta9)- sqrt((r0 + R) ^ 2 * cos(theta9) ^ 2 - r0
^ 2 - 2 * r0 * R);
l9 = ((r10 + l10) * sin(angel + theta10)) / sin(angel - theta9) - r9;

theta4 = -atan(((r9 + l9) * sin(theta9)) / (2 * (R + r0) - (r9 + l9)
* cos(theta9)));
r4 = (r0 + R) * cos(theta4) - sqrt((r0 + R) ^ 2 * cos(theta4) ^ 2 -
r0 ^ 2 - 2 * r0 * R);
l4 = (2 * (R + r0) - (r9 + l9) * cos(theta9)) / cos(theta4) - r4;

theta5 = -atan(((r10 + l10) * sin(theta10)) / (2 * (R + r0) - (r10 +
l10) * cos(theta10)));
r5 = (r0 + R) * cos(theta5) - sqrt((r0 + R) ^ 2 * cos(theta5) ^ 2 -
r0 ^ 2 - 2 * r0 * R);
l5 = (2 * (R + r0) - (r10 + l10) * cos(theta10)) / cos(theta5) - r5;

allI = [l1 l2 l3 l4 l5 l6 l7 l8 l9 l10; theta1 theta2 theta3 theta4
theta5 theta6 theta7 theta8 theta9 theta10; r1 r2 r3 r4 r5 r6 r7 r8
r9 r10];
    y = allI(1:3, lnum);

end
```

m.file 2

```
function y = Icalc(l1, theta, cCat, lnum)
global r0;
sstar = 1e4;
kstar = 0.16e4;
Rinfinity = 1 + kstar / sstar - sqrt((kstar/sstar) ^ 2  + 2 * (kstar
/ sstar));
b = sqrt((1 + kstar / sstar) ^ 2 - 1);

y = 0;
for i = 1 : lnum
    ltr = intensity(l1, theta, i);
      y = y + r0 * (1 - Rinfinity ^ 2) * exp(-2 * b * sstar * cCat *
ltr(1, 1)) / ltr(3 , 1);
end
end
```

m.file 3

```
function result = latest(cCat, I0, LA, K1, Kminus, Kprim )
```

```
global R r0;


deltatheta = 0.5;
deltal = 0.5;

theta0 = acos(sqrt(2 * R * r0 + r0 ^ 2) / (R + r0));
result = 0;
for theta = -theta0 : deltatheta : theta0
    r1 = real(cos(theta) .* (R + r0) - sqrt(cos(theta) .^ 2 .* ( R +
  r0) .^ 2 - r0 .^ 2 - 2 .* R .* r0));
    r2 = real(cos(theta) .* (R + r0) + sqrt(cos(theta) .^ 2 .* ( R +
  r0) .^ 2 - r0 .^ 2 - 2 .* R .* r0));
    for l = 0 : deltal : r2 - r1
        LVREA =  I0 .* Icalc(l, theta, cCat, 10);
          LVRPA = 0;
          for lambda = 414 : 1 : 500
           LVRPA = LVRPA +  lambda ;
         end
        LVRPA = LVRPA .* LVREA .* 1.0e-9 ./ (6.626e-34 .* 2.998e8) ;
result = result + (Kprim .* LVREA .^ 0.52) ./  (Kminus +(Kprim .*
LVREA .^ 0.52)  + K1 .* LA ).* (r1 + l) .* deltal .* deltatheta;

    end
end
result = real(result .* 0.04 .* 3.14 .* R^2 .* cCat.* 15 .* 6.92e-
3.* 1e5 .*  K1 .*   LA );

end
```

m.file 4

```
function sumobj = objective(K)
global cCatV I0V LAV H2V ;
sumobj = 0;
for i = 1 : 64
    sumobj = sumobj + (latest(cCatV(i), I0V(i), LAV(i), K(1), K(2),
K(3)) - H2V(i)) .^ 2;
end
end
```

m.file 5

```
global cCatV I0V LAV H2V;
global R r0;

R = 1;
r0 = 4;

% optimization
```

```
cCatV = [   0.000666667 0.000666667 0.000666667 0.000666667
0.000666667 0.000666667 0.000666667  0.000666667  0.00033   0.00033
0.00033 0.00033 0.00033 0.00033 0.00033     0.00033 0.0002  0.0002
0.0002  0.0002  0.0002  0.0002  0.0002  0.0002      6.66667E-05
6.66667E-05 6.66667E-05 6.66667E-05 6.66667E-05 6.66667E-05
6.66667E-05 6.66667E-05     0.000666667 0.000666667 0.000666667
0.000666667 0.000666667 0.000666667 0.000666667 0.000666667
0.000666667 0.000666667 0.000666667 0.000666667 0.000666667
0.000666667 0.000666667 0.000666667 0.000666667 0.000666667
0.000666667 0.000666667 0.000666667 0.000666667 0.000666667
0.000666667 0.000666667 0.000666667 0.000666667     ];

I0V = [ 6   6   6   6   6   6   6   6   6   6   6   6   6   6   6
6 6 6   6   6   6 6 6 6 6 6 6 6 6 6 6  6  4 4 4 4 4 4 4 4
2 2 2 2 2 2 2 2     6 6 6 6 6 6 6 6     6 6 6 6 6 6 6 6  ];

LAV = [  2.643865466    2.419267808 2.04    1.8 1.74    1.6     1.64
1.513326644         2.651970426 2.433840484 2.03    1.94    1.81
1.7 1.64    1.566402594       2.555035344   2.444225056 2.042 1.91
1.84    1.72    1.64 1.499068156     2.558400147    2.457985438 2.2
2.04    1.94    1.83    1.74    1.445405951       2.642792559
2.428495855 2.034   1.9 1.8 1.74    1.68    1.57    2.313961914
2.221257162 2.1 2.002   1.93    1.65    1.43    1.41
1.306677779 1.287771601 1.0156  0.9834  0.91    0.8 0.85    0.7
0.536582311 0.528961169 0.5 0.48    0.44 0.42   0.3034  0.25];

H2V = [  0.190010004    0.204980489 0.184252125 0.154178811
0.15674665  0.126673336 0.139167861 0.121824245     0.122468673
0.151082849 0.110053717 0.101691185 0.11560127  0.076685991
0.066384888 0.091565363  0.096927689    0.090085735 0.066138894
0.070700197 0.071840523 0.062033721 0.055419832 0.050174333
0.068887667 0.03455903  0.024191321 0.0215741   0.016127547
0.019698647 0.016012351 0.01358345          0.119139201 0.12723604
0.11798251  0.120295892 0.112199053 0.113355745 0.114512436
0.226939522     0.105872937 0.105872937 0.089761838 0.069047568
0.074801532 0.069047568 0.063293604 0.050634883     0.164351838
0.11055149  0.105251468 0.094201174 0.089010873 0.086151098
0.078115511 0.071027011             0.10514741  0.040509512
0.03886796  0.029912001 0.029113393 0.028011339 0.027630213
0.026831043     ];

options = optimset('PlotFcns',@optimplotfval);
[x, fval] = fminsearch(@objective,[1,1,1],options);
```

m.file 6

```
% Cumulative hydrogen  with the change of intensity

xlabel('time [min]');
ylabel('H2 evolution [Mmol]');
```

```
z=[ 2.666666667  2.643865466    2.419267808 2.04    1.8 1.74    1.6
1.64    1.513326644 ];
result=[    0 0.190010004   0.204980489 0.184252125 0.154178811
0.15674665  0.126673336 0.139167861 0.121824245 ];
y = zeros(1,9);
for i=1:9
    y(i)=latest(0.0006666,2.6,z(i),0.0767,0.0223, 0.3289);
    if i > 1
        y(i) = y(i) * 1800 + y(i - 1);
        result(i) = result(i) * 1800 + result(i - 1);
    else
        y(i) = y(i) * 1800;
        result(i) = result(i) * 1800;
    end
end


plot([ 0, 30, 60, 90, 120, 150, 180, 210, 240], y(1:9) )
hold on
plot([ 0, 30, 60, 90, 120, 150, 180, 210, 240], result(1:9),
'color', 'k', 'LineStyle' , 'none', 'Marker', '+' )
hold on

z=[ 2.666666667 2.642792559 2.428495855 2.034   1.9 1.8 1.74    1.68
1.57];
result=[ 0  0.198950899 0.119139201 0.12723604  0.11798251
0.120295892 0.112199053 0.113355745 0.114512436];
y = zeros(1,9);
for i=1:9
    y(i)=latest(0.000666,1.2,z(i),0.0767,0.0223, 0.3289);
    if i > 1
        y(i) = y(i) * 1800 + y(i - 1);
        result(i) = result(i) * 1800 + result(i - 1);
    else
        y(i) = y(i) * 1800;
        result(i) = result(i) * 1800;
    end
end

plot([0  30, 60, 90, 120, 150, 180, 210, 240],y(1:9))
hold on
plot([ 0 30, 60, 90, 120, 150, 180, 210, 240], result(1:9), 'color',
'k', 'LineStyle' , 'none', 'Marker', '*')
hold on

z=[ 2.666666667  2.313961914    2.221257162 2.1 2.002   1.93    1.65
1.43    1.41  ];
result=[ 0  0.105872937 0.105872937 0.089761838 0.069047568
0.074801532 0.069047568 0.063293604 0.050634883   ];
y = zeros(1,9);
for i=1:9
    y(i)=latest(0.000666,0.3,z(i),0.0767,0.0223, 0.3289);
    if i > 1
        y(i) = y(i) * 1800 + y(i - 1);
        result(i) = result(i) * 1800 + result(i - 1);
    else
        y(i) = y(i) * 1800;
        result(i) = result(i) * 1800;
    end
end
```

```
  plot([ 0, 30, 60, 90, 120, 150, 180, 210, 240],y(1:9))
hold on
plot([0,  30, 60, 90, 120, 150, 180, 210, 240], result(1:9),
'color', 'k', 'LineStyle' , 'none', 'Marker', 'o')
hold on
```

m.file 7

```
% Cumulative hydrogen evolution with the change of photolyte
concentration

xlabel('time [min]');
ylabel('H2 evolution [Mmol]');


z=[ 2.666666667 2.643865466 2.519267808 2   1.578656095 1.559846497
1.544645697 1.527945554 1.413326644 ];
result=[ 0  0.190010004 0.204980489 0.184252125 0.154178811
0.15674665  0.126673336 0.139167861 0.121824245 ];
y = zeros(1,9);
for i=1:9
    y(i)=latest(0.0006666,3,z(i),0.0767,0.0223, 0.3289);
    if i > 1
        y(i) = y(i) * 1800 + y(i - 1);
        result(i) = result(i) * 1800 + result(i - 1);
    else
        y(i) = y(i) * 1800;
        result(i) = result(i) * 1800;
    end
end


plot([0, 30, 60, 90, 120, 150, 180, 210, 240], y(1:9) )
hold on
plot([0, 30, 60, 90, 120, 150, 180, 210, 240], result(1:9), 'color',
'k', 'LineStyle' , 'none', 'Marker', '+', 'DisplayName', '2.67' )
hold on



z=[ 1.33    1.306677779 1.287771601 1.0156  0.9834  0.91    0.8 0.85
0.7  ];
result=[ 0 0.164351838  0.11055149  0.105251468 0.094201174
0.089010873 0.086151098 0.078115511 0.071027011      ];
y = zeros(1,9);
for i=1:9
    y(i)=latest(0.000666,3,z(i),0.0767,0.0223, 0.3289);
    if i > 1
        y(i) = y(i) * 1800 + y(i - 1);
        result(i) = result(i) * 1800 + result(i - 1);
    else
```

```
        y(i) = y(i) * 1800;
        result(i) = result(i) * 1800;
    end
end



plot([0, 30, 60, 90, 120, 150, 180, 210, 240],y(1:9))
hold on
plot([0, 30, 60, 90, 120, 150, 180, 210, 240], result(1:9), 'color',
'k', 'LineStyle' , 'none', 'Marker', '*','DisplayName', '1.33')
hold on
res=300;

z=[ 0.66    0.536582311 0.528961169 0.5 0.48    0.44 0.42    0.3034
0.25 ];
result=[ 0 0.10514741   0.060509512 0.05886796  0.055912001
0.042113393 0.040011339 0.039630213 0.039831043      ];
y = zeros(1,9);
for i=1:9
    y(i)=latest(0.000666,3,z(i),0.0767,0.0223, 0.3289);
    if i > 1
        y(i) = y(i) * 1800 + y(i - 1);
        result(i) = result(i) * 1800 + result(i - 1);
    else
        y(i) = y(i) * 1800;
        result(i) = result(i) * 1800;
    end
end



plot([0, 30, 60, 90, 120, 150, 180, 210, 240],y(1:9))
hold on
plot([0, 30, 60, 90, 120, 150, 180, 210, 240], result(1:9), 'color',
'k', 'LineStyle' , 'none', 'Marker', 'o')
hold on
```

m.file 8

```
% cumulative hydrogen with the change of the catalyst loading

xlabel('time [min]');
ylabel('H2 evolution [Mmol]');


z=[ 2.6666667   2.643865466 2.419267808 2.04    1.8 1.74    1.6
1.64    1.513326644 ];
result=[  0 0.190010004 0.204980489 0.184252125 0.154178811
0.15674665  0.126673336 0.139167861 0.121824245 ];
y = zeros(1,9);
for i=1:9
    y(i)=latest(0.0006666,2.5,z(i),0.0767,0.0223, 0.3289);
    if i > 1
        y(i) = y(i) * 1800 + y(i - 1);
        result(i) = result(i) * 1800 + result(i - 1);
    else
        y(i) = y(i) * 1800;
```

```
        result(i) = result(i) * 1800;
    end
end


plot ([0, 30, 60, 90, 120, 150, 180, 210, 240], y(1:9))
hold on
plot ([ 0, 30, 60, 90, 120, 150, 180, 210, 240], result(1:9),
'color', 'k', 'LineStyle' , 'none', 'Marker', '+' )
hold on


z=[ 2.666666667 2.651970426 2.433840484 2.03    1.94    1.81    1.7
1.64    1.566402594  ];
result=[ 0  0.162468673 0.161082849 0.130053717 0.131691185
0.1260127   0.11685991  0.10384888  0.090065363  ];
y = zeros(1,9);
for i=1:9
    y(i)=latest(0.00033,2.5,z(i),0.0767,0.0223, 0.3289);
    if i > 1
        y(i) = y(i) * 1800 + y(i - 1);
        result(i) = result(i) * 1800 + result(i - 1);
    else
        y(i) = y(i) * 1800;
        result(i) = result(i) * 1800;
    end
end


plot([0, 30, 60, 90, 120, 150, 180, 210, 240],y(1:9))
hold on
plot([0, 30, 60, 90, 120, 150, 180, 210, 240], result(1:9), 'color',
'k', 'LineStyle' , 'none', 'Marker', '*')
hold on

z=[ 2.666666667 2.555035344 2.444225056 2.042 1.91  1.84    1.72
1.64 1.499068156 ];
result=[ 0  0.12927689  0.10085735  0.096138894 0.090700197
0.090840523 0.072033721 0.075419832 0.070174333    ];
y = zeros(1,9);
for i=1:9
    y(i)=latest(0.0002,2.5,z(i),0.0767,0.0223, 0.3289);
    if i > 1
        y(i) = y(i) * 1800 + y(i - 1);
        result(i) = result(i) * 1800 + result(i - 1);
    else
        y(i) = y(i) * 1800;
        result(i) = result(i) * 1800;
    end
end


plot([0, 30, 60, 90, 120, 150, 180, 210, 240],y(1:9))
hold on
plot([0 ,30, 60, 90, 120, 150, 180, 210, 240], result(1:9), 'color',
'k', 'LineStyle' , 'none', 'Marker', 'o')
hold on
```

```
z=[ 2.666666667 2.558400147 2.457985438 2.2 2.04    1.94    1.83
1.74    1.445405951  ];
result=[ 0      0.06887667  0.05455903  0.044191321 0.0315741
0.02127547  0.02198647  0.021012351 0.02358345     ];
y = zeros(1,9);
for i=1:9
    y(i)=latest(6.66667E-05,2.5,z(i),0.0767,0.0223, 0.3289);
    if i > 1
        y(i) = y(i) * 1800 + y(i - 1);
        result(i) = result(i) * 1800 + result(i - 1);
    else
        y(i) = y(i) * 1800;
        result(i) = result(i) * 1800;
    end
end


plot([0, 30, 60, 90, 120, 150, 180, 210, 240],y(1:9))
hold on
plot([0, 30, 60, 90, 120, 150, 180, 210, 240], result(1:9), 'color',
'k', 'LineStyle' , 'none', 'Marker', 'diamond')
hold on
```